



DRBEM APPLICATIONS IN FLUID DYNAMICS PROBLEMS AND DQM  
SOLUTIONS OF HYPERBOLIC EQUATIONS

A THESIS SUBMITTED TO  
THE GRADUATE SCHOOL OF APPLIED MATHEMATICS  
OF  
MIDDLE EAST TECHNICAL UNIVERSITY

BY

BENİSEN PEKMEN

IN PARTIAL FULFILLMENT OF THE REQUIREMENTS  
FOR  
THE DEGREE OF PHILOSOPHY OF DOCTORATE  
IN  
SCIENTIFIC COMPUTING

2014



Approval of the thesis:

**DRBEM APPLICATIONS IN FLUID DYNAMICS PROBLEMS AND DQM  
SOLUTIONS OF HYPERBOLIC EQUATIONS**

submitted by **BENGIŞEN PEKMEN** in partial fulfillment of the requirements for  
the degree of **Philosophy of Doctorate in Department of Scientific Computing,  
Middle East Technical University** by,

Prof. Dr. Bülent Karasözen  
Director, Graduate School of **Applied Mathematics**

\_\_\_\_\_

Prof. Dr. Bülent Karasözen  
Head of Department, **Scientific Computing**

\_\_\_\_\_

Prof. Dr. Münevver Tezer-Sezgin  
Supervisor, **Department of Mathematics, METU**

\_\_\_\_\_

**Examining Committee Members:**

Prof. Dr. Haluk Aksel  
Department of Mechanical Engineering, METU

\_\_\_\_\_

Prof. Dr. Münevver Tezer-Sezgin  
Department of Mathematics, METU

\_\_\_\_\_

Assoc. Prof. Dr. Ömür Uğur  
Scientific Computing, METU

\_\_\_\_\_

Assoc. Prof. Dr. Canan Bozkaya  
Department of Mathematics, METU

\_\_\_\_\_

Assoc. Prof. Dr. Burak Aksoylu  
Department of Mathematics, TOBB ETU

\_\_\_\_\_

**Date:** 26.03.2014



**I hereby declare that all information in this document has been obtained and presented in accordance with academic rules and ethical conduct. I also declare that, as required by these rules and conduct, I have fully cited and referenced all material and results that are not original to this work.**

Name, Last Name: BENGİSEN PEKMEN

Signature :



## ABSTRACT

### DRBEM APPLICATIONS IN FLUID DYNAMICS PROBLEMS AND DQM SOLUTIONS OF HYPERBOLIC EQUATIONS

Pekmen, Bengisen

Ph.D., Department of Scientific Computing

Supervisor : Prof. Dr. Münevver Tezer-Sezgin

2014, 191 pages

In this thesis, problems of fluid dynamics defined by the two-dimensional convection-diffusion type partial differential equations (PDEs) are solved using the dual reciprocity boundary element method (DRBEM). The terms other than the Laplacian are treated as inhomogeneous terms in the DRBEM application. Once the both sides are multiplied by the fundamental solution of Laplace equation, and then integrated over the domain, all the domain integrals are transformed to boundary integrals using the Green's identities. The inhomogeneous terms are approximated with radial basis functions, and the space derivatives in convective terms are easily handled by using the DRBEM coordinate matrix constructed from the radial basis functions. The discretization of the boundary is achieved with linear elements. For the solution of unsteady problems, first order Backward-Euler and third order Houbolt time integration schemes are used. The boundary only nature of DRBEM provides one to obtain the results in a small computational cost compared to the domain discretization methods. Incompressible fluid flow in cavities, natural and mixed convection flow in enclosures are simulated when the medium is porous or non-porous, and with or without magnetic effect. The numerical results are visualized for different non-dimensional physical parameters in terms of streamlines, isotherms, vorticity, induced magnetic field lines and current density contours.

In the thesis, the differential quadrature method (DQM) is also used for solving especially problems defined by hyperbolic equations and nonlinear in nature. DQM is



made use of discretizing both time and space domains, and the solution is obtained at one stroke or blockwise without the need of an iteration. The nonlinearities are handled using an iteration procedure. Accurate results are obtained using considerably small number of Gauss-Chebyshev-Lobatto discretization points at very small expense. Test problems include Klein-Gordon, sine-Gordon equations, hyperbolic telegraph equations, and viscous Burgers' equation.

*Keywords* : DRBEM, Magnetohydrodynamics (MHD), DQM, natural and mixed convection flow

## ÖZ

### AKIŞKANLAR DİNAMİĞİ PROBLEMLERİNDE KARŞILIKLI SINIR ELEMANLARI METODUNUN UYGULAMALARI VE HİPERBOLİK DENKLEMLERİN DİFERANSİYEL KARELEME METODU İLE ÇÖZÜMLERİ

Pekmen, Bengisen

Doktora, Bilimsel Hesaplama Bölümü

Tez Yöneticisi : Prof. Dr. Münevver Tezer-Sezgin

2014, 191 sayfa

Bu tezde, iki boyutlu konveksiyon-difüzyon tipi kısmi diferansiyel denklemler tarafından tanımlanan akışkanlar dinamiği problemleri karşılıklı sınır elemanları yöntemi ile çözülmüştür. Laplace teriminin dışındaki terimler karşılıklı sınır elemanları yöntemi uygulamasında homojen olmayan terimler olarak kabul edilir. Her iki taraf, Laplace denkleminin temel çözümü ile çarpılır ve sonra tanım kümesi üzerinde integrali alınır. Tüm tanım kümesi üzerindeki integraller Green eşitliklerini kullanarak sınır integraline dönüştürülür. Homojen olmayan terimler, radyal temel fonksiyonları ile yaklaştırılır, ve uzay türevleri için radyal temel fonksiyonlarından oluşturulan koordinat matrisi kullanılır. Sınırın ayrıklaştırılması doğrusal elemanlar ile elde edilir. Zamana bağlı problemlerin çözümünde birinci dereceden Geri-Euler ve üçüncü dereceden Houbolt zaman yönünde ilerleme metotları kullanılmaktadır. Karşılıklı sınır elemanları metodunun sadece sınırı ayrıklaştırması, tanım kümesini ayrıklaştıran metotlara göre küçük bir maliyetle sonuçları elde etmeyi sağlar. Ortam gözenekli ya da gözeneksiz ve manyetik etki varken ya da yokken, oyuklardaki sıkıştırılamayan sıvı akışı ve kapalı sistemlerde doğal ve karışık konveksiyon akış problemleri çözülerek profilleri sunulmuştur. Sayısal sonuçlar, farklı fiziksel parametreler için sıvı akımı konturları, eş ısı eğrileri, girdap konturları, indüklenen manyetik alan doğruları ve akım yoğunluğu konturları olarak görselleştirilmektedir.

Tezde, diferansiyel kareleme metodu da, özellikle, doğrusal olmayan hiperbolik den-

klemlerle tanımlı problemleri çözmek için kullanılmaktadır. Diferansiyel kareleme metodu hem zaman hem uzay tanım kümelerini ayrıklaştırarak kullanılır, ve çözüm ardışık yöntem gerek olmaksızın blok blok veya tek bir etapta elde edilir. Doğrusal olmayan durumlar bir ardışık prosedürü kullanarak işlenir. Hassas sonuçlar oldukça az sayıda Gauss-Chebyshev-Lobatto ayrıklaştırma noktalarını kullanarak küçük maliyetle elde edilir. Test problemleri Klein-Gordon, sine-Gordon denklemleri, hiperbolik telegraf denklemleri ve viskoz Burgers denklemini içerir.

*Anahtar Kelimeler:* Karşılıklı Sınır Elemanları Metodu, Manyetohidrodinamik akış, Diferansiyel Kareleme Metodu, doğal ve karışık konveksiyon akış

*To Habibe and Selçuk*



## ACKNOWLEDGMENTS

I would like to express great appreciation to my thesis supervisor Prof. Dr. Münevver Tezer-Sezgin for her strong guidance, encouragement and valuable advices during the development and preparation of this thesis.

I thank to thesis committee members Prof. Dr. M. Haluk Aksel and Assoc. Prof. Dr. Ömür Uğur for their valuable suggestions through my thesis progress presentations. I also thank to other members Assoc. Prof. Dr. Canan Bozkaya and Assoc. Prof. Dr. Burak Aksoylu.

I also thank to the trustees of Atılım University for financial support of international conferences that I intended, and to all staff in Department of Mathematics in Atılım University. In particular, I owe very much thanks to the old chairman Asst. Prof. Dr. O. Tuncay Başkaya, and the new chairman Prof. Dr. Tanıl Ergenç for their tolerance about giving time to make my Ph.D. studies possible.

Special thanks go to my mum Mrs. Habibe Pekmen devoted her life to me, and my dad Mr. Selçuk Pekmen guarding me and mum against each difficulty in our life.

And, the last but not the least, my friend Ferid deserves much thanks for manipulating my complicated and endless figures in one figure, and also for sincere friendship.



## TABLE OF CONTENTS

ABSTRACT . . . . .	vii
ÖZ . . . . .	ix
ACKNOWLEDGMENTS . . . . .	xiii
TABLE OF CONTENTS . . . . .	xv
LIST OF FIGURES . . . . .	xxi
LIST OF TABLES . . . . .	xxvii
LIST OF ABBREVIATIONS . . . . .	xxix

### CHAPTERS

1	INTRODUCTION . . . . .	1
1.1	Fluid dynamics, Magnetohydrodynamics and heat transfer equations . . . . .	2
1.1.1	Navier-Stokes equations . . . . .	2
1.1.2	Natural and mixed convection flows . . . . .	3
1.1.3	Mixed convection flow through a porous medium . . . . .	5
1.1.4	Mixed convection flow in a porous medium under the effect of a magnetic field . . . . .	7
1.1.5	Full Magnetohydrodynamic (MHD) flow equations . . . . .	8
1.1.6	MHD duct flow . . . . .	13
1.2	Literature survey . . . . .	14



1.3	Plan of the thesis . . . . .	24
1.4	Originality of the thesis . . . . .	25
2	DRBEM SOLUTION OF FREE/MIXED CONVECTION FLOWS WITH- OUT OR WITH MAGNETIC EFFECT . . . . .	27
2.1	The dual reciprocity boundary element method . . . . .	27
2.1.1	Boundary discretization with linear elements . . . . .	30
2.1.2	DRBEM for time-dependent equations : $\nabla^2 u = b(x, y, t, \dot{u})$ . . . . .	33
2.1.3	DRBEM for nonlinear convection-diffusion equa- tions : $\nabla^2 u = b(x, y, t, u, \dot{u}, u_x, u_y)$ . . . . .	34
2.1.4	Computation of second order space derivatives us- ing coordinate matrix . . . . .	35
2.1.5	Time integration schemes . . . . .	35
2.1.5.1	Backward-Euler method . . . . .	35
2.1.5.2	Houbolt method . . . . .	36
2.2	DRBEM application to free or mixed convection flows . . . . .	36
2.2.1	Numerical solution of mixed convection flow in a porous medium by DRBEM . . . . .	37
2.2.2	DRBEM solution of free convection in porous en- closures under the effect of a magnetic field . . . . .	42
2.2.2.1	Square cavity case . . . . .	44
2.2.2.2	Isosceles trapezoidal cavity case . . . . .	48
2.2.2.3	Right-angle trapezoidal cavity case . . . . .	53
2.2.3	DRBEM solution of unsteady MHD free convec- tion in a square cavity . . . . .	56
2.2.4	Unsteady mixed convection in a porous lid-driven enclosure under a magnetic field . . . . .	59

3	DRBEM APPLICATIONS TO FULL MHD EQUATIONS . . . . .	67
3.1	MHD flow and heat transfer with magnetic potential in a porous medium ( $\psi - A - T - w$ ) . . . . .	68
3.2	MHD flow and heat transfer with magnetic induction ( $\psi - T - B_x - B_y - w$ ) . . . . .	79
3.2.1	Lid-driven cavity MHD flow . . . . .	80
3.2.2	MHD flow in a lid-driven cavity with a centered square blockage . . . . .	84
3.3	Buoyancy MHD flow with magnetic potential ( $\psi - T - A - j - w$ )	91
3.3.1	Case 1. Staggered double lid-driven cavity MHD flow	93
3.3.2	Case 2. Backward facing step MHD flow . . . . .	99
3.4	Incompressible MHD flow with magnetic potential ( $\psi - A - w$ )	104
3.4.1	Case 1. Lid-driven cavity MHD flow . . . . .	105
3.4.2	Case 2. MHD flow over a square cylinder . . . . .	109
4	DQM TIME-DQM SPACE APPLICATIONS TO HYPERBOLIC and COUPLED PARABOLIC EQUATIONS . . . . .	115
4.1	Differential quadrature method . . . . .	116
4.1.1	Polynomial-based differential quadrature (PDQ) method	116
4.1.2	Fourier expansion-based differential quadrature (FDQ) method . . . . .	118
4.1.3	Grid points distribution . . . . .	119
4.2	One- and two-dimensional hyperbolic telegraph equations . .	120
4.2.1	One-dimensional hyperbolic telegraph equation . .	121
4.2.1.1	Test problem. . . . .	123
4.2.2	Two-dimensional hyperbolic telegraph equation . .	125

	4.2.2.1	Test problem 1. . . . .	127
	4.2.2.2	Test problem 2. . . . .	127
	4.2.2.3	Test problem 3. . . . .	128
4.3		Klein-Gordon and sine-Gordon equations . . . . .	130
	4.3.1	Klein-Gordon equation (KGE) . . . . .	131
	4.3.2	sine-Gordon equation (SGE) . . . . .	133
	4.3.3	Solution procedure . . . . .	135
	4.3.4	Klein-Gordon problems . . . . .	136
	4.3.4.1	Quadratic Klein-Gordon equation . . .	136
	4.3.4.2	Kink Wave (Cubic Klein-Gordon equation) . . . . .	137
	4.3.4.3	Single-Soliton. . . . .	138
	4.3.4.4	Double Soliton. . . . .	140
	4.3.5	sine-Gordon problems. . . . .	142
	4.3.5.1	Test sine-Gordon problem. . . . .	142
	4.3.5.2	Line soliton in an inhomogeneous medium	143
	4.3.5.3	Circular ring solitons . . . . .	145
	4.3.5.4	Collision of two circular solitons . . .	148
	4.3.5.5	Collision of four circular solitons . . .	148
4.4		The Burgers equations in one- and two-space . . . . .	151
	4.4.1	The coupled Burgers' equations in one-space . . .	151
	4.4.1.1	Test problem for 1D viscous Burgers' equation . . . . .	152
	4.4.2	The Burgers equations in two-spaces . . . . .	153

4.4.2.1	Test problem for 2D viscous Burgers' equation. . . . .	154
4.5	MHD flow in a rectangular duct . . . . .	156
5	CONCLUSION . . . . .	163
	REFERENCES . . . . .	165
APPENDICES		
A	Non-dimensionalizations . . . . .	179
A.1	Stream function equation . . . . .	179
A.2	Energy equation . . . . .	179
A.3	Induction, magnetic potential and current density equations . . . . .	180
A.4	Vorticity transport equation . . . . .	183
B	Composite quadrature rules with equally spaced points . . . . .	187
B.1	Composite trapezoidal rule . . . . .	187
B.2	Composite Simpson's rule . . . . .	187
B.3	Composite Simpson's 3/8 rule . . . . .	187
	CURRICULUM VITAE . . . . .	189



## LIST OF FIGURES

Figure 2.1 Configuration of the region and the boundary conditions. . . . .	28
Figure 2.2 Internal angle at the node $i$ . . . . .	29
Figure 2.3 Configuration for linear elements. . . . .	31
Figure 2.4 Problem 2.2.1 configuration. . . . .	37
Figure 2.5 Problem 2.2.1: $Pr = 0.71$ , $Gr = 10^3$ , $\epsilon_p = 1$ , $\gamma = 0.1$ . . . . .	40
Figure 2.6 Problem 2.2.1: $Pr = 0.71$ , $Da = 0.01$ , $\epsilon_p = 1$ , $\gamma = 0.5$ . . . . .	40
Figure 2.7 Problem 2.2.1: $Da = 0.01$ , $Gr = 10^3$ , $\epsilon_p = 1$ , $\gamma = 0.5$ . . . . .	40
Figure 2.8 Problem 2.2.1: Mid-u-velocity profile and average Nusselt number on the heated wall. . . . .	41
Figure 2.9 Problem 2.2.1: Average Nusselt number variations with $\epsilon_p$ on the heated wall. . . . .	41
Figure 2.10 Problem 2.2.2 configurations. . . . .	42
Figure 2.11 Problem 2.2.2.1: $Ra = 10^5$ , $\varphi = \pi/6$ . . . . .	46
Figure 2.12 Problem 2.2.2.1: $Ha = 50$ , $\varphi = \pi/6$ . . . . .	47
Figure 2.13 Problem 2.2.2.1: $Ha = 50$ , $Ra = 10^5$ , $N = 168$ , $K = 400$ . . . . .	48
Figure 2.14 Problem 2.2.2.2: $Ra = 10^3$ , $\varphi = 0$ , $N = 148$ , $K = 1127$ . . . . .	50
Figure 2.15 Problem 2.2.2.2: $Ha = 5$ , $\theta_s = 72^0$ , $\varphi = 0$ . . . . .	51
Figure 2.16 Problem 2.2.2.2: $Ra = 10^3$ , $Ha = 5$ . . . . .	52
Figure 2.17 Problem 2.2.2.3: Streamlines and isotherms in right-angle trapezoidal cavity, $Ra = 10^3$ . . . . .	54
Figure 2.18 Problem 2.2.2.3: Streamlines and isotherms in right-angle trapezoidal cavity, $Ha = 10$ . . . . .	55
Figure 2.19 Problem 2.2.3: Square porous enclosure. . . . .	56
Figure 2.20 Problem 2.2.3: Isotherms and streamlines at steady-state with different $Ha$ values fixing $Ra = 10^3$ . . . . .	58

Figure 2.21 Problem 2.2.3: Steady-state isotherms and streamlines w.r.t varying $Ra$ fixing $Ha = 25$ , $\varphi = \pi/6$ , $\Delta t = 0.01$ . . . . .	58
Figure 2.22 Problem 2.2.3: Heat generation and absorption fixing $Ha = 10$ , $Ra = 10^3$ , $\varphi = \pi/6$ , $\Delta t = 0.1$ . . . . .	58
Figure 2.23 Problem 2.2.4 configuration. . . . .	59
Figure 2.24 Problem 2.2.4: Darcy variation with $Gr = Re = 100$ , $Ha = Ra_I = 0$ , $\Delta t = 0.25$ . . . . .	62
Figure 2.25 Problem 2.2.4: Hartmann variation with $Da = 0.1$ , $Gr = Re = 100$ , $Ra_I = 0$ , $\Delta t = 0.5(Ha = 10)$ ; $\Delta t = 0.1(\gamma = 0.1, Ha = 100)$ . . . . .	62
Figure 2.26 Problem 2.2.4: Reynolds variation with $Da = 0.1$ , $Gr = 10^4$ , $Ha = Ra_I = 0$ , $\Delta t = 0.5(Re = 50)$ ; $\Delta t = 0.1(Re = 500)$ . . . . .	63
Figure 2.27 Problem 2.2.4: Grashof variation with $Da = 0.1$ , $Re = 100$ , $Ha = Ra_I = 0$ , $\Delta t = 0.5(Gr = 10^3)$ ; $\Delta t = 0.1(Gr = 10^5)$ . . . . .	63
Figure 2.28 Problem 2.2.4: Internal Rayleigh number variation with $Da = 0.01$ , $Gr = 100$ , $Re = 1000$ , $Ha = 0$ , $\Delta t = 0.5$ . . . . .	64
Figure 2.29 Problem 2.2.4: Mid-velocity profiles as $Ha$ varies fixing $Da = 0.1$ , $Gr = Re = 100$ , $Ra_I = 0$ . . . . .	64
Figure 2.30 Problem 2.2.4: Average Nusselt number. . . . .	64
Figure 3.1 Problem 3.1 configuration. . . . .	69
Figure 3.2 Problem 3.1: $Gr = Re = Rem = 100$ , $Pr = 1$ , $Ha = 5$ , $\Delta t = 0.25$ . . . . .	73
Figure 3.3 Problem 3.1: $Da = 0.1$ , $Pr = 1$ , $Gr = Re = 100$ , $Ha = 5$ , $\Delta t = 0.25$ . . . . .	74
Figure 3.4 Problem 3.1: $Da = 0.1$ , $Pr = 1$ , $Gr = Re = Rem = 100$ ; $\Delta t = 0.25(Ha = 5, 25)$ ; $\Delta t = 0.2, \gamma = 0.5(Ha = 50)$ ; $\Delta t = 0.1, \gamma = 0.1(Ha = 100)$ ; $\Delta t = 0.01, \gamma = 0.1(Ha = 300)$ . . . . .	75
Figure 3.5 Problem 3.1: $x$ -direction external magnetic field with $Da = 0.1$ , $Pr = 1$ , $Gr = Re = Rem = 100$ ; $\Delta t = 0.25(Ha = 5, 25)$ ; $\Delta t = 0.2, \gamma = 0.5(Ha = 50)$ ; $\Delta t = 0.1, \gamma = 0.1(Ha = 100)$ . . . . .	76
Figure 3.6 Problem 3.1: $Da = 0.1$ , $Pr = 1$ , $Gr = 10^4$ , $Ha = 5$ , $Rem = 100$ , $\Delta t = 0.25$ . . . . .	77
Figure 3.7 Problem 3.1: $Da = 0.1$ , $Pr = 1$ , $Re = Rem = 100$ , $Ha = 5$ ; $\Delta t = 0.25(Gr = 10^3, 10^4)$ ; $\Delta t = 0.1(Gr = 10^5)$ ; $\Delta t = 0.1, \gamma = 0.1(Gr = 10^6)$ . . . . .	77

Figure 3.8 Problem 3.1: Average Nusselt number variation with $Gr = Re = 100, Pr = 1$ . . . . .	78
Figure 3.9 Problem 3.1: Drag coefficient observation with $Gr = Re = 100, Pr = 1$ . . . . .	78
Figure 3.10 Problem 3.2.1 configuration. . . . .	81
Figure 3.11 Problem 3.2.1: $Rem = 100, Ra = Ha = 10, Pr = 0.1, \Delta t = 0.25$ . . . . .	82
Figure 3.12 Problem 3.2.1: $Rem = 40, Re = 400, Ra = 1000, Pr = 0.1, \Delta t = 0.5 (Ha = 5), \Delta t = 0.2 (Ha = 50), \Delta t = 0.1$ with $\gamma = 0.1 (Ha = 100)$ . . . . .	83
Figure 3.13 Problem 3.2.1: $Re = 400, Ha = 10, Ra = 1000, Pr = 0.1, \Delta t = 0.25$ . . . . .	83
Figure 3.14 Problem 3.2.1: $Re = 400, Rem = Ha = 10, Pr = 0.1, \Delta t = 0.25$ . . . . .	84
Figure 3.15 Problem 3.2.2: Configuration of square obstacle in a square cavity. . . . .	85
Figure 3.16 Problem 3.2.2: Streamlines and isotherms in terms of Richardson variation, $Pr = 0.71, Re = 100, L_s = 0.25$ . . . . .	86
Figure 3.17 Problem 3.2.2: $Re = 100, Rem = 1, Ha = 10, Pr = 0.1, \Delta t = 0.25 (Ra = 10^3, Ra = 10^4), \Delta t = 0.1 (Ra = 10^5), \Delta t = 0.01$ with $\gamma = 0.1 (Ra = 10^6)$ . . . . .	87
Figure 3.18 Problem 3.2.2: $Rem = 100, Ha = 10, Pr = 0.1, Ra = 10^3, \Delta t = 0.25 (Re = 100, 400, 1000), \Delta t = 0.1 (Re = 2500)$ . . . . .	88
Figure 3.19 Problem 3.2.2: $Re = 100, Ha = 10, Pr = 0.1, Ra = 10^3, \Delta t = 0.25$ . . . . .	88
Figure 3.20 Problem 3.2.2: $Re = Rem = 100, Ra = 10^3, Pr = 0.1, \Delta t = 0.25 (Ha = 5, Ha = 25), \Delta t = 0.25$ with $\gamma = 0.5 (Ha = 50), \Delta t = 0.1$ with $\gamma = 0.1 (Ha = 100)$ . . . . .	89
Figure 3.21 Problem 3.2.2: Observation on streamlines, $Re = Rem = 100, Ra = 10^3, Pr = 0.1$ . . . . .	90
Figure 3.22 Problem 3.3.1: Staggered double lid-driven cavity. . . . .	93
Figure 3.23 Problem 3.3.1: $Rem = 100, Ha = 10, Ra = 10, Pr = 0.1, \Delta t = 0.2$ . . . . .	95
Figure 3.24 Problem 3.3.1: $Re = 400, Ha = 10, Ra = 10^3, Pr = 0.1, \Delta t = 0.01, 0.1, 0.1$ . . . . .	96
Figure 3.25 Problem 3.3.1: $Re = 400, Rem = 10, Ra = 10^3, Pr = 0.1, \Delta t = 0.1 (Ha = 5, 50), \Delta t = 0.1$ with $\gamma = 0.5 (Ha = 100)$ . . . . .	96



Figure 3.26 Problem 3.3.1: Streamlines $Re = 100, Pr = 0.1, Ra = 10^3$ . . . . .	97
Figure 3.27 Problem 3.3.1: Magnetic potential $Re = 100, Pr = 0.1, Ra = 10^3$	97
Figure 3.28 Problem 3.3.1: $Re = 400, Rem = Ha = 10, Pr = 0.1, \Delta t = 0.1$ .	98
Figure 3.29 Problem 3.3.1: $\overline{Nu}_t$ at the hot top wall is observed w.r.t $Ha$ and $Rem$ .	98
Figure 3.30 Problem 3.3.2: Backward facing step MHD flow configuration. . . . .	99
Figure 3.31 Problem 3.3.2: Streamlines in BFS for incompressible fluid flow for varying $Re$ . . . . .	101
Figure 3.32 Problem 3.3.2: Streamlines in natural convection flow varying $Ra$ . . . . .	101
Figure 3.33 Problem 3.3.2: $Rem = 10, Ha = 5, Ra = 10^3, Pr = 0.1$ . . . . .	102
Figure 3.34 Problem 3.3.2: $Re = Rem = 100, Ra = 10^3, Pr = 0.1$ . . . . .	102
Figure 3.35 Problem 3.3.2: $Re = 100, Ha = 5, Ra = 10^3, Pr = 0.1$ . . . . .	103
Figure 3.36 Problem 3.3.2: $Re = Rem = 100, Ha = 5, Pr = 0.1$ . . . . .	103
Figure 3.37 Problem 3.4.1: Configuration of the lid-driven cavity MHD flow. . . . .	106
Figure 3.38 Problem 3.4.1: $Rem = 100, Ha = 10, \Delta t = 0.25$ . . . . .	107
Figure 3.39 Problem 3.4.1: $Re = 100, Ha = 10, \Delta t = 0.1$ . . . . .	107
Figure 3.40 Problem 3.4.1: $Re = Rem = 100, \Delta t = 0.5, 0.2, 0.1$ , for $Ha =$ $5, 50, 100$ . . . . .	108
Figure 3.41 Problem 3.4.1: Velocity profiles at mid-sections of the cavity with various $Ha$ . . . . .	108
Figure 3.42 Problem 3.4.2: Configuration of the MHD flow past a square cylinder.	109
Figure 3.43 Problem 3.4.2: Streamlines at steady-state, $Rem = 10, Ha = 5$ . . . . .	110
Figure 3.44 Problem 3.4.2: Streamlines at steady-state, $Re = 100, Rem = 10$ . . . . .	111
Figure 3.45 Problem 3.4.2: Magnetic potential lines at steady-state, $Re = 100, Ha =$ $5$ . . . . .	111
Figure 3.46 Problem 3.4.2: Streamlines at transient levels, $Re = 300, Rem =$ $10, Ha = 5$ . . . . .	112
Figure 3.47 Problem 3.4.2: Streamlines at transient levels, $Re = 300, Rem =$ $10, Ha = 5$ . . . . .	113
Figure 4.1 Non-uniform grid distribution examples. . . . .	120

Figure 4.2 Problem 4.2.1.1: Numerical and exact solutions at different times with $\Delta t = 0.25$ , $N = 17$ using Neumann BCs. . . . .	124
Figure 4.3 Problem 4.2.2.3: RMS error versus ES grid points in time direction.	130
Figure 4.4 Problem 4.2.2.3: RMS error versus GCL grid points in time direction.	130
Figure 4.5 Time blocks for 1D KGE. . . . .	133
Figure 4.6 Time blocks for 2D sine-Gordon equation. . . . .	135
Figure 4.7 Problem 4.3.4.2: Space-time graph of numerical solution of Kink Wave up to $t = 12$ . . . . .	139
Figure 4.8 Problem 4.3.4.3: Surface plot of Single-Soliton. . . . .	140
Figure 4.9 Problem 4.3.4.4: Surface plot of collision of two solitons at $t = 7.5$ .	142
Figure 4.10 Problem 4.3.5.1: Plots for test sine-Gordon problem. . . . .	143
Figure 4.11 Problem 4.3.5.2: Line soliton in an inhomogenous medium. . . . .	144
Figure 4.12 Problem 4.3.5.3: Circular ring solitons. . . . .	147
Figure 4.13 Problem 4.3.5.4: Collision of two circular solitons . . . . .	149
Figure 4.14 Problem 4.3.5.5: Collision of four circular solitons . . . . .	150
Figure 4.15 Problem 4.5: $Ha = 10$ , $T = 0.5$ , $N = M = 21$ , $L = 6$ . . . . .	158
Figure 4.16 Problem 4.5: Surface and contour plots of velocity and induced magnetic field lines with $Ha = 10$ . . . . .	159
Figure 4.17 Problem 4.5: Surface and contour plots of velocity and induced magnetic field lines with $Ha = 100$ , $T = 0.3$ , $N = M = 36$ , $L = 4$ . . . . .	160
Figure 4.18 Problem 4.5: Surface and contour Plots of velocity and induced magnetic field lines with $Ha = 500$ , $T = 0.3$ , $N = M = 61$ , $L = 4$ . . . . .	161



## LIST OF TABLES

Table 2.1 Problem 2.2.2.1: Average Nusselt number in square cavity. . . . .	49
Table 2.2 Problem 2.2.2.2: Average Nusselt number in isosceles trapezoidal cavity. . . . .	53
Table 2.3 Problem 2.2.3: The average Nusselt numbers $\overline{Nu}$ for $Ra = 1000$ with $Q = 1$ . . . . .	58
Table 3.1 Problem 3.1: Comparison of $\overline{Nu}$ at the top wall, $Pr = 0.71$ . . . . .	71
Table 3.2 Problem 3.1: Grid analysis with $Da = 0.1$ , $Pr = 1$ , $Gr = Re = Rem = 100$ . . . . .	71
Table 3.3 Problem 3.2.1: CPU times and $\overline{Nu}$ on the heated wall with $Re = 1$ , $Pr = 0.71$ , $Gr = 10^4$ , $\Delta t = 0.01$ . . . . .	81
Table 3.4 Average Nusselt number through the heated left wall. . . . .	92
Table 3.5 Problem 3.3.1: Analyzing the grid independence. . . . .	93
Table 3.6 Problem 3.4: $ \psi_{\min} $ values of streamlines of Navier-Stokes flow in a lid-driven cavity. . . . .	105
Table 4.1 Problem 4.2.1.1: RMS errors with $N = 11$ using Dirichlet BCs. . . . .	124
Table 4.2 Problem 4.2.1.1: RMS errors with $\Delta t = 0.25$ with Neumann BCs. . . . .	124
Table 4.3 Problem 4.2.2.1: Relative errors. . . . .	127
Table 4.4 Problem 4.2.2.2: Relative errors with different values of $\alpha$ . . . . .	128
Table 4.5 Problem 4.2.2.3: RMS errors for $u(x,t)$ using $M = N = 11$ , $L = 13$ . . . . .	129
Table 4.6 Problem 4.3.4.1: Errors in quadratic Klein-Gordon equation. . . . .	137
Table 4.7 Problem 4.3.4.2: Errors for Kink Wave with different number of grid points in space at $t = 1$ . . . . .	138
Table 4.8 Problem 4.3.4.2: Errors for Kink Wave at different times. . . . .	138
Table 4.9 Problem 4.3.4.3: Errors for Single Soliton with different number of grid points in space at $t = 1$ . . . . .	140

Table 4.10 Problem 4.3.4.3: Errors for Single Soliton at different times. . . . .	140
Table 4.11 Problem 4.3.4.4: Errors for Double Soliton at different times with $E(0) = 0.237807$ . . . . .	141
Table 4.12 Problem 4.3.5.1: Errors for sine-Gordon test problem. . . . .	143
Table 4.13 Problem 4.3.5.3: The energy of the circular ring soliton when $E(0) =$ 150.7983. . . . .	145
Table 4.14 Problem 4.4.1.1: Errors for 1D Burgers' equations with $N = 51$ , $L =$ 11. . . . .	153
Table 4.15 Problem 4.4.2.1: $L_\infty$ errors for 2D Burgers' equations for various values of $L$ and $Re$ . . . . .	155
Table 4.16 Problem 4.4.2.1: 2D Burgers' equations solution with $Re = 100$ , $N =$ $M = 21$ , $L = 13$ at $t = 0.5, 2$ . . . . .	155
Table 4.17 Problem 4.4.2.1: 2D Burgers' equations with $Re = 1000$ , $N = M =$ 23, $bl = 9$ , $L = 7$ at $t = 0.5, 2$ . . . . .	156

## LIST OF ABBREVIATIONS

$u$	$x$ -component of the velocity of the fluid
$v$	$y$ -component of the velocity of the fluid
$w$	vorticity
$\psi$	stream function
$p$	pressure
$L$	characteristic length; number of grid points in time domain in DQM
$U$	characteristic velocity
$\nu$	kinematic viscosity of the fluid
$\mu$	dynamic viscosity of the fluid
$Re$	Reynolds number ( $UL/\nu$ )
$\rho_0$	reference density of the fluid
$\rho$	fluid density
$\beta$	thermal expansion coefficient
$\alpha$	thermal diffusivity
$c_p$	specific heat at constant pressure
$k_f$	thermal conductivity of the fluid
$k_s$	thermal conductivity of the solid
$g$	gravitational acceleration
$T$	Temperature
$T_h$	Temperature of the hot wall
$T_c$	Temperature of the cold wall
$\Delta T$	temperature difference
$Pr$	Prandtl number ( $\nu/\alpha$ )
$Ra$	Rayleigh number ( $g\beta\Delta TL^3/(\nu\alpha)$ )
$Gr$	Grashof number ( $Ra/Pr$ )
$\mu_e$	effective dynamic viscosity
$\alpha_e$	effective thermal diffusivity of the porous medium
$\epsilon_p$	porosity of the porous medium
$\kappa$	permeability of the porous meidum
$V_c$	control volume

$c_F$	inertia coefficient
$d_p$	diameter of a pore
$k_e$	effective thermal conductivity of the porous medium
$(\rho c_p)_f$	thermal capacity of the fluid
$(\rho c_p)_s$	thermal capacity of the solid
$(\rho c_p)_e$	effective thermal capacity of the porous medium
$B_0$	magnitude of the applied magnetic field
$\sigma$	electrical conductivity of the fluid
$Ha$	Hartmann number ( $B_0\sqrt{\kappa\sigma/\mu}$ ) in a porous; ( $B_0L\sqrt{\sigma/\nu\rho}$ ) in a non-porous medium
$Da$	Darcy number ( $\kappa/L^2$ )
$\mu_m$	magnetic permeability of the fluid
$\epsilon_0$	permittivity of free space
$q$	total charge density
<b>J</b>	current density
<b>B</b>	magnetic flux density
$B_x$	$x$ -component of induced magnetic field
$B_y$	$y$ -component of induced magnetic field
<b>E</b>	electric field
<b>F<sub>l</sub></b>	Lorentz force
$Rem$	magnetic Reynolds number ( $UL\mu_m\sigma$ )
<b>A</b>	magnetic potential
$\eta$	magnetic diffusivity $\eta = 1/(\sigma\mu_m)$
$q_0'''$	heat generation ( $Wm^{-3}$ )
$Q$	heat generation parameter
$\varphi$	inclination angle of the applied magnetic field
$\gamma$	relaxation parameter
$N$	number of boundary points in DRBEM; number of $x$ -direction grid points in DQM
$K$	number of interior points in DRBEM
$M$	number of $y$ -direction grid points in DQM

# CHAPTER 1

## INTRODUCTION

A fluid is distinguished from a solid with its continuous deformation when it is exposed to a force. The fluid dynamics deals with the motion of a fluid and energy exchange in the fluid. Thus, the fundamental equations of fluid dynamics are based on the continuity equation, the momentum equations and the energy equation (the Navier-Stokes equations plus the energy equation).

If the energy transfer is due to the temperature difference, then it is called heat transfer. The diffusion of energy is referred to as conduction, and the convection is the transfer of energy due to the movement of the fluid.

Even though different types of regions (in which the fluid flows) such as cavities or channels are considered in most of the studies, the fluid flow through a porous medium has also taken a great deal of attention due to the applications arising in geophysics, insulation for buildings, packed sphere beds and chemical catalytic reactors. In different combinations of models (Darcy, Brinkman, Forchheimer), convective flows in porous media are investigated extensively.

The effect of an externally applied magnetic field on the fluid flow and heat transfer has also attracted a great deal of interest. When the fluid is electrically conducting, fluid and the externally applied magnetic field interact with each other, and generate an electromotive force resulting with induced current density which causes the induced magnetic field. The total magnetic field (external and induced) interacts with the induced current density such that the Lorentz force emerges. The model equations are the Maxwell's equations from electrodynamics combined with the Navier-Stokes equations from fluid dynamics. In some cases, the induced magnetic field is neglected due to the little impact of velocity field on the total magnetic field.

Some remarkable fluid properties which are mostly mentioned throughout the thesis may be summarized as follows. *Viscosity* of a fluid is the resistance of the fluid to shear stresses. The kinematic viscosity  $\nu$  and the dynamic viscosity  $\mu$  are related to each other with the relation  $\nu = \mu/\rho$ , where  $\rho$  is the fluid density. If  $\rho$  is constant, then the fluid is called *incompressible*. Viscous flows are classified as laminar and turbulent flows. If a fluid flows in a smooth or regular path, the flow is called as *laminar flow*. The converse is the *turbulent flow*. Viscous forces in laminar flow, and inertial forces in turbulent flow are dominant, respectively. *Newtonian fluid* (air, water, gasoline) is a



fluid that the viscous stresses are linearly related to the strain rate.

## 1.1 Fluid dynamics, Magnetohydrodynamics and heat transfer equations

### 1.1.1 Navier-Stokes equations

The fluid motion is characterized by the Navier-Stokes equations. In most of the engineering problems such as modeling the turbulent hydrodynamic problems, flow around an airfoil etc., Navier-Stokes equations are encountered.

These equations may be formed in different ways as the velocity-pressure, the stream function only (fourth order), the velocity-vorticity and the stream function-vorticity forms. Each of these forms has advantages and disadvantages. The difficulty in velocity-pressure form is the absence of boundary conditions for the pressure field, and the non-existence of pressure variable in the continuity equation. However, the solution of Navier-Stokes equations will be in original variables as the velocity and pressure. The disadvantage of the stream function only (fourth order) formulation is the necessity of two boundary conditions at one boundary point. Although the velocity-vorticity formulation eliminates the pressure term, an additional criterion is examined to check the continuity condition. The stream function-vorticity formulation is an efficient formulation due to the elimination of pressure together with automatic satisfaction of continuity equation. This formulation is not suitable for three dimension due to the definition of stream function or computational complexity. On account of the two-dimensional flow consideration, the stream function-vorticity form of the Navier-Stokes equations has been adopted throughout the thesis.

Basic equations for unsteady, two-dimensional, laminar flow of an incompressible, viscous fluid without body forces are given in terms of velocity and pressure of the fluid

$$\nabla \cdot \mathbf{u} = 0 \quad (\text{continuity equation}) \quad (1.1a)$$

$$\nu \nabla^2 \mathbf{u} = \frac{\partial \mathbf{u}}{\partial t} + \mathbf{u} \cdot \nabla \mathbf{u} + \frac{1}{\rho} \nabla p \quad (\text{momentum equations}) \quad (1.1b)$$

where  $\mathbf{u} = (u, v)$  is the velocity field of the fluid,  $\rho$  is the fluid density,  $\nu$  is the kinematic viscosity and  $p$  is the pressure. The flow is driven by means of a pressure gradient  $\nabla p$ .

For obtaining dimensionless equations, the following non-dimensional variables are defined as

$$x' = \frac{x}{L}, \quad y' = \frac{y}{L}, \quad u' = \frac{u}{U}, \quad v' = \frac{v}{U}, \quad t' = \frac{tU}{L}, \quad p' = \frac{p}{\rho U^2}, \quad (1.2)$$

where  $L$  is the characteristic length,  $U$  is the characteristic velocity. Substituting these variables into Eqs.(1.1a)-(1.1b), and then dropping the prime notations, the non-dimensional governing Navier-Stokes equations in  $(u - v - p)$  form are expressed as

$$\frac{\partial u}{\partial x} + \frac{\partial v}{\partial y} = 0 \quad (1.3a)$$

$$\frac{1}{Re} \nabla^2 u = \frac{\partial u}{\partial t} + u \frac{\partial u}{\partial x} + v \frac{\partial u}{\partial y} + \frac{\partial p}{\partial x} \quad (1.3b)$$

$$\frac{1}{Re} \nabla^2 v = \frac{\partial v}{\partial t} + u \frac{\partial v}{\partial x} + v \frac{\partial v}{\partial y} + \frac{\partial p}{\partial y}, \quad (1.3c)$$

where  $Re = UL/\nu$  is the Reynolds number which is the ratio of inertial forces to viscous forces. In general, the laminar flow is characterized by  $Re < 2100$ .

In order to satisfy the continuity condition, stream function is defined as ( $\mathbf{u} = \nabla \times \psi$ )

$$u = \frac{\partial \psi}{\partial y}, \quad v = -\frac{\partial \psi}{\partial x}. \quad (1.4)$$

By the definition of vorticity,  $\mathbf{w} = \nabla \times \mathbf{u}$ , and Eq.(1.4), the stream function equation is derived as

$$w = \frac{\partial v}{\partial x} - \frac{\partial u}{\partial y} = \frac{\partial}{\partial x} \left( -\frac{\partial \psi}{\partial x} \right) - \frac{\partial}{\partial y} \left( \frac{\partial \psi}{\partial y} \right) = -\nabla^2 \psi. \quad (1.5)$$

If Eq.(1.3c) and Eq.(1.3b) are differentiated with respect to  $x$  and  $y$ , respectively, and then subtracted from each other, the vorticity transport equation is obtained as

$$\frac{1}{Re} \nabla^2 w = \frac{\partial w}{\partial t} + \frac{\partial \psi}{\partial y} \frac{\partial w}{\partial x} - \frac{\partial \psi}{\partial x} \frac{\partial w}{\partial y}. \quad (1.6)$$

Equations (1.5)-(1.6) constitute now the laminar, time dependent flow of an incompressible, viscous fluid in a two-dimensional region. Since the boundary information is usually given for the velocity of the fluid, stream function and/or its normal derivatives are available on the boundary through the relation (1.4). But, the vorticity is unknown and must be determined by some means on the boundary. This is another drawback of stream function-vorticity formulation although the continuity equation is automatically satisfied, and the number of equations is reduced.

### 1.1.2 Natural and mixed convection flows

The driving force for natural (free) convection in a fluid flow is the temperature variation of the fluid in the region considered. When the fluid is heated, density decreases and the fluid rises. In a gravitational field, the net force between this movement and the gravitational force emerges which is referred to as *buoyancy force*. Thus, the Navier-Stokes equations accompanied with the energy equation define the natural convection flow.

Natural convection flow has many applications such as building insulation, solar collectors, ovens and rooms etc. Further, free convection flows may occur in bounded or unbounded regions.

When the fluid motion is generated by an external force such as a pump, fan or lid as well as the temperature difference on the walls of the region, it is called forced convection. The most encountered physical problems of forced convection are the lid-driven cavity problems.

Mixed convection flow is associated with both natural and forced convection flows according to the dominance of external force or temperature difference. The interaction between natural and forced convection has numerous applications as in thermal energy storage tanks, air-conditioned rooms, etc.

The fluid properties are assumed to be constant except density in the buoyancy term. Buoyancy force is added to  $y$ -component of momentum equation (assuming  $+y$ -direction of gravitational acceleration vector) according to Boussinesq approximation which is

$$\rho = \rho_0[1 - \beta(T - T_c)], \quad (1.7)$$

where  $\rho$  is the fluid density,  $\rho_0$  is the density of the fluid at the reference temperature  $T_0 = T_c$ ,  $\beta$  is the thermal expansion coefficient defined as  $\beta = (-1/\rho) (\partial\rho/\partial T)_p$  at constant pressure,  $T$  is the temperature of the fluid,  $T_c$  is the cold wall temperature.

The two-dimensional mixed convection flow of an incompressible fluid is considered neglecting viscous dissipation<sup>1</sup> and thermal radiation<sup>2</sup>. Then, the governing equations involving Navier-Stokes equations and energy equations are

$$\nabla \cdot \mathbf{u} = 0 \quad (1.8a)$$

$$\nu \nabla^2 \mathbf{u} = \frac{\partial \mathbf{u}}{\partial t} + \mathbf{u} \cdot \nabla \mathbf{u} + \frac{1}{\rho} \nabla p + \mathbf{g} \beta (T - T_c) \quad (1.8b)$$

$$\alpha \nabla^2 T = \frac{\partial T}{\partial t} + \mathbf{u} \cdot \nabla T, \quad (1.8c)$$

where  $\alpha = k_f/(\rho c_p)$  is the thermal diffusivity with thermal conductivity  $k_f$  and specific heat capacity  $c_p$ ,  $\mathbf{g}$  is the gravitational acceleration vector.

In order to make these governing equations dimensionless, the following non-dimensional parameters are defined as

$$x' = \frac{x}{L}, \quad y' = \frac{y}{L}, \quad u' = \frac{u}{U}, \quad v' = \frac{v}{U}, \quad t' = \frac{tU}{L}, \quad p' = \frac{p}{\rho U^2}, \quad T' = \frac{T - T_c}{T_h - T_c}, \quad (1.9)$$

where  $T_h$  is the heated wall temperature. Substituting Eq.(1.9) into Eqs.(1.8), and then dropping the prime notation and eliminating the pressure terms using the definitions of stream function and vorticity (Eqs.(1.4)-(1.5)) and then cross differentiating, subtracting, the non-dimensional governing equations in terms of stream function  $\psi$ ,

---

<sup>1</sup> The irreversible conversion of work done against viscous forces into internal (thermal) energy.

<sup>2</sup> Electromagnetic radiation emitted by accelerated charged particles (due to heat) in matter.

temperature  $T$  and vorticity  $w$  are written as

$$\nabla^2\psi = -w \quad (1.10a)$$

$$\frac{1}{Re}\nabla^2w = \frac{\partial w}{\partial t} + u\frac{\partial w}{\partial x} + v\frac{\partial w}{\partial y} - \frac{Gr}{Re^2}\frac{\partial T}{\partial x} \quad (1.10b)$$

$$\frac{1}{PrRe}\nabla^2T = \frac{\partial T}{\partial t} + u\frac{\partial T}{\partial x} + v\frac{\partial T}{\partial y}, \quad (1.10c)$$

where the non-dimensional physical parameters are

$$Pr = \frac{\nu}{\alpha}, \quad Ra = \frac{g\beta\Delta TL^3}{\nu\alpha} = GrPr \quad (1.11)$$

with the gravitational acceleration  $g$  and the temperature difference  $\Delta T = T_h - T_c$  between hot and cold walls.

Prandtl number  $Pr$  is  $\simeq 0.71$  for air and gaseous helium,  $Pr \simeq 7$  in water and  $Pr \simeq 0.015$  for mercury. Liquid metals provide the flows with  $Pr \ll 1$  such that heat diffuses faster than the momentum diffusion.

Grashof number  $Gr$  is the ratio of buoyancy force to viscous force. The Richardson number  $Ri = Gr/Re^2$  determines whether the flow is natural, forced or mixed convection flow. The heat transfer is natural convection if  $Ri \gg 1$ , forced convection if  $Ri \ll 1$  and mixed convection if  $Ri \approx 1$ .

The ratio of convective heat transfer to conductive heat transfer is referred to as *Nusselt number*. Integrating the convective heat transfer coefficient and dividing it by surface (enclosure) length  $L$ , the average Nusselt number  $\overline{Nu}$  is utilized as [137]

$$\overline{Nu} = \frac{\int_0^L h_x dx}{L}, \quad \text{where } h_x = \frac{k_f \left( \frac{\partial T}{\partial y} \right)_{y=L}}{T_h - T_c}. \quad (1.12)$$

### 1.1.3 Mixed convection flow through a porous medium

Porous medium is characterized by pores between at least two homogeneous material constituents.

Darcy (1856) investigated the ratio of the water volume passing through a sand layer to the pressure drop across the length of the layer. This ratio is a relation for hydraulic conductivity  $\alpha_h$  as [111]

$$\alpha_h = \frac{UL}{\Delta p}, \quad (1.13)$$

where  $U$  is the fluid velocity,  $L$  is the layer length of the porous medium, and  $\Delta P$  hydrostatic pressure difference between the entrance and the exit of the porous medium layer. Then, this relation is extended to

$$\alpha_h = \frac{UL}{\Delta p} = \frac{\kappa}{\mu} \Rightarrow \frac{\Delta p}{L} = \left( \frac{\mu}{\kappa} \right) U, \quad (1.14)$$

where  $\kappa$  is the permeability of the porous medium, and  $\mu$  is the dynamic viscosity of the fluid. The latter equation is called as Darcy's law, and it may be written in differential form as [111]

$$-\nabla p - \frac{\mu}{\kappa} \mathbf{u} = 0, \quad (1.15)$$

where the second term is mentioned as viscous or Darcy drag.

Brinkman (1949) generalized the Darcy's law combining the fluid-fluid viscous shear ( $\mu \nabla^2 \mathbf{u}$ ) and the internal fluid-solid viscous drag ( $(\mu/\kappa) \mathbf{u}$ ). Thus, Darcy-Brinkman equation for flow through porous media was defined as

$$\nabla p = \mu_e \nabla^2 \mathbf{u} - \frac{\mu}{\kappa} \mathbf{u}, \quad (1.16)$$

where  $\mu_e$  is the effective viscosity of the porous medium, and  $\mu_e = \epsilon_p \mu$  with  $\epsilon_p = V_f/V_c$  as the porosity of the porous medium with volume of the fluid  $V_f$  and the control volume  $V_c$ .

Later on, inertial terms are also added to Eq.(1.16). The generalized form of the momentum equation in a porous medium is given as [111, 159]

$$\frac{\mu_e}{\rho} \nabla^2 \mathbf{u} = \frac{1}{\epsilon_p} \frac{\partial \mathbf{u}}{\partial t} + \frac{1}{\epsilon_p^2} \mathbf{u} \cdot \nabla \mathbf{u} + \frac{\nabla p}{\rho} + \frac{\mu}{\rho \kappa} \mathbf{u} + \frac{c_F}{\sqrt{\kappa}} |\mathbf{u}| \mathbf{u}, \quad (1.17)$$

where  $|\mathbf{u}| = \sqrt{u^2 + v^2}$ , and

$$c_F = \frac{1.75(1 - \epsilon_p)}{d_p \epsilon_p^3} \quad \text{and} \quad \kappa = \frac{d_p^2 \epsilon_p^3}{150(1 - \epsilon_p)^2}, \quad (1.18)$$

the form coefficient and the permeability of the porous medium, respectively, with diameter  $d_p$  of the particle of fibre. The last term in Eq.(1.17) is called as Forchheimer terms. In general, non-Darcy effect on the flow is considered with the Darcy-Brinkman-Forchheimer model. That is, the quadratic drag terms (or Forchheimer terms) gain importance when the fluid velocity is high (at higher  $Re$  numbers) [116].

In local thermal equilibrium situation (the negligible temperature difference between the solid and fluid phases), energy equation for porous medium is stated as

$$k_e \nabla^2 T = (\rho c_p)_e \frac{\partial T}{\partial t} + (\rho c_p)_f \mathbf{u} \cdot \nabla T, \quad (1.19)$$

where  $k_e (= \epsilon_p k_f + (1 - \epsilon_p) k_s)$  is the effective thermal conductivity,  $k_s$  is the thermal conductivity of the solid,  $c_p$  is the specific heat at constant pressure,  $(\rho c_p)_f$  is the thermal capacity of the fluid,  $(\rho c_p)_e (= \epsilon_p (\rho c_p)_f + (1 - \epsilon_p) (\rho c_p)_s)$  is the effective thermal capacity of the porous medium, and  $(\rho c_p)_s$  is the thermal capacity of the solid.

Mixed convection flow through a porous medium has taken great deal of attention in the last few years due to the large number of applications as geothermal energy systems, storage of nuclear waste, etc. Books by Pop and Ingham [125], Ingham and Pop [70], Nield and Bejan [116], and Martynenko and Khramtsov [93] also have lots of details and application examples on convective flows in porous media. In this thesis,

the Brinkman-extended Darcy equations (and also Darcy-Brinkman model) are studied, i.e. Forchheimer terms (nonlinear inertial effects) in Eq.(1.17) are not considered.

Assuming the isotropic, homogeneous porous medium saturated with an incompressible, viscous fluid, the continuity equation, equations of motion (setting  $\epsilon_p = 1$ ) and the energy equation for mixed convection flow are given as [67, 80]

$$\nabla \cdot \mathbf{u} = 0 \quad (1.20a)$$

$$\nu_e \nabla^2 \mathbf{u} = \frac{\partial \mathbf{u}}{\partial t} + \mathbf{u} \cdot \nabla \mathbf{u} + \frac{1}{\rho} \nabla p + \frac{\nu}{\kappa} \mathbf{u} + \mathbf{g} \beta (T - T_c) \quad (1.20b)$$

$$\alpha_e \nabla^2 T = \frac{\partial T}{\partial t} + \mathbf{u} \cdot \nabla T, \quad (1.20c)$$

where  $\nu_e = \mu_e/\rho$  is the effective kinematic viscosity,  $\alpha_e = k_e/(\rho c_p)_f$  is the effective thermal diffusivity with the effective thermal conductivity  $k_e$ .

In a similar way, applying the cross-differentiation with the definitions of vorticity  $w = \partial v/\partial x - \partial u/\partial y$  and stream function  $u = \partial \psi/\partial y$ ,  $v = -\partial \psi/\partial x$  to the Eqs.(1.20), pressure terms are eliminated, and the vorticity transport equation is obtained.

For non-dimensionalization, the following dimensionless variables are defined as [80]

$$\begin{aligned} x' &= \frac{x}{L}, \quad y' = \frac{y}{L}, \quad u' = \frac{u}{U}, \quad v' = \frac{v}{U}, \\ t' &= \frac{tU}{L}, \quad T' = \frac{T - T_c}{T_h - T_c}, \quad w' = \frac{wL}{U}, \quad \psi' = \frac{\psi}{UL}, \end{aligned} \quad (1.21)$$

where  $U$  is the characteristic velocity,  $L$  is the characteristic length,  $T_c$  is the cold wall temperature, and  $T_h$  is the heated wall temperature. The non-dimensional form of the Brinkman-extended Darcy equations (1.20) in terms of stream function, vorticity and temperature is derived as follows

$$\nabla^2 \psi = -w \quad (1.22a)$$

$$\frac{1}{PrRe} \nabla^2 T = \frac{\partial T}{\partial t} + u \frac{\partial T}{\partial x} + v \frac{\partial T}{\partial y}, \quad (1.22b)$$

$$\frac{1}{Re} \nabla^2 w = \frac{\partial w}{\partial t} + u \frac{\partial w}{\partial x} + v \frac{\partial w}{\partial y} - \frac{Gr}{Re^2} \frac{\partial T}{\partial x} + \frac{w}{DaRe}, \quad (1.22c)$$

where  $\mu_e = \mu$ ,  $\nu_e = \nu$  are set while  $\epsilon_p = 1$  is fixed, Prandtl ( $Pr$ ), Reynolds ( $Re$ ), Grashof ( $Gr$ ) and Darcy ( $Da$ ) numbers (dimensionless parameters) are given as

$$Pr = \frac{\nu}{\alpha_e}, \quad Re = \frac{UL}{\nu}, \quad Gr = \frac{g\beta\Delta TL^3}{\nu^2}, \quad Da = \frac{\kappa}{L^2}.$$

#### 1.1.4 Mixed convection flow in a porous medium under the effect of a magnetic field

When the porous medium is also exposed to an externally applied magnetic field, momentum equations contain the electromagnetic force effect in terms of the strength  $B_0$

of the applied magnetic field. Mixed convection flow in a porous medium under the effect of a magnetic field has also taken the great interest, especially in the applications as heat exchanger devices, MHD accelerators and generators, packed bed reactors, etc.

Neglecting the induced magnetic field in the fluid, the momentum equations, under the effect of horizontally applied magnetic field, become

$$\nu_e \nabla^2 u = \frac{\partial u}{\partial t} + u \frac{\partial u}{\partial x} + v \frac{\partial u}{\partial y} + \frac{1}{\rho} \frac{\partial p}{\partial x} + \frac{\nu}{\kappa} u \quad (1.23a)$$

$$\nu_e \nabla^2 v = \frac{\partial v}{\partial t} + u \frac{\partial v}{\partial x} + v \frac{\partial v}{\partial y} + \frac{1}{\rho} \frac{\partial p}{\partial y} + \frac{\nu}{\kappa} v - g\beta(T - T_c) + \frac{\sigma B_0^2}{\rho} v, \quad (1.23b)$$

where  $\sigma$  is the electrical conductivity of the fluid,  $B_0$  is the magnitude of the applied magnetic field. The  $y$ -momentum equation includes the last term with the effect of horizontally applied magnetic field.

The non-dimensional governing equations in terms of stream function  $\psi$ , temperature  $T$ , vorticity  $w$  using the same non-dimensional variables as in Eq.(1.21) are written as

$$\nabla^2 \psi = -w \quad (1.24a)$$

$$\frac{1}{PrRe} \nabla^2 T = \frac{\partial T}{\partial t} + u \frac{\partial T}{\partial x} + v \frac{\partial T}{\partial y}, \quad (1.24b)$$

$$\frac{1}{Re} \nabla^2 w = \frac{\partial w}{\partial t} + u \frac{\partial w}{\partial x} + v \frac{\partial w}{\partial y} - \frac{Gr}{Re^2} \frac{\partial T}{\partial x} + \frac{w}{DaRe} + \frac{Ha^2}{Re} \frac{\partial v}{\partial x}, \quad (1.24c)$$

where the non-dimensional parameter Hartmann number  $Ha$  is  $B_0 \sqrt{(\kappa\sigma)/\mu}$ , which is the ratio of Lorentz force to viscous (shear) force ( $\nu_e \nabla^2 \mathbf{u}$ ).

### 1.1.5 Full Magnetohydrodynamic (MHD) flow equations

Magnetohydrodynamics (MHD) is a branch of science dealing with the magnetic field in electrically conducting fluids. An externally applied magnetic field interacts with the conducting fluid (e.g. plasma or liquid metal), and fluid motion changes. The external magnetic field influences the fluid motion (this influence is expressed mathematically by including the electromagnetic force in the equations of motion) and the fluid motion changes in turn (through Ohm's Law) the magnetic field. The interaction of the velocity and magnetic fields involving both hydrodynamic and electromagnetic phenomena determines the simultaneous consideration of the fluid mechanics equations and the electromagnetic field equations making most MHD problems difficult to study.

The great deal of interest on this subject is encountered due to its crucial applications in geophysics, plasma physics, MHD generators, MHD pumps, instruments measuring blood pressure, hydromagnetic dynamos, cooling of nuclear reactors etc.

In physical and mathematical basis, MHD equations are comprised of the Navier-Stokes equations of fluid dynamics and Maxwell's equations of electromagnetics. The main difficulty for obtaining an analytical or numerical solution of these equations is that the satisfaction of divergence-free conditions on velocity and magnetic field.

Maxwell's equations for neither magnetic nor dielectric materials are stated as [37]

$$\nabla \times \mathbf{B} = \mu_m \left( \mathbf{J} + \epsilon_0 \frac{\partial \mathbf{E}}{\partial t} \right) \quad \text{Ampere's Law} \quad (1.25a)$$

$$\nabla \times \mathbf{E} = -\frac{\partial \mathbf{B}}{\partial t} \quad \text{Differential form of Faraday's Law} \quad (1.25b)$$

$$\nabla \cdot \mathbf{E} = \frac{q}{\epsilon_0} \quad \text{Gauss's Law} \quad (1.25c)$$

$$\nabla \cdot \mathbf{B} = 0 \quad \text{Solenoidal nature of } \mathbf{B}, \quad (1.25d)$$

where  $\mu_m$  is the magnetic permeability,  $q$  is the total charge density (free and bound charges),  $\epsilon_0$  is the permittivity of free space,  $\mathbf{J}$  is the current density,  $\mathbf{E}$  is the electric field and  $\mathbf{B}$  is the magnetic field.

The displacement current  $\epsilon_0 \partial \mathbf{E} / \partial t$  is neglected in Ampere's law since the propagation of electromagnetic waves is not considered [109, 141].

Ohm's law characterizing the ability of materials to transport electric charge under an applied magnetic field is expressed in reference of laboratory frame as [109, 141]

$$\mathbf{J} = q\mathbf{u} + \sigma (\mathbf{E} + \mathbf{u} \times \mathbf{B}), \quad (1.26)$$

where  $\sigma$  is the electrical conductivity. The convection current  $q\mathbf{u}$  is neglected in the electromagnetic approximation due to the dominance of conduction proportion to  $\sigma$ .

The total force per unit volume acting on the conducting fluid is demonstrated as

$$\mathbf{F}_l = q\mathbf{E} + \mathbf{J} \times \mathbf{B}, \quad (1.27)$$

where the term  $q\mathbf{E}$  is neglected since the speed of electrons in conducting fluid is less than the speed of light [37, 141].

Thus, MHD equations are stated as

$$\nabla \times \mathbf{B} = \mu_m \mathbf{J} \quad \text{Ampere's Law} \quad (1.28a)$$

$$\nabla \times \mathbf{E} = -\frac{\partial \mathbf{B}}{\partial t} \quad \text{Faraday's Law} \quad (1.28b)$$

$$\mathbf{J} = \sigma (\mathbf{E} + \mathbf{u} \times \mathbf{B}) \quad \text{Ohm's Law} \quad (1.28c)$$

$$\mathbf{F}_l = \mathbf{J} \times \mathbf{B} \quad \text{Lorentz force,} \quad (1.28d)$$

with the conservation of charge  $\nabla \cdot \mathbf{J} = 0$  and the solenoidal nature of magnetic field  $\nabla \cdot \mathbf{B} = 0$ .

Momentum equations in an incompressible flow consist of the velocity components and pressure gradient. In full MHD, Lorentz force is added to momentum equations as a body force. Therefore, full MHD equations consist of momentum equations and induction equations if there is no any other source in the system.

Taking the curl of both sides of the Eq.(1.28a) and Eq.(1.28c), the following equations are written as

$$\nabla \times (\nabla \times \mathbf{B}) = \mu_m (\nabla \times \mathbf{J}) \quad (1.29a)$$

$$\nabla \times \mathbf{J} = \sigma (\nabla \times \mathbf{E}) + \sigma (\nabla \times (\mathbf{u} \times \mathbf{B})). \quad (1.29b)$$



Substitution of Eq.(1.29b) into Eq.(1.29a) gives

$$\nabla \times (\nabla \times \mathbf{B}) = \mu_m \sigma (\nabla \times \mathbf{E}) + \mu_m \sigma (\nabla \times (\mathbf{u} \times \mathbf{B})). \quad (1.30)$$

Then, using the Faraday's law Eq.(1.28b) and the identity  $\nabla \times (\nabla \times \mathbf{B}) = \nabla(\nabla \cdot \mathbf{B}) - \nabla^2 \mathbf{B} = -\nabla^2 \mathbf{B}$  due to the solenoidal nature of  $\mathbf{B}$ , Eq.(1.30) is rewritten as

$$\frac{1}{\mu_m \sigma} \nabla^2 \mathbf{B} = \frac{\partial \mathbf{B}}{\partial t} - \nabla \times (\mathbf{u} \times \mathbf{B}). \quad (1.31)$$

In the presence of heat transfer and induced magnetic field, momentum equations will include buoyancy force as well as the Lorentz force. Assuming the constant fluid properties ( $\mu_m$ ,  $\sigma$ ,  $\nu$ ) except density variation following the Boussinesq approximation, and neglecting Hall effect<sup>3</sup>, Joule heating effect<sup>4</sup> and the viscous dissipation in energy equation, the two-dimensional full MHD equations with heat transfer for an incompressible, viscous fluid are

$$\nabla \cdot \mathbf{u} = 0 \quad (1.32a)$$

$$\nu \nabla^2 \mathbf{u} = \frac{\partial \mathbf{u}}{\partial t} + \mathbf{u} \cdot \nabla \mathbf{u} + \frac{1}{\rho} \nabla p + \mathbf{g} \beta (T - T_c) - \frac{1}{\rho} (\mathbf{J} \times \mathbf{B}) \quad (1.32b)$$

$$\frac{1}{\mu_m \sigma} \nabla^2 \mathbf{B} = \frac{\partial \mathbf{B}}{\partial t} - \nabla \times (\mathbf{u} \times \mathbf{B}) \quad (1.32c)$$

$$\alpha \nabla^2 T = \frac{\partial T}{\partial t} + \mathbf{u} \cdot \nabla T, \quad (1.32d)$$

where  $\mathbf{u} = \langle u, v, 0 \rangle$  is the velocity field and  $\mathbf{B} = \langle B_x, B_y, 0 \rangle$  is the induced magnetic field. These vector form of the equations may be rewritten explicitly as

$$\frac{\partial u}{\partial x} + \frac{\partial v}{\partial y} = 0 \quad (1.33a)$$

$$\nu \nabla^2 u = \frac{\partial u}{\partial t} + u \frac{\partial u}{\partial x} + v \frac{\partial u}{\partial y} + \frac{1}{\rho} \frac{\partial p}{\partial x} + \frac{B_y}{\rho \mu_m} \left( \frac{\partial B_y}{\partial x} - \frac{\partial B_x}{\partial y} \right) \quad (1.33b)$$

$$\nu \nabla^2 v = \frac{\partial v}{\partial t} + u \frac{\partial v}{\partial x} + v \frac{\partial v}{\partial y} + \frac{1}{\rho} \frac{\partial p}{\partial y} - \frac{B_x}{\rho \mu_m} \left( \frac{\partial B_y}{\partial x} - \frac{\partial B_x}{\partial y} \right) - g \beta (T - T_c) \quad (1.33c)$$

$$\frac{1}{\sigma \mu_m} \nabla^2 B_x = \frac{\partial B_x}{\partial t} + u \frac{\partial B_x}{\partial x} + v \frac{\partial B_x}{\partial y} - B_x \frac{\partial u}{\partial x} - B_y \frac{\partial u}{\partial y} \quad (1.33d)$$

$$\frac{1}{\sigma \mu_m} \nabla^2 B_y = \frac{\partial B_y}{\partial t} + u \frac{\partial B_y}{\partial x} + v \frac{\partial B_y}{\partial y} - B_x \frac{\partial v}{\partial x} - B_y \frac{\partial v}{\partial y} \quad (1.33e)$$

$$\alpha \nabla^2 T = \frac{\partial T}{\partial t} + u \frac{\partial T}{\partial x} + v \frac{\partial T}{\partial y} \quad (1.33f)$$

The stream function-vorticity formulation is derived similarly as before (done for Navier-Stokes equations) with the help of vorticity  $\mathbf{w} = \nabla \times \mathbf{u} = (0, 0, w)$  as in Eq.(1.5) and  $u = \partial \psi / \partial y$ ,  $-v = \partial \psi / \partial x$  definitions.

<sup>3</sup> This effect is important for ionized gases in the case of a strong magnetic field.

<sup>4</sup> Heat generated by the current (emerging from an applied potential difference to a resistor) passing through a resistor.

Differentiating Eq.(1.33c) and Eq.(1.33b) with respect to  $x$  and  $y$ , respectively, and then subtracting from each other, pressure terms are eliminated, and vorticity transport equation is obtained as

$$\begin{aligned} \nu \nabla^2 w = & \frac{\partial w}{\partial t} + u \frac{\partial w}{\partial x} + v \frac{\partial w}{\partial y} - g\beta \frac{\partial T}{\partial x} \\ & - \frac{1}{\rho\mu_m} \left[ B_x \frac{\partial}{\partial x} \left( \frac{\partial B_y}{\partial x} - \frac{\partial B_x}{\partial y} \right) + B_y \frac{\partial}{\partial y} \left( \frac{\partial B_y}{\partial x} - \frac{\partial B_x}{\partial y} \right) \right]. \end{aligned} \quad (1.34)$$

For non-dimensionalization, the dimensionless variables are defined as

$$\begin{aligned} x' = \frac{x}{L}, \quad y' = \frac{y}{L}, \quad u' = \frac{u}{U}, \quad v' = \frac{v}{U}, \quad t' = \frac{tU}{L}, \quad \psi' = \frac{\psi}{UL} \\ w' = \frac{wL}{U}, \quad T' = \frac{T - T_c}{T_h - T_c}, \quad B'_x = \frac{B_x}{B_0}, \quad B'_y = \frac{B_y}{B_0}, \end{aligned} \quad (1.35)$$

where  $B_0$  is the magnitude of the applied magnetic field. Hence, the non-dimensional form of the Eqs.(1.33) is obtained as (Appendix A)

$$\nabla^2 \psi = -w \quad (1.36a)$$

$$\begin{aligned} \frac{1}{Re} \nabla^2 w = & \frac{\partial w}{\partial t} + u \frac{\partial w}{\partial x} + v \frac{\partial w}{\partial y} - \frac{Ra}{PrRe} \frac{\partial T}{\partial x} \\ & - \frac{Ha^2}{ReRem} \left[ B_x \frac{\partial}{\partial x} \left( \frac{\partial B_y}{\partial x} - \frac{\partial B_x}{\partial y} \right) + B_y \frac{\partial}{\partial y} \left( \frac{\partial B_y}{\partial x} - \frac{\partial B_x}{\partial y} \right) \right] \end{aligned} \quad (1.36b)$$

$$\frac{1}{Rem} \nabla^2 B_x = \frac{\partial B_x}{\partial t} + u \frac{\partial B_x}{\partial x} + v \frac{\partial B_x}{\partial y} - B_x \frac{\partial u}{\partial x} - B_y \frac{\partial u}{\partial y} \quad (1.36c)$$

$$\frac{1}{Rem} \nabla^2 B_y = \frac{\partial B_y}{\partial t} + u \frac{\partial B_y}{\partial x} + v \frac{\partial B_y}{\partial y} - B_x \frac{\partial v}{\partial x} - B_y \frac{\partial v}{\partial y} \quad (1.36d)$$

$$\frac{1}{PrRe} \nabla^2 T = \frac{\partial T}{\partial t} + u \frac{\partial T}{\partial x} + v \frac{\partial T}{\partial y}, \quad (1.36e)$$

where

$$Re = \frac{UL}{\nu}, \quad Rem = UL\sigma\mu_m, \quad Ra = \frac{g\beta\Delta TL^3}{\nu\alpha}, \quad Pr = \frac{\nu}{\alpha}, \quad Ha = B_0 L \sqrt{\frac{\sigma}{\nu\rho}}. \quad (1.37)$$

The magnetic Reynolds number  $Rem$  represents the ratio of advection ( $\nabla \times (\mathbf{u} \times \mathbf{B})$ ) to diffusion of  $\mathbf{B}$  ( $\nabla^2 \mathbf{B} / \sigma\mu_m$ ). If  $Rem \gg 1$ , advection dominates over diffusion whereas diffusion dominates over advection if  $Rem \ll 1$ . In other words,  $\mathbf{u}$  has little impact on  $\mathbf{B}$  if  $Rem \ll 1$ . In this case, induced magnetic field is neglected, and the damping effect on fluid motion is only the applied magnetic field.

Notice that if the induced magnetic field is neglected in an enclosure under the influence of a horizontally applied magnetic field, the induced magnetic field will be  $\mathbf{B} = (B_0, 0, 0)$ . Garandet et al. [58] showed that the two equations Ohm's Law  $\mathbf{J} = \sigma(-\nabla\vartheta + \mathbf{u} \times \mathbf{B})$  (where  $\vartheta$  is the electrical potential) and the conservation of

current  $\nabla \cdot \mathbf{J} = 0$  are reduced to  $\nabla^2 \vartheta = 0$  of which has a unique solution  $\nabla \vartheta = 0$  since there is an electrically insulating boundary around the enclosure. Thus,  $\mathbf{J}$  is reduced to  $\sigma(\mathbf{u} \times \mathbf{B})$  where  $\mathbf{u} = (u, v, 0)$ , and

$$\mathbf{u} \times \mathbf{B} = \begin{bmatrix} \vec{i} & \vec{j} & \vec{k} \\ u & v & 0 \\ B_0 & 0 & 0 \end{bmatrix} = -vB_0\vec{k}$$

$$\mathbf{J} \times \mathbf{B} = \sigma(\mathbf{u} \times \mathbf{B}) \times \mathbf{B} = \begin{bmatrix} \vec{i} & \vec{j} & \vec{k} \\ 0 & 0 & -\sigma v B_0 \\ B_0 & 0 & 0 \end{bmatrix} = -\sigma v B_0^2 \vec{j}.$$

As a conclusion, the term  $\sigma v B_0^2$  is seen in the  $v$ -component of momentum equation Eq.(1.23b) as a last term.

Ampere's Law (1.28a) enables us to write the current density equation, i.e.  $\mu_m \mathbf{j} = \nabla \times \mathbf{B}$  where  $\mathbf{j} = (0, 0, j)$  in terms of induced magnetic field components

$$j = \frac{1}{\mu_m} \left( \frac{\partial B_y}{\partial x} - \frac{\partial B_x}{\partial y} \right). \quad (1.38)$$

A Poisson type equation for the current density may also be obtained by using Eq.(1.38). Differentiating (1.33d) and (1.33e) with respect to  $y$  and  $x$ , respectively, then subtracting from each other and using the divergence free conditions  $\nabla \cdot \mathbf{u} = 0$  and  $\nabla \cdot \mathbf{B} = 0$ , the current density equation is deduced as

$$\frac{1}{\sigma} \nabla^2 j = \mu_m \left( \frac{\partial j}{\partial t} + u \frac{\partial j}{\partial x} + v \frac{\partial j}{\partial y} \right) - \left( B_x \frac{\partial w}{\partial x} + B_y \frac{\partial w}{\partial y} \right) - 2 \left[ \frac{\partial B_x}{\partial x} \left( \frac{\partial v}{\partial x} + \frac{\partial u}{\partial y} \right) + \frac{\partial v}{\partial y} \left( \frac{\partial B_x}{\partial y} + \frac{\partial B_y}{\partial x} \right) \right]. \quad (1.39)$$

Defining the non-dimensional variable  $j' = j/(B_0 U \sigma)$  (Appendix A), Eq.(1.39) in non-dimensional form is expressed as (dropping the prime notation)

$$\nabla^2 j = Re_m \left( \frac{\partial j}{\partial t} + u \frac{\partial j}{\partial x} + v \frac{\partial j}{\partial y} \right) - \left( B_x \frac{\partial w}{\partial x} + B_y \frac{\partial w}{\partial y} \right) - 2 \left[ \frac{\partial B_x}{\partial x} \left( \frac{\partial v}{\partial x} + \frac{\partial u}{\partial y} \right) + \frac{\partial v}{\partial y} \left( \frac{\partial B_x}{\partial y} + \frac{\partial B_y}{\partial x} \right) \right]. \quad (1.40)$$

Using the similar idea of satisfying the continuity equation, the solenoidal nature of  $\mathbf{B}$  is also satisfied defining a vector potential  $\mathbf{A}$  as  $\mathbf{B} = \nabla \times \mathbf{A}$  in which  $\mathbf{A} = (0, 0, A)$ . In this fashion,  $B_x = \partial A / \partial y$ ,  $B_y = -\partial A / \partial x$ . Employing either one of the Eqs.(1.33d) or (1.33e), magnetic vector potential equation is rendered as

$$\frac{1}{\sigma \mu_m} \nabla^2 A = \frac{\partial A}{\partial t} + u \frac{\partial A}{\partial x} + v \frac{\partial A}{\partial y}. \quad (1.41)$$

The non-dimensional variable  $A' = A/(B_0 L)$  (Appendix A) provides us to get the non-dimensional form of the Eq.(1.41) as (dropping the prime notation again)

$$\frac{1}{Rem} \nabla^2 A = \frac{\partial A}{\partial t} + u \frac{\partial A}{\partial x} + v \frac{\partial A}{\partial y}. \quad (1.42)$$

There is also a relation between magnetic potential  $A$  and current density  $j$  as

$$j = \frac{1}{\mu_m} \left( \frac{\partial B_y}{\partial x} - \frac{\partial B_x}{\partial y} \right) = \frac{1}{\mu_m} \left( \frac{\partial}{\partial x} \left( -\frac{\partial A}{\partial x} \right) - \frac{\partial}{\partial y} \left( \frac{\partial A}{\partial y} \right) \right) \Rightarrow \nabla^2 A = -\mu_m j \quad (1.43)$$

which is similar to the relation  $\nabla^2 \psi = -w$  between stream function and vorticity.

### 1.1.6 MHD duct flow

The problem of MHD flow through channels is frequently encountered in nuclear reactors, MHD flow meters, MHD generators, pumps and accelerator. The concerned fluid is incompressible, viscous, electrically conducting and driven down the duct by means of a constant pressure gradient.

The fluid is subjected to an applied magnetic field parallel to the  $x$ -axis, and the velocity and the induced magnetic field are in the  $z$ -direction which is the axis of the duct. Thus, there is only one component of the velocity vector  $\mathbf{u} = (0, 0, V)$ , and the magnetic field vector  $\mathbf{B} = (B_0, 0, B)$ . Further, the pressure depends on  $z$ . The dimensional governing equations are

$$\mu \nabla^2 V + \frac{B_0}{\mu_m} \frac{\partial B}{\partial x} = \frac{\partial p}{\partial z} + \rho \frac{\partial V}{\partial t}, \quad \eta \nabla^2 B + B_0 \frac{\partial V}{\partial x} = \frac{\partial B}{\partial t}. \quad (1.44)$$

Once the non-dimensionalization is done following the explanations in [141], the dimensionless time-dependent governing equations are

$$\nabla^2 V + Ha \frac{\partial B}{\partial x} = -1 + \frac{\partial V}{\partial t}, \quad \nabla^2 B + Ha \frac{\partial V}{\partial x} = \frac{\partial B}{\partial t}, \quad (1.45)$$

in  $\Omega \times [0, \infty)$  with the initial conditions

$$V(x, y, 0) = B(x, y, 0) = 0, \quad (x, y) \in \Omega. \quad (1.46)$$

and the boundary conditions

$$V(x, y, t) = B(x, y, t) = 0, \quad (x, y) \in \partial\Omega. \quad (1.47)$$

$V(x, y, t)$  and  $B(x, y, t)$  are the velocity and the induced magnetic fields in the  $z$ -direction.  $Ha$  is the Hartmann number. The given no-slip boundary conditions ensure that the duct walls are insulating.

Eq.(1.45) may be decoupled by the change of variables

$$\Psi = V + B, \quad \Phi = V - B, \quad (1.48)$$

leading to the following two equations

$$\nabla^2 \Psi + Ha \frac{\partial \Psi}{\partial x} - \frac{\partial \Psi}{\partial t} = -1, \quad (1.49a)$$

$$\nabla^2 \Phi - Ha \frac{\partial \Phi}{\partial x} - \frac{\partial \Phi}{\partial t} = -1, \quad (1.49b)$$

with the initial and boundary conditions

$$\Psi(x, y, 0) = \Phi(x, y, 0) = 0, \quad (x, y) \in \Omega \quad (1.50)$$

$$\Psi(x, y, t) = \Phi(x, y, t) = 0, \quad (x, y) \in \partial\Omega. \quad (1.51)$$

In this thesis, Eqs.(1.49) with Eqs.(1.50)-(1.51) are solved applying DQM both in time and space directions. The solution procedure will be given in Chapter 4.

## 1.2 Literature survey

A rapid increase in computer technology brings together the new solution ideas for complex problems in fluid mechanics and heat transfer. This new research area has become known as computational fluid dynamics (CFD) in which the governing partial differential or integral equations are solved computationally (or numerically).

The first and the old numerical method for solving PDE is the finite difference method (FDM). Taylor-series expansions are employed for obtaining different difference quotients. In FDM, the domain is discretized by grid or mesh points [88]. The derivatives in the governing equations are approximated at these grid points with any type of difference quotients. Then, a set of algebraic equations generated by block structured matrices are obtained. Although FD schemes are easy to implement, they are not practical in problems of complex geometry.

For larger or complicated domains, finite element method (FEM) would be an alternative in numerical world. This method divides the domain into subdomains which are represented by finite elements [131]. Then, all sets of subdomain equations are assembled in a global banded or block system matrix. As mesh is refined being the geometry larger and larger, computational cost increases gradually. This reduces the practicality of the method. Furthermore, FEM is not efficient in infinite regions.

Finite volume method (FVM) has also taken the great deal of attention in fluid dynamics in the last few decades. FVM is useful on arbitrary geometries since the physical domain is subdivided into control volumes surrounding each grid. Conservation principles are automatically satisfied in this control volume [124]. Using the divergence theorem, the volume integral representation of each volume is converted to the surface integrals which are evaluated as fluxes through the boundaries of the control volume. Flux computations on irregular geometries require much effort.

Differential quadrature method (DQM) also discretizes the domain. The derivatives in PDE are approximated by a weighted linear summation of functional values at all grid points [142]. The whole algebraic system of equations is solved at one time. Accuracy of the method is very high using considerably small number of grids, particularly non-uniform grids due to the stability. In complex geometries, the efficiency of the method decreases due to the increase in computational cost.

Boundary element method (BEM) approximates the solution of a partial differential equation (PDE) through the boundary, and then computes interior solutions using this

boundary solution. The domain integrals resulting from the weighted residuals are transformed to boundary integrals with the help of fundamental solution and divergence theorem. The mathematical basis and application of the method are found in the inventor's book [24]. The main drawback of the method is the existence of domain integrals due to the inhomogeneity in the equation. The dual reciprocity BEM (DRBEM) has been devised for handling this domain integral and also transforming it to the boundary [122]. BEM has a strong advantage also in solving problems in infinite or semi-infinite domains with respect to other domain discretization methods. The basis of DRBEM is to keep the Laplace term on one side, and to treat the other terms as inhomogeneity on the other side. Both sides are multiplied by the fundamental solution of Laplace equation, and then integrated over the domain. The key point of the DRBEM is to convert all domain integrals to boundary integrals using Green's identities. The radial basis functions (RBFs) ease the approximation of inhomogeneity and particular solutions.

As a basis to CFD, the Navier-Stokes equations (NS) are solved by almost all numerical methods and some of them are summarized below.

The oldest and the most famous study utilizing the implicit multigrid method for solving the NS equations in a lid-driven cavity is given by Ghia et al. in [62]. They have solved the model lid-driven cavity flow problem for high values of Reynolds number ( $10^4$ ) by using  $257 \times 257$  grid points. Gartling [59] solved the NS equations for 2D, steady, incompressible flow using a Galerkin based FEM, and tested the flow over a backward-facing step (BFS). A nine-node biquadratic Lagrange interpolation for the velocity components, and a linear and discontinuous pressure approximation between elements are taken in the computations up to  $Re = 800$ . Shu and Richard [144] applied the generalized DQM to the two-dimensional incompressible NS equations in stream function-vorticity formulation for obtaining numerical results of flow past a circular cylinder. Biswas et al. [18] used FVM with central difference scheme for the convection-diffusion terms of NS equations, and a pressure correction equation for the pressure. The laminar incompressible BFS flow for a wide range of Reynolds number and aspect ratios (A.R.) is tested. Ramsak et al. [128] applied the multi domain BEM to 2D, unsteady NS equations in stream function-vorticity formulation, and tested the procedure in BFS flow and flow over a cylinder. The multi domain DRBEM provides one to take into account the larger geometry in BFS or flow over a cylinder. NS equations in a lid-driven cavity are also solved using piecewise linear finite elements in the study [61] in terms of stream function-vorticity. In this study, the advective terms in the vorticity equation are linearized and unknown vorticity boundary conditions are handled by a technique uncoupling both variables. Choi et al. [31] solved the unsteady NS equations using DRBEM with an algorithm based on fractional step method in which a fully explicit second order Adams-Bashfort scheme is used for convection terms. One of the model is chosen as lid-driven cavity, and  $Re$  is taken up to 400. The resulting systems of equations are solved by GMRES using at most  $40 \times 40$  linear boundary elements. The Taylor-Green vortex and the lid-driven square cavity flows are numerically depicted. Kalita and Gupta [73] developed a new, second order finite difference approximations both in time and space to solve NS equations, and applied this methodology to lid-driven cavity, BFS flows and flow over a cylinder. Tsai et al. [152] proposed robust and flexible localized DQM with a fourth order equation for boundary

conditions of NS equations. In their study, BFS and lid-driven cavity flows are chosen as test problems.

Not only one sided lid-driven cavity wall problems but also two-sided lid-driven cavity wall problems are also reported. Nithiarasu et al. [117] solved NS equations in the staggered double driven cavity with the explicit characteristic-based split (CBS) scheme in view of steady and unsteady flows inside a non-rectangular double-driven cavity. DQM and wavelet-based discrete singular method (DSC) are also used by Meraji et al. [95] and Zhou et al. [166], respectively, in the same geometry.

Some numerical approaches are also performed on the incompressible flow through the channel involving an obstacle (circular/rectangular). The channel flow around a hindrance has become a prominent physical problem due to its various applications in engineering such as building aerodynamics, flow meters, electronic cooling, heat exchange systems. Yoshida et al. [162] solved the flow past a rectangular cylinder using FEM adopting a unique direct time integration. Mukhopadhyay et al. [110] also investigated the confined wakes behind a square cylinder in a channel dividing the domain into Cartesian cells and using staggered grids. Later, Breuer et al. [25] used two different numerical schemes which are lattice-Boltzmann and finite volume method (FVM) to ensure the reliability of the computations for the flow around a square cylinder. Zhang et al. [165] used the numerical manifold method based on Galerkin-weighted residuals method for the solution of the incompressible flow over a square cylinder with low Reynolds numbers.

In the presence of temperature difference of the fluid, particularly in an enclosure, as a benchmark problem, natural convection flow in a square cavity of which the side walls are differentially heated is solved by G. de Vahl Davis in 1983 [38] using the central FD scheme. In this study, Rayleigh number is used between  $10^3$  and  $10^6$  with uniform mesh sizes ranging from  $11 \times 11$  to  $81 \times 81$ . In 1990, Lin et al. [89] examined the laminar, buoyancy-assisting mixed convection flow in a BFS geometry with an expansion ratio of 2 using  $250 \times 70$  grid points FD scheme based on SIMPLE algorithm. In 1992, Moallemi and Jung [101] exhibit the importance of Prandtl number in laminar mixed convection flow, and they found that the buoyancy effect on the flow becomes more prominent for large values of  $Pr$ . In the following year, Iwatsu et al. [72] analyzed the mixed convection flow of a viscous fluid in a lid-driven cavity using FDM. They obtained results for the main flow characteristics using  $Ra = GrPr = 0 - 10^6$  and  $Re = 0 - 3000$ . Laminar natural convection flow in inclined cavities is studied by El-Refaee et al. [57] in the stream function-vorticity formulation using the fast false implicit transient scheme algorithm. Chang et al. [28] investigated the natural convection flow using the alternating direction implicit (ADI) method with non-uniform grids concerning a BFS type enclosure. They used  $80 \times 80$  grids for Rayleigh number values in a range  $10^3 - 10^8$  and  $Pr = 0.71$ . Shu and Wee [145] solved the natural convection flow combining the SIMPLE idea with the generalized DQM. They enforced the continuity condition on the boundary, and proposed a boundary condition for pressure correction equation. The characteristics of heat transfer in the fluid region coupled with heat transfer in solid region is studied by Kanna et al. [74] using ADI method. The unsteady mixed convection flow in a cavity with a horizontally oscillating lid is studied by using a Galerkin finite element scheme in [78]. The dimensionless

parameters are taken in the range  $Re = 10^2 - 10^3$ ,  $Gr = 10^2 - 10^5$ ,  $Pr = 0.71$ , and the lid oscillation frequency ranging from 0.1 to 5. Using the same method, Khanafer concentrated on the laminar mixed convection pulsating flow past a BFS in [77] using a lid-oscillation frequency between 0.1 and 5. They found that the average wall friction coefficient increases with an increase in oscillation frequency. Kumar et al. [84] examined the solutal and thermal buoyancy forces together in a BFS channel flow using also the Galerkin method of weighted residuals to observe recirculatory flow pattern and its effects on heat and mass transfer under varying buoyancy ratios and Richardson number. 2D natural convection in a rectangular cavity is solved by Lo et al. [92] in velocity-vorticity formulation using DQM. For vorticity boundary conditions, higher order polynomial approximations are used. Aydin [10] utilized the stabilized FEM to the natural convection flow in primitive variables formulation on different type of geometries. The proposed method provides stable solution and avoids oscillations (especially in pressure) and is more effective and convergent as compared to the streamline-upwind/Petrov Galerkin (SUPG) stabilization.

The fluid flow and heat transfer characteristics with obstacles inside the cavity are also investigated by some researchers. This configuration has important industrial applications in geophysical systems and convection in buildings with natural cooling flow. Most of the numerical studies concentrated on obstacles as a circular cylinder inside an enclosure. Kim et al. [83] investigated the natural convection flow with a uniformly heated circular cylinder immersed in a square enclosure using immersed boundary method to describe the importance of the location of the hot circular cylinder. The same problem is also analyzed by Hussain et al. [69] using the finite volume method with  $Pr = 0.71$  and  $Ra = 10^3 - 10^6$ . Different positions of inner cylinder are studied. Using a commercial code FLUENT, mixed convection in a lid-driven enclosure with a circular body is examined also taking into account the conduction equation inside the cylinder in [118]. Three different temperature boundary conditions (isothermal, conductive, adiabatic) for the inner cylinder, and two different orientations ( $+y$  or  $-y$  directions) of the moving lid for simulation of aiding and opposing flows are presented. Adding joule heating and magnetic field effects to the system, Rahman et al. [126] have shown the significant effect of the cylinder obstacle on the fluid flow using Galerkin finite element method with 38229 nodes with 5968 element grid system. The energy equation in the solid region is coupled to momentum and energy equations for the fluid in the cavity. They found that the increase in the intensity of the applied magnetic field has a retarding effect on the fluid circulation causing the lower temperature gradients (conductive heat transfer).

Natural and/or mixed convection flows in enclosures containing square shaped obstacles are also encountered in some of the studies. Ha et al. [65] used the domain decomposed Chebyshev spectral collocation method to observe the natural convection with a square body located at the center of the computational domain for a range of Rayleigh numbers. They have also taken into consideration varying thermal boundary conditions on the square body as cold, neutral, hot isothermal, and adiabatic body conditions. Bhave et al. [16] analyzed the optimal square body size and the corresponding maximum heat transfer as a function of Rayleigh and Prandtl numbers. In their study, non-dimensional parameters ranges are  $Ra = 10^3 - 10^6$ ,  $Pr = 0.071, 0.71, 7.1$ . Finite volume method with  $100 \times 100$  mesh size has been used for solving mass, momentum



and energy equations inside the enclosure when the square blockage was adiabatic. Laminar mixed convection is studied in a square cavity with a heated square blockage immersed using finite volume method in [71]. A CFD code ANSYS FLUENT is used for calculations. The Nusselt number at the blockage surface for various values of Richardson number  $Ri = 0.01 - 100$  in different blockage sizes and locations is investigated fixing  $Re = 100$  and  $Pr = 0.71$ .

In a porous medium, numerical studies for natural, forced and mixed convection flows have also attracted the great deal of attention. Khanafer et al. [80] analyzed the mixed convection flow in a lid-driven cavity filled with a Darcian fluid saturated porous medium taking into account the internal heat generation. The numerical method was the finite-volume approach along with the ADI procedure. Effect of the parameters as  $Ri$ ,  $Da$  and internal  $Ra$  on the mixed convection flow in the cavity is investigated. Baytas and Pop [14] transformed Darcy and energy equations and solved the problem of natural convection in a porous parallelogram enclosure numerically using the ADI finite difference method. In primitive variables formulation, Sarler et al. [157] solved the Darcy model of natural convection (without convection-diffusion terms in the momentum equation) in differentially heated rectangular cavities using DRBEM with augmented scaled thin plate splines. Both constant and linear elements are used in a uniform and non-uniform mesh arrangements. Then, using the same method, they [158] extended the Darcy model to Darcy-Brinkman porous media involving the viscous term in the momentum equations. FEM with GMRES, which is a Krylov subspace based solver, is applied to solve natural convection in trapezoidal porous enclosures by Kumar and Kumar [85] using parallel computation. Saeid et al. [134] studied the Darcy-Frochheimer model in a square porous cavity using the finite volume method and QUICK scheme for convection terms in energy equation. It is found that the increase in inertial effects parameter suppresses the heat transfer in the cavity. Using the FVM based FD scheme in partially heated lid-driven porous enclosure, Darcy-Brinkman-Forchheimer equations are solved by Oztop in [119]. The highest heat transfer occurs with the heater located at the vertical wall. With the same numerical approach, Oztop [120] also examined natural convection in partially cooled and inclined rectangular enclosures filled with porous medium. Both studies [119, 120] consider the porosity as 0.9 and use  $48 \times 48$  grid points. In [120], it is found that inclination angle of the enclosure has a strong influence on the flow and heat transfer as well as aspect ratio. The problem of steady natural convection flow in a right-angle triangular, inclined trapezoidal, and right-angle trapezoidal enclosures filled with a porous medium are solved by the finite difference method using successive under relaxation for the solution of algebraic equations in [155, 153, 154] respectively. The effects of inclination angle, aspect ratio and  $Ra$  variation on the flow are examined. Vishnuvardhanarao et al. [156] solved the laminar mixed convection flow in a parallel two-sided lid-driven porous, differentially heated square cavity by using the finite volume approach with third order accurate upwind scheme. Their study is conducted by varying the key parameters using  $121 \times 121$  grid points. It is found that the average Nusselt number approaches 1 as  $Gr$  reaches  $10^3$ . Basak et al. [13] solved the mixed convection flow in a lid-driven square cavity with linearly heated side walls by penalty finite element method using bi-quadratic elements. They applied the same method to solve mixed convection in a porous square cavity neglecting Forchheimer terms with various thermal wall boundary conditions in [12]. Ramakrishna et al. [127] focuses on

the effect of thermal aspect ratio and thermal boundary conditions in terms of Bejan's heatlines again by using penalty FEM with bi-quadratic elements. They found that the dominance of lid-driven effect at low  $Da = 10^{-5}$  while the dominance of buoyancy at high  $Da = 10^{-4}, 10^{-3}$  is pronounced.

In the presence of a magnetic field, the natural, forced or mixed convection flows have also been studied. At most of these studies, induced magnetic field inside the fluid is neglected due to the assumption of small magnetic Reynolds number which is the case in industrial applications.

In a non-porous medium, Al-Najem et al. [5] investigated the influence of the magnetic field on the heat transfer process inside tilted enclosures for a wide range of inclination angles at moderate and high Grashof numbers by using the ADI scheme. It is found that the strong magnetic field suppresses the convection current, and the magnetic field has negligible effect on the heat transfer for small inclination angles. Chamkha [27] examined the unsteady, laminar, mixed convection flow in the presence of heat generation (or absorption) and an applied magnetic field using the finite volume approach along with ADI method. Ece and Büyük [56] solved natural convection flow of a viscous and incompressible fluid in an inclined enclosure in the presence of a magnetic field by using differential quadrature method discretizing the whole enclosure by using rectangles. It is found that magnetic field suppresses the convective flow and the heat transfer rate. Sathiyamoorthy and Chamkha [136] presented the penalty FEM with bi-quadratic rectangular elements to solve the natural convection flow of electrically conducting liquid gallium. They showed that average Nusselt number decreases non-linearly by increasing Hartmann number for any inclined angle. Lo [91] employed the DQM in a unit square cavity as well as the cavities with aspect ratios 2 and 3 to observe the MHD free convection in an enclosure using velocity-vorticity formulation. The system of equations is solved by bi-conjugate gradient iterative solver technique with the parameters  $Gr = 10^4 - 10^5$ ,  $Ha = 0 - 100$ ,  $Pr = 0.01 - 10$  and  $A.R. = 1 - 3$ . They conclude that the heat transfer is maximum for higher  $Pr$  (for a fixed  $Gr$  and  $Ha = 0$ ), and it decreases with the increase in the intensity of the magnetic field.

In an inclined porous layer, Bian et al. [17] investigated the effect of an electromagnetic field on natural convection flow using control volume finite difference method. It is found that the temperature and velocity fields are significantly modified under the effect of an applied magnetic field. Using a control volume algorithm, Khanafer and Chamkha [79] obtained the numerical results to simulate the hydromagnetic natural convection flow in an inclined porous enclosure in the Brinkman-extended Darcy model. The control volume method is used to solve the governing equations for  $Ha = 0 - 150$ ,  $Da = 10^{-4} - 0$ , and inclination angle ranging from  $0^\circ$  to  $90^\circ$  fixing  $Pr = 7$  and  $Ra = 64 \times 10^5$ . The effects of both magnetic field and porous medium were found to reduce the heat transfer and fluid circulation within the cavity. Grosan et al. [64] presented the influence of both the strength and inclination angle of the magnetic field on convective modes of unsteady free convection flow in a porous square cavity. A central FD scheme is used for discretization with the parameters  $Ha = 0 - 50$ ,  $Ra = 10 - 10^5$ ,  $A.R. = 0.01 - 1$  and the inclination angle of magnetic field ranging in  $0, \pi/6, \pi/4, \pi/2$ . They also studied a similar problem in [132] in

the case of unsteady free convection flow within a square cavity filled with a porous medium taking into account the internal heat generation parameter. ADI method is employed with  $87 \times 87$  grid field with a non-uniform grid distribution near the walls. The effect of a magnetic field on steady convection in a trapezoidal enclosure filled with a fluid-saturated porous medium is figured out using central finite difference method by Saleh et al. [135]. Costa et al. [35] applied a two-dimensional equal-order control volume based finite element method with sensitive relaxation parameters to solve natural convection flow in differentially heated square enclosures filled with fluid-saturated porous media under the effect of a magnetic field induced by two electric currents. It is found that the natural convection inside the enclosure decreases under the influence of the induced magnetic field, and thus, the heat transfer is reduced. Hasanpour et al. [66] used the lattice Boltzmann method to depict the Prandtl number effect on MHD mixed convection flow in a porous (the Brinkman-Forchheimer model) lid-driven cavity. They showed that the reduction of fluid movement inside the enclosure with the increase in Hartmann and the decrease in the Darcy numbers. The magnetic field effect on steady free convection in different types of porous enclosures is presented using DRBEM by Pekmen and Tezer-Sezgin [123]. It is observed that the increase in the strength of the magnetic field causes the suppression on the motion of the fluid and the conductive heat transfer using considerably small number boundary points.

MHD flow, in terms of the velocity and induced magnetic field of the fluid, through rectangular or circular ducts (pipes) are solved with several numerical approaches. In MHD duct (pipe) flows there are only one component of velocity and induced magnetic current in the direction of the axis of the pipe. Tezer-Sezgin and Aydin [149] solved MHD duct problem by using DRBEM with different form of the radial basis functions, and constant elements. The inhomogeneity is approximated by osculating radial basis functions which uses derivative information also. Tezer-Sezgin [148] applied the polynomial and Fourier based DQM to the MHD equations in a rectangular duct under a transverse external oblique magnetic field for moderate values of Hartmann number. Neslitürk and Tezer-Sezgin [115] proposed a stabilized FEM using the residual-free bubble functions for solving steady MHD duct flow. By means of this stabilization, the results at very high Hartmann ( $Ha$ ) numbers are obtained. Implementing BEM with constant elements in [150] for different geometries of the duct cross-section, the well-known characteristics of MHD flow which are the boundary layer formation near the walls and the flattening tendency in both the velocity and induced magnetic field are observed with the increase in  $Ha$ . Bozkaya et al. [19] solved the unsteady MHD duct flow in a rectangular duct with insulating walls combining the DRBEM in space with DQM in time. The resulting overdetermined system of algebraic equations are handled by the least-squares method. Zhang et al. [164] proposed the two-level element free Galerkin (TLEFG) method for solving the steady MHD duct flow equations. It is found that the TLEFG captures the results at very large  $Ha$  numbers. Finite volume spectral element method is carried out for solving unsteady MHD flow through a rectangular pipe by Shakeri et al. [140]. Hosseinzadeh et al. [68] solved the rectangular and circular cross-sectioned MHD duct flow by BEM with the constant and linear elements modifying the fundamental solution to be able to represent the results for large values of  $Ha$ .

Incompressible MHD flows are also considered when induced magnetic field lies in the

plane where the 2D motion occurs. In this case, both the velocity and induced current will have two components (in  $x$ - and  $y$ -directions). The electric current density and electric field are normal to this plane. Armero et al. [9] applied the Galerkin mixed FEM to the incompressible MHD equations examining the time integration algorithms which are long-term dissipative and unconditionally stable. They have solved plane Hartmann flow and MHD flow past a circular cylinder. FEM with some new stabilization techniques is used for solving incompressible MHD equations in [11, 33, 60]. In all these studies, the MHD flow in backward facing step is solved. In order to simulate the 2D incompressible MHD flow, Peaceman and Rachford alternating-direction implicit (ADI) scheme is performed at low magnetic Reynolds number by Navarro et al. in [113]. Plane Hartmann flow and MHD lid-driven cavity flow problems are solved in stream function-vorticity-current density-induced magnetic current and vector potential. Bozkaya and Tezer-Sezgin [20] have solved the full MHD problem in terms of stream function, vorticity, magnetic induction components and current density using DRBEM. The lid-driven cavity and backward-facing step flows are chosen as test problems.

MHD flow with heat transfer is also a prominent problem from the physical point of view. Abbassi and Nasrallah [3] investigated the MHD flow with heat transfer in a backward-facing step using a modified control volume FEM using standard staggered grid. The applied magnetic field is normal to the plane. The SIMPLER algorithm has been used in terms of velocity-pressure unknowns, and ADI scheme is performed for the time evolution. Sentürk et al. [138] presented a Lax-Wendroff type matrix distribution scheme combining a dual-time stepping technique with multi-stage Runge-Kutta algorithm to solve the steady/unsteady magnetized/neutral convection problems with the effect of heat transfer. MHD lid-driven cavity flow, natural convection flow in thermally driven cavity and MHD flow past a circular cylinder problems are solved.

In this thesis, DQM applications on linear or nonlinear hyperbolic type of PDEs are also studied. Therefore, the related numerical studies are given from now on.

The hyperbolic partial differential equations are described as initial value problems due to the time variation. The space domain of dependence for a finite time interval is considered to be finite for the equations considered in the thesis. Further, the hyperbolic telegraph equation is encountered in atomic physics and in signal analysis, and the hyperbolic telegraph, Klein-Gordon, sine-Gordon and 2D Burgers' equations are a few examples of hyperbolic type PDEs considered in the thesis.

For one-dimensional hyperbolic telegraph equation there are several studies which give numerical solutions. Mohebbi and Dehghan [107] give a high-order compact finite difference approximation of fourth order in space, and use collocation method for the time direction. In [51], a scheme similar to finite difference method is proposed using collocation points and approximating the solution with thin plate splines radial basis functions. Dehghan et al. [44] and Saadatmandi et al. [133] make use of Chebyshev cardinal functions and shifted Chebyshev polynomials, respectively, for expanding the approximate solution of one-dimensional hyperbolic telegraph equation. In [133], the advantage is to obtain the closed form of the approximate solution. Dehghan and Ghesmati [42] have applied dual reciprocity boundary element method (DRBEM) for solv-

ing second-order one-dimensional hyperbolic telegraph equation, and Crank-Nicolson finite difference has been used for the time discretization.

Dehghan and Mohebbi [47] have used the same idea given in [107] for solving the two-dimensional linear hyperbolic telegraph equation which is the combination of finite difference in space and collocation in time directions. In [104], Mohanty and Jain introduced a new unconditionally stable alternating direction implicit (ADI) scheme of second order accurate for two-dimensional telegraph equation. The solution is progressed in time direction by splitting the systems in  $x$ - and  $y$ - directions, and solving two systems for each time level. Mohanty [102] and Mohanty et al. [106] extended their studies for linear hyperbolic equations with variable coefficients in two-space dimensions. Mohanty [103] and Mohanty et al. [105] also extended solution procedure by ADI method to two- and three-space dimensional hyperbolic telegraph equations. Ding and Zhang [54] proposed a three level compact difference scheme of fourth order for the solution of two-dimensional, second-order, inhomogeneous linear hyperbolic equation for positive coefficients. Meshless method has also been used by Dehghan et al. [40, 52] for solving two-dimensional telegraph equation. The conventional moving least squares approximation is exploited in order to interpolate the solution by using monomials from the Pascal triangle in [40], and thin plate splines radial basis functions are used for the approximation of the solution in [52]. In both of these studies, another time integration scheme has been used (finite difference) for the time derivatives, and the solutions are obtained iteratively.

The Klein-Gordon equation (KGE) arises in many scientific areas such as nonlinear optics, solid state physics and quantum field theory [161]. This equation has a great importance in relativistic quantum mechanics, which is used to describe spinless particles. Furthermore, soliton-like structures have gained a great deal of interest in the last years. Soliton waves do not create any deformation due to dispersion while progressing. Soliton solutions are encountered in various nonlinear differential equations such as Korteweg & de Vries equation, the Schrödinger equation, the sine-Gordon equation. The two-dimensional sine-Gordon equation (SGE) arises in quantum tunnelling related with Josephson junction.

Several solution procedures have been developed for solving KGE numerically. In [48], a fourth order compact method in space and fourth order A-stable diagonally implicit RK-Nyström method in time are used resulting with nonlinear second order system of ODEs. Rashidinia et al. [129] developed a numerical solution by using cubic B-spline collocation method on the uniform mesh points. Moreover, a method based on the tension spline function and finite difference approximations is used in [130]. Dehghan and Ghesmati [39] obtained numerical solutions of the KGE by BEM and DRBEM. To improve the results, a predictor-corrector (PC) scheme for nonlinearity is used. Lakestani and Dehghan [86] presented two numerical techniques based on the finite difference and collocation methods. As a meshless approach, Dehghan and Shokri [53] used collocation points and thin plate splines radial basis functions. For a generalized nonlinear KGE, a finite element collocation approach using cubic B-splines is employed by Khuri and Sayfy in [82].

Differential Transform Method is used to solve KGE by Kanth and Anura in [75]. Ab-

basabandy [2] and Shakeri et al. [139] considered the series expansion of solution in He's variational iteration method. Bratsos [23] investigated a PC scheme using rational approximants of second order of matrix exponential term in a three time level recurrence relation. Wazwaz used tanh method for analytical treatment of KGE in [160]. The extended tanh method, the rational hyperbolic functions method, and the rational exponential functions method to generate new solutions are also used by Wazwaz [161].

One-dimensional sine-Gordon equation (SGE) is studied with different numerical methods as collocation [49], boundary integral approach [45], and finite difference method with DIRKN methods [108]. For the two-dimensional SGE (for damped and undamped cases), Christiansen and Lomdahl have used both the method of lines and leap-frog scheme to two spatial dimensions in [32]. Argyris [8] presented a semidiscrete Galerkin approach using four-noded bilinear finite elements in combination with a generalized Newmark integration scheme. Djidjeli et al. [55] applied a two-step, one parameter method for the reduced form of sine-Gordon equation into second-order ordinary differential equations, and global extrapolation in both time and space is used to improve the accuracy. Finite difference scheme in space is employed with fourth order rational approximants of the matrix exponential term in a three time level recurrence relation, and a new method based on a predictor-corrector scheme to avoid nonlinearity in [21]. With the similar approach, Bratsos transformed sine-Gordon equation to a second order initial value problem using the method of lines in [22]. Two-dimensional SGE has been solved using the dual reciprocity boundary element method converting the domain integrals of nonlinear and inhomogenous terms to boundary integrals, and a PC scheme is used to overcome nonlinearity in the resulting ODE's [96]. Dehghan and Ghesmati proposes the meshless local radial point interpolation method (LRPIM) where the shape functions are constructed using radial basis functions and a time stepping method is used for the time derivatives employing PC scheme to eliminate nonlinearity in [41]. The meshless local Petrov-Galerkin (MLPG) method is also developed by Mirzaei and Dehghan [97]. A numerical scheme based on collocation and the thin plate spline (TPS) radial basis function is proposed in [50]. The study in [46] presents DRBEM using linear radial basis functions for the solution of sine-Gordon equation.

The other prominent PDE as a basic example is the system of nonlinear 2D Burgers' equations considered as a prerequisite to the study of Navier-Stokes equations without pressure term and continuity equation. In Khater et al. [81], a spectral collocation method based on Chebyshev polynomials is proposed to solve 1D, 2D and systems of 2D Burgers' equations, and the nonlinearity is elaborated by reducing the system to ordinary differential equations which are solved by Runge-Kutta method of order four. In [43], numerical results of coupled viscous Burger equations are given by using the Adomian-Padé technique (combination of Adomian decomposition method and Padé approximation ADM-PADÉ). They showed that ADM-PADÉ gives faster convergence and higher accuracy than ADM. In [167], the discrete Adomian decomposition method is proposed to numerically solve the two-dimensional Burgers' nonlinear difference equations obtained by using fully implicit finite difference scheme. The quasi-linear two-dimensional unsteady Burgers' equations are converted to the characteristic diffusion equations, and the meshless method (method of fundamental solutions) is used in [163]. Liu and Shi [90] illustrated the Lattice Boltzmann Method which is based

on Boltzmann transport equation for the time rate of change of the particle distribution function in a particular state.

Some analytical solution techniques for solving nonlinear 2D Burgers' equations may be mentioned as follows. One-dimensional Burgers and coupled Burgers equations are solved by He's variational iteration method in [4]. They compared the obtained solutions with the ADM solutions showing the difficulty in calculating ADM polynomials. Moreover, a semi numerical analytical technique, the differential transform method (DTM) [1] gives highly accurate results or approximate solutions for the Burgers and coupled Burgers equations. Mittal and Arora [98] presented a numerical scheme for solving coupled viscous Burgers' equations in one-space using Crank-Nicolson method for the time integration, and cubic B-spline functions for space discretization. The cubic B-spline method is simple and straight forward. As the authors indicated, the accuracy of solution reduces as time increases due to the truncation errors in FDM, although they have used very small time step.

The use of DQM both in space and time directions is encountered in [146]. The authors proposed to solve time dependent problems (including only first order time derivatives as in Navier-Stokes equations) by a block-marching methodology in the time direction. In each time block, DQM is applied both in space and time directions. The novelty of this approach is in the higher order of accuracy and less computational effort compared to 4-stage Runge-Kutta method. In this thesis, DQM is used both in space and time directions in solving Klein-Gordon, sine-Gordon, Burgers' and MHD duct flow time dependent equations. In the time direction, solutions are improved blockwise to certain time levels as well as considering the time as a whole level.

### **1.3 Plan of the thesis**

In the thesis, Chapter 1 introduces the governing equations of the problems considered together with their physical importance. The equations of a two-dimensional, laminar, unsteady flow of an incompressible, Newtonian fluid in the presence of heat transfer or an applied magnetic field or both are introduced. Non-dimensionalizations of the governing equations for each problem are also carried introducing dimensionless problem parameters either in the first Chapter or in the Appendices.

In Chapter 2, the dual reciprocity boundary element method (DRBEM) is explained on mathematical basis. Linear elements for boundary discretization are adopted.

In Chapter 3, the DRBEM applications to some fluid dynamics problems either in porous or non-porous enclosures under the effect of an externally applied magnetic field are presented. Lid-driven square cavity, staggered double lid-driven cavity MHD flow, MHD flow in a cavity containing a centered non-conducting square blockage, backward-facing step MHD flow and MHD flow over a cylinder are given as test problems.

Chapter 4 consists of the DQM applications to hyperbolic PDEs (hyperbolic telegraph equation, Klein-Gordon and sine-Gordon equations) in one and two-space variables,

parabolic PDEs (Burgers' equations) and MHD duct flow.

In the Conclusion chapter, overall important numerical and physical results, and the future works are mentioned.

#### **1.4 Originality of the thesis**

In this thesis, the DRBEM is employed in solving mixed and natural convection flow problems in porous enclosures with or without the effect of an applied magnetic field for the first time. Also, the full MHD equations (the induced magnetic field is taken into consideration) together with energy equation are solved numerically using DRBEM. The different geometries of cavities or channels are chosen as test problems. In all numerical results, the variation of dimensionless parameters is analyzed in terms of streamlines, isotherms, vorticity, induced magnetic field lines (or magnetic potential or current density lines). Boundary-only nature of DRBEM utilizing the linear boundary elements with polynomial radial basis functions proved its strength in the chosen problems using considerably less number of grid points than the other domain discretization methods.

The other original part of the thesis is the application of differential quadrature method both in time and space domains solving especially hyperbolic PDEs. This enables one to reach to the required time level either at one stroke or blockwise without the need of an iterative procedure.





## CHAPTER 2

### DRBEM SOLUTION OF FREE/MIXED CONVECTION FLOWS WITHOUT OR WITH MAGNETIC EFFECT

The boundary element method (BEM) is a boundary-only numerical method for solving partial differential equations (PDEs). The solution is obtained in terms of boundary values only which provides less computational cost and the reduction in the dimensionality of the problem. The residual obtained by substituting approximate solution to the differential equation is weighted in the domain by multiplying with the fundamental solution of the differential equation. Then the application of divergence theorem transforms domain integrals to boundary integrals. However, the application of BEM to a non-homogeneous PDE results in a domain integral. In this case, the problem dimension is not reduced and the method becomes unattractive.

In order to alleviate this drawback of BEM, new methodologies trying to convert all domain integrals into boundary integrals are developed. One of the most outstanding method is the dual reciprocity boundary element method (DRBEM). Keeping the Laplace term of the differential equation on one side, DRBEM treats the terms on the other side as inhomogeneous terms. Inhomogeneity is expressed as a linear combination of coordinate functions based on distances of two points in the closed problem domain, which are related to Laplacian of corresponding particular solutions. The multiplication of both sides by the fundamental solution of Laplace equation, and then the integration over the domain gives the domain integrals. These domain integrals on both sides are transformed into boundary integrals using the Green's identities. Coordinate functions are usually the radial basis functions which use distances of fixed and free points.

DRBEM has many applications in scientific area such as elastodynamics, fluid dynamics, electrostatics, heat transfer, etc. In this chapter, DRBEM is introduced adopting linear boundary elements, and then some applications of DRBEM to specific fluid dynamics problems are presented.

#### 2.1 The dual reciprocity boundary element method

In this section, the boundary integral equation for Poisson's equation is derived as in [24, 122], and then the DRBEM is introduced for transforming domain integral due

to the right hand side function to the boundary integral.

Consider the Poisson's equation in 2D

$$\nabla^2 u = b(x, y), \quad (x, y) \in \Omega, \quad (2.1)$$

with the boundary conditions

$$u(x, y) = \bar{u}(x, y), \quad (x, y) \in \Gamma_1 \quad (\text{Dirichlet type}), \quad (2.2)$$

$$q(x, y) = \frac{\partial u}{\partial n} = \bar{q}(x, y), \quad (x, y) \in \Gamma_2 \quad (\text{Neumann type}), \quad (2.3)$$

where  $\nabla^2$  is the Laplace operator,  $\bar{u}, \bar{q}$  are given functions,  $\mathbf{n}$  is the outward normal to the boundary  $\Gamma = \Gamma_1 \cup \Gamma_2$  is the boundary of  $\Omega$ , and  $b(x, y)$  is a known function. Also, note that (Figure 2.1)

$$u(x, y) = \begin{cases} \bar{u}(x, y), & (x, y) \in \Gamma_1 \\ \tilde{u}(x, y), & (x, y) \in \Gamma_2 \end{cases}, \quad q(x, y) = \begin{cases} \tilde{q}(x, y), & (x, y) \in \Gamma_1 \\ \bar{q}(x, y), & (x, y) \in \Gamma_2, \end{cases} \quad (2.4)$$

where  $\tilde{u}$  and  $\tilde{q}$  are unknowns on the boundary  $\Gamma_2$  and  $\Gamma_1$ , respectively.

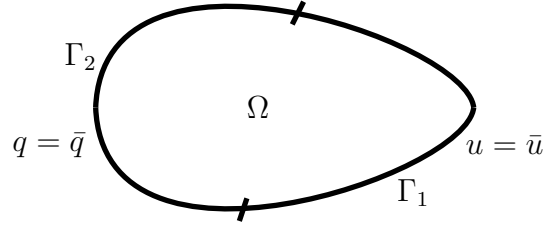


Figure 2.1: Configuration of the region and the boundary conditions.

DRBEM uses the fundamental solution  $u^* = \frac{1}{2\pi} \ln\left(\frac{1}{r}\right)$  of Laplace equation, which satisfies  $\nabla^2 u^* = -\delta(x - x_i) = -\delta^i$  with the Dirac delta function having the properties

$$\delta^i = \begin{cases} \infty & \text{if } x = x_i \\ 0 & \text{if } x \neq x_i \end{cases}, \quad \int_{\Omega} \delta^i(x) d\Omega = 1 \quad (2.5)$$

$$\int_{\Omega} h(x) \delta^i d\Omega = \begin{cases} h(x_i) & \text{if } x_i \in \Omega \\ 0 & \text{if } x_i \notin \Omega, \end{cases} \quad (2.6)$$

for a continuous function  $h(x)$  at  $x_i$ .

Multiplying both side of Eq.(2.1) by the fundamental solution  $u^*$ , and integrating over the domain, the weighted residual statement is obtained

$$\int_{\Omega} (\nabla^2 u - b) u^* d\Omega = 0. \quad (2.7)$$

By means of Green's identity <sup>1</sup>, and insertion of the boundary conditions (2.2)-(2.3) using Eq.(2.4), Eq.(2.7) is rearranged as

$$\int_{\Omega} (u \nabla^2 u^* - b u^*) d\Omega + \int_{\Gamma} \frac{\partial u}{\partial n} u^* d\Gamma - \int_{\Gamma} \frac{\partial u^*}{\partial n} u d\Gamma = 0 \quad (2.8)$$

$$\int_{\Omega} u \nabla^2 u^* d\Omega - \int_{\Omega} b u^* d\Omega = - \int_{\Gamma_2} \bar{q} u^* d\Gamma_2 - \int_{\Gamma_1} \tilde{q} u^* d\Gamma_1 + \int_{\Gamma_2} \tilde{u} q^* d\Gamma_2 + \int_{\Gamma_1} \bar{u} q^* d\Gamma_1, \quad (2.9)$$

where  $q^* = \partial u^* / \partial n$  (normal derivative of  $u^*$ ).

Using the property (2.6) in the first term of the left hand side in Eq.(2.9),

$$\int_{\Omega} u \nabla^2 u^* d\Omega = \int_{\Omega} u (-\delta^i) d\Omega = -c_i u_i, \quad (2.10)$$

where the constant  $c_i$  is

$$c_i = \begin{cases} \frac{\theta_i}{2\pi}, & \text{if } i \in \Gamma, \\ 1, & \text{if } i \in \Omega \setminus \Gamma, \end{cases} \quad (2.11)$$

with the internal angle  $\theta_i$  at  $x_i$  (Figure 2.2), Eq.(2.9) becomes

$$c_i u_i + \int_{\Omega} b u^* d\Omega + \int_{\Gamma} u q^* d\Gamma = \int_{\Gamma} q u^* d\Gamma. \quad (2.12)$$

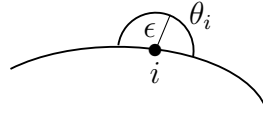


Figure 2.2: Internal angle at the node  $i$ .

The transformation of the domain integral in Eq.(2.12) due to the function  $b(x, y)$  into the boundary integral is the key point of the DRBEM. The right hand side function  $b$  is approximated as [122]

$$b_i = \sum_{j=1}^{N+K} f_{ij} \alpha_j, \quad (2.13)$$

where  $\alpha_j$ 's are sets of initially unknown coefficients,  $N$  is the number of boundary nodes,  $K$  is the number of interior points,  $f$ 's are approximating functions. Eq.(2.13) may also be expressed in matrix-vector form as

$$\mathbf{b} = \mathbf{F}\boldsymbol{\alpha}, \quad (2.14)$$

---

<sup>1</sup> Green's First Identity

$$\begin{aligned} \int_{\Omega} u^* \nabla^2 u d\Omega &= \int_{\Gamma} u^* \frac{\partial u}{\partial n} d\Gamma - \int_{\Omega} \nabla u \nabla u^* d\Omega, \\ \int_{\Omega} \nabla u \nabla u^* d\Omega &= \int_{\Gamma} u \frac{\partial u^*}{\partial n} d\Gamma - \int_{\Omega} u \nabla^2 u^* d\Omega \end{aligned}$$

where  $i = 1, 2, \dots, N + K$ ,  $\mathbf{b} = \{b_i\} = \{b_1, b_2, \dots, b_{N+K}\}$ , the symmetric coordinate matrix  $\mathbf{F}$  constructed by  $f_j$ 's columnwise is of size  $(N + K) \times (N + K)$ . Different types of  $f$ 's have been proposed so far. At most of the studies, polynomial form of the RBFs ( $f = 1 + r + \dots + r^n$ ) as a function of distance  $r$  ( $r_{ij} = \sqrt{(x_i - x_j)^2 + (y_i - y_j)^2}$ , distance between the fixed  $i$  and field  $j$  points) is encountered. In 1994, Golberg et al. [63] introduced the augmented thin plate splines [76]. These type of RBFs are also efficiently employed in most of the applications as in [26]. Partridge [121] discussed which  $f$  function will be suitable in which type of problem.

The particular solutions  $\hat{u}_{ij}$ 's are related to  $f_{ij}$ 's with the relation  $\nabla^2 \hat{u}_{ij} = f_{ij}$ . So, Eq.(2.13) is written as

$$b_i = \sum_{j=1}^{N+K} \alpha_j \nabla^2 \hat{u}_{ij}, \quad i = 1, 2, \dots, N + K. \quad (2.15)$$

Substitution of Eq.(2.15) into Eq.(2.12) yields

$$c_i u_i + \int_{\Gamma} u q^* d\Gamma - \int_{\Gamma} q u^* d\Gamma = - \sum_{j=1}^{N+K} \alpha_j \int_{\Omega} \nabla^2 \hat{u}_{ij} u^* d\Omega. \quad (2.16)$$

Applying integration by parts and Green's theorem to the right hand side of Eq.(2.16), a boundary integral equation for each source node  $i$  is occurred as

$$c_i u_i + \int_{\Gamma} u q^* d\Gamma - \int_{\Gamma} q u^* d\Gamma = \sum_{j=1}^{N+K} \alpha_j \left( c_i \hat{u}_{ij} + \int_{\Gamma} q^* \hat{u}_{ij} d\Gamma - \int_{\Gamma} u^* \hat{q}_{ij} d\Gamma \right), \quad (2.17)$$

where  $\hat{q}_{ij} = \partial \hat{u}_{ij} / \partial n$  with the outward unit normal  $\mathbf{n}$  to  $\Gamma$ .

The boundary of the region  $\Omega$  may be discretized in different forms of the elements such as constant, linear, quadratic or cubic. In this thesis, linear element discretization of boundary is adopted.

### 2.1.1 Boundary discretization with linear elements

Once the boundary is discretized into  $N_e$  number of linear elements (Fig. 2.3), Eq.(2.17) may be written as

$$\begin{aligned} c_i u_i + \sum_{e=1}^{N_e} \int_{\Gamma_k} \left( \sum_{k=1}^2 u_k N_k \right) q^* d\Gamma_k - \sum_{e=1}^{N_e} \int_{\Gamma_k} \left( \sum_{k=1}^2 q_k N_k \right) u^* d\Gamma_k \\ = \sum_{j=1}^{N+K} \alpha_j \left[ c_i \hat{u}_{ij} + \sum_{e=1}^{N_e} \int_{\Gamma_k} \left( \sum_{k=1}^2 \hat{u}_{jk} N_k \right) q^* d\Gamma_k - \sum_{e=1}^{N_e} \int_{\Gamma_k} \left( \sum_{k=1}^2 \hat{q}_{jk} N_k \right) u^* d\Gamma_k \right], \end{aligned} \quad (2.18)$$

where  $N_1$  and  $N_2$  are interpolating functions, and  $N_e = N$  with linear elements. It is not possible to take  $u$  and  $q$  outside of the integrals due to the linear variation of them over each element. Therefore, the integrals are to be evaluated numerically.

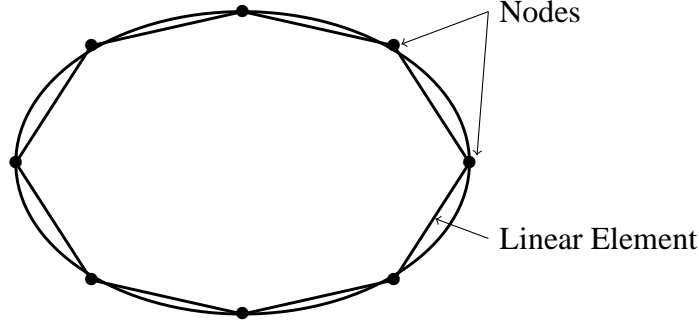


Figure 2.3: Configuration for linear elements.

In local coordinate system,  $\xi \in [-1, 1]$ , with the help of interpolating functions, the values of  $u$  and  $q$  at any point on the element are given as [24, 122]

$$u(\xi) = N_1 u_1 + N_2 u_2 \quad (2.19a)$$

$$q(\xi) = N_1 q_1 + N_2 q_2, \quad (2.19b)$$

where  $N_1 = \frac{1 - \xi}{2}$ ,  $N_2 = \frac{1 + \xi}{2}$ . The first and second integrals on the left hand side of Eq.(2.19a) is transformed to the local coordinate system as

$$\int_{\Gamma_k} u q^* d\Gamma_k = \int_{-1}^1 u(\xi) q^* \frac{\ell_e}{2} d\xi = h_{ik}^1 u_1 + h_{ik}^2 u_2 \quad (2.20a)$$

$$\int_{\Gamma_k} q u^* d\Gamma_k = \int_{-1}^1 q(\xi) u^* \frac{\ell_e}{2} d\xi = g_{ik}^1 u_1 + g_{ik}^2 u_2 \quad (2.20b)$$

where  $\ell_e$  is the length of the linear boundary element, and for each element  $k$ ,

$$h_{ik}^1 = \frac{1}{2\pi} \int_{-1}^1 \frac{(\mathbf{r}_k - \mathbf{r}_i) \cdot \mathbf{n}}{|\mathbf{r}_k - \mathbf{r}_i|^2} N_1 \frac{\ell_e}{2} d\xi, \quad h_{ik}^2 = \frac{1}{2\pi} \int_{-1}^1 \frac{(\mathbf{r}_k - \mathbf{r}_i) \cdot \mathbf{n}}{|\mathbf{r}_k - \mathbf{r}_i|^2} N_2 \frac{\ell_e}{2} d\xi \quad (2.21a)$$

$$g_{ik}^1 = \frac{1}{2\pi} \int_{-1}^1 \ln \frac{1}{|\mathbf{r}_k - \mathbf{r}_i|} N_1 \frac{\ell_e}{2} d\xi, \quad g_{ik}^2 = \frac{1}{2\pi} \int_{-1}^1 \ln \frac{1}{|\mathbf{r}_k - \mathbf{r}_i|} N_2 \frac{\ell_e}{2} d\xi, \quad (2.21b)$$

where superscripts 1, 2 refer to the starting and the end points of an element. The integrals in Eq.(2.21) are evaluated by Gaussian quadrature. BEM matrices are formed with the assembly of  $h_{ik}$ 's and  $g_{ik}$ 's at the nodes shared by two elements.

Smoothness of linear boundary elements causes the internal angle  $\theta_i$  at  $x_i$  to be  $\pi$  such that  $c_i$  becomes  $1/2$ . Defining  $H_{ik} = \overline{H}_{ik} + \frac{1}{2}\delta_{ik}$  with Kronecker delta function  $\delta_{ik}$  (if  $i = k$ ,  $\delta_{ik} = 1$ ; else  $\delta_{ik} = 0$ ), Eq.(2.19a) may be rewritten as

$$\sum_{k=1}^N H_{ik} u_k - \sum_{k=1}^N G_{ik} q_k = \sum_{j=1}^{N+K} \alpha_j \left( \sum_{k=1}^N H_{ik} \hat{u}_{kj} - \sum_{k=1}^N G_{ik} \hat{q}_{kj} \right). \quad (2.22)$$

Note that since the node 2 of element  $k - 1$  is the same point as node 1 of element  $k$ , entries of the matrix  $\overline{H}_{ik}$  will be the summation of  $h_{ik}^1$  and  $h_{i,k-1}^2$ .

If  $i = k_1$  or  $i = k_2$ , the diagonal entries are [24, 122]

$$H_{ii} = - \sum_{k=1, i \neq k}^N H_{ik} \quad (2.23a)$$

$$G_{ii} = \frac{\ell_e}{2} \left( \frac{1}{2} - \ln \ell_e \right), \quad \text{if } i = k_1, \quad (2.23b)$$

$$G_{ii} = \frac{\ell_e}{2} \left( \frac{3}{2} - \ln \ell_e \right), \quad \text{if } i = k_2, \quad (2.23c)$$

where  $k_1$  and  $k_2$  are the first and second nodes of element  $k$ , respectively.

Eq.(2.22) is stated in matrix-vector form as

$$\mathbf{H}_b \mathbf{u}_b - \mathbf{G}_b \mathbf{q}_b = \left( \mathbf{H}_b \widehat{\mathbf{U}}_b - \mathbf{G}_b \widehat{\mathbf{Q}}_b \right) \boldsymbol{\alpha}, \quad (2.24)$$

where subscript ‘b’ denotes ‘boundary’, and the matrices  $\mathbf{H}_b$ ,  $\mathbf{G}_b$ ,  $\widehat{\mathbf{U}}_b$ ,  $\widehat{\mathbf{Q}}_b$  are of size  $N \times N$ ,  $N \times N$ ,  $N \times (N + K)$ ,  $N \times (N + K)$ , respectively, and the vectors  $\mathbf{u}_b$ ,  $\mathbf{q}_b$ ,  $\boldsymbol{\alpha}$  are of length  $N$ ,  $N$ ,  $N + K$ , respectively.

Once the boundary-only system Eq.(2.24) is solved, then the interior solution is obtained with the relation

$$c_i u_i = - \sum_{k=1}^N H_{ik} u_k + \sum_{k=1}^N G_{ik} q_k + \sum_{j=1}^{N+K} \alpha_j \left( \hat{u}_{ij} + \sum_{k=1}^N H_{ik} \hat{u}_{kj} - \sum_{k=1}^N G_{ik} \hat{q}_{kj} \right), \quad (2.25)$$

where  $c_i = 1$  for the interior points. This expression may also be demonstrated in matrix-vector form as

$$\mathbf{I} \mathbf{u}_i = -\mathbf{H}_i \mathbf{u}_b + \mathbf{G}_i \mathbf{q}_b + \left( \mathbf{I} \widehat{\mathbf{U}}_i + \mathbf{H}_i \widehat{\mathbf{U}}_b - \mathbf{G}_i \widehat{\mathbf{Q}}_b \right) \boldsymbol{\alpha}, \quad (2.26)$$

where subscript ‘i’ refers to interior ( $i = 1, 2, \dots, K$ ), and the matrices  $\mathbf{H}_i$ ,  $\mathbf{G}_i$ ,  $\widehat{\mathbf{U}}_i$  are of sizes  $K \times N$ ,  $K \times N$ ,  $K \times (K + N)$ , respectively,  $\mathbf{I}$  is the  $K \times K$  identity matrix.

Combining the Eqs.(2.24) and (2.26), the whole system may be illustrated as

$$\begin{bmatrix} \mathbf{H}_b & \mathbf{0} \\ \mathbf{H}_i & \mathbf{I} \end{bmatrix} \begin{Bmatrix} \mathbf{u}_b \\ \mathbf{u}_i \end{Bmatrix} - \begin{bmatrix} \mathbf{G}_b & \mathbf{0} \\ \mathbf{G}_i & \mathbf{0} \end{bmatrix} \begin{Bmatrix} \mathbf{q}_b \\ \mathbf{0} \end{Bmatrix} = \left( \begin{bmatrix} \mathbf{H}_b & \mathbf{0} \\ \mathbf{H}_i & \mathbf{I} \end{bmatrix} \begin{bmatrix} \widehat{\mathbf{U}}_b \\ \widehat{\mathbf{U}}_i \end{bmatrix} - \begin{bmatrix} \mathbf{G}_b & \mathbf{0} \\ \mathbf{G}_i & \mathbf{0} \end{bmatrix} \begin{bmatrix} \widehat{\mathbf{Q}}_b \\ \mathbf{0} \end{bmatrix} \right) \boldsymbol{\alpha}. \quad (2.27)$$

Going back to Eq.(2.14), and writing  $\boldsymbol{\alpha} = \mathbf{F}^{-1} \mathbf{b}$  instead of the vector  $\boldsymbol{\alpha}$ , Eq.(2.27) may be formed in a compact form as

$$\mathbf{H} \mathbf{u} - \mathbf{G} \mathbf{q} = (\mathbf{H} \widehat{\mathbf{U}} - \mathbf{G} \widehat{\mathbf{Q}}) \mathbf{F}^{-1} \mathbf{b}. \quad (2.28)$$

By taking  $\mathbf{S} = (\mathbf{H} \widehat{\mathbf{U}} - \mathbf{G} \widehat{\mathbf{Q}}) \mathbf{F}^{-1}$ , Eq.(2.28) is simplified as

$$\mathbf{H} \mathbf{u} - \mathbf{G} \mathbf{q} = \mathbf{S} \mathbf{b}. \quad (2.29)$$

By means of the relation between the particular solution and the polynomial RBF  $f$ ,  $\hat{u}$  and  $\hat{q}$  are extracted as follows. Using the relation in polar coordinates (for axisymmetric case)

$$\nabla^2 \hat{u} = \frac{1}{r} \frac{\partial}{\partial r} \left( r \frac{\partial \hat{u}}{\partial r} \right) = 1 + r + \dots + r^n = f, \quad (2.30)$$

the corresponding particular solution  $\hat{u}$  is derived as

$$\hat{u} = \frac{r^2}{4} + \frac{r^3}{9} + \dots + \frac{r^{n+2}}{(n+2)^2}. \quad (2.31)$$

Then,

$$\begin{aligned} \hat{q} &= \frac{\partial \hat{u}}{\partial n} = \frac{\partial \hat{u}}{\partial r} \frac{\partial r}{\partial n} = \frac{\partial \hat{u}}{\partial r} \left( \frac{\partial r}{\partial x} \frac{\partial x}{\partial n} + \frac{\partial r}{\partial y} \frac{\partial y}{\partial n} \right) \\ &= \left( r_x \frac{\partial x}{\partial n} + r_y \frac{\partial y}{\partial n} \right) \left( \frac{1}{2} + \frac{r}{3} + \dots + \frac{r^n}{n+2} \right), \end{aligned} \quad (2.32)$$

where  $\mathbf{r} = (r_x, r_y)$ ,  $r = |\mathbf{r}|$ , and  $\frac{\partial r}{\partial x} = \frac{r_x}{r}$ ,  $\frac{\partial r}{\partial y} = \frac{r_y}{r}$ . Thus, the entries of matrices  $\hat{\mathbf{U}}$  and  $\hat{\mathbf{Q}}$  are computed by putting columnwise  $\hat{u}_{ij}$  and  $\hat{q}_{kj}$ , respectively, where  $i, j = 1, 2, \dots, N + K$  and  $k = 1, 2, \dots, N$ .

Eq.(2.29) is reduced to the system of equations of the form  $\mathbf{C}\mathbf{x} = \mathbf{d}$  shuffling the known and unknown boundary information.  $\mathbf{x}$  is the  $(N + K) \times 1$  vector of  $N$  unknown boundary values of  $\mathbf{u}$  or  $\mathbf{q}$ ,  $K$  unknown interior values of  $\mathbf{u}$ , and the vector  $\mathbf{d}$  consists of all  $N + K$  known values after shuffling.

In the next two sections, DRBEM application is employed for time dependent PDEs and diffusion-convection type equations.

### 2.1.2 DRBEM for time-dependent equations : $\nabla^2 u = b(x, y, t, \dot{u})$

Consider the simplest unsteady diffusion equation

$$\nabla^2 u = \frac{\partial u}{\partial t}. \quad (2.33)$$

The application of DRBEM to Eq.(2.33) results in matrix-vector as

$$\mathbf{H}\mathbf{u} - \mathbf{G}\mathbf{q} = \mathbf{S}\mathbf{b}, \quad (2.34)$$

where  $\mathbf{b} = \{b_i\} = \{\partial u_i / \partial t\}$ ,  $i = 1, 2, \dots, N + K$ .

Using a proper time integration scheme and shuffling with the related known and unknown boundary information, the system solution is obtained at  $N + K$  points at transient time levels.



### 2.1.3 DRBEM for nonlinear convection-diffusion equations : $\nabla^2 u = b(x, y, t, u, \dot{u}, u_x, u_y)$

If the inhomogeneity includes the time derivative of the unknown as well as convection terms, i.e.

$$\nabla^2 u = \underbrace{\frac{\partial u}{\partial t} + u \frac{\partial u}{\partial x} + v \frac{\partial u}{\partial y}}_{\mathbf{b}=\mathbf{F}\boldsymbol{\alpha}}, \quad (2.35)$$

the application of DRBEM gives, matrix-vector form of Eq.(2.35) as

$$\mathbf{H}\mathbf{u} - \mathbf{G}\mathbf{q} = \mathbf{S} \left( \frac{\partial u}{\partial t} + u \frac{\partial u}{\partial x} + v \frac{\partial u}{\partial y} \right). \quad (2.36)$$

The expression  $\mathbf{b} = \mathbf{F}\boldsymbol{\alpha}$  can also be used for the solution as

$$\mathbf{u} = \mathbf{F}\boldsymbol{\beta}, \quad \boldsymbol{\beta} \neq \boldsymbol{\alpha}. \quad (2.37)$$

Differentiation of both sides of Eq.(2.37) with respect to  $x$  and  $y$  gives

$$\frac{\partial \mathbf{u}}{\partial x} = \frac{\partial \mathbf{F}}{\partial x} \boldsymbol{\beta} \quad \text{and} \quad \frac{\partial \mathbf{u}}{\partial y} = \frac{\partial \mathbf{F}}{\partial y} \boldsymbol{\beta}, \quad (2.38)$$

where the matrices  $\partial \mathbf{F} / \partial x$  and  $\partial \mathbf{F} / \partial y$  are skew-symmetric (i.e.  $A = -A^T$ ). From the relation Eq.(2.37), replacing  $\boldsymbol{\beta} = \mathbf{F}^{-1}\mathbf{u}$  into the Eq.(2.38) gives

$$\frac{\partial \mathbf{u}}{\partial x} = \frac{\partial \mathbf{F}}{\partial x} \mathbf{F}^{-1} \mathbf{u} \quad \text{and} \quad \frac{\partial \mathbf{u}}{\partial y} = \frac{\partial \mathbf{F}}{\partial y} \mathbf{F}^{-1} \mathbf{u}. \quad (2.39)$$

In order to handle the multiplication of a vector with a matrix in nonlinear terms, the diagonal matrices  $[\mathbf{u}]_d$  and  $[\mathbf{v}]_d$  are formed as

$$[\mathbf{u}]_d = \begin{bmatrix} u_1 & 0 & \dots & 0 \\ 0 & u_2 & \dots & 0 \\ \vdots & \vdots & \ddots & \vdots \\ 0 & 0 & \dots & u_{N+K} \end{bmatrix}, \quad [\mathbf{v}]_d = \begin{bmatrix} v_1 & 0 & \dots & 0 \\ 0 & v_2 & \dots & 0 \\ \vdots & \vdots & \ddots & \vdots \\ 0 & 0 & \dots & v_{N+K} \end{bmatrix}. \quad (2.40)$$

Now, Eq.(2.36) is rearranged as

$$\mathbf{H}\mathbf{u} - \mathbf{G}\mathbf{q} = \mathbf{S} \left( \dot{u} + [\mathbf{u}]_d \frac{\partial \mathbf{F}}{\partial x} \mathbf{F}^{-1} \mathbf{u} + [\mathbf{v}]_d \frac{\partial \mathbf{F}}{\partial y} \mathbf{F}^{-1} \mathbf{u} \right). \quad (2.41)$$

Let  $\mathbf{M} = \mathbf{S} \left( [\mathbf{u}]_d \frac{\partial \mathbf{F}}{\partial x} \mathbf{F}^{-1} + [\mathbf{v}]_d \frac{\partial \mathbf{F}}{\partial y} \mathbf{F}^{-1} \right)$ . Then, Eq.(2.41) will be

$$(\mathbf{H} - \mathbf{M})\mathbf{u} - \mathbf{G}\mathbf{q} = \mathbf{S}\dot{\mathbf{u}}. \quad (2.42)$$

The system of Eq.(2.42) is iteratively solved for increasing time levels using any time integration scheme (stable ones are preferred to be able to use large time increments).

### 2.1.4 Computation of second order space derivatives using coordinate matrix

In the previous section, the convection terms containing the first order derivatives are computed by DRBEM with the help of coordinate matrix  $\mathbf{F}$ . If there are terms containing second order derivatives in addition to convection terms, computation of these second order derivatives are achieved again with the coordinate matrix.

Second order space derivatives may be expressed in two ways. The first one is

$$\frac{\partial^2 \mathbf{u}}{\partial x^2} = \frac{\partial^2 \mathbf{F}}{\partial x^2} \mathbf{F}^{-1} \mathbf{u} \quad \text{and} \quad \frac{\partial^2 \mathbf{u}}{\partial y^2} = \frac{\partial^2 \mathbf{F}}{\partial y^2} \mathbf{F}^{-1} \mathbf{u}. \quad (2.43)$$

It is worth to mention here that polynomial radial basis functions containing linear term  $r$  are not suitable if the second derivatives are to be treated by Eq.(2.43). This is due to the singularity at  $r = 0$ . As an example, let  $f = 1 + r$  be taken. Then,

$$\frac{\partial f}{\partial x} = \frac{\partial f}{\partial r} \frac{\partial r}{\partial x} = \frac{r_x}{r} \quad (2.44)$$

$$\frac{\partial^2 f}{\partial x^2} = \frac{\partial}{\partial x} \left( \frac{\partial f}{\partial x} \right) = \frac{\partial}{\partial x} \left( \frac{r_x}{r} \right) = \frac{r^2 - r_x^2}{r^3}, \quad (2.45)$$

where  $r_x = x_i - x_k$ . Note that the term  $(r^2 - r_x^2)/r^3$  goes to  $\infty$  as  $r$  goes to zero since  $r^3$  goes to zero faster than  $r^2$ .

The second way is to use the first order derivative representation given in Eq.(2.39) [112]. With the same idea for obtaining Eq.(2.39), let

$$\frac{\partial \mathbf{u}}{\partial x} = \mathbf{F} \boldsymbol{\gamma}, \quad \boldsymbol{\gamma} \neq \boldsymbol{\beta} \neq \boldsymbol{\alpha}. \quad (2.46)$$

Differentiating both sides of this expression with respect to  $x$  (or  $y$ ), and replacing  $\boldsymbol{\gamma}$  from Eq.(2.46) and using Eq.(2.39) yields

$$\frac{\partial^2 \mathbf{u}}{\partial x^2} = \frac{\partial \mathbf{F}}{\partial x} \boldsymbol{\gamma} = \frac{\partial \mathbf{F}}{\partial x} \mathbf{F}^{-1} \frac{\partial \mathbf{u}}{\partial x} = \frac{\partial \mathbf{F}}{\partial x} \mathbf{F}^{-1} \left( \frac{\partial \mathbf{F}}{\partial x} \mathbf{F}^{-1} \mathbf{u} \right). \quad (2.47)$$

### 2.1.5 Time integration schemes

In this section, two types of finite difference schemes derived from Taylor series expansion are introduced. These time integration schemes are going to be used throughout the thesis.

#### 2.1.5.1 Backward-Euler method

Backward-Euler method is a first order, implicit method, and eases the formation of iterative systems between more than two PDE equations.

Notationally, consider  $u(x, y, t_m) = u^m$ . Expanding the Taylor series about  $t_m = t_{m+1} - \Delta t$ , the first order derivative is extracted as

$$\begin{aligned}
u^m &= u^{m+1} - \Delta t \left. \frac{\partial u}{\partial t} \right|^{m+1} + \frac{\Delta t^2}{2!} \left. \frac{\partial^2 u}{\partial t^2} \right|^{m+1} - \dots \\
\left. \frac{\partial u}{\partial t} \right|^{m+1} &= \frac{u^{m+1} - u^m}{\Delta t} + \mathcal{O}(\Delta t).
\end{aligned} \tag{2.48}$$

### 2.1.5.2 Houbolt method

A third order, implicit time integration scheme which is called Houbolt method [7], is derived by Taylor expansions written about  $t_{m+1}$  by taking as  $t_m = t_{m+1} - \Delta t$ ,  $t_{m-1} = t_{m+1} - 2\Delta t$ ,  $t_{m-2} = t_{m+1} - 3\Delta t$ , respectively. Therefore,

$$\begin{aligned}
-18 \left/ u^m \right. &= u^{m+1} - \Delta t \left. \frac{\partial u}{\partial t} \right|^{m+1} + \frac{\Delta t^2}{2!} \left. \frac{\partial^2 u}{\partial t^2} \right|^{m+1} - \frac{\Delta t^3}{3!} \left. \frac{\partial^3 u}{\partial t^3} \right|^{m+1} + \frac{\Delta t^4}{4!} \left. \frac{\partial^4 u}{\partial t^4} \right|^{m+1} - \dots \\
+9 \left/ u^{m-1} \right. &= u^{m+1} - 2\Delta t \left. \frac{\partial u}{\partial t} \right|^{m+1} + \frac{4\Delta t^2}{2!} \left. \frac{\partial^2 u}{\partial t^2} \right|^{m+1} - \frac{8\Delta t^3}{3!} \left. \frac{\partial^3 u}{\partial t^3} \right|^{m+1} + \frac{16\Delta t^4}{4!} \left. \frac{\partial^4 u}{\partial t^4} \right|^{m+1} - \dots \\
-2 \left/ u^{m-2} \right. &= u^{m+1} - 3\Delta t \left. \frac{\partial u}{\partial t} \right|^{m+1} + \frac{9\Delta t^2}{2!} \left. \frac{\partial^2 u}{\partial t^2} \right|^{m+1} - \frac{27\Delta t^3}{3!} \left. \frac{\partial^3 u}{\partial t^3} \right|^{m+1} + \frac{81\Delta t^4}{4!} \left. \frac{\partial^4 u}{\partial t^4} \right|^{m+1} - \dots \\
11u^{m+1} &= 11u^{m+1}
\end{aligned}$$

Multiplying with the indicated numbers of both sides of the first three equations, and adding the four equations, Houbolt method for the first order time derivative is obtained as

$$\begin{aligned}
11u^{m+1} - 18u^m + 9u^{m-1} - 2u^{m-2} &= 6\Delta t \left. \frac{\partial u}{\partial t} \right|^{m+1} - \mathcal{O}(\Delta t^4) \\
\left. \frac{\partial u}{\partial t} \right|^{m+1} &= \frac{1}{6\Delta t} (11u^{m+1} - 18u^m + 9u^{m-1} - 2u^{m-2}) + \mathcal{O}(\Delta t^3),
\end{aligned} \tag{2.49}$$

which is order of  $\Delta t^3$ .

## 2.2 DRBEM application to free or mixed convection flows

In this section, natural or mixed convection flows either under the effect of an applied magnetic field or without magnetic effect in porous enclosures are simulated using DRBEM. An isotropic, homogeneous porous medium saturated with an incompressible fluid is considered. The thermal and physical properties of the fluid are assumed to be constant except for the density variation according to Boussinesq approximation. The fluid and the solid particles are also assumed to be in local thermal equilibrium. The viscous dissipation is neglected. The Forchheimer terms (quadratic drag terms) are also neglected in the momentum equations. In the cases of the effect of an applied

magnetic field, induced magnetic field is also neglected together with Joule heating effects. The governing equations are introduced, and then the application of DRBEM to these equations is presented. The solution procedure is summarized, and the results are visualized in terms of either  $\psi - T$  or  $\psi - T - w$ .

### 2.2.1 Numerical solution of mixed convection flow in a porous medium by DRBEM

Initially, DRBEM is applied to solve the steady, two-dimensional mixed convection flow in a porous square cavity with differentially heated and moving side walls. The problem geometry consisting of the cross-section of a unit square cavity which has the moving lids on the left and right walls is depicted in Figure 2.4. The velocity  $v = 1$  on the vertical walls with  $u = \psi = 0$ ; and  $u = v = \psi = 0$  on the horizontal walls. The right wall is the hot ( $T_h = 1$ ), and the left wall is the cold ( $T_c = 0$ ) wall while the top and bottom walls are adiabatic ( $\partial T/\partial n = 0$ ). Vorticity boundary conditions are unknown, and are going to be derived with the help of DRBEM coordinate matrix  $\mathbf{F}$  during the iterative solution procedure.

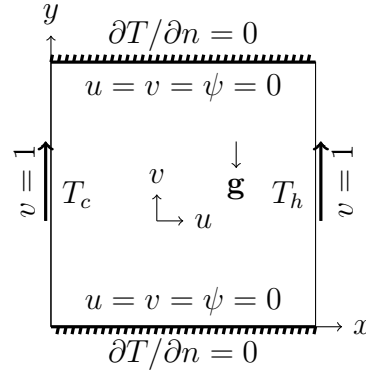


Figure 2.4: Problem 2.2.1 configuration.

The non-dimensional governing equations for the two-dimensional, steady, laminar mixed convection flow in an incompressible fluid-saturated porous medium in terms of stream function  $\psi$ -temperature  $T$ -vorticity  $w$  are [36]

$$\nabla^2 \psi = -w \quad (2.50a)$$

$$\frac{1}{\epsilon_p Re} \nabla^2 w = \frac{1}{\epsilon_p^2} \left( u \frac{\partial w}{\partial x} + v \frac{\partial w}{\partial y} \right) - \frac{Gr}{Re^2} \frac{\partial T}{\partial x} + \frac{1}{Da Re} w \quad (2.50b)$$

$$\frac{1}{Pr Re} \nabla^2 T = u \frac{\partial T}{\partial x} + v \frac{\partial T}{\partial y} \quad (2.50c)$$

where  $\epsilon_p$  is the porosity of the porous medium,  $u = \partial\psi/\partial y$ ,  $v = -\partial\psi/\partial x$ ,  $w = \partial v/\partial x - \partial u/\partial y$ . Non-dimensional physical parameters are Reynolds, Grashof, Darcy and Prandtl numbers, respectively, given as

$$Re = \frac{UL}{\nu_e}, \quad Gr = \frac{g\beta\Delta TL^3}{\nu_e^2}, \quad Da = \frac{\kappa}{L^2}, \quad Pr = \frac{\nu_e}{\alpha_e}, \quad (2.51)$$

with characteristic velocity  $U$ , characteristic length  $L$ , gravitational acceleration  $g$ , effective kinematic viscosity  $\nu_e$ , permeability of the porous medium  $\kappa$ , thermal expansion coefficient  $\beta$ , temperature difference  $\Delta T = T_h - T_c$ , effective thermal diffusivity  $\alpha_e$  of the porous medium. The steady equations (2.50) are constructed keeping the porosity  $\epsilon_p$  in Eq.(1.17) of Chapter 1, and applying the same non-dimensional variables.

Once the linear boundary elements are used for the discretization of the boundary, matrix-vector form for Eqs.(2.50) are written as

$$\mathbf{H}\psi^{m+1} - \mathbf{G}\psi_q^{m+1} = -\mathbf{S}w^m \quad (2.52a)$$

$$(\mathbf{H} - PrRe\mathbf{S}\mathbf{M})T^{m+1} - \mathbf{G}T_q^{m+1} = 0 \quad (2.52b)$$

$$\left( \mathbf{H} - \frac{Re}{\epsilon_p}\mathbf{S}\mathbf{M} - \frac{\epsilon_p}{Da}\mathbf{S} \right) w^{m+1} - \mathbf{G}w_q^{m+1} = -\epsilon_p \frac{Gr}{Re} \mathbf{S} \frac{\partial \mathbf{F}}{\partial \mathbf{x}} \mathbf{F}^{-1} T^{m+1} \quad (2.52c)$$

where  $\mathbf{S} = (\mathbf{H}\hat{\mathbf{U}} - \mathbf{G}\hat{\mathbf{Q}})\mathbf{F}^{-1}$ ,  $\mathbf{M} = \left( [\mathbf{u}]_d \frac{\partial \mathbf{F}}{\partial \mathbf{x}} \mathbf{F}^{-1} + [\mathbf{v}]_d \frac{\partial \mathbf{F}}{\partial \mathbf{y}} \mathbf{F}^{-1} \right)$ , the diagonal matrices  $[\mathbf{u}]_d, [\mathbf{v}]_d$  are formed by the vectors  $u^{m+1} = (\partial \mathbf{F} / \partial \mathbf{y}) \mathbf{F}^{-1} \psi^{m+1}$ ,  $v^{m+1} = -(\partial \mathbf{F} / \partial \mathbf{x}) \mathbf{F}^{-1} \psi^{m+1}$ , respectively, and  $m$  is the iteration level.

Unknown vorticity boundary conditions are obtained from the definition of  $w$  as

$$w = \frac{\partial v}{\partial x} - \frac{\partial u}{\partial y} = \frac{\partial \mathbf{F}}{\partial \mathbf{x}} \mathbf{F}^{-1} v - \frac{\partial \mathbf{F}}{\partial \mathbf{y}} \mathbf{F}^{-1} u, \quad (2.53)$$

with the help of coordinate matrix  $\mathbf{F}$ . Also, all the space derivatives on the right hand sides in Eqs.(2.50) are computed by using DRBEM coordinate matrix  $\mathbf{F}$ , i.e.

$$\frac{\partial T}{\partial x} = \frac{\partial \mathbf{F}}{\partial \mathbf{x}} \mathbf{F}^{-1} T, \quad \frac{\partial w}{\partial y} = \frac{\partial \mathbf{F}}{\partial \mathbf{y}} \mathbf{F}^{-1} w. \quad (2.54)$$

Systems of equations (2.52a)-(2.52c) are solved iteratively for the unknowns  $\psi, T, w$ , and normal derivatives  $\psi_q, T_q, w_q$  with initial  $w$  and  $T$  values, and the iterations continue until the criterion

$$\frac{\|\psi^{m+1} - \psi^m\|_\infty}{\|\psi^{m+1}\|_\infty} + \frac{\|T^{m+1} - T^m\|_\infty}{\|T^{m+1}\|_\infty} + \frac{\|w^{m+1} - w^m\|_\infty}{\|w^{m+1}\|_\infty} < \epsilon \quad (2.55)$$

is satisfied where  $\epsilon = 10^{-5}$  is the tolerance for stopping the iterations.

In order to accelerate the convergence for large values of problem parameters a relaxation parameter  $0 < \gamma \leq 1$  determined by trial and error is used for the vorticity as  $w^{m+1} \leftarrow \gamma w^{m+1} + (1 - \gamma)w^m$ . Further, average Nusselt number through the heated wall is computed by  $\overline{Nu} = \int_0^1 (\partial T / \partial x)|_{x=1} dy$  utilizing the composite Simpson's rule (Appendix B).

In the numerical computations of stream function, vorticity and temperature in a square cavity with heated and upwards moving vertical walls, radial basis function  $f = 1 + r$ , and 8-point Gaussian quadrature are used for the construction of BEM matrices  $\mathbf{F}, \mathbf{H}$

and  $G$ .  $N = 96$ ,  $K = 625$  are taken, and  $Re = 100$  is fixed. Cavity contains a fluid saturated porous medium with  $\epsilon_p \leq 1$ . Mixed convection flow behavior in this porous medium is depicted in terms of streamlines, isotherms, and vorticity contours for various values of  $Da$ ,  $Gr$  and  $Pr$ .

As  $Da$  decreases (Figure 2.5), permeability decreases and causes a force opposite to the flow direction which tends to resist the flow. This means that the fluid flows slowly. While the center of streamlines is in the direction of moving lids, they cluster along the left and right boundaries forming boundary layers, and the effects of moving walls almost disappear. Isotherms become almost perpendicular to the top and bottom walls pointing to the increase in conduction dominated effect. Circulation in the vorticity through the upper corners due to the effect of moving lids diminishes, and strong boundary layers are formed through the right and left walls leaving a stagnant region at the center.

As  $Gr$  increases, the left counter-clockwise secondary cell starts to be squeezed through the left wall, and the clockwise primary cell is centered. Buoyancy effect is pronounced due to the increase in  $Ri = Gr/Re^2$ . That is, natural convection is high. Actually, this can be seen in isotherms at  $Gr = 10^5$ . While the isotherms pronounce the forced convection with  $Gr = 10^3$ ,  $Da = 0.01$  ( $Ri = 0.1$ ) in Figure 2.5, they cluster through the left and right walls forming strong temperature gradients for  $Gr = 10^5$  (Figure 2.6). Even though there is a Darcy effect with strength  $Da = 0.01$ , we are able to observe the characteristics of mixed convection flow in a non-porous medium in the cavity [72]. Vorticity almost covers the cavity with new cells through the left and right walls, and spreads also along the top and bottom walls.

The increase in  $Pr$  only affects the isotherms (as is seen in Figure 2.7) due to the dominance of convection terms in the temperature equation.

The decrease in the velocity of the fluid with the decrease in  $Da$  number is shown in Figure 2.8a with the u-velocity profile through  $x = 0.5$ . The dominance of natural convection with high  $Gr$  is depicted in Figure 2.8b. When  $Gr$  is increased,  $\overline{Nu}$  values also increase. Average Nusselt number is almost the same for all values of Grashof number with  $Da \leq 10^{-4}$  due to the dominance of conduction. However,  $\overline{Nu}$  increases as  $Da$  increases showing the increase in the heat transfer.

Finally, we show how the heat transfer is affected by different values of porosity. As is seen in Figure 2.9a,  $\overline{Nu}$  increases at all  $\epsilon_p$  values as  $Da$  increases. High  $\overline{Nu}$  values are obtained by small  $\epsilon_p$  values which yield the increase in convective heat transfer. Here, forced convection is dominant ( $Ri < 1$ ). As the natural convective effect increases  $Ri > 1$  (Figure 2.9b), it is found that  $\overline{Nu}$  takes larger values with  $\epsilon_p = 0.8$  than the other ones. Namely, the natural convection is pronounced with the increase in  $\epsilon_p$ .

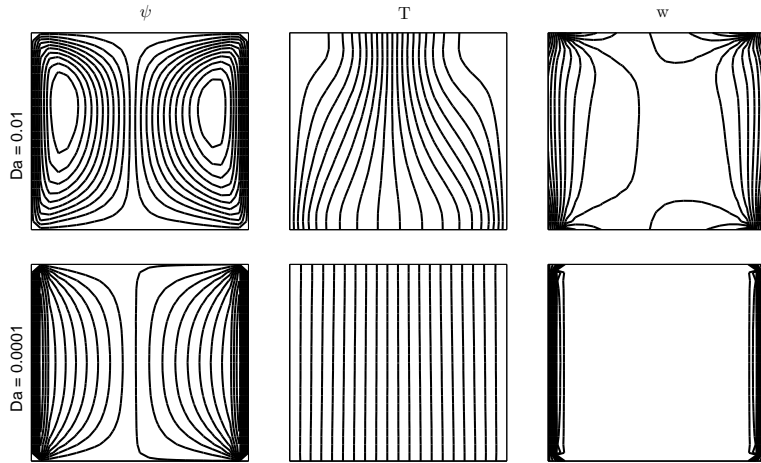


Figure 2.5: Problem 2.2.1:  $Pr = 0.71$ ,  $Gr = 10^3$ ,  $\epsilon_p = 1$ ,  $\gamma = 0.1$

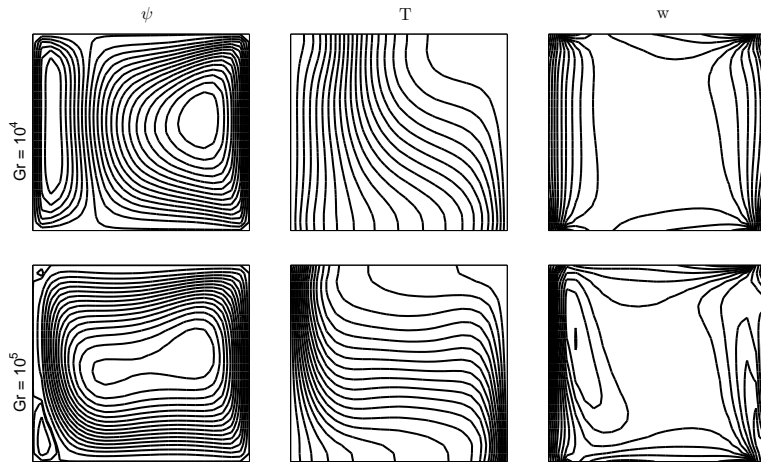


Figure 2.6: Problem 2.2.1:  $Pr = 0.71$ ,  $Da = 0.01$ ,  $\epsilon_p = 1$ ,  $\gamma = 0.5$

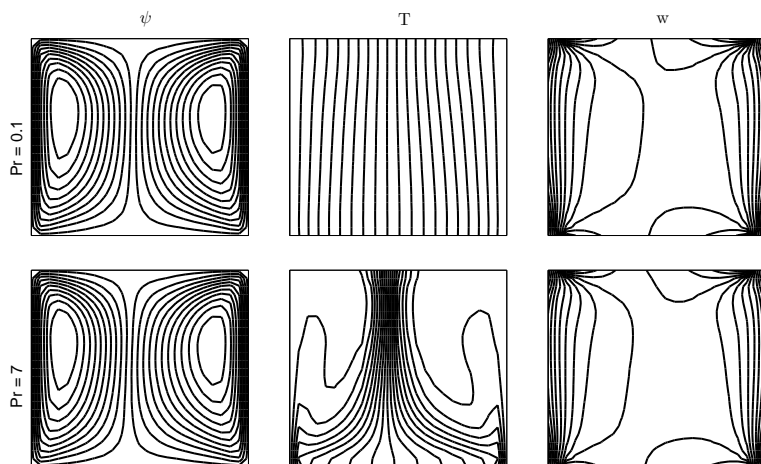


Figure 2.7: Problem 2.2.1:  $Da = 0.01$ ,  $Gr = 10^3$ ,  $\epsilon_p = 1$ ,  $\gamma = 0.5$

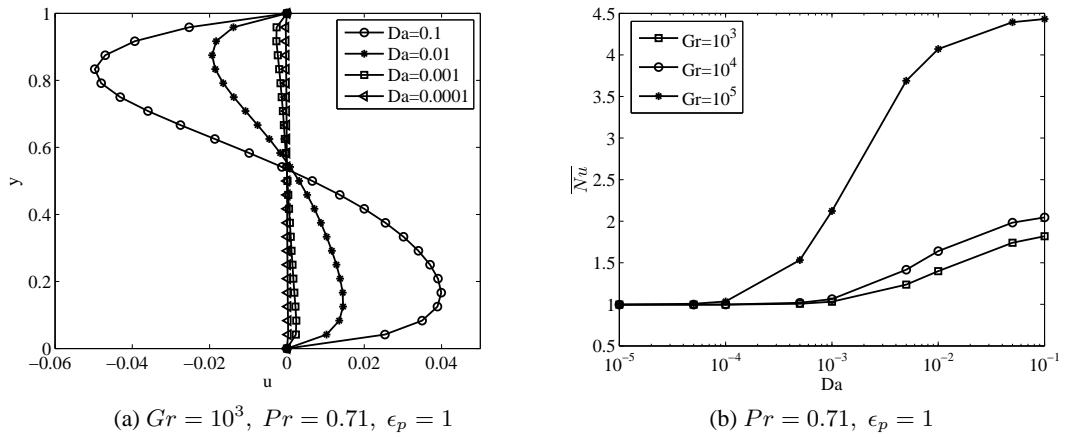


Figure 2.8: Problem 2.2.1: Mid-u-velocity profile and average Nusselt number on the heated wall.

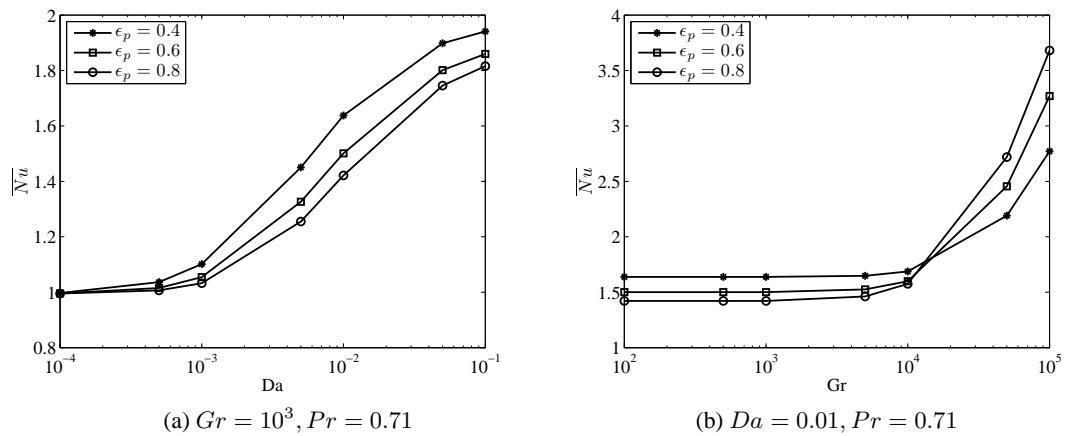


Figure 2.9: Problem 2.2.1: Average Nusselt number variations with  $\epsilon_p$  on the heated wall.



## 2.2.2 DRBEM solution of free convection in porous enclosures under the effect of a magnetic field

In different cross sections as square, isosceles trapezoidal and right-angle trapezoidal enclosures depicted in Figure 2.10, Darcy-Brinkman model is considered. In the configurations,  $\mathbf{B}$  is the applied magnetic field with an inclination angle  $\varphi$ ,  $\mathbf{g}$  is the gravitational acceleration vector, the jagged walls are adiabatic ( $\partial T/\partial n = 0$ ), and  $q_0'''$  is the internal heat generation.

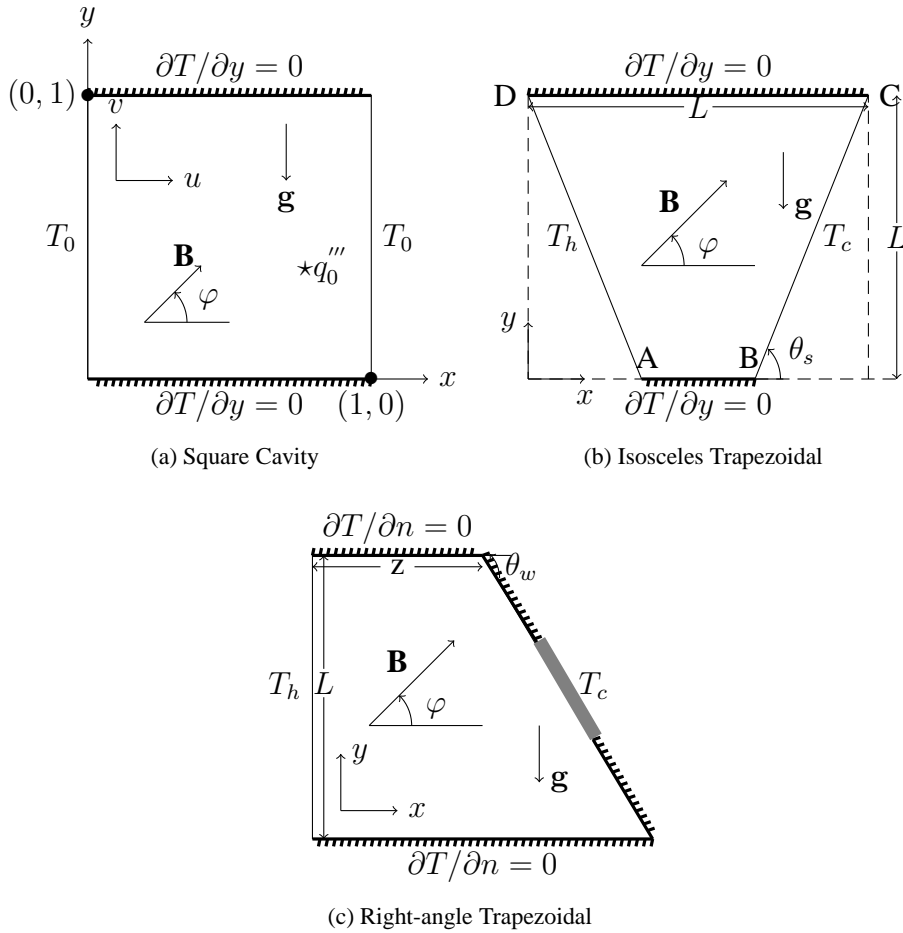


Figure 2.10: Problem 2.2.2 configurations.

The governing equations in  $(u - v - p - T)$  form is

$$\frac{\partial u}{\partial x} + \frac{\partial v}{\partial y} = 0 \quad (2.56a)$$

$$u = -\frac{\kappa}{\mu} \frac{\partial p}{\partial x} - \frac{\sigma \kappa B_0^2}{\mu} (v \sin \varphi \cos \varphi - u \sin^2 \varphi) \quad (2.56b)$$

$$v = -\frac{\kappa}{\mu} \frac{\partial p}{\partial y} - \frac{\sigma \kappa B_0^2}{\mu} (u \sin \varphi \cos \varphi - v \cos^2 \varphi) + \frac{\kappa \beta g}{\nu} (T - T_c) \quad (2.56c)$$

$$u \frac{\partial T}{\partial x} + v \frac{\partial T}{\partial y} = \alpha_e \left( \frac{\partial^2 T}{\partial x^2} + \frac{\partial^2 T}{\partial y^2} \right) + \frac{q_0'''}{\rho_0 c_p}, \quad (2.56d)$$

where  $\kappa$  is the permeability of the porous medium,  $\mu$  is the dynamic viscosity,  $B_0$  is the magnitude of  $\mathbf{B}$ ,  $\sigma$  is the electrical conductivity of the fluid,  $\nu$  is the kinematic viscosity,  $\beta$  is the thermal expansion coefficient,  $c_p$  is the specific heat at constant pressure,  $\rho_0$  is the reference density and  $\alpha_e$  is the effective thermal diffusivity.

Using dimensionless variables

$$x' = \frac{x}{L}, \quad y' = \frac{y}{L}, \quad u' = \frac{L}{\alpha_e} u, \quad v' = \frac{L}{\alpha_e} v, \quad T' = \frac{T - T_c}{T_d}, \quad (2.57)$$

where  $T_d = T_h - T_c$  in trapezoidal enclosures,  $T_d = (q_0''' l^2 / k)$  in square cavity, and then, applying the vorticity definition to eliminate the pressure terms, non-dimensional form of the Eq.(2.56) in terms of  $\psi - T$  may be written as

$$\frac{\partial^2 \psi}{\partial x^2} + \frac{\partial^2 \psi}{\partial y^2} = -Ra \frac{\partial T}{\partial x} - Ha^2 \left( \frac{\partial^2 \psi}{\partial y^2} \sin^2 \varphi + \frac{\partial^2 \psi}{\partial x \partial y} \sin(2\varphi) + \frac{\partial^2 \psi}{\partial x^2} \cos^2 \varphi \right) \quad (2.58a)$$

$$\frac{\partial^2 T}{\partial x^2} + \frac{\partial^2 T}{\partial y^2} = \frac{\partial \psi}{\partial y} \frac{\partial T}{\partial x} - \frac{\partial \psi}{\partial x} \frac{\partial T}{\partial y} - Q \quad (2.58b)$$

where  $Q = 1$  which is the heat generation parameter for the square cavity while  $Q = 0$  for trapezoidal cavities, and Rayleigh  $Ra$  and Hartmann  $Ha$  numbers for the porous medium, respectively, are

$$Ra = \frac{g \kappa \beta L T_d}{\alpha_e \nu}, \quad Ha^2 = \frac{\sigma \kappa B_0^2}{\mu}. \quad (2.59)$$

The second order space derivatives in Eq.(2.58a) are handled by Eq.(2.43), and radial basis functions are taken as  $\tilde{f} = 1 + r^2 + r^3$  for the stream function equation and  $\bar{f} = 1 + r$  or  $\bar{f} = 1 + r + r^2$  for the temperature equation. Hence, the entries of coordinate matrices and  $\hat{\mathbf{U}}$ ,  $\hat{\mathbf{Q}}$  will be different for coupled equations (2.58a)-(2.58b).

DRBEM application to this coupled Eqs.(2.58) with an iteration to eliminate nonlinearity results in the following matrix-vector form of the equations

$$(\mathbf{H} + \tilde{\mathbf{S}}\mathbf{R})\psi^{m+1} - \mathbf{G}\psi_q^{m+1} = -Ra \tilde{\mathbf{S}} \frac{\partial \tilde{\mathbf{F}}}{\partial \mathbf{x}} \tilde{\mathbf{F}}^{-1} T^m \quad (2.60a)$$

$$(\mathbf{H} - \bar{\mathbf{S}}\mathbf{M})T^{m+1} - \mathbf{G}T_q^{m+1} = -\bar{\mathbf{S}}Q \quad (2.60b)$$

where  $\mathbf{S}$ ,  $\mathbf{R}$ ,  $\mathbf{M}$  are the matrices

$$\tilde{\mathbf{S}} = \left( \mathbf{H}\tilde{\mathbf{U}} - \mathbf{G}\tilde{\mathbf{Q}} \right) \tilde{\mathbf{F}}^{-1}, \quad \bar{\mathbf{S}} = \left( \mathbf{H}\bar{\mathbf{U}} - \mathbf{G}\bar{\mathbf{Q}} \right) \bar{\mathbf{F}}^{-1} \quad (2.61)$$

$$\mathbf{R} = Ha^2 \left( \sin^2 \varphi \frac{\partial^2 \tilde{\mathbf{F}}}{\partial \mathbf{y}^2} \tilde{\mathbf{F}}^{-1} + \sin(2\varphi) \frac{\partial^2 \tilde{\mathbf{F}}}{\partial \mathbf{x} \partial \mathbf{y}} \tilde{\mathbf{F}}^{-1} + \cos^2 \varphi \frac{\partial^2 \tilde{\mathbf{F}}}{\partial \mathbf{x}^2} \tilde{\mathbf{F}}^{-1} \right) \quad (2.62)$$

$$\mathbf{M} = \frac{\partial \bar{\mathbf{F}}}{\partial \mathbf{y}} \bar{\mathbf{F}}^{-1} [\psi]_{\mathbf{d}} \frac{\partial \bar{\mathbf{F}}}{\partial \mathbf{x}} \bar{\mathbf{F}}^{-1} - \frac{\partial \bar{\mathbf{F}}}{\partial \mathbf{x}} \bar{\mathbf{F}}^{-1} [\psi]_{\mathbf{d}} \frac{\partial \bar{\mathbf{F}}}{\partial \mathbf{y}} \bar{\mathbf{F}}^{-1} \quad (2.63)$$

and  $Q$  is a constant vector,  $m$  is the iteration number,  $[\psi]_{\mathbf{d}}$  is the diagonal matrix constructed by the vector  $\psi^{m+1}$  at each iteration. Shuffling the known and unknown boundary information and rearranging the Eqs.(2.60) in the form  $\mathbf{C}\mathbf{x} = \mathbf{d}$ , the Gaussian elimination with partial pivoting is used for the solution.

Step by step, iterative procedure works as

1.  $T^0$  is taken as zero everywhere except on the boundary. Then, stream function is obtained from Eq.(2.60a).
2. Due to the presence of dimensionless physical parameters  $Ra$  and  $Ha$  in the stream function equation, a relaxation parameter  $0 < \gamma \leq 1$  for  $\psi$  is employed as

$$\psi^{m+1} \leftarrow (1 - \gamma)\psi^{m+1} + \gamma\psi^m \quad (2.64)$$

for accelerating convergence.

3. Stopping criteria is

$$\frac{\|\psi^{m+1} - \psi^m\|_{\infty}}{\|\psi^{m+1}\|_{\infty}} < \epsilon \quad \text{or} \quad \frac{\|T^{m+1} - T^m\|_{\infty}}{\|T^{m+1}\|_{\infty}} < \epsilon, \quad (2.65)$$

where  $\epsilon = 1e - 7$  is the tolerance.

### 2.2.2.1 Square cavity case

The results are obtained using  $\tilde{f} = 1 + r^2 + r^3$  for  $\psi$  and  $\bar{f} = 1 + r$  for  $T$ , and 8-points Gaussian quadrature is used for boundary integrations.

Computations are carried for  $10^3 \leq Ra \leq 10^7$ ,  $Ha \leq 200$  and for magnetic field inclination angle  $\varphi = 0, \pi/6, \pi/4, \pi/2$ . The number of linear boundary elements  $N$  is kept around 144, and results are obtained at 289 interior points. For small  $Ha$ , we need to take more elements since the convection due to temperature becomes dominant especially for large values of  $Ra$ .

Figure 2.11 shows  $Ha$  variation for a fixed  $Ra = 10^5$  and inclination angle of magnetic field  $\varphi = \pi/6$ . As  $Ha$  increases, maximum value of streamlines drops implying flattening tendency of velocity profile for increasing Hartmann number. Boundary layers (intensification of stream function lines having equal values of streamline contours), and stagnant cores close to the side walls in streamlines tend to move through the center of the cavity forming also an intensive layer between them in the direction of the applied magnetic field. Isotherms become parallel to the left and right walls for  $Ha = 100$  due to the dominance of pure conduction.

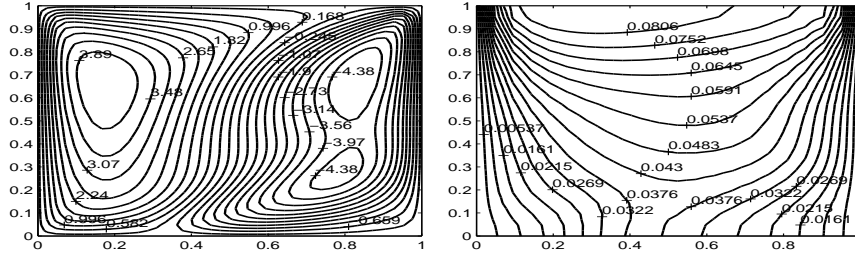
As  $Ra$  is increased, maximum value of stream function increases as is shown in Figure 2.12. This means that the fluid gains acceleration. For high  $Ra$ , relaxation parameter

$\gamma$  is needed and the number of boundary elements is increased to capture reasonable physical behavior. Thermal boundary layer formation starts for increasing  $Ra$  and the cores become close to the side walls. Isotherms are distorted from being parallel to the side walls for high  $Ra$ , covering almost all parts of the cavity. Thus, decreasing  $Ra$  for a fixed  $Ha$ , and increasing  $Ha$  for a fixed  $Ra$  have the same effects on isotherms.

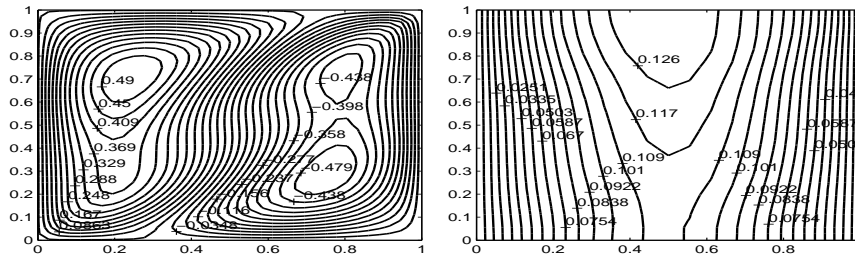
When the inclination angle  $\varphi$  of magnetic field is changed (see Figure 2.13), an intensive layer formation for  $\psi$  is observed in the direction of the external magnetic field. By the reported  $\psi_{\max}$  values, it can be said that the motion of a fluid inside the cavity accelerates when the direction of the magnetic field is changed from the horizontal ( $\varphi = 0$ ) to the vertical direction ( $\varphi = \pi/2$ ). Isotherms are not affected much with the change in  $\varphi$ .

These behaviors of flow and heat transfer due to the variations of  $Ra$ ,  $Ha$  and inclination angle  $\varphi$  are expected results for natural convection flow. When the fluid is heated, the fluid particles become less dense and raise, then the heated hot fluid particles transfer energy to the cooler fluid particles and the process continues. So, a convective flow emerges inside the cavity. Flattening tendency in the flow and the retarding effect of the Lorentz force are observed as the drop in  $\psi_{\max}$  for increasing values of  $Ha$ .

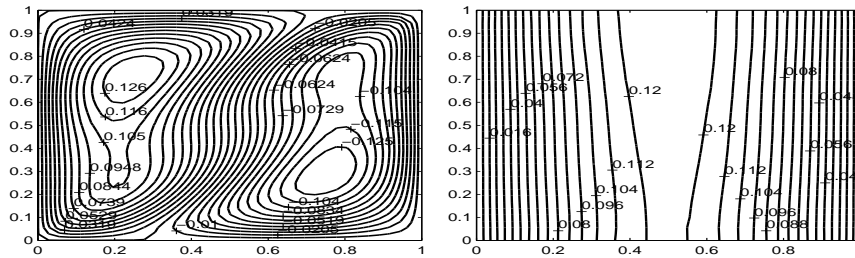
Average Nusselt number is the ratio of convective heat transfer to conductive heat transfer. Table 2.1 presents the average Nusselt number (computed by composite Simpson's rule on the left wall) variation with respect to varying  $Ha$  and  $Ra$  values. As  $Ha$  becomes larger than 50, the strength of the heat transfer is progressively withheld and  $\overline{Nu}$  attempts to the conductive heat transfer mode. Therefore,  $\overline{Nu}$  remains almost the same after  $Ha = 50$  in Table 2.1a which means that the convection and conduction change in the same proportion. This is also investigated with the  $\overline{Nu}$  values in Table 2.1b until  $Ra = 10^5$ . The stronger magnetic field is needed for large values of  $Ra > 10^5$  in order to keep on the value  $\overline{Nu} = 0.4905$ .



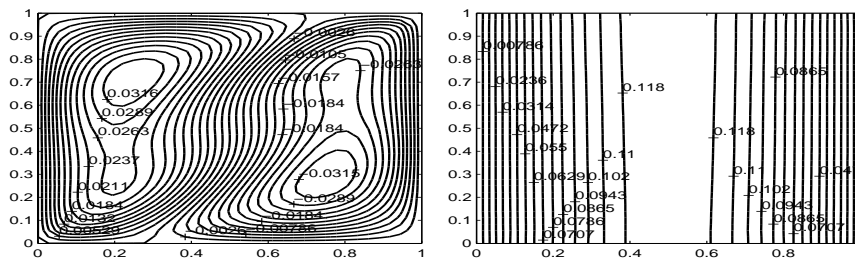
(a)  $Ha = 10$ ,  $\gamma = 0.4$ ,  $\Psi_{\max} = 4.2798226$ ,  $T_{\max} = 0.08594$



(b)  $Ha = 50$ ,  $\Psi_{\max} = 0.5270314$ ,  $T_{\max} = 0.13407$

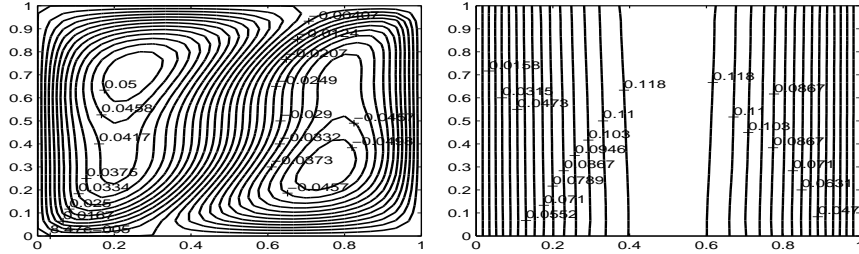


(c)  $Ha = 100$ ,  $\Psi_{\max} = 0.1354132$ ,  $T_{\max} = 0.12800$

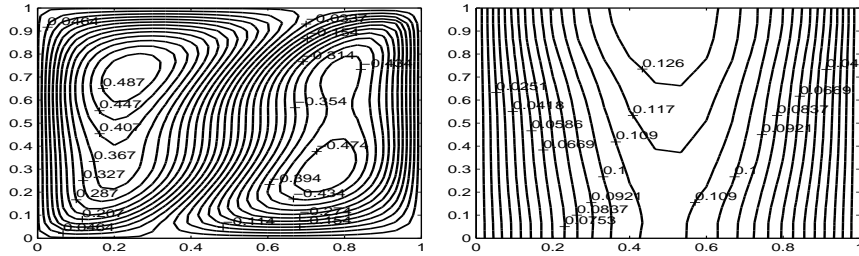


(d)  $Ha = 200$ ,  $\Psi_{\max} = 0.0338361$ ,  $T_{\max} = 0.12575$

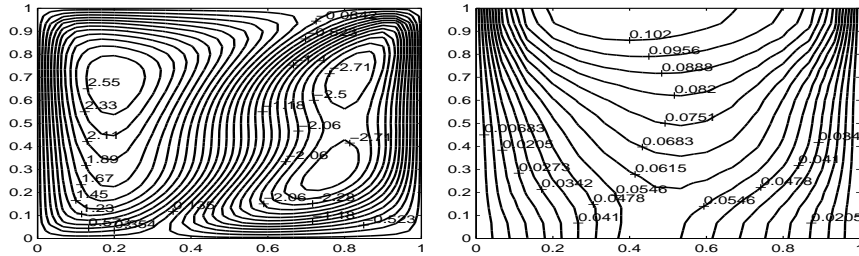
Figure 2.11: Problem 2.2.2.1:  $Ra = 10^5$ ,  $\varphi = \pi/6$



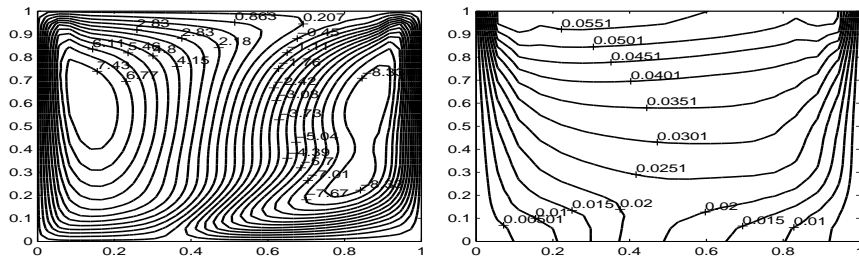
(a)  $Ra = 10^4$ ,  $\Psi_{\max} = 0.0538415$ ,  $T_{\max} = 0.12617$



(b)  $Ra = 10^5$ ,  $\Psi_{\max} = 0.5227590$ ,  $T_{\max} = 0.13390$

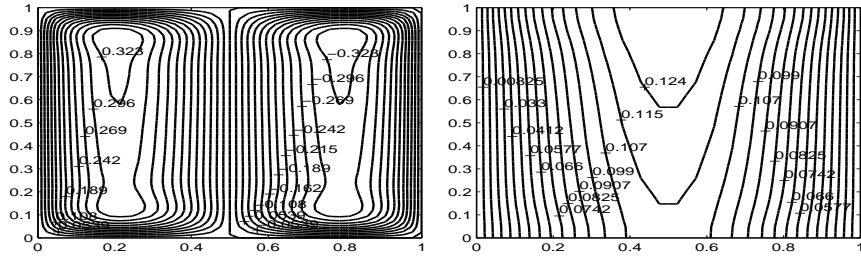


(c)  $Ra = 10^6$ ,  $\gamma = 0.5$ ,  $\Psi_{\max} = 2.7653297$ ,  $T_{\max} = 0.10928$

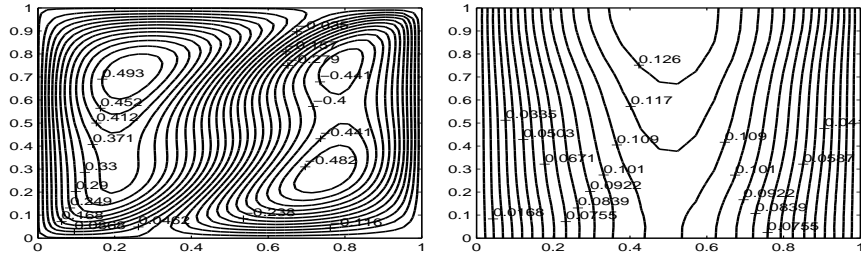


(d)  $Ra = 10^7$ ,  $\gamma = 0.65$ ,  $\Psi_{\max} = 8.0341900$ ,  $T_{\max} = 0.06012$

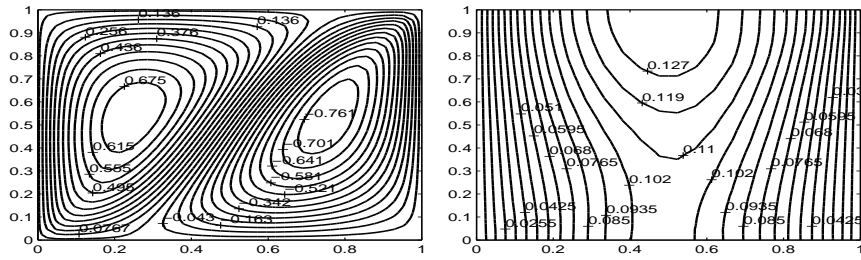
Figure 2.12: Problem 2.2.2.1:  $Ha = 50$ ,  $\varphi = \pi/6$



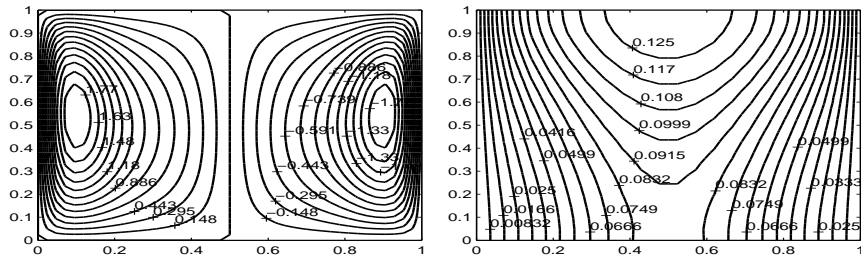
(a)  $\varphi = 0$ ,  $\Psi_{\max} = 0.3487151$ ,  $T_{\max} = 0.13198$



(b)  $\varphi = \pi/6$ ,  $\Psi_{\max} = 0.5334784$ ,  $T_{\max} = 0.13418$



(c)  $\varphi = \pi/4$ ,  $\Psi_{\max} = 0.7345081$ ,  $T_{\max} = 0.13597$



(d)  $\varphi = \pi/2$ ,  $\Psi_{\max} = 1.9165567$ ,  $T_{\max} = 0.13314$

Figure 2.13: Problem 2.2.2.1:  $Ha = 50$ ,  $Ra = 10^5$ ,  $N = 168$ ,  $K = 400$

### 2.2.2.2 Isosceles trapezoidal cavity case

For the computations of isosceles trapezoidal enclosure, only 3-points Gaussian quadrature is used for boundary integrals, and  $\tilde{f} = 1 + r^2 + r^3$ ,  $\bar{f} = 1 + r + r^2$  are taken for

Table 2.1: Problem 2.2.2.1: Average Nusselt number in square cavity.

(a) $Ra = 10^4, \varphi = \pi/6$			(b) $Ha = 50, \varphi = \pi/6$		
Ha	$\overline{Nu}$	$\gamma$	Ra	$\overline{Nu}$	$\gamma$
0	0.4314	0.75	$10^3$	0.4905	0
10	0.4903	0.4	$10^4$	0.4906	0
50	0.4920	0	$10^5$	0.4904	0
100	0.4919	0	$10^6$	0.4807	0.5
200	0.4919	0	$10^7$	0.4518	0.65

the radial functions unless otherwise declared. The inclination angle of the wall  $\theta_s$  is taken as  $72^\circ$  at all test problems. In the figures, minus sign refers to the direction of the flow circulation due to the convection in this trapezoidal cavity problem. Inclination angle of the applied magnetic field is zero. 148 linear boundary elements and 1127 interior points are used.

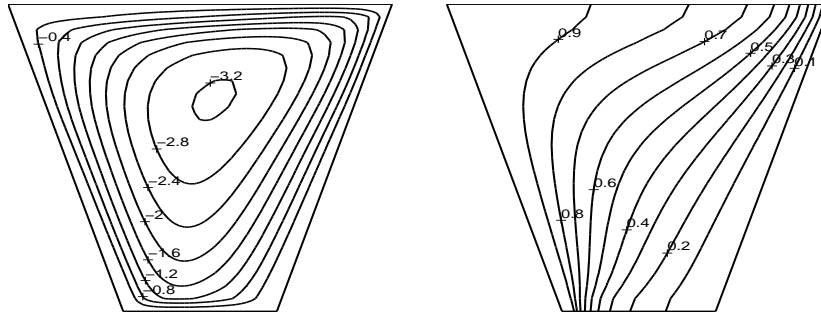
As  $Ha$  increases, as can be seen from Figure 2.14, boundary layer formation on the top wall is strongly observed since applied magnetic field is parallel to the top and bottom walls. Bottom wall boundary layer is also formed for  $Ha \geq 20$ . Isotherms become almost perpendicular to the top and bottom walls due to pure conduction when  $Ha$  is large. Further, the minimum value of stream function decreases. This means that the convective motion weakens. When  $Ha$  is small, convection is from the left hot wall through the cold right wall.

As  $Ra$  is increased, a relaxation parameter is needed for smoothing the streamlines due to the dominance of  $Ra\partial T/\partial x$  for  $Ha = 5, \varphi = 0$ . The minimum value of stream function increases. Isotherms are nearly parallel to the top and bottom walls as  $Ra$  reaches to  $10^4$ , and thermal boundary layers are formed at the side walls. Again, the convection is from the left to the right wall (Figure 2.15c).

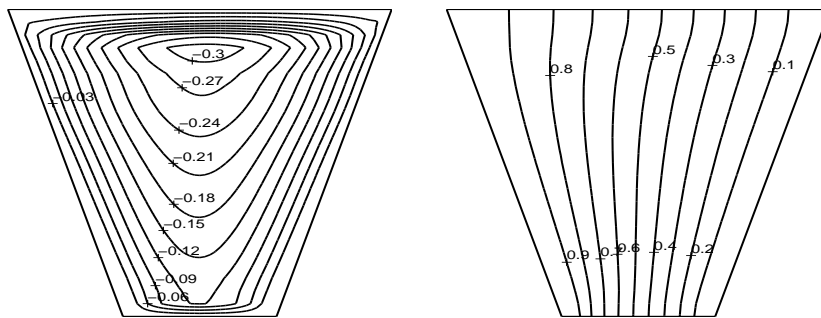
When the inclination angle of the magnetic field changes, the flow circulation is also observed in the direction of the magnetic field ( $\varphi = \pi/6, \pi/4$ ) as is depicted in Figure 2.16.

In Table 2.2,  $\overline{Nu}$  values along the left hot wall are obtained by using  $\bar{f} = 1 + r$  and composite Simpson's Rule, and the inclination angle  $\varphi = 0$  is fixed. For a fixed  $Ra = 10^3$ ,  $\overline{Nu}$  decreases as  $Ha$  increases and remains in the conduction dominated situation for a large  $Ha$  value as can be seen in Table 2.2a. On the other hand,  $\overline{Nu}$  increases as  $Ra$  increases for a fixed  $Ha = 5$ . Moreover, for a large value of  $Ha = 50$ ,  $\overline{Nu}$  settles down at a constant value which means that the pure conduction is dominated (see Table 2.2b). The same discussion may be illustrated in Figure 2.2 which is also observed in [135].

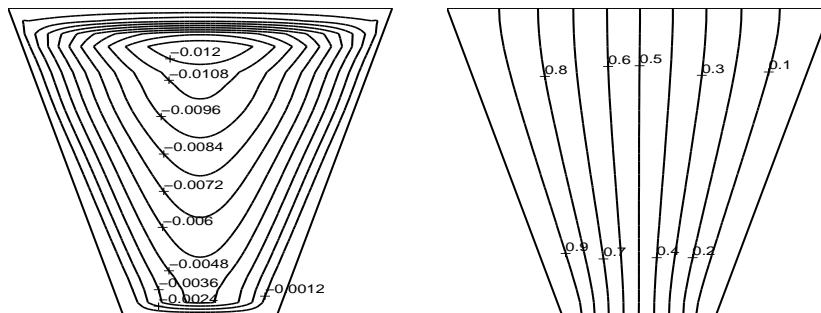




(a)  $Ha = 5$ ,  $\Psi_{\min} = -3.2413$

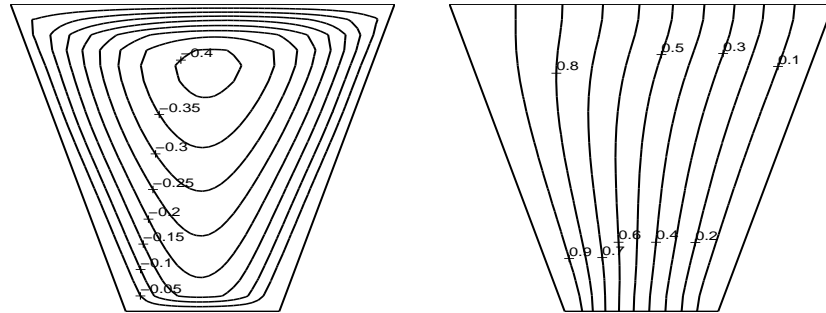


(b)  $Ha = 20$ ,  $\Psi_{\min} = -0.3152$

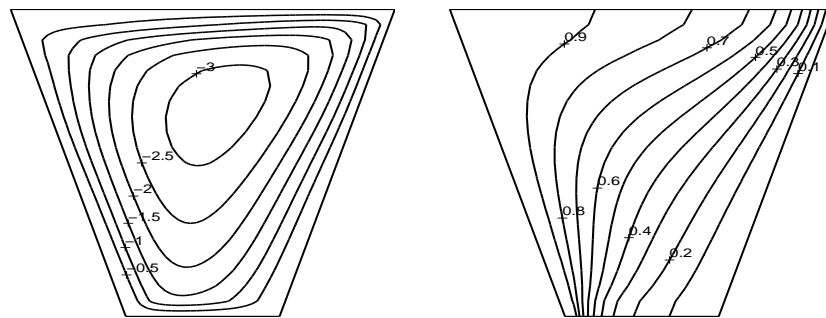


(c)  $Ha = 100$ ,  $\Psi_{\min} = -0.0132$

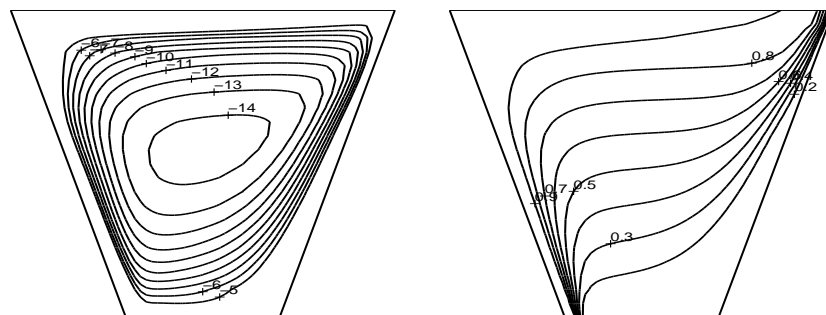
Figure 2.14: Problem 2.2.2.2:  $Ra = 10^3$ ,  $\varphi = 0$ ,  $N = 148$ ,  $K = 1127$



(a)  $Ra = 10^2$ ,  $\Psi_{\min} = -0.4165$

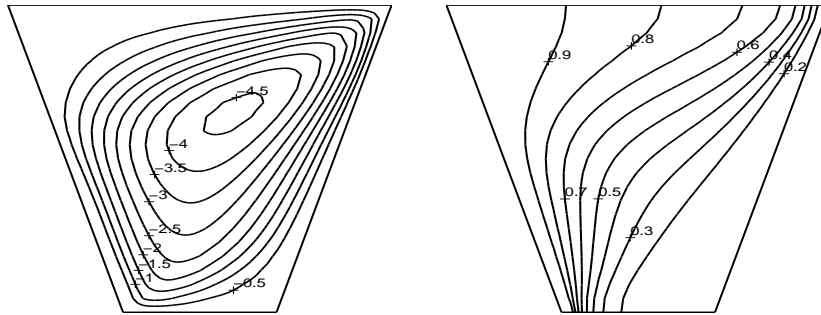


(b)  $Ra = 10^3$ ,  $\Psi_{\min} = -3.2444$

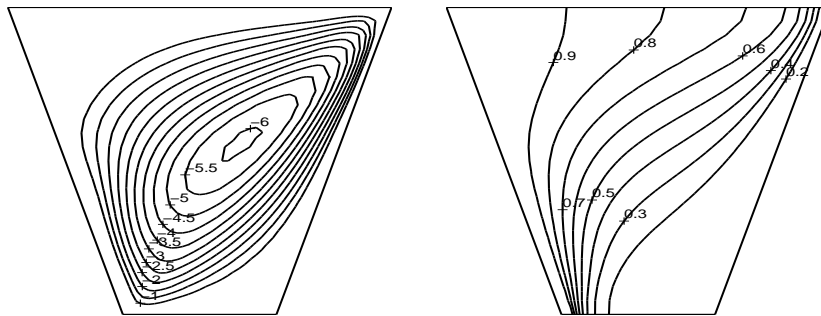


(c)  $Ra = 10^4$ ,  $\gamma = 0.4$ ,  $\Psi_{\min} = -14.4238$

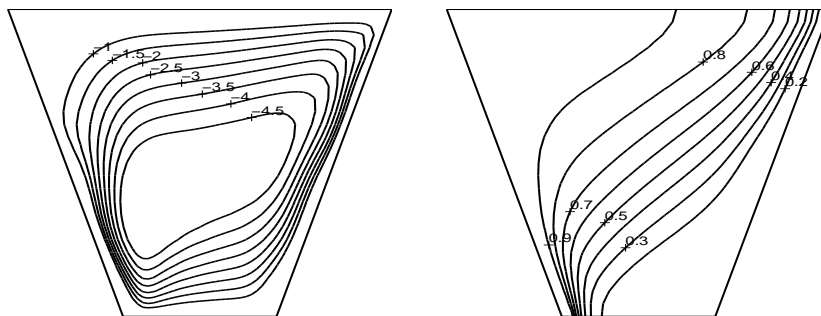
Figure 2.15: Problem 2.2.2.2:  $Ha = 5$ ,  $\theta_s = 72^\circ$ ,  $\varphi = 0$



(a)  $\varphi = \pi/6$ ,  $\Psi_{\min} = -4.6258$



(b)  $\varphi = \pi/4$ ,  $\Psi_{\min} = -6.1366$



(c)  $\varphi = \pi/2$ ,  $\Psi_{\min} = -5.4592$

Figure 2.16: Problem 2.2.2.2:  $Ra = 10^3$ ,  $Ha = 5$

Table 2.2: Problem 2.2.2.2: Average Nusselt number in isosceles trapezoidal cavity.

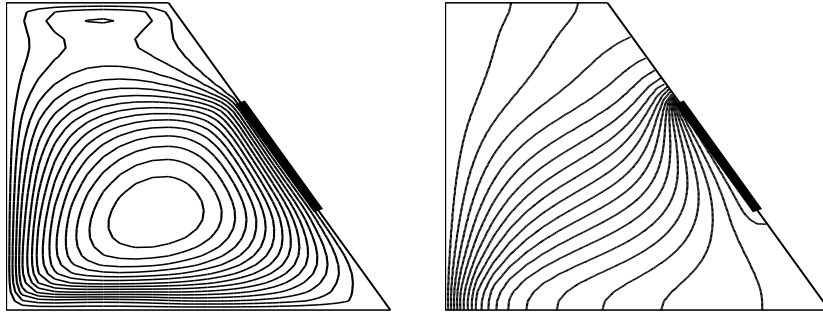
(a) Ha varies		(b) Ra varies				
Ha	$\overline{Nu}$	Ha=5		Ha=50		
		Ra	$\overline{Nu}$	$\gamma$	$\overline{Nu}$	$\gamma$
5	2.5485	$10^2$	1.5852	0	1.5670	0
20	1.5712	$10^3$	2.5485	0	1.5659	0
50	1.5659	$10^4$	8.8427	0.4	1.5825	0
100	1.5668					

### 2.2.2.3 Right-angle trapezoidal cavity case

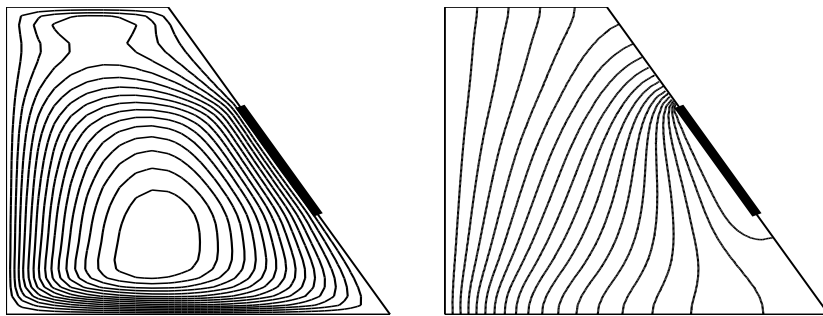
The behaviors of the flow and the temperature in a right-angle trapezoidal cavity are investigated by using  $\tilde{f} = 1 + r^2 + r^3$ ,  $\bar{f} = 1 + r$ , respectively, and 8–points Gaussian quadrature is used for computing the boundary integrals. Minus sign in streamlines refers to clockwise direction of the flow. Inclination angle of the magnetic field  $\varphi$  and the angle in the top wall  $\theta_w$  are fixed as 0 and  $60^\circ$ , respectively. The right wall has a partially cooled wall.

As  $Ha$  varies as is shown in Figure 2.17, boundary layer occurs on the bottom wall and partially cooled wall. For increasing  $Ha \geq 20$  numbers, isotherms are almost perpendicular to the top and bottom walls due to pure conduction. Furthermore, minimum values of stream function decreases. In other words, fluid flows slowly. The numerical results shown in Figure 2.17 are obtained by using 122 number of boundary elements and 858 interior points. For small  $Ha$  number, a cell emerges through the top wall in streamlines while it is dispersed and forms a boundary layer on the top wall for a large  $Ha$  number as 50. Isotherms tend to move from the hot left wall to the cold portion of the inclined wall but still being perpendicular to the adiabatic parts of the right wall.

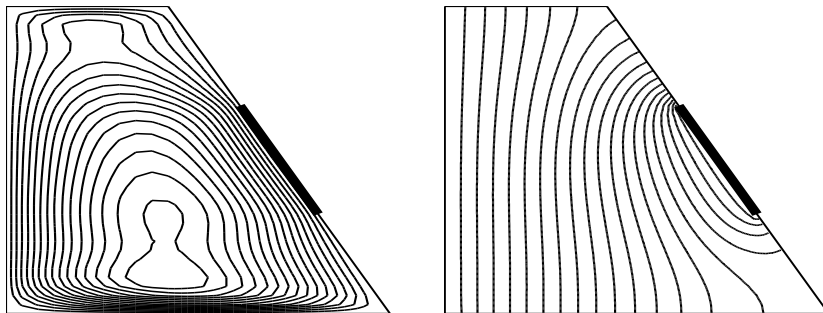
When  $Ra$  increases for a fixed number  $Ha = 10$ , a cell emerges in streamlines as can be seen in Figure 2.18c. Besides, boundary layer formation on the top of new cell and bottom wall together with partially cooled wall is well observed. Isotherms show almost parallel distribution to the horizontal walls with increasing values of  $Ra$  due to the increase in dominance of convective heat transfer. Isotherms try to be perpendicular to the adiabatic parts of the inclined wall, and then form thermal boundary layers when  $Ra$  is increased.



(a)  $Ha = 5$ ,  $\Psi_{\min} = -3.1370$

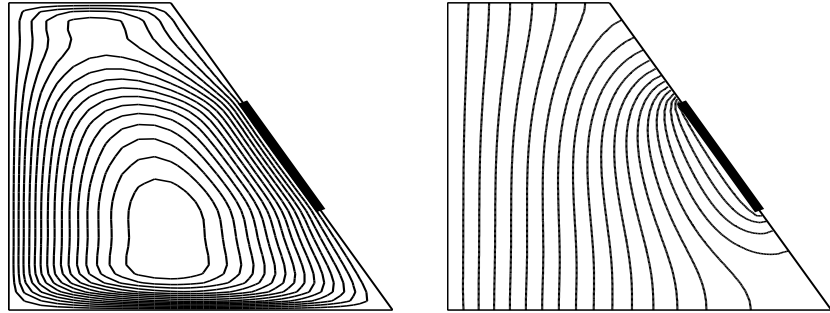


(b)  $Ha = 10$ ,  $\Psi_{\min} = -1.0020$

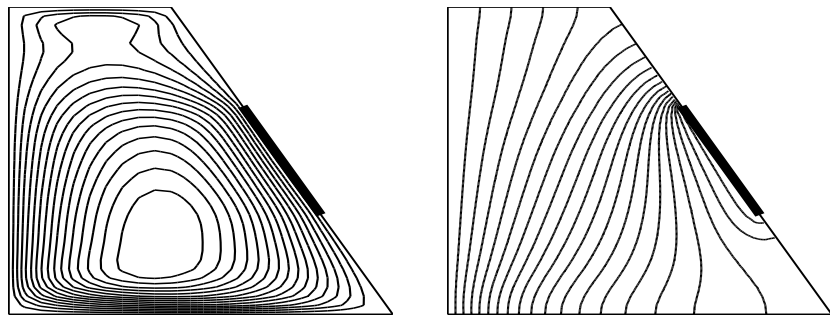


(c)  $Ha = 50$ ,  $\Psi_{\min} = -0.0422$

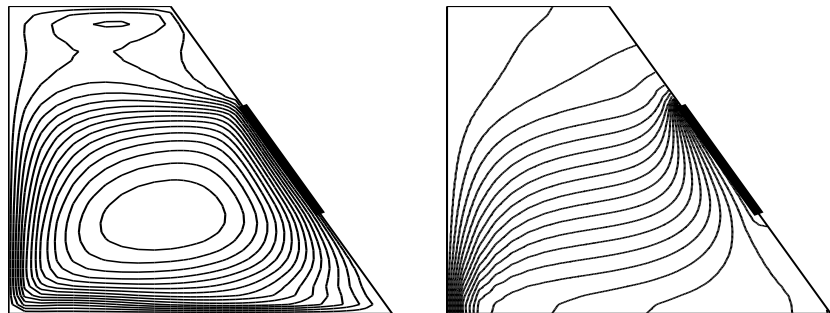
Figure 2.17: Problem 2.2.2.3: Streamlines and isotherms in right-angle trapezoidal cavity,  $Ra = 10^3$ .



(a)  $Ra = 10^2$ ,  $\Psi_{\min} = -0.1002$



(b)  $Ra = 10^3$ ,  $\Psi_{\min} = -1.0020$



(c)  $Ra = 10^4$ ,  $\gamma = 0.2$ ,  $\Psi_{\min} = -6.0093$

Figure 2.18: Problem 2.2.2.3: Streamlines and isotherms in right-angle trapezoidal cavity,  $Ha = 10$ .

### 2.2.3 DRBEM solution of unsteady MHD free convection in a square cavity

The problem in the previous section is concerned once again. The differences are time derivative of the temperature and internal heat generation parameter in the energy equation, and the boundary conditions of temperature. The problem is configured as in Fig. 2.19.

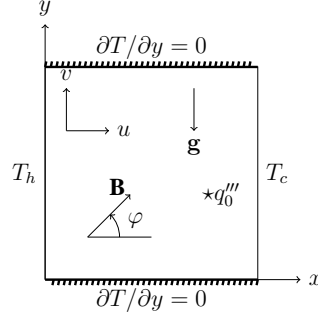


Figure 2.19: Problem 2.2.3: Square porous enclosure.

The non-dimensional governing equations are written as

$$\nabla^2 \psi = -Ra \frac{\partial T}{\partial x} - Ha^2 \left( \frac{\partial^2 \psi}{\partial y^2} \sin^2 \varphi + \frac{\partial^2 \psi}{\partial x \partial y} \sin(2\varphi) + \frac{\partial^2 \psi}{\partial x^2} \cos^2 \varphi \right) \quad (2.66a)$$

$$\nabla^2 T = \frac{\partial T}{\partial t} + \frac{\partial \psi}{\partial y} \frac{\partial T}{\partial x} - \frac{\partial \psi}{\partial x} \frac{\partial T}{\partial y} - Q \quad (2.66b)$$

with the initial and boundary conditions

$$\begin{aligned} \psi = T = 0, \text{ at } t = 0 \\ \psi = 0, T = 1/2, \text{ at } x = 0 \\ \psi = 0, T = -1/2, \text{ at } x = 1 \\ \psi = 0, \frac{\partial T}{\partial y} = 0, \text{ at } y = 0 \text{ and } y = 1. \end{aligned} \quad (2.67)$$

$Ra = g\kappa\beta(T_h - T_c)L/(\alpha_e\nu)$  is the Rayleigh number for a porous medium,  $Ha = \sigma\kappa B_0^2/\mu$  is the Hartmann number for the porous medium,  $Q = Ra_I/Ra$  with  $Ra_I = q_0''' L^2/(k(T_h - T_c))$  (internal Rayleigh number) is the heat generation parameter,  $T_h$  and  $T_c$  denote hot right and cold left walls,  $k$  is the thermal conductivity.

Employing the Backward-Euler finite difference scheme for the time derivative, the system of equations in matrix-vector form resulting with DRBEM application are given as

$$(\mathbf{H} + \mathbf{SR})\psi^{m+1} - \mathbf{G}\psi_q^{m+1} = -Ra \mathbf{S} \frac{\partial \mathbf{F}}{\partial \mathbf{x}} \mathbf{F}^{-1} T^m \quad (2.68a)$$

$$(\mathbf{H} - \tilde{\mathbf{S}}\mathbf{M} - \frac{\tilde{\mathbf{S}}}{\Delta t})T^{m+1} - \mathbf{G}T_q^{m+1} = -\frac{\tilde{\mathbf{S}}}{\Delta t}T^m - \tilde{\mathbf{S}}Q \quad (2.68b)$$

where  $m$  refers the time level, and the matrices are

$$\mathbf{S} = (\mathbf{H}\hat{\mathbf{U}} - \mathbf{G}\hat{\mathbf{Q}}) \mathbf{F}^{-1}, \quad \tilde{\mathbf{S}} = (\mathbf{H}\tilde{\mathbf{U}} - \mathbf{G}\tilde{\mathbf{Q}}) \tilde{\mathbf{F}}^{-1} \quad (2.69)$$

$$\mathbf{R} = \text{Ha}^2 \left( \sin^2\varphi \frac{\partial^2 \mathbf{F}}{\partial \mathbf{y}^2} \mathbf{F}^{-1} + \sin(2\varphi) \frac{\partial^2 \mathbf{F}}{\partial \mathbf{x} \partial \mathbf{y}} \mathbf{F}^{-1} + \cos^2\varphi \frac{\partial^2 \mathbf{F}}{\partial \mathbf{x}^2} \mathbf{F}^{-1} \right) \quad (2.70)$$

$$\mathbf{M} = \frac{\partial \tilde{\mathbf{F}}}{\partial \mathbf{y}} \tilde{\mathbf{F}}^{-1} [\psi]_{\mathbf{d}} \frac{\partial \tilde{\mathbf{F}}}{\partial \mathbf{x}} \tilde{\mathbf{F}}^{-1} - \frac{\partial \tilde{\mathbf{F}}}{\partial \mathbf{x}} \tilde{\mathbf{F}}^{-1} [\psi]_{\mathbf{d}} \frac{\partial \tilde{\mathbf{F}}}{\partial \mathbf{y}} \tilde{\mathbf{F}}^{-1}, \quad (2.71)$$

where the diagonal matrix  $[\psi]_{\mathbf{d}}$  are constructed by the vector  $\psi^{m+1}$  at each iteration. In this way, time-integration scheme may be considered as a semi-implicit iterative procedure. The reduced form of both of these equations in the form of  $\mathbf{C}\mathbf{x} = \mathbf{d}$  is solved by Gaussian elimination with partial pivoting. Stopping criteria in the iteration is the same as before.

Table 2.3 reports average Nusselt number (computed at the left hot wall by  $-\int_0^1 (\partial T / \partial x)|_{x=0} dy$  using the composite Simpson's 3/8 rule (Appendix B)) values at steady-state for a fixed  $Ra = 10^3$  with  $Ha = 1, 10$ , respectively. The time iteration occurs with  $\Delta t = 0.01$ . These results are in good agreement with the results in [132]. 168 boundary element, 1681 interior points are used to obtain the results for  $Ha = 1$  with a relaxation parameter  $\gamma = 0.5$ , and  $f = \tilde{f} = 1 + r + r^2$ . On the other hand, the results for  $Ha = 10$  are obtained by 192 boundary elements and 529 interior points without using a relaxation parameter, and  $f = 1 + r^3$ ,  $\tilde{f} = 1 + r$ . It can be deduced that the number of boundary elements and interior points affect the results. Furthermore, the sharp decrease in average Nusselt number with the increase in Hartmann number points to the inhibitive effect of magnetic field on heat transfer.

Figure 2.20 describes the variation of  $Ha$  at a fixed Rayleigh number  $Ra = 10^3$  and two different inclination angle of magnetic field  $\varphi$ . For a small value of  $Ha = 1$ , the behavior of the fluid does not change much with the inclination angle  $\varphi$ . Side layers are formed for isotherms, and streamlines, and a core region for streamlines at the center of the cavity is observed. However, for increasing values of  $Ha$ , fluid flows in the direction of applied magnetic field, and strong boundary layer formation occurs at vertical walls with  $\varphi = \pi/2$ .

When the Rayleigh number is increased with a fixed  $Ha = 25$  (Figure 2.21), the isotherms which are nearly perpendicular to horizontal walls become nearly parallel to them. This demonstrates the increase in convection dominated effect. Temperature gradient is pronounced at the left bottom and right up corners. Boundary layer formation is also observed on vertical walls for high  $Ra$  value.

As the heat generation parameter  $Q$  is increased or decreased (internal Rayleigh number varies), the primary cell in streamlines reflected with respect to the direction of the inclination angle as  $Q = -1$  without changing the velocity of the fluid.



Table 2.3: Problem 2.2.3: The average Nusselt numbers  $\overline{Nu}$  for  $Ra = 1000$  with  $Q = 1$ .

$\varphi$	$Ha = 1$		$Ha = 10$	
	$\overline{Nu}$	[132]	$\overline{Nu}$	[132]
0	9.1782	9.1489	0.7637	0.7952
$\pi/6$	9.8091	9.7976	0.8551	0.8796
$\pi/4$	10.4477	10.4437	0.9340	0.9620
$\pi/2$	11.8925	11.9196	0.7873	0.8065

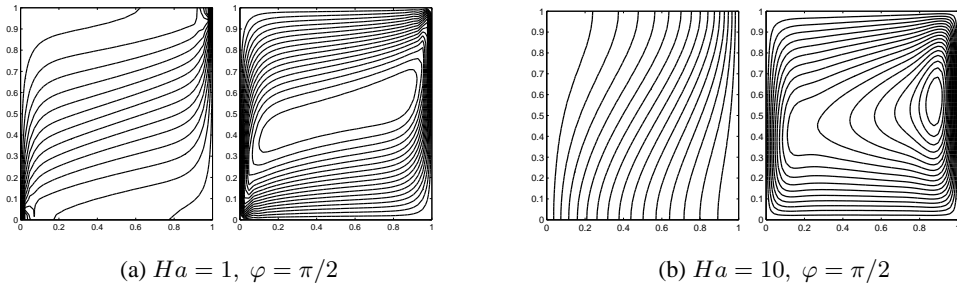


Figure 2.20: Problem 2.2.3: Isotherms and streamlines at steady-state with different  $Ha$  values fixing  $Ra = 10^3$ .

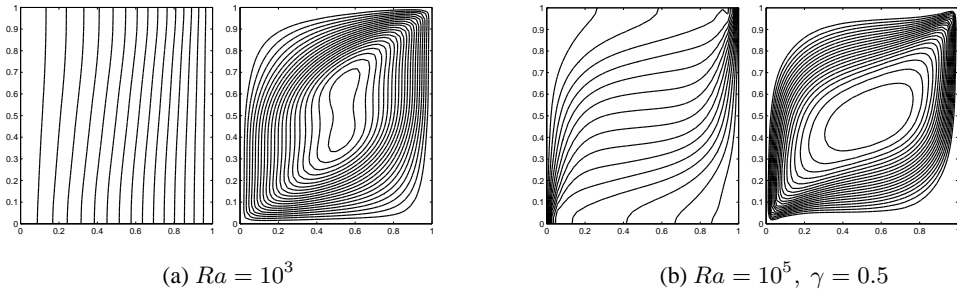


Figure 2.21: Problem 2.2.3: Steady-state isotherms and streamlines w.r.t varying  $Ra$  fixing  $Ha = 25, \varphi = \pi/6, \Delta t = 0.01$

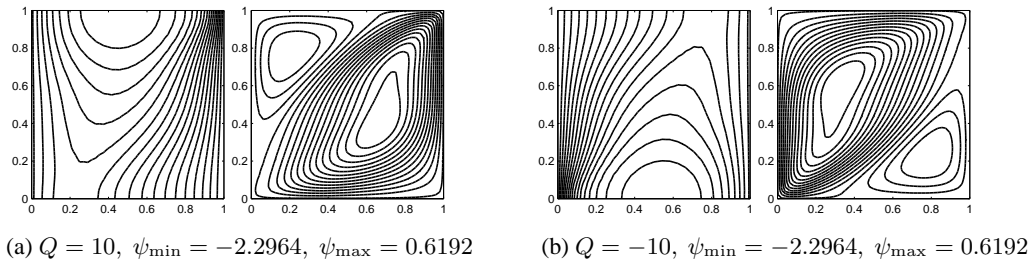


Figure 2.22: Problem 2.2.3: Heat generation and absorption fixing  $Ha = 10, Ra = 10^3, \varphi = \pi/6, \Delta t = 0.1$ .

## 2.2.4 Unsteady mixed convection in a porous lid-driven enclosure under a magnetic field

The two-dimensional, unsteady, laminar, incompressible mixed convection flow in a porous lid-driven cavity is considered under the effect of an horizontally applied magnetic field.

The governing non-dimensional equations (setting  $\epsilon_p = 1$ ) in terms of stream function  $\psi$ -temperature  $T$ -vorticity  $w$  are presented as

$$\nabla^2 \psi = -w \quad (2.72a)$$

$$\frac{1}{Re} \nabla^2 w = \frac{\partial w}{\partial t} + u \frac{\partial w}{\partial x} + v \frac{\partial w}{\partial y} - \frac{Gr}{Re^2} \frac{\partial T}{\partial x} + \frac{w}{DaRe} + \frac{Ha^2}{Re} \frac{\partial v}{\partial x} \quad (2.72b)$$

$$\frac{1}{PrRe} \nabla^2 T = \frac{\partial T}{\partial t} + u \frac{\partial T}{\partial x} + v \frac{\partial T}{\partial y} - \frac{Ra_I}{Ra_E} \frac{1}{PrRe} \quad (2.72c)$$

where the dimensionless parameters  $Da$ ,  $Gr$ ,  $Re$ ,  $Ha$ ,  $Pr$ ,  $Ra_I$ ,  $Ra_E$  are Darcy, Grashof, Reynolds, Hartmann, Prandtl, internal Rayleigh and external Rayleigh numbers are

$$\begin{aligned} Re &= \frac{UL}{\nu}, & Gr &= \frac{g\beta\Delta TL^3}{\nu^2}, & Da &= \frac{\kappa}{L^2}, & Ha^2 &= \frac{B_0^2 \kappa \sigma}{\mu} \\ Pr &= \frac{\nu}{\alpha_e}, & Ra_I &= \frac{g\beta q''' L^5}{\nu \alpha_e k_e}, & Ra_E &= \frac{g\beta\Delta TL^3}{\nu \alpha_e} = Gr.Pr \end{aligned} \quad (2.73)$$

The problem is configured in Figure 2.23 where the left and right walls are adiabatic, top wall is the heated wall while the bottom is the cold wall,  $u = v = \psi$  are all zero on all boundaries except the moving top wall with velocity  $u = 1$ ,  $\mathbf{B}$  is the horizontally applied magnetic field with magnitude  $B_0$  and  $\mathbf{g}$  is the gravitational acceleration vector.

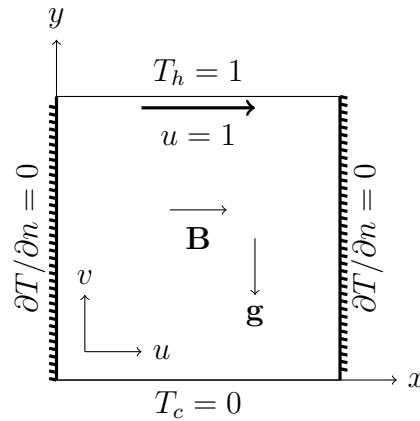


Figure 2.23: Problem 2.2.4 configuration.

By means of coordinate matrix  $\mathbf{F}$  and the third order backward difference time integration scheme, Houbolt method (Eq.(2.49)), the iteration with respect to time is carried

between the system of equations for  $\psi$ ,  $w$  and  $T$  as

$$\mathbf{H}\psi^{m+1} - \mathbf{G}\psi_q^{m+1} = -\mathbf{S}w^m \quad (2.74a)$$

$$u^{m+1} = \frac{\partial \mathbf{F}}{\partial \mathbf{y}} \mathbf{F}^{-1} \psi^{m+1}, \quad v^{m+1} = -\frac{\partial \mathbf{F}}{\partial \mathbf{x}} \mathbf{F}^{-1} \psi^{m+1} \quad (2.74b)$$

$$\mathbf{H}w^{m+1} - \mathbf{G}w_q^{m+1} = \text{ReS} \left[ \left. \frac{\partial w}{\partial t} \right|^{m+1} + \mathbf{M}w^{m+1} \right] \quad (2.74c)$$

$$- \frac{Gr}{\text{Re}} \mathbf{S} \frac{\partial \mathbf{F}}{\partial \mathbf{x}} \mathbf{F}^{-1} T^{m+1} + \mathbf{S} \frac{w^{m+1}}{Da} + Ha^2 \mathbf{S} \frac{\partial \mathbf{F}}{\partial \mathbf{x}} \mathbf{F}^{-1} v^{m+1}$$

$$\mathbf{H}T^{m+1} - \mathbf{G}T_q^{m+1} = Pr \text{ReS} \left[ \left. \frac{\partial T}{\partial t} \right|^{m+1} + \mathbf{M}T^{m+1} \right] - \mathbf{S} \frac{Ra_I}{Ra_E} \quad (2.74d)$$

where  $\mathbf{S} = (\mathbf{H}\hat{\mathbf{U}} - \mathbf{G}\hat{\mathbf{Q}})\mathbf{F}^{-1}$ ,  $\mathbf{M} = \left( [\mathbf{u}]_d \frac{\partial \mathbf{F}}{\partial \mathbf{x}} \mathbf{F}^{-1} + [\mathbf{v}]_d \frac{\partial \mathbf{F}}{\partial \mathbf{y}} \mathbf{F}^{-1} \right)$ ,  $m$  shows the time iteration, the diagonal matrices  $[\mathbf{u}]_d$  and  $[\mathbf{v}]_d$  of size  $(N + K) \times (N + K)$  are constructed by the vectors  $u^{m+1}$ ,  $v^{m+1}$ , respectively.  $Ra_I/Ra_E$  is a constant vector of size  $N + K$ .

Once the time derivatives are replaced with Eq.(2.49) and the known and unknown information are shuffled, the system of equations (2.74a)-(2.74d) is solved by direct Gaussian elimination with partial pivoting.

The iterative solution procedure is as follows

1.  $w^0$  and  $T^0$  are taken as zero everywhere except on the boundary.
2.  $\psi^{m+1}$  is solved in (2.74a) using the values of  $w$  from  $m$ th iteration. Then, the velocities  $u^{m+1}$ ,  $v^{m+1}$  are computed using  $\psi^{m+1}$  in Eq.(2.74b).
3. Boundary conditions for  $u$ ,  $v$  are inserted in equations (2.74b).
4. The energy equation is solved for  $T^{m+1}$  from Eq.(2.74d) with the temperature boundary conditions.
5. Vorticity boundary conditions are employed by using the definition of vorticity and the coordinate matrix  $\mathbf{F}$

$$w = \frac{\partial v}{\partial x} - \frac{\partial u}{\partial y} = \frac{\partial \mathbf{F}}{\partial \mathbf{x}} \mathbf{F}^{-1} v^{m+1} - \frac{\partial \mathbf{F}}{\partial \mathbf{y}} \mathbf{F}^{-1} u^{m+1}. \quad (2.75)$$

6. Vorticity  $w^{m+1}$  is obtained from Eq.(2.74c).
7. Iterations continues until the criterion [79]

$$\frac{\|\psi^{m+1} - \psi^m\|_\infty}{\|\psi^{m+1}\|_\infty} + \frac{\|T^{m+1} - T^m\|_\infty}{\|T^{m+1}\|_\infty} + \frac{\|w^{m+1} - w^m\|_\infty}{\|w^{m+1}\|_\infty} < \epsilon \quad (2.76)$$

is satisfied, where  $\epsilon = 1e - 05$ .

8. Average Nusselt number on hot top wall is computed as

$$\overline{Nu} = \int_0^1 \left. \frac{\partial T}{\partial y} \right|_{y=1} dx \quad (2.77)$$

by using the composite Simpson's rule.

The results are obtained by using  $f = 1 + r$  radial basis functions in coordinate matrix  $\mathbf{F}$ . Further, 8-point Gaussian quadrature is used for the integrals in  $\mathbf{H}$  and  $\mathbf{G}$  matrices. In general, 120 linear boundary elements and 841 interior points, and  $Pr = 0.71$  are taken in all computations. Once the vorticity is computed, for large values of  $Ha$ , a relaxation parameter  $0 < \gamma < 1$  is utilized as

$$w^{m+1} \leftarrow \gamma w^{m+1} + (1 - \gamma)w^m. \quad (2.78)$$

As  $Da$  decreases (Figure 2.24), fluid flows slowly due to the decrease in permeability [80], and the effect of moving lid disappears. Isotherms tend to become parallel to the horizontal walls which indicates the conductive heat transfer. Vorticity is concentrated to the top wall being stagnant at the center.

With the increase in  $Ha$  (Figure 2.25), heat transfer is suppressed on isotherms vanishing the forced convection by moving lid. The cells in the upper mid part of the cavity in both streamlines and vorticity become prominent while the lower mid part becomes stagnant in the cavity. The fluid velocity through the bottom mid part nearly becomes zero as can be seen from the mid  $v$  velocity profiles (Figure 2.29), and the fluid motion is enforced through the top by increasing the intensity of the horizontally applied magnetic field as is seen from the mid  $u$  velocity.

As  $Re$  increases (Figure 2.26), a second counter-rotating cell emerges in streamlines while the effect of the moving lid increases on the top cell forming strong boundary layer from left to right on the top wall. Isotherms circulate inside the cavity forming the strong temperature gradient through the bottom wall. Similarly, the increase in buoyancy parameter, Richardson number  $Ri = Gr/Re^2$  (Figure 2.27), divides the streamlines into secondary and tertiary counter clockwise cells while the isotherms show the conduction dominated behavior, and vorticity forms new cell resembling the streamlines.

The increase in the internal Rayleigh number only alters the isotherms as can be seen from Figure 2.28. The boundary layer formation on the top and bottom walls is pronounced pointing to the increase in temperature variation due to the increase in internal heat.

When the average Nusselt number  $\overline{Nu}$  is taken into consideration (Figures 2.30a-2.30b) on the top lid, one can see that  $\overline{Nu}$  is almost the same for all values of  $Da$  when  $Ri > 1$  ( $Re \leq 10$ ) fixing  $Gr = 10^2$ ,  $Ra_I = 0$ ,  $Ha = 0$ . On the other hand,  $\overline{Nu}$  increases as  $Da$  increases for  $Ri \leq 1$  due to the increase in inertial forces as  $Re$  ( $Re > 10$ ) increases (Figure 2.30a) which demonstrates the increase in convective heat transfer. When  $Gr = 10^2$ ,  $Re = 10^2$ ,  $Ra_I = 0$  are fixed,  $\overline{Nu}$  decreases and

becomes almost the same for all  $Da$  values as  $Ha$  increases (Figure 2.30b). As  $Ha$  decreases, the increase in  $\overline{Nu}$  is well observed, and the values of  $\overline{Nu}$  is larger for large values of  $Da$  which points to the increase in convection.

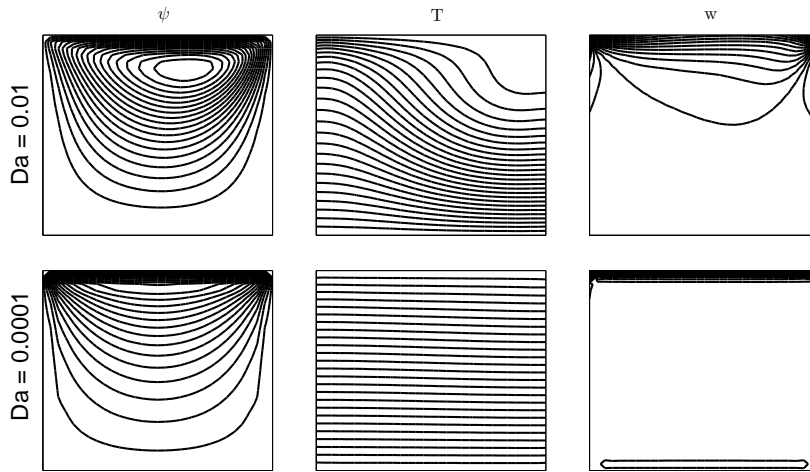


Figure 2.24: Problem 2.2.4: Darcy variation with  $Gr = Re = 100$ ,  $Ha = Ra_I = 0$ ,  $\Delta t = 0.25$ .

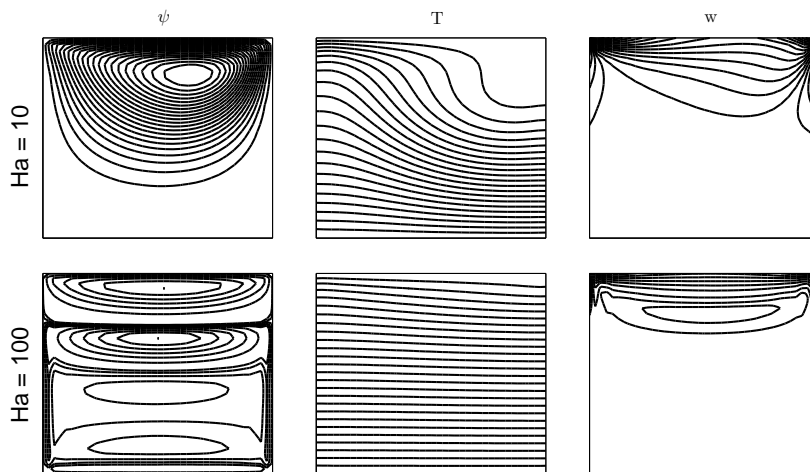


Figure 2.25: Problem 2.2.4: Hartmann variation with  $Da = 0.1$ ,  $Gr = Re = 100$ ,  $Ra_I = 0$ ,  $\Delta t = 0.5(Ha = 10)$ ;  $\Delta t = 0.1(\gamma = 0.1, Ha = 100)$ .

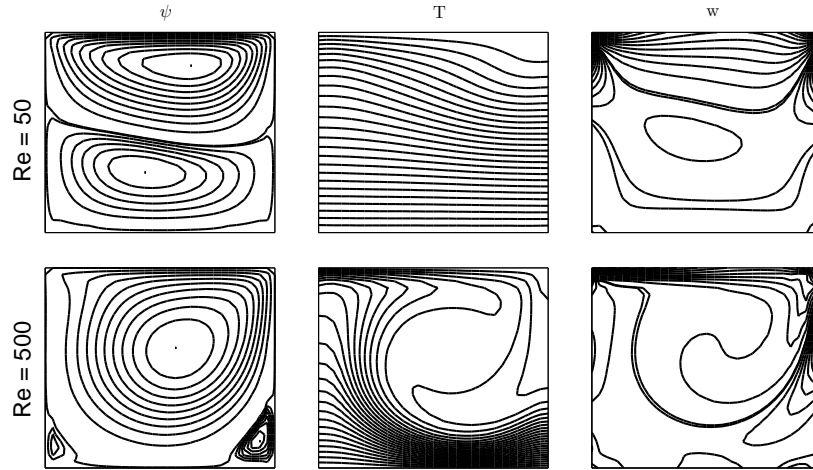


Figure 2.26: Problem 2.2.4: Reynolds variation with  $Da = 0.1$ ,  $Gr = 10^4$ ,  $Ha = Ra_I = 0$ ,  $\Delta t = 0.5(Re = 50)$ ;  $\Delta t = 0.1(Re = 500)$ .

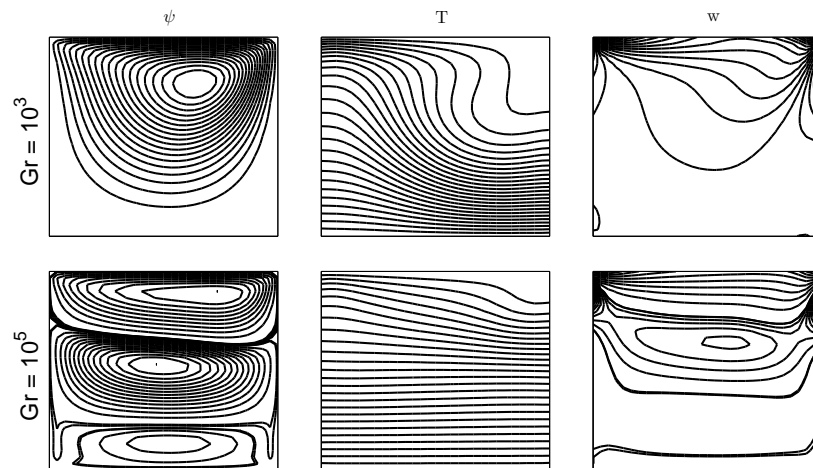


Figure 2.27: Problem 2.2.4: Grashof variation with  $Da = 0.1$ ,  $Re = 100$ ,  $Ha = Ra_I = 0$ ,  $\Delta t = 0.5(Gr = 10^3)$ ;  $\Delta t = 0.1(Gr = 10^5)$ .

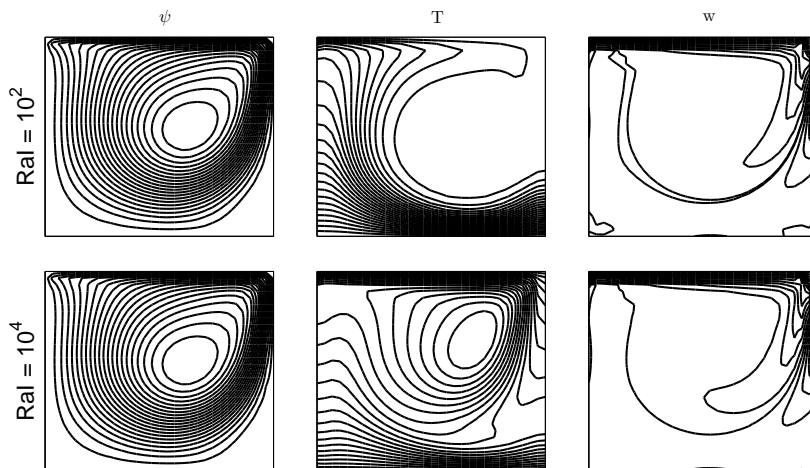


Figure 2.28: Problem 2.2.4: Internal Rayleigh number variation with  $Da = 0.01$ ,  $Gr = 100$ ,  $Re = 1000$ ,  $Ha = 0$ ,  $\Delta t = 0.5$

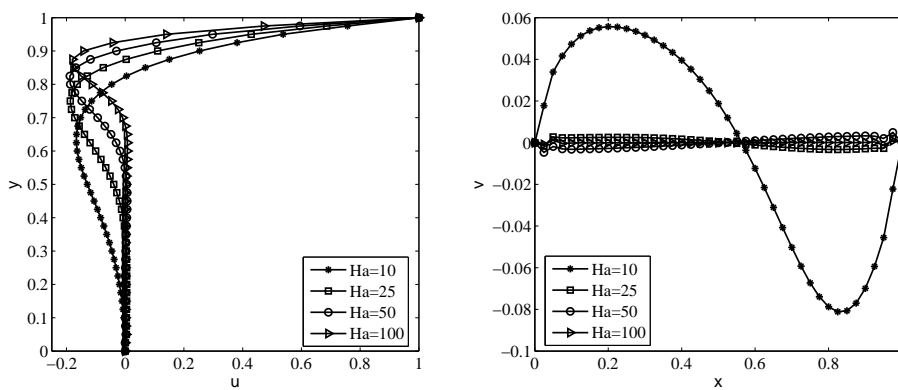


Figure 2.29: Problem 2.2.4: Mid-velocity profiles as  $Ha$  varies fixing  $Da = 0.1$ ,  $Gr = Re = 100$ ,  $Ra_I = 0$ .

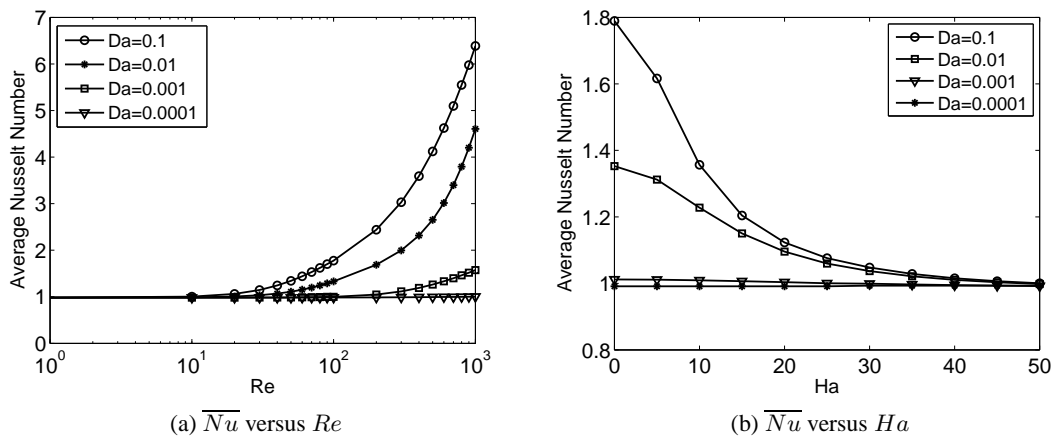


Figure 2.30: Problem 2.2.4: Average Nusselt number.

In this chapter, the natural or mixed convection flow problems in porous enclosures have been solved utilizing the dual reciprocity boundary element method. DRBEM provides one to obtain the expected behavior of the solution in a cheap computational expense due to the boundary-only nature of the method. The numerical modeling have been done in terms of stream function, temperature and vorticity. The time derivatives in unsteady problems are handled by implicit finite difference methods while the spatial discretization is achieved by DRBEM.

The heat transfer under the non-magnetic or magnetic effect in porous enclosures have been investigated. In both cases, the decrease in permeability of porous medium (the decrease in  $Da$  number) suppresses the heat transfer as well as slowing the fluid movement. Also, the same behavior is observed in the strength of an externally applied magnetic field due to the retarding effect of Lorentz force. The vertical direction of the magnetic field has an accelerating effect on the fluid motion in the square cavity case.

The other physical dimensionless parameters show the main characteristics of the natural or mixed convection flow. Buoyancy has a stabilizing effect on the fluid flow. When the Richardson number ( $Ri = Gr/Re^2$ ) is increased, the buoyancy effect outweighs the effect of the moving lids if they exist. In that case, the buoyancy-driven flow is referred to as natural convection flow. Isotherms are clustered through the heated corner and cross cold corner almost becoming parallel to the other sides of the enclosure in a two-sided lid-driven cavity case. The thin thermal boundary layers along the side walls are developed with the convective heat transfer. The higher porosity provides the higher heat transfer and fluid velocity if  $Ri \gg 1$ . In the top lid movement only, circulation in the isotherms is restricted to the sliding lid, and the conductive heat transfer in the middle and bottom parts of the cavity is observed. In the case of  $Ri \approx 1$ , the two driving mechanisms, either lid or buoyancy, balance each other forming the symmetric eddies in counter-clockwise direction. For small values of Prandtl number, the conductive heat transfer is pronounced while the convection increases with the increase in Prandtl number. A strong circulation is observed in isotherms as Prandtl number increases, and the core of the cavity becomes stagnant, and the significance of buoyancy is seen through the side walls.





## CHAPTER 3

### DRBEM APPLICATIONS TO FULL MHD EQUATIONS

In this chapter, MHD flow with or without heat transfer is considered in enclosures. These are the lid-driven porous or non-porous cavity, the lid-driven cavity containing a square blockage at the center, and the staggered double lid-driven cavity. Also, MHD flow in a channel containing a backward facing step, and MHD flow over a square cylinder placed in a channel are considered and numerical solutions are presented for several problem parameters. In all these problems, induced magnetic field is taken into account, and it contributes to the equations as magnetic potential, current density or induced magnetic field components.

The interaction between the conducting fluid and an applied magnetic field causes an electromotive force resulting with induced currents of order  $\sigma(\mathbf{u} \times \mathbf{B})$ . According to Ampère's Law, an induced magnetic field is generated by induced currents. This induced magnetic field  $\mathbf{B}$  and the induced current density  $\mathbf{J}$  develop the Lorentz force  $\mathbf{B} \times \mathbf{J}$ . In most of the studies, induced magnetic field is neglected due to the small magnetic Reynolds number. In consideration of the induced magnetic field as an unknown, the governing equations consisting of the combination of Navier-Stokes and Maxwell's equations will also contain the induction equations, and so they are referred as full MHD equations. These are already given in Chapter 1 (1.1.5) in detail. In dimensional form, the full MHD equations in the presence of temperature difference for an incompressible, viscous fluid are expressed as

$$\frac{\partial u}{\partial x} + \frac{\partial v}{\partial y} = 0 \quad (3.1a)$$

$$\nu \nabla^2 u = \frac{\partial u}{\partial t} + u \frac{\partial u}{\partial x} + v \frac{\partial u}{\partial y} + \frac{1}{\rho} \frac{\partial p}{\partial x} + \frac{B_y}{\rho \mu_m} \left( \frac{\partial B_y}{\partial x} - \frac{\partial B_x}{\partial y} \right) \quad (3.1b)$$

$$\nu \nabla^2 v = \frac{\partial v}{\partial t} + u \frac{\partial v}{\partial x} + v \frac{\partial v}{\partial y} + \frac{1}{\rho} \frac{\partial p}{\partial y} - \frac{B_x}{\rho \mu_m} \left( \frac{\partial B_y}{\partial x} - \frac{\partial B_x}{\partial y} \right) - g\beta(T - T_c) \quad (3.1c)$$

$$\frac{1}{\sigma \mu_m} \nabla^2 B_x = \frac{\partial B_x}{\partial t} + u \frac{\partial B_x}{\partial x} + v \frac{\partial B_x}{\partial y} - B_x \frac{\partial u}{\partial x} - B_y \frac{\partial u}{\partial y} \quad (3.1d)$$

$$\frac{1}{\sigma \mu_m} \nabla^2 B_y = \frac{\partial B_y}{\partial t} + u \frac{\partial B_y}{\partial x} + v \frac{\partial B_y}{\partial y} - B_x \frac{\partial v}{\partial x} - B_y \frac{\partial v}{\partial y} \quad (3.1e)$$

$$\alpha \nabla^2 T = \frac{\partial T}{\partial t} + u \frac{\partial T}{\partial x} + v \frac{\partial T}{\partial y}. \quad (3.1f)$$

This chapter presents the DRBEM solution of the different forms of the non-dimensional full MHD equations with or without heat transfer, and the numerical simulation of these equations in different geometries. Nondimensionalization of these full MHD equations are given in Appendix A. Once the dimensionless governing equations are derived, DRBEM is applied to all equations leaving only Laplacian terms on the left hand side, and treating all the other terms as inhomogeneity ( $\mathbf{b}$  as mentioned in Eq.(2.14) which is approximated by radial basis functions). In the DRBEM formulation of the full MHD equations given in the following sections, the same BEM matrices  $\mathbf{H}$ ,  $\mathbf{G}$ ,  $\hat{\mathbf{U}}$ ,  $\hat{\mathbf{Q}}$  constructed as in Eq.(2.27), and the coordinate matrix  $\mathbf{F}$  as in Eq.(2.14) are utilized.

Further, at all application problems in this chapter, the two-dimensional, unsteady, laminar flow of an incompressible, viscous, electrically conducting fluid is considered under the effect of an externally applied magnetic field neglecting the Joule heating, viscous dissipation and Hall effects. Also, induced magnetic field equations are considered due to the large values of magnetic Reynolds number ( $Rem \geq 1$ ).

### 3.1 MHD flow and heat transfer with magnetic potential in a porous medium

$$(\psi - A - T - w)$$

This problem is an extension of the problem given in section 2.2.4 in the sense that induced magnetic field is present in the fluid. Thus, the related equations for induced magnetic field are included, and are combined to give magnetic potential  $A$  using the definitions  $B_x = \partial A / \partial y$ ,  $B_y = -\partial A / \partial x$  in either one of the induction equations (1.36c)-(1.36d). Magnetic potential  $A$  is considered as unknown in the governing equations.

The two-dimensional, laminar flow in a unit lid-driven square cavity filled with an incompressible, electrically conducting fluid-saturated porous medium is considered. The fluid is permeated by a uniform externally applied (in the vertical direction) magnetic field of strength  $B_0$  (Figure 3.1). The physical properties of the fluid, which is in local thermal equilibrium with the porous medium, are constant except the density variation in the buoyant term of the momentum equation according to Boussinesq approximation. The physical problem is referred as Brinkman-extended Darcy model due to the absence of quadratic drag terms (Forchheimer terms) in the momentum equation. The porous medium is assumed to be hydrodynamically, thermally, electrically isotropic (neutral) and homogeneous.

The non-dimensional governing equations in terms of stream function  $\psi$ -vorticity  $w$ -temperature  $T$ -magnetic potential  $A$  are given in non-dimensional form as (Chapter 1, section 1.1.5, Appendix A)

$$\nabla^2 \psi = -w \tag{3.2a}$$

$$\frac{1}{PrRe} \nabla^2 T = \frac{\partial T}{\partial t} + u \frac{\partial T}{\partial x} + v \frac{\partial T}{\partial y} \tag{3.2b}$$

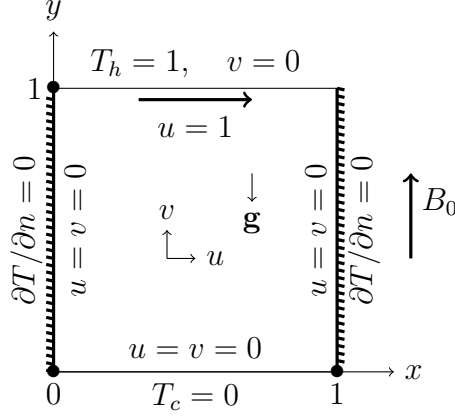


Figure 3.1: Problem 3.1 configuration.

$$\frac{1}{Rem} \nabla^2 A = \frac{\partial A}{\partial t} + u \frac{\partial A}{\partial x} + v \frac{\partial A}{\partial y} \quad (3.2c)$$

$$\begin{aligned} \frac{1}{Re} \nabla^2 w = & \frac{\partial w}{\partial t} + u \frac{\partial w}{\partial x} + v \frac{\partial w}{\partial y} - \frac{Gr}{Re^2} \frac{\partial T}{\partial x} + \frac{w}{DaRe} \\ & - \frac{Ha^2}{Re Rem} \left[ B_x \frac{\partial}{\partial x} \left( \frac{\partial B_y}{\partial x} - \frac{\partial B_x}{\partial y} \right) + B_y \frac{\partial}{\partial y} \left( \frac{\partial B_y}{\partial x} - \frac{\partial B_x}{\partial y} \right) \right] \end{aligned} \quad (3.2d)$$

in which the Reynolds number  $Re$ , Prandtl number  $Pr$ , Grashof number  $Gr = Ra/Pr$ , Hartmann number  $Ha$ , and magnetic Reynolds number  $Rem$  are

$$\begin{aligned} Re = \frac{UL}{\nu}, \quad Gr = \frac{g\beta\Delta TL^3}{\nu^2}, \quad Ra = \frac{g\beta\Delta TL^3}{\alpha_e \nu}, \quad Da = \frac{\kappa}{L^2}, \\ Pr = \frac{\nu}{\alpha_e}, \quad Ha = \sqrt{\frac{B_0^2 \kappa \sigma}{\mu}}, \quad Rem = \mu_m \sigma UL, \end{aligned}$$

and the term  $w/(DaRe)$  in Eq.(3.2d) exists due to presence of the porous medium. In Eq.(3.2), the continuity condition of velocity field and the divergence-free condition of induced magnetic field are satisfied with the relations  $u = \partial\psi/\partial y$ ,  $v = -\partial\psi/\partial x$ ,  $B_x = \partial A/\partial y$ ,  $B_y = -\partial A/\partial x$ , respectively.

The third order backward difference formula (Houbolt time integration scheme given in Eq.(2.49)) for the time derivatives is utilized. Then, the iteration with respect to time is settled between the DRBEM formulation of the governing Eqs.(3.2) in the form of

$$\mathbf{H}\psi^{m+1} - \mathbf{G}\psi_q^{m+1} = -\mathbf{S}w^m \quad (3.3a)$$

$$u^{m+1} = \mathbf{D}_y\psi^{m+1}, \quad v^{m+1} = -\mathbf{D}_x\psi^{m+1} \quad (3.3b)$$

$$\mathbf{H}T^{m+1} - \mathbf{G}T_q^{m+1} = Pr Re \mathbf{S} \left[ \left. \frac{\partial T}{\partial t} \right|^{m+1} + \mathbf{M}T^{m+1} \right] \quad (3.3c)$$

$$\mathbf{H}A^{m+1} - \mathbf{G}A_q^{m+1} = Rem \mathbf{S} \left[ \left. \frac{\partial A}{\partial t} \right|^{m+1} + \mathbf{M}A^{m+1} \right] \quad (3.3d)$$

$$B_x^{m+1} = \mathbf{D}_y A^{m+1}, \quad B_y^{m+1} = -\mathbf{D}_x A^{m+1} \quad (3.3e)$$

$$\begin{aligned} \mathbf{H}w^{m+1} - \mathbf{G}w_q^{m+1} = \text{ReS} \left[ \left. \frac{\partial w}{\partial t} \right|^{m+1} + \mathbf{M}w^{m+1} \right] - \frac{Gr}{Re} \mathbf{S} \mathbf{D}_x T^{m+1} + \frac{1}{Da} \mathbf{S} w^{m+1} \\ - \frac{Ha^2}{Rem} \mathbf{S} \left( [\mathbf{B}_x]_d \mathbf{D}_x z^{m+1} + [\mathbf{B}_y]_d \mathbf{D}_y z^{m+1} \right), \end{aligned} \quad (3.3f)$$

where

$$\begin{aligned} \mathbf{S} = (\mathbf{H}\hat{\mathbf{U}} - \mathbf{G}\hat{\mathbf{Q}})\mathbf{F}^{-1}, \quad \mathbf{D}_x = \frac{\partial \mathbf{F}}{\partial \mathbf{x}} \mathbf{F}^{-1}, \quad \mathbf{D}_y = \frac{\partial \mathbf{F}}{\partial \mathbf{y}} \mathbf{F}^{-1}, \\ \mathbf{M} = ([\mathbf{u}]_d \mathbf{D}_x + [\mathbf{v}]_d \mathbf{D}_y), \quad z^{m+1} = \mathbf{D}_x B_y^{m+1} - \mathbf{D}_y B_x^{m+1}. \end{aligned}$$

Second order derivatives appearing in the vorticity equation (3.3f) are calculated using the products of  $\mathbf{D}_x$  and  $\mathbf{D}_y$  with the coordinate matrix  $\mathbf{F}$  as explained in Eq.(2.47). Diagonal matrices  $[\mathbf{u}]_d, [\mathbf{v}]_d, [\mathbf{B}_x]_d, [\mathbf{B}_y]_d$ , formed by the vectors  $u^{m+1}, v^{m+1}, B_x^{m+1}, B_y^{m+1}$  diagonally, are all of size  $(N + K) \times (N + K)$  where  $N$  is the number of boundary elements and  $K$  is the number of interior points, and  $m$  shows the iteration step with respect to time.

After the replacement of time derivatives and shuffling for known and unknown boundary information, the system of equations (3.3a), (3.3c), (3.3d) and (3.3f) is solved by direct Gaussian elimination with partial pivoting.

The solution procedure advances in the following steps. Initially (at  $t = 0$ ),  $T, A$  and  $w$  are all taken as zero (except on the boundary). First two time iterations are carried with Backward-Euler scheme. Then the iteration continues with Houbolt time integration scheme.  $\psi^{m+1}$  is solved in (3.3a) using the values of  $w$  from  $m$ th iteration. Then, the velocities  $u^{m+1}, v^{m+1}$  are computed using  $\psi^{m+1}$  from Eq.(3.3b) inserting the boundary conditions for  $u$  and  $v$ . The energy equation is solved for  $T^{m+1}$  from Eq.(3.3c). The boundary conditions for magnetic potential  $A$  are derived from the definitions of  $B_x$  and  $B_y$  in terms of  $A$  such that  $A = -x + C'$  is found if the applied magnetic field is in  $+y$ -direction, i.e.  $B_x = 0, B_y = 1$ . The constant  $C'$  is taken as zero similar to the idea in the boundary conditions of stream function  $\psi$ . The magnetic potential equation, Eq.(3.3d), is solved for  $A^{m+1}$ . Induced magnetic field components  $B_x^{m+1}, B_y^{m+1}$  are computed using  $A^{m+1}$  from Eq.(3.3e) inserting  $\mathbf{B} = (0, B_0, 0) = (0, 1, 0)$  on the boundary.

Vorticity boundary conditions are found by using the definition of vorticity with the help of coordinate matrix  $F$

$$w = \frac{\partial v}{\partial x} - \frac{\partial u}{\partial y} = \mathbf{D}_x v^{m+1} - \mathbf{D}_y u^{m+1}. \quad (3.4)$$

Then, vorticity  $w^{m+1}$  is obtained from Eq.(3.3f).

Iterations continues until the criterion [79]

$$\frac{\|\psi^{m+1} - \psi^m\|_\infty}{\|\psi^{m+1}\|_\infty} + \frac{\|T^{m+1} - T^m\|_\infty}{\|T^{m+1}\|_\infty} + \frac{\|A^{m+1} - A^m\|_\infty}{\|A^{m+1}\|_\infty} + \frac{\|w^{m+1} - w^m\|_\infty}{\|w^{m+1}\|_\infty} < \epsilon \quad (3.5)$$

is satisfied with  $\epsilon = 1e - 05$ , and the solution is obtained at steady-state.

Once the whole system is solved, average Nusselt number on the heated top wall is computed using Eq.(2.77). Drag Coefficient through the moving wall is also achieved by [30]

$$c_D = -\frac{2}{Re} \frac{\partial u}{\partial y} \Big|_{y=1}. \quad (3.6)$$

As a validation case for the proposed numerical scheme based on DRBEM, the average Nusselt numbers are computed when  $Ha = 0$ ,  $Da = \infty$  are taken to reduce the problem to the mixed convection flow in a lid-driven cavity [72]. It can be seen from Table 3.1 that good agreement is obtained in spite of using small number of boundary elements (at most  $N = 96$ ,  $K = 961$ ) compared to the study [72] (in which at least  $128 \times 128$  mesh size is utilized).

Table 3.1: Problem 3.1: Comparison of  $\overline{Nu}$  at the top wall,  $Pr = 0.71$ .

Re	$Gr = 10^2$		$Gr = 10^4$	
	[72]	Present	[72]	Present
100	1.94	1.94	1.34	1.33
400	3.84	3.84	3.62	3.61
1000	6.33	6.32	6.29	6.29

The numerical results are performed using quadratic ( $f = 1 + r + r^2$ ) radial basis functions in forming coordinate matrix  $\mathbf{F}$ . Further, 16-point Gaussian quadrature is used for evaluating the integrals in  $\mathbf{H}$  and  $\mathbf{G}$  matrices. In all the computations,  $Pr = 1$  is fixed (corresponding to ionized gases [6]). The numbers of boundary elements  $N$  and arbitrarily taken interior points  $K$  are needed to be increased when the problem parameters take large values, especially with high Hartmann number, due to the dominance of reaction terms in the vorticity equation. This is verified in Table 3.2 in terms of average Nusselt number for increasing values of Hartmann number. As can be seen, not much of a significant variation in the mean Nusselt number on the hot top wall is observed after  $N = 120$  up to  $Ha = 100$ . Therefore, in general, 120 linear boundary elements and 841 interior points are adopted in the computations. Only for  $Ha = 100$  and  $Ha = 300$ ,  $N = 160$  and  $N = 176$  are used in the computations, respectively.

Table 3.2: Problem 3.1: Grid analysis with  $Da=0.1$ ,  $Pr=1$ ,  $Gr=Re=Rem=100$ .

N	K	$\overline{Nu}$			
		Ha=25	Ha=50	Ha=100	Ha=300
80	361	1.7789	1.4001	1.1318	1.0164
120	841	1.8227	1.4709	1.2079	1.0261
160	1521	1.8177	1.4747	1.2292	1.0479
176	1849	1.8122	1.4702	1.2305	1.0540
192	2209	1.8062	1.4645	1.2297	1.0541

As  $Da$  decreases (Figure 3.2), fluid flows slowly due to the decrease in permeability of porous medium. The effect of moving lid diminishes and the center of the streamlines

clusters through the top wall. Isotherms become nearly perpendicular to the vertical walls referring to the conductive heat transfer. Magnetic potential lines parallel to vertical walls occur showing the increase in diffusive terms in magnetic potential equation. Vorticity forms strong boundary layers due to the dominance of reaction term with the decrease in  $Da$ .

For large values of  $Rem$  (Figure 3.3), the expected variation is observed in magnetic potential due to the increase in dominance of convection terms in magnetic potential equation. Magnetic potential lines try to circulate through the center of the cavity and obey the movement of the lid. For a further increase in  $Rem$  ( $Rem = 100$ ), circulation enlarges and clusters near the left wall. Not much of a change is observed in streamlines, isotherms, and vorticity.

Since the applied magnetic field is in  $+y$ -direction, boundary layer (Hartmann layers) formation in the flow through the vertical walls as well as the horizontal walls (side layers) are well observed with the increase in  $Ha$  in Figure 3.4. Even secondary flows appear close to the vertical walls with the increasing intensity of external magnetic field as approached to 100 and then 300. Isotherms become parallel to horizontal walls. This indicates that the increase in the intensity of the applied magnetic field has an inhibitive effect on the heat transfer. Vorticity is also concentrated close to the walls as  $Ha$  increases (action takes place near the walls). The intensified magnetic field makes the magnetic potential lines perpendicular to the top and bottom walls which points to the decrease in the effect of the induced magnetic field. That is, external magnetic field in  $+y$ -direction is more powerful forcing magnetic potential inside the cavity to be in its direction. Instead of decreasing time increment  $\Delta t$  for large values of  $Ha$ , once the vorticity transport equation (which contains  $Ha^2$  in reaction terms) is solved, a relaxation parameter  $0 < \gamma < 1$  is used for accelerating convergence of vorticity as  $w^{m+1} \leftarrow \gamma w^{m+1} + (1 - \gamma)w^m$ .

When the direction of the external magnetic field is changed to the  $x$ -direction, the same effect is observed in terms of Hartmann and side layers. That is, firstly the external magnetic field forces to separate the flow, and then the lid effect diminishes leaving the center region almost stagnant. Boundary layers now obey the rule that Hartmann layers are formed on the horizontal sides of the cavity, and side layers are on the top and bottom walls as can be seen from Figure 3.5. If the external magnetic field is inclined with an angle from the  $x$ -axis, the behavior of the flow takes the direction of the magnetic field forming the loops and the boundary layers. Magnetic potential lines inside the cavity also show the direction of the externally applied inclined magnetic field.

With the increase of Reynolds number value (Figure 3.6), clockwise rotating (primary) cell adjacent to the upper moving wall becomes larger while the counter-rotating cell (secondary cell) shrinks into two small bottom corner eddies. This is due to the buoyancy parameter  $Ri = Gr/Re^2$  decrease which results in a decrease in the intensity of the inertia term. Both isotherms and vorticity circulate in the cavity as  $Re$  increases due to the dominance of the convection terms. Similarly, the increase in  $Gr$  causes three cells to emerge in the flow ( $\psi$  and  $w$ ), and the center of the primary cell moves in the direction of moving lid remarkably as can be seen from Figure 3.7. Conduction

dominated effect reveals in isotherms due to the increase in buoyancy effect. On the moving lid of the cavity, perturbation is pronounced in magnetic potential lines.

As expected, the decrease in the heat transfer with the increase in  $Ha$  number may also be visualized by average Nusselt number variation on the hot top wall as shown in Figure 3.8a. The decrease in  $\overline{Nu}$  is seen as  $Ha$  increases due to the retarding effect of Lorentz force. For large values of  $Da$ , magnetic Reynolds number enhances convective heat transfer as can be seen from the increase in  $\overline{Nu}$  in Figure 3.8b. However, heat transfer turns into the conductive heat transfer as  $Da$  decreases even though  $Rem$  increases. Overall, not much of an effect of  $Rem$  on the heat transfer is revealed.

In Figure 3.9a, the increase in drag coefficient through the moving wall with the increase in  $Ha$  points to the increase in shear stress ( $-\mu\partial u/\partial y$ ). The variation in  $Rem$  has no effect on drag coefficient as can be seen from Figure 3.9b.

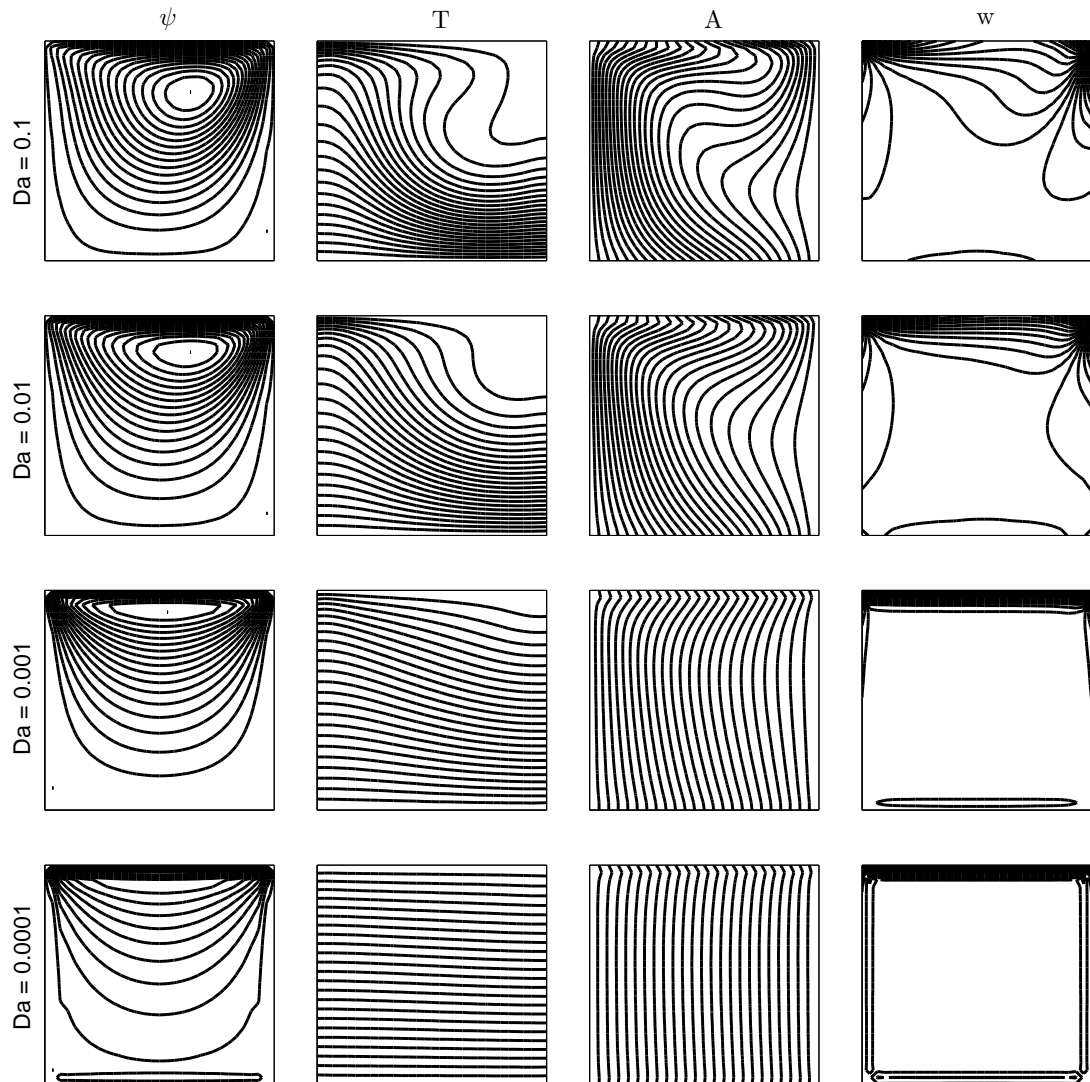


Figure 3.2: Problem 3.1:  $Gr = Re = Rem = 100$ ,  $Pr = 1$ ,  $Ha = 5$ ,  $\Delta t = 0.25$ .



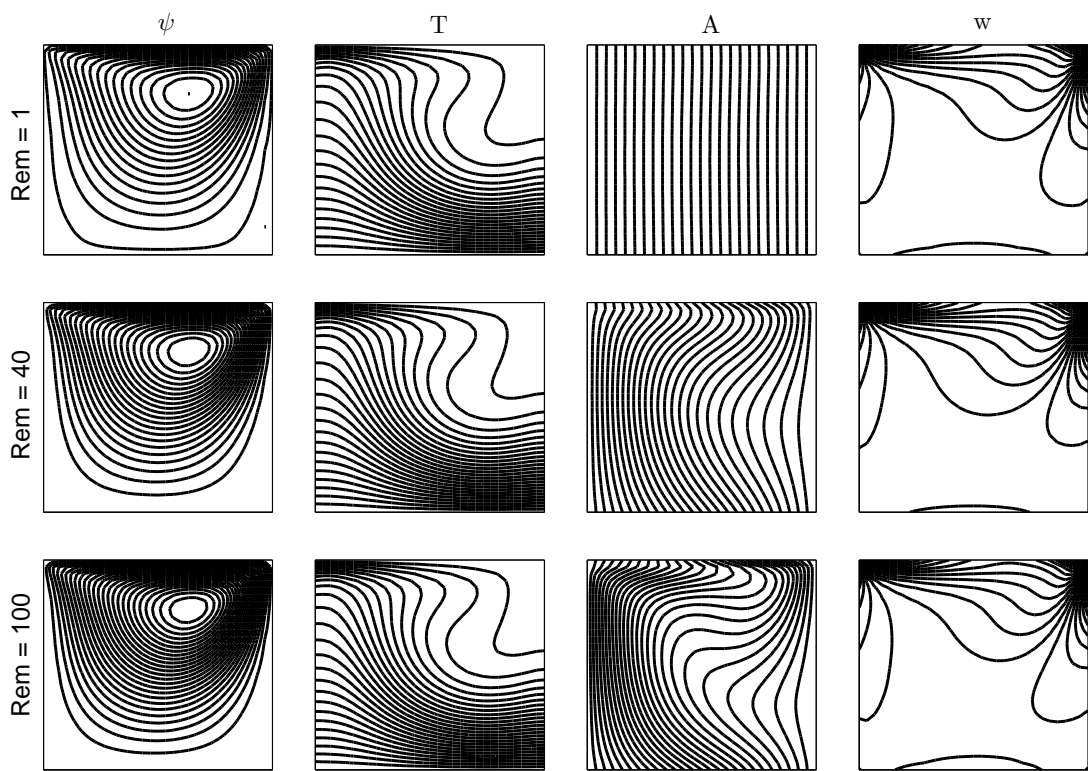


Figure 3.3: Problem 3.1:  $Da = 0.1$ ,  $Pr = 1$ ,  $Gr = Re = 100$ ,  $Ha = 5$ ,  $\Delta t = 0.25$ .

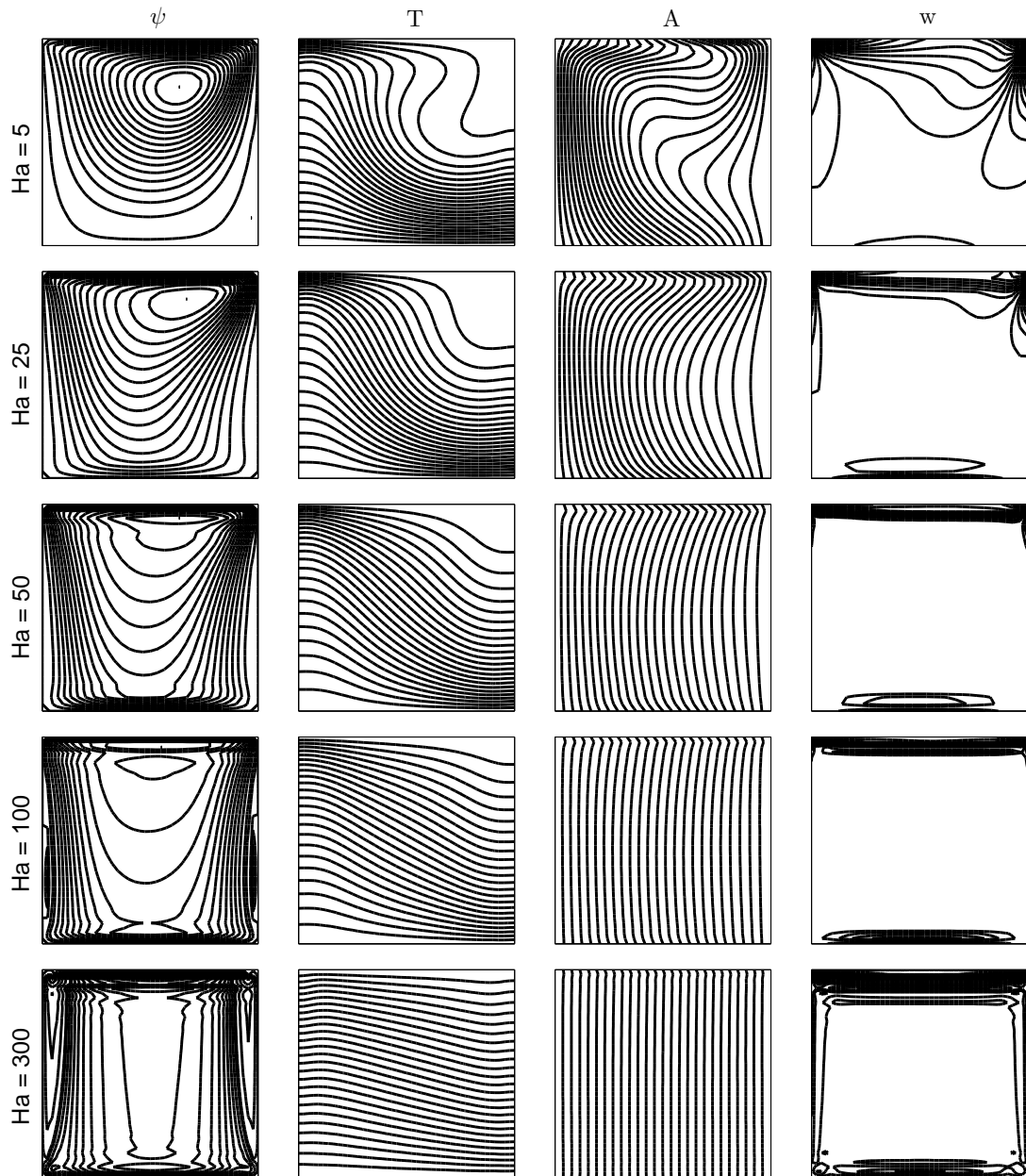


Figure 3.4: Problem 3.1:  $Da = 0.1$ ,  $Pr = 1$ ,  $Gr = Re = Rem = 100$ ;  $\Delta t = 0.25$  ( $Ha = 5, 25$ );  $\Delta t = 0.2, \gamma = 0.5$  ( $Ha = 50$ );  $\Delta t = 0.1, \gamma = 0.1$  ( $Ha = 100$ );  $\Delta t = 0.01, \gamma = 0.1$  ( $Ha = 300$ ).

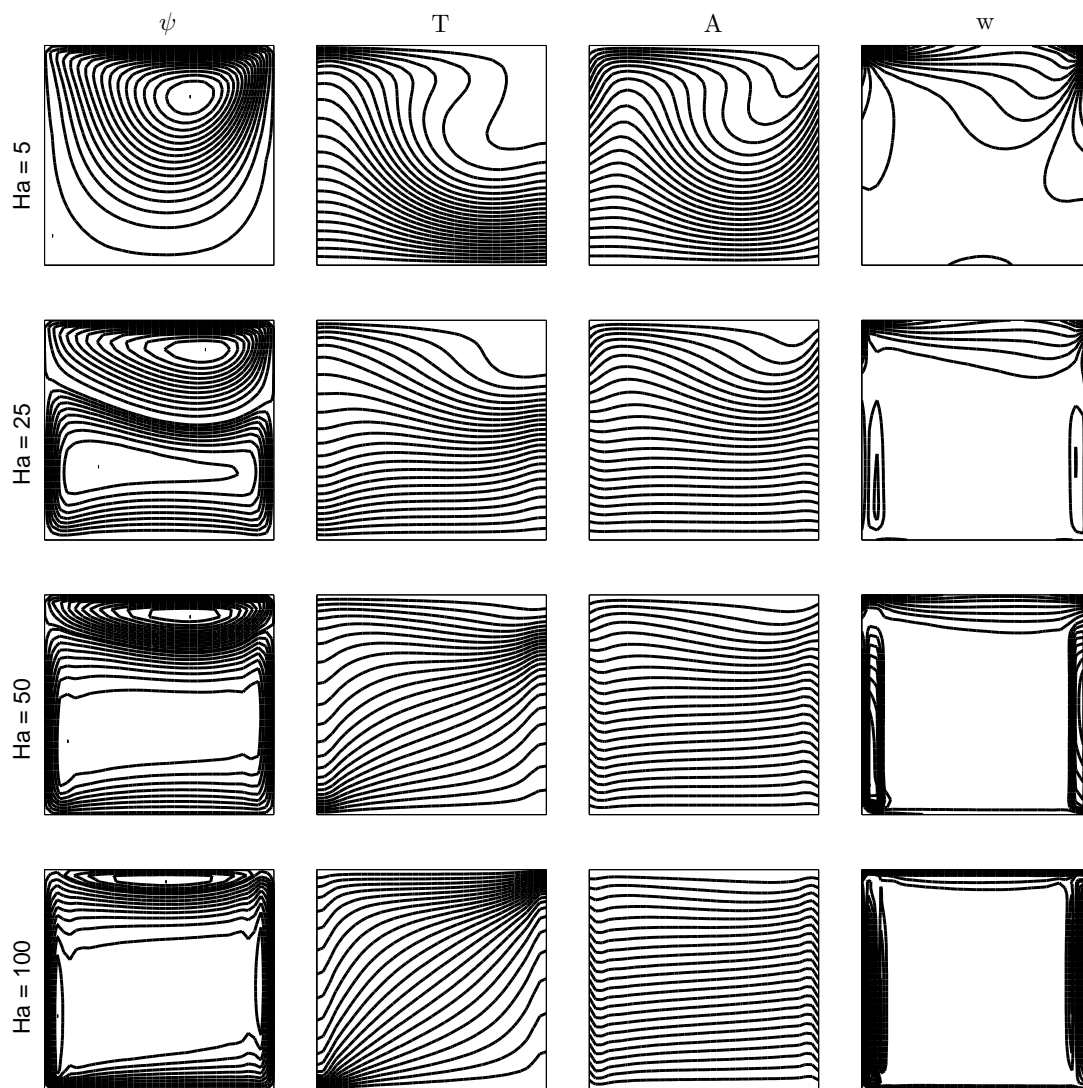


Figure 3.5: Problem 3.1:  $x$ -direction external magnetic field with  $Da = 0.1$ ,  $Pr = 1$ ,  $Gr = Re = Rem = 100$ ;  $\Delta t = 0.25(Ha = 5, 25)$ ;  $\Delta t = 0.2, \gamma = 0.5(Ha = 50)$ ;  $\Delta t = 0.1, \gamma = 0.1(Ha = 100)$ .

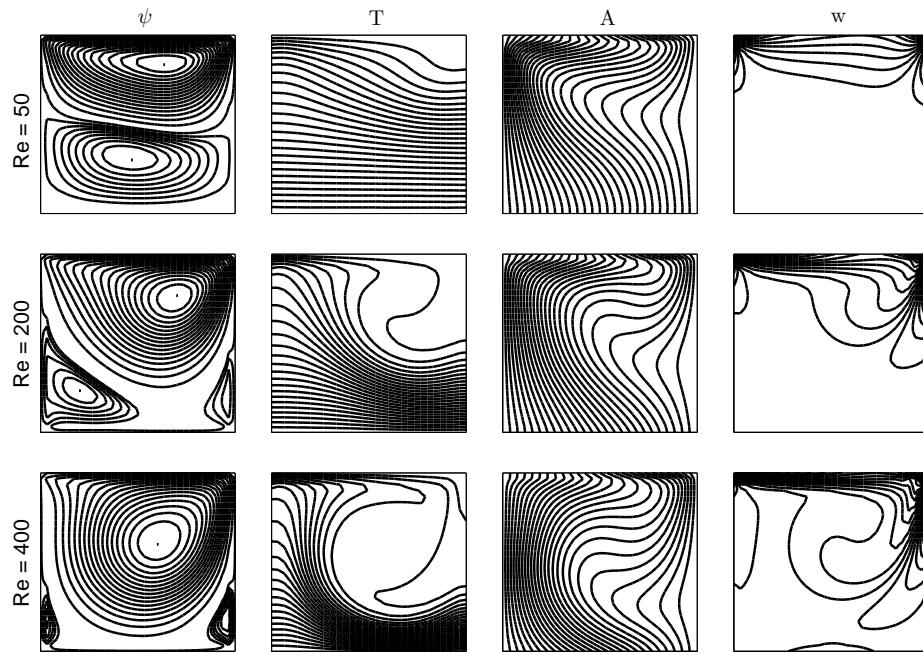


Figure 3.6: Problem 3.1:  $Da = 0.1$ ,  $Pr = 1$ ,  $Gr = 10^4$ ,  $Ha = 5$ ,  $Re = 100$ ,  $\Delta t = 0.25$ .

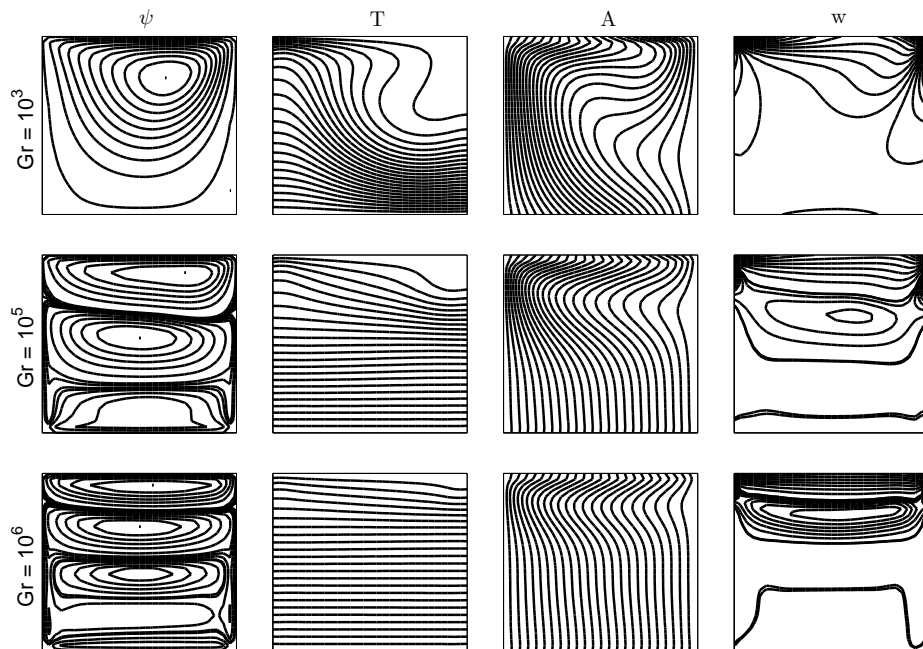
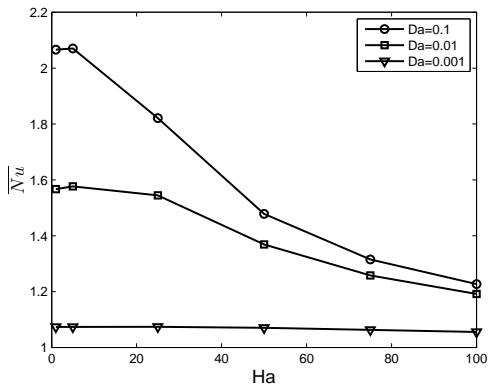
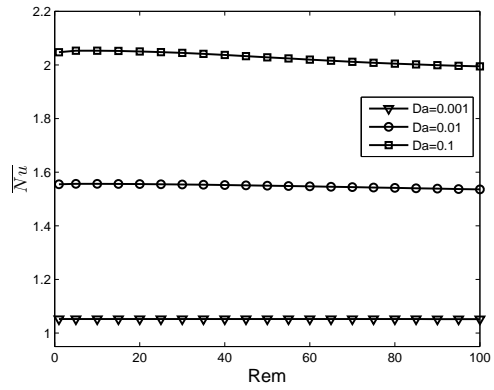


Figure 3.7: Problem 3.1:  $Da = 0.1$ ,  $Pr = 1$ ,  $Re = Rem = 100$ ,  $Ha = 5$ ;  $\Delta t = 0.25(Gr = 10^3, 10^4)$ ;  $\Delta t = 0.1(Gr = 10^5)$ ;  $\Delta t = 0.1, \gamma = 0.1(Gr = 10^6)$ .

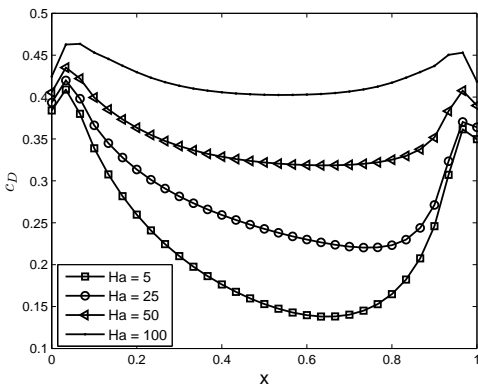


(a)  $Rem = 10, N = 160, K = 1521$

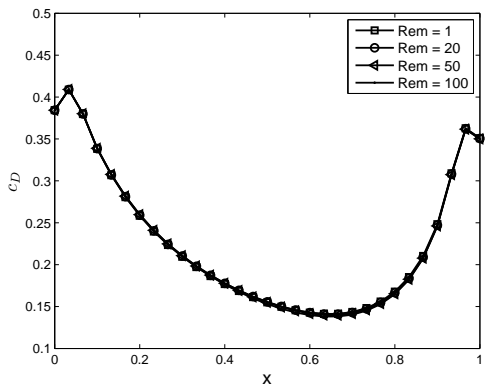


(b)  $Ha = 10, N = 128, K = 961$

Figure 3.8: Problem 3.1: Average Nusselt number variation with  $Gr = Re = 100, Pr = 1$ .



(a)  $Da = 0.1, Rem = 100$



(b)  $Da = 0.1, Ha = 5$

Figure 3.9: Problem 3.1: Drag coefficient observation with  $Gr = Re = 100, Pr = 1$ .

### 3.2 MHD flow and heat transfer with magnetic induction ( $\psi - T - B_x - B_y - w$ )

In this problem, induced magnetic field is computed in its original components  $B_x$  and  $B_y$  instead of magnetic potential  $A$ , and the medium is considered as non-porous.

The governing non-dimensional equations in terms of stream function  $\psi$ , temperature  $T$ , induced magnetic field components  $B_x$ ,  $B_y$ , and vorticity  $w$  are

$$\nabla^2 \psi = -w \quad (3.7a)$$

$$\frac{1}{PrRe} \nabla^2 T = \frac{\partial T}{\partial t} + u \frac{\partial T}{\partial x} + v \frac{\partial T}{\partial y} \quad (3.7b)$$

$$\frac{1}{Rem} \nabla^2 B_x = \frac{\partial B_x}{\partial t} + u \frac{\partial B_x}{\partial x} + v \frac{\partial B_x}{\partial y} - B_x \frac{\partial u}{\partial x} - B_y \frac{\partial u}{\partial y} \quad (3.7c)$$

$$\frac{1}{Rem} \nabla^2 B_y = \frac{\partial B_y}{\partial t} + u \frac{\partial B_y}{\partial x} + v \frac{\partial B_y}{\partial y} - B_x \frac{\partial v}{\partial x} - B_y \frac{\partial v}{\partial y} \quad (3.7d)$$

$$\begin{aligned} \frac{1}{Re} \nabla^2 w = & \frac{\partial w}{\partial t} + u \frac{\partial w}{\partial x} + v \frac{\partial w}{\partial y} - \frac{Ra}{PrRe^2} \frac{\partial T}{\partial x} \\ & - \frac{Ha^2}{ReRem} \left[ B_x \frac{\partial}{\partial x} \left( \frac{\partial B_y}{\partial x} - \frac{\partial B_x}{\partial y} \right) + B_y \frac{\partial}{\partial y} \left( \frac{\partial B_y}{\partial x} - \frac{\partial B_x}{\partial y} \right) \right], \end{aligned} \quad (3.7e)$$

where the dimensionless parameters are Reynolds  $Re$ , Prandtl  $Pr$ , Hartmann  $Ha$ , magnetic Reynolds  $Rem$ , and Rayleigh  $Ra$  numbers.

Being used the space derivatives in vector  $\mathbf{b}$  by the coordinate matrix  $\mathbf{F}$ , and discretized the time derivatives with Backward-Euler finite difference formula, the iteration with respect to time for  $\psi$ ,  $T$ ,  $B_x$ ,  $B_y$ , and  $w$  is given as

$$\mathbf{H}\psi^{m+1} - \mathbf{G}\psi_q^{m+1} = -\mathbf{S}w^m \quad (3.8a)$$

$$u^{m+1} = \mathbf{D}_y \psi^{m+1}, \quad v^{m+1} = -\mathbf{D}_x \psi^{m+1} \quad (3.8b)$$

$$\left( \mathbf{H} - \frac{PrRe}{\Delta t} \mathbf{S} - PrRe \mathbf{S} \mathbf{M} \right) T^{m+1} - \mathbf{G} T_q^{m+1} = -\frac{PrRe}{\Delta t} \mathbf{S} T^m \quad (3.8c)$$

$$\begin{aligned} \left( \mathbf{H} - \frac{Rem}{\Delta t} \mathbf{S} - Rem \mathbf{S} \mathbf{M} + Rem \mathbf{S} \mathbf{D}_x [\mathbf{u}]_d^{m+1} \right) B_x^{m+1} - \mathbf{G} B_{xq}^{m+1} = & \\ & - \frac{Rem}{\Delta t} \mathbf{S} B_x^m - Rem \mathbf{S} [\mathbf{B}_y]_d^m \mathbf{D}_y u^{m+1} \end{aligned} \quad (3.8d)$$

$$\begin{aligned} \left( \mathbf{H} - \frac{Rem}{\Delta t} \mathbf{S} - Rem \mathbf{S} \mathbf{M} + Rem \mathbf{S} \mathbf{D}_y [\mathbf{v}]_d^{m+1} \right) B_y^{m+1} - \mathbf{G} B_{yq}^{m+1} = & \\ & - \frac{Rem}{\Delta t} \mathbf{S} B_y^m - Rem \mathbf{S} [\mathbf{B}_x]_d^m \mathbf{D}_x v^{m+1} \end{aligned} \quad (3.8e)$$

$$\begin{aligned} \left( \mathbf{H} - \frac{Re}{\Delta t} \mathbf{S} - Re \mathbf{S} \mathbf{M} \right) w^{m+1} - \mathbf{G} w_q^{m+1} = & -\frac{Re}{\Delta t} \mathbf{S} w^m \\ & - \frac{Ha^2}{Rem} \mathbf{S} \left( [\mathbf{B}_x]_d^{m+1} \mathbf{D}_x \{\zeta\} + [\mathbf{B}_y]_d^{m+1} \mathbf{D}_y \{\zeta\} \right) - \frac{Ra}{PrRe} \mathbf{S} \mathbf{D}_x T^{m+1} \end{aligned} \quad (3.8f)$$

where

$$\mathbf{S} = \left( \mathbf{H}\widehat{\mathbf{U}} - \mathbf{G}\widehat{\mathbf{Q}} \right) \mathbf{F}^{-1}, \quad \mathbf{D}_x = \frac{\partial \mathbf{F}}{\partial \mathbf{x}} \mathbf{F}^{-1}, \quad \mathbf{D}_y = \frac{\partial \mathbf{F}}{\partial \mathbf{y}} \mathbf{F}^{-1}$$

$$\mathbf{M} = [\mathbf{u}]_d^{m+1} \mathbf{D}_x + [\mathbf{v}]_d^{m+1} \mathbf{D}_y, \quad \{\zeta\} = \mathbf{D}_x B_y^{m+1} - \mathbf{D}_y B_x^{m+1},$$

$[\mathbf{B}_x]_d^{m+1}, [\mathbf{B}_y]_d^{m+1}, [\mathbf{u}]_d^{m+1}, [\mathbf{v}]_d^{m+1}$  enter into the system as diagonal matrices of size  $(N + K) \times (N + K)$ , and  $m$  shows the iteration step. The arranged form of the equations (with the known and unknown information on the boundary) is solved by Gaussian elimination with partial pivoting.

Initially,  $w^0, B_x^0, B_y^0, T^0$  are taken as zero everywhere (except on the boundary). Once the stream function is computed from Eq.(3.8a), velocity components are determined by using Eq.(3.8b) inserting the boundary conditions. Then, temperature equation (3.8c) and induction equations (3.8d)-(3.8e) are solved with the insertion of their boundary conditions. Vorticity boundary conditions are computed by using Eq.(3.4). Then, the vorticity transport equation (3.8f) is solved by using these vorticity boundary conditions. The solution process continues in this way until the criterion

$$\sum_{k=1}^5 \frac{\|\phi_k^{m+1} - \phi_k^m\|_\infty}{\|\phi_k^{m+1}\|_\infty} < \epsilon = 1e - 4 \quad (3.9)$$

is satisfied where  $\phi_k$  stands for  $\psi, T, B_x, B_y$  and  $w$  values at the boundary and interior points, respectively.

Once the vorticity equation Eq.(3.8f) is solved, in order to accelerate the convergence of vorticity to steady-state which is rather difficult to converge than the other unknowns, a relaxation parameter  $0 < \gamma < 1$  is used as  $w^{m+1} \leftarrow \gamma w^{m+1} + (1 - \gamma)w^m$  for large values of parameters in reaction terms.

The depicted contours from left to right are streamlines, isotherms, vorticity lines, and induced magnetic field vector  $(B_x, B_y)$  at steady-state.

### 3.2.1 Lid-driven cavity MHD flow

The electrically conducting fluid is moving down the channel with a pressure gradient and an imposed magnetic field is in the  $+y$ -direction which is also perpendicular to the axis of the channel ( $z$ -axis). The flow is fully developed, thus the cross-section of the channel is taken as the domain of the problem (lid-driven cavity).

The two-dimensional, unsteady, laminar, incompressible MHD flow and heat transfer in lid-driven cavity is considered. The problem configuration with boundary conditions is depicted as in Figure 3.10.

The computed results are obtained using the radial basis function  $f = 1 + r$ , and 16-point Gaussian quadrature for the integrals in the BEM matrices  $\mathbf{H}$  and  $\mathbf{G}$ . In general,  $N = 120$  boundary elements,  $K = 840$  interior points are used.

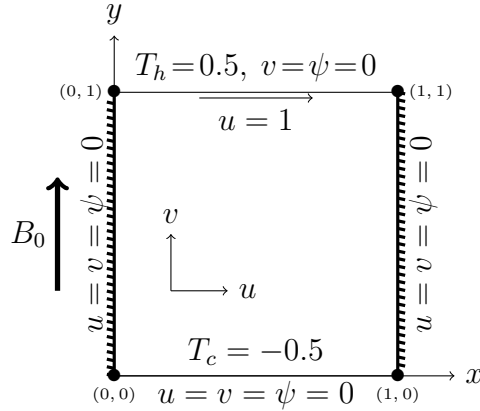


Figure 3.10: Problem 3.2.1 configuration.

Table 3.3: Problem 3.2.1: CPU times and  $\overline{Nu}$  on the heated wall with  $Re = 1$ ,  $Pr = 0.71$ ,  $Gr = 10^4$ ,  $\Delta t = 0.01$ .

Ha	Present Study				[34]	
	15 × 15		25 × 25		15 × 15	
	$Nu$	CPU	$Nu$	CPU	$Nu$	CPU
0	2.17	2.59	2.08	37.92	2.02	50.60
10	1.82	3.15	1.74	95.43	1.70	34.03
25	1.20	4.52	1.18	61.51	1.17	42.59
50	1.01	4.76	1.01	59.55	0.97	25.53

The presented numerical procedure is validated neglecting the induced magnetic field as in the case of [34] (in which the top and bottom walls are adiabatic while the left wall is hot and the right wall is cold, and no-slip boundary conditions are imposed on the walls). The average Nusselt numbers ( $\overline{Nu} = -\int_0^1 (\partial T / \partial x) dy$ ) computed by composite Simpson's rule (Appendix B) are in good agreement with the ones computed in [34]. The computational cost (CPU time in seconds) of the present study is naturally less than the one in the domain discretization methods due to the use of boundary elements only as can be seen in Table 3.3 (e.g. 15 × 15 grid, 56 boundary elements only).

As  $Re$  increases (Figure 3.11), the center of the streamlines in the direction of moving lid shifts through the center of the cavity forming new secondary eddies at the bottom corners. The dominance of convection is observed in isotherms forming the strong temperature gradients clustered at the top left and bottom right corners. Vorticity is transported inside the cavity forming boundary layers on the top moving lid and right wall close to the upper corner. This shows the concentration of flow through upper right corner. Induced magnetic field is not affected much with the increase in  $Re$ .

With an increase in  $Ha$  (Figure 3.12), fluid flows slowly due to the retarding effect of Lorentz force. Two new cells on the right and left parts of cavity are observed in streamlines. Heat is transferred by conduction as can be seen from isotherms. Induced magnetic field lines become perpendicular to horizontal walls due to the decrease in the dominance of convection terms in the induction equations. Also, this points to the



dominance of external magnetic field which is in the  $+y$ -direction. Vorticity concentrates completely near on the wall with the moving lid being stagnant at the center as the intensity of magnetic field increases (i.e.  $Ha$  increases).

An increase in magnetic Reynolds number  $Rem$  has a great influence on the induced magnetic field only. It shows circulation at the center of the cavity due to the dominance of convection terms in the induction equations, and the effect of external magnetic field diminishes (Figure 3.13).

As  $Ra$  increases (Figure 3.14), the isotherms indicate the conduction dominated effect due to the dominance of the buoyancy force. Small counter-clockwise eddy in streamlines with  $Ra = 10^3$  occupies the mid-part of the cavity with  $Ra = 10^4$ , and one more clockwise cell emerges through the bottom part of the cavity as  $Ra$  reaches to the value  $Ra = 10^5$ .

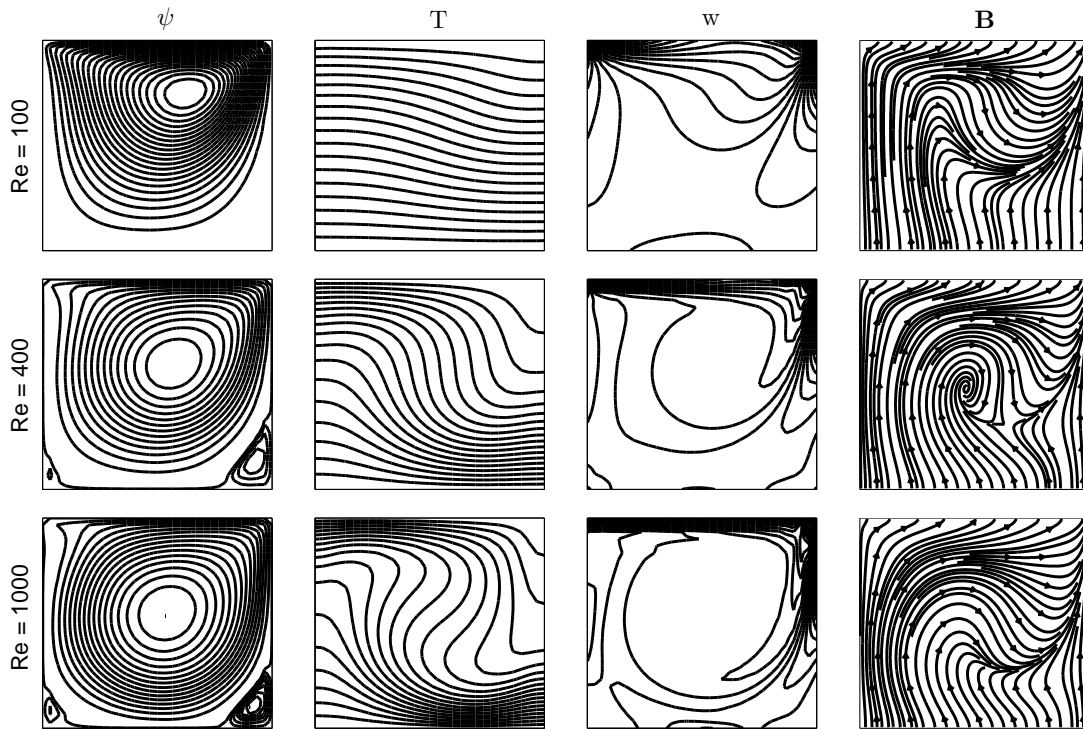


Figure 3.11: Problem 3.2.1:  $Rem = 100$ ,  $Ra = Ha = 10$ ,  $Pr = 0.1$ ,  $\Delta t = 0.25$ .

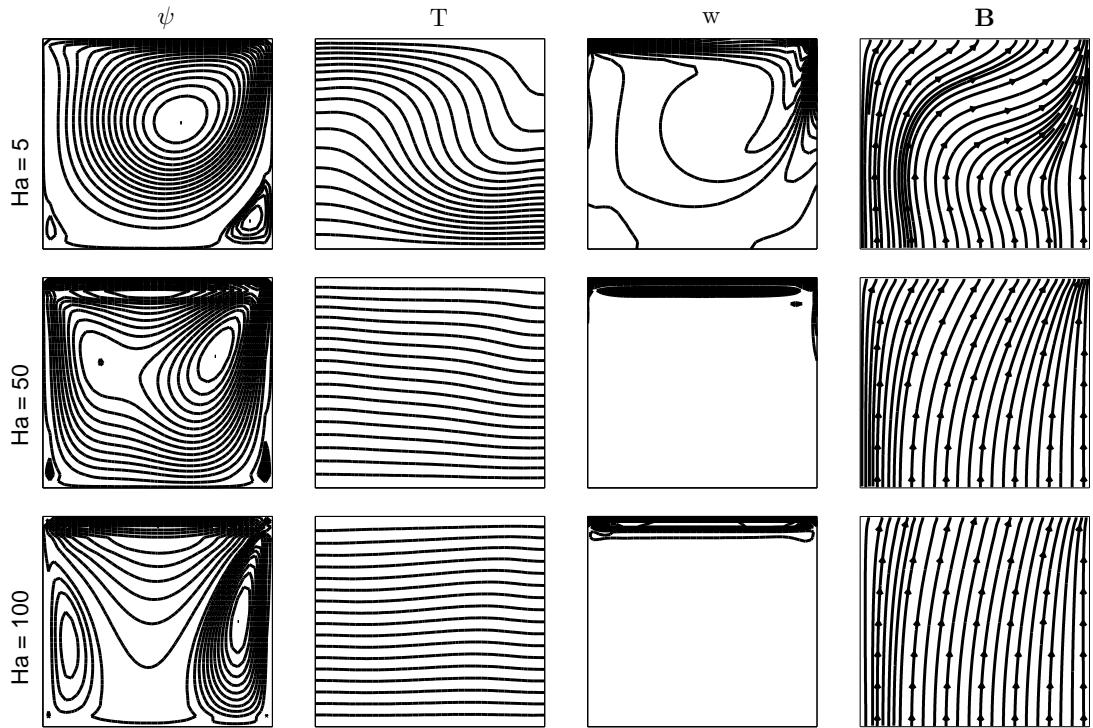


Figure 3.12: Problem 3.2.1:  $Rem = 40$ ,  $Re = 400$ ,  $Ra = 1000$ ,  $Pr = 0.1$ ,  $\Delta t = 0.5$  ( $Ha = 5$ ),  $\Delta t = 0.2$  ( $Ha = 50$ ),  $\Delta t = 0.1$  with  $\gamma = 0.1$  ( $Ha = 100$ ).

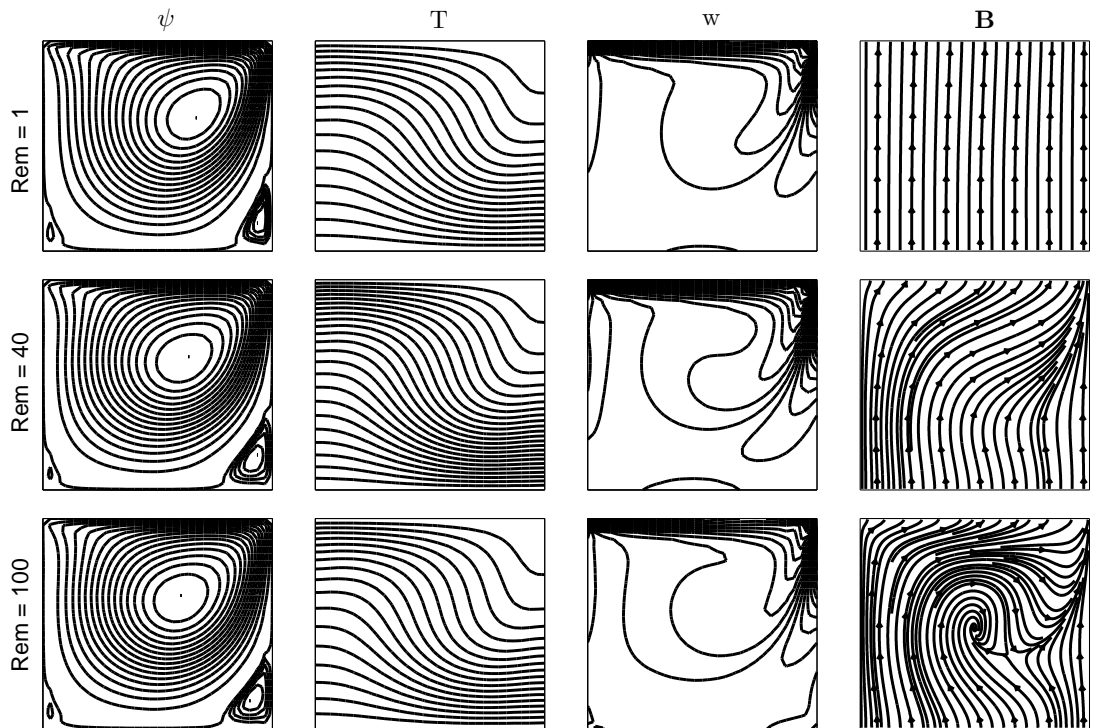


Figure 3.13: Problem 3.2.1:  $Re = 400$ ,  $Ha = 10$ ,  $Ra = 1000$ ,  $Pr = 0.1$ ,  $\Delta t = 0.25$ .

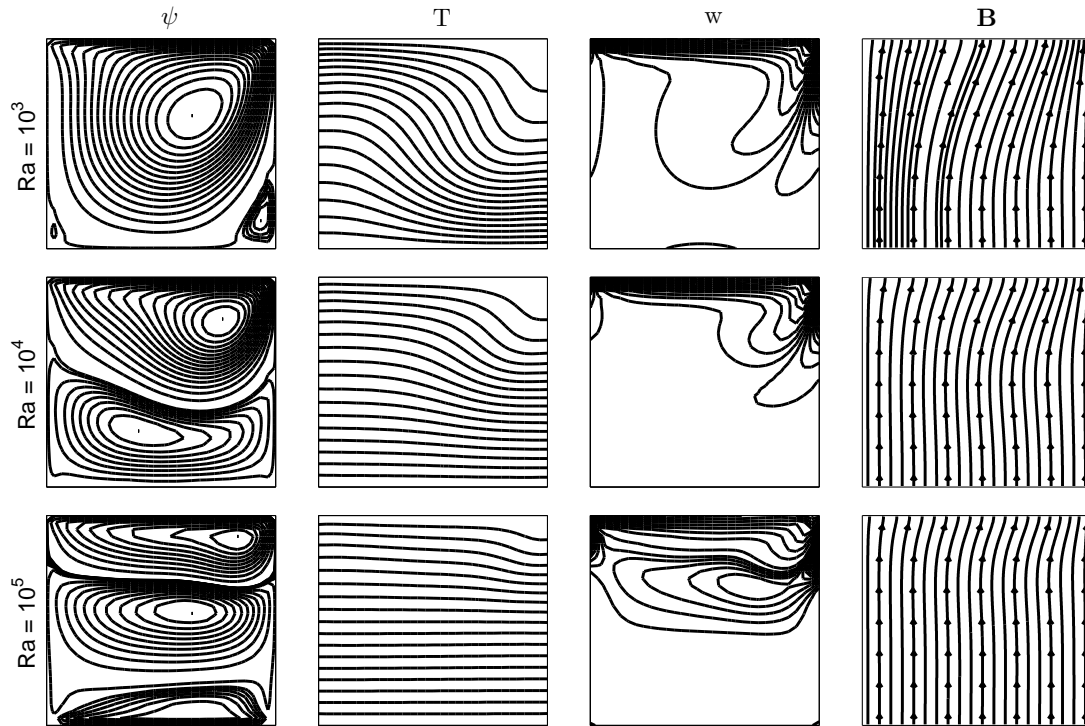


Figure 3.14: Problem 3.2.1:  $Re = 400$ ,  $Rem = Ha = 10$ ,  $Pr = 0.1$ ,  $\Delta t = 0.25$ .

### 3.2.2 MHD flow in a lid-driven cavity with a centered square blockage

The MHD flow problem has taken much interest due to the heat transfer alterations in the presence of obstructions in enclosures. The domain of this problem is described in Figure 3.15. The stream function is set to zero on outer boundaries and it is unknown but a constant on the inner square boundary [87]. This constant value of boundary streamline on the square cylinder is determined considering the streamline values when the square blockage is absent. Outer walls are cold  $T_c = 0$  while the wall around the square obstacle is heated  $T_s = 1$ . Heat transfer inside the blockage is neglected due to the small value of thermal diffusivity of the solid and its isothermal structure.

The blockage is assumed to be non-conducting producing negligible induced magnetic field ( $Rem$  is assumed to be very small in the blockage). On both the cavity and solid blockage walls  $x$ -component of magnetic field is taken as zero,  $y$ -component as one since external magnetic field is applied in the  $y$ -direction. The vorticity boundary conditions are not known. They are going to be obtained during the solution procedure by using the definition of vorticity and DRBEM coordinate matrix  $\mathbf{F}$ .

The numerical results are obtained with the same process as explained in the previous section. In the computations,  $L_s = 0.25$  is fixed using  $N = 208$  linear boundary elements with  $K = 880$  interior points.  $\psi = -0.05$  is taken on the blockage walls by looking at the average  $\psi$  value at the center of the cavity in the absence of blockage and heat transfer.

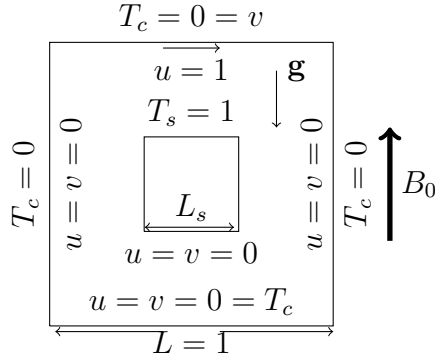


Figure 3.15: Problem 3.2.2: Configuration of square obstacle in a square cavity.

Figure 3.16 shows that the results using DRBEM in solving the mixed convection flow in a lid-driven cavity with a square blockage, are consistent with the results given in [71] (in terms of  $Ri = Ra/(PrRe^2)$ ).

In this problem, for  $Ra = 10^3$ , the center of the primary cell is seen through the moving lid and a secondary flow is observed at the left bottom corner of the cavity. With  $Ra = 10^4$ , the primary cell is shrunk through the right mid part while the secondary flow occupies the left part of the cavity. A symmetric behavior in streamlines starts to be pronounced vanishing the effect of moving lid with  $Ra = 10^5$  and  $10^6$ . Vorticity shows a similar behavior to streamlines as  $Ra$  increases. This is the common effect of large  $Ra$  values on the flow. Furthermore, isotherms also start to be circulated from hot blockage to the cold walls forming strong temperature gradient through the moving top wall due to the increase in natural convection (buoyancy). Induced magnetic field lines are also affected with the increase in  $Ra$ , and small perturbation from bottom to the top wall is observed. Here,  $Rem = 1$  is purposely taken to observe the effect of the solid blockage for large  $Ra$  (Figure 3.17).

Blockage causes the secondary flow to develop at a lower value of  $Re$  compared to cavity without blockage. With the increase in  $Re$ , the center of the streamlines which is close to the moving lid again moves to the center of the cavity but to the right of the blockage (Figure 3.18). Meantime, secondary flow becomes prominent close to the left wall of the cavity. Isotherms are not altered much. But, for large values of  $Re$ , a boundary layer is pronounced on the left and bottom walls of the square blockage due to the secondary flow on the left wall of the cavity. Vorticity is transported inside the cavity as  $Re$  increases. Induced magnetic field vector tending to the direction of moving lid is not affected much.

As expected, the variation of  $Rem$  has the influence only on the induced magnetic field lines as can also be seen in Figure 3.19. Induced magnetic field lines obey the direction of moving lid with the increase in  $Rem$  while the square blockage squeezes them between the blockage and the right wall of the cavity.

As  $Ha$  increases (Figure 3.20), due to the  $+y$ -directed applied magnetic field, the center of the primary cell in streamlines shift through the center of the cavity nearly conflicting with the square blockage. Further, the secondary flow at the left wall of

the cavity becomes smaller, and a tertiary flow emerges at the top wall. Not much effect of  $Ha$  on isotherms is observed. This may be due to the small number of  $Pr$ . Strongly applied magnetic field (large  $Ha$ ) directs the induced magnetic field lines in its direction. This is why  $Rem = 100$  has been taken to start with a turbulence at the right upper corner with small  $Ha$ .

The aim of this example is to examine the effects of both external magnetic field and the blockage in the cavity. Therefore, the streamline value on the blockage walls is exposed to the change as  $Ha$  increases. This is depicted in Figure 3.21. In the absence of a square obstacle (Figure 3.21a), clockwise directed primary cell is divided into two parts and squeezed through the left and right walls, and a counter-rotating cell is intensified covering the center of the cavity as  $Ha$  increases. As can be seen, the value of stream function changes, especially at the center of the cavity. Due to this change in the flow, the stream function value which is denoted by  $\psi_c$  on the square obstacle is taken accordingly with the values shown in Figure 3.21a. Then, the effects of both applied magnetic field and blockage placed in the center of the cavity, on the flow are shown in Figure 3.21b. It is observed that secondary flow developed with  $Ha = 5$  through the left wall becomes larger, and the center of the primary cell shifts through the right wall. Further, the primary cell is pronounced between the right wall of the obstacle and the right wall of the cavity while a counter-rotating cell emerges from the top wall of the cavity to the top wall of the square blockage. Retarding effect of Lorentz force starts much earlier (even with  $Ha = 5$ ) and gives symmetric secondary flow cells on the left and right of the blockage when  $Ha = 50$ . Further, the increase in  $Ha$  ( $Ha = 100$ ) squeezes all the flow cells to the boundaries of the cavity. This is the well known boundary layer formation in the flow for large  $Ha$ .

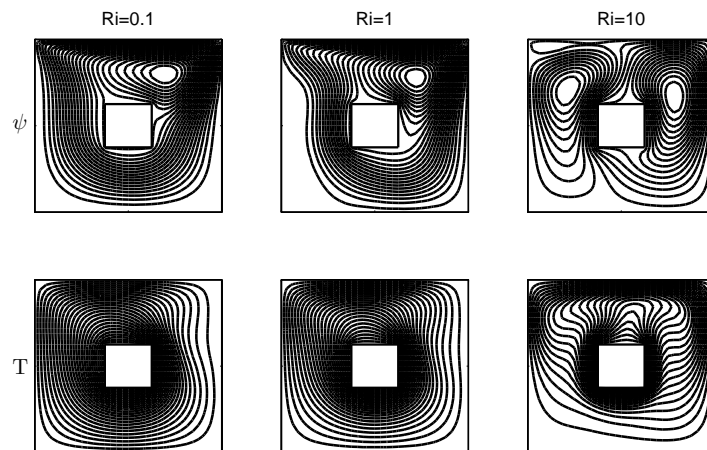


Figure 3.16: Problem 3.2.2: Streamlines and isotherms in terms of Richardson variation,  $Pr = 0.71$ ,  $Re = 100$ ,  $L_s = 0.25$ .

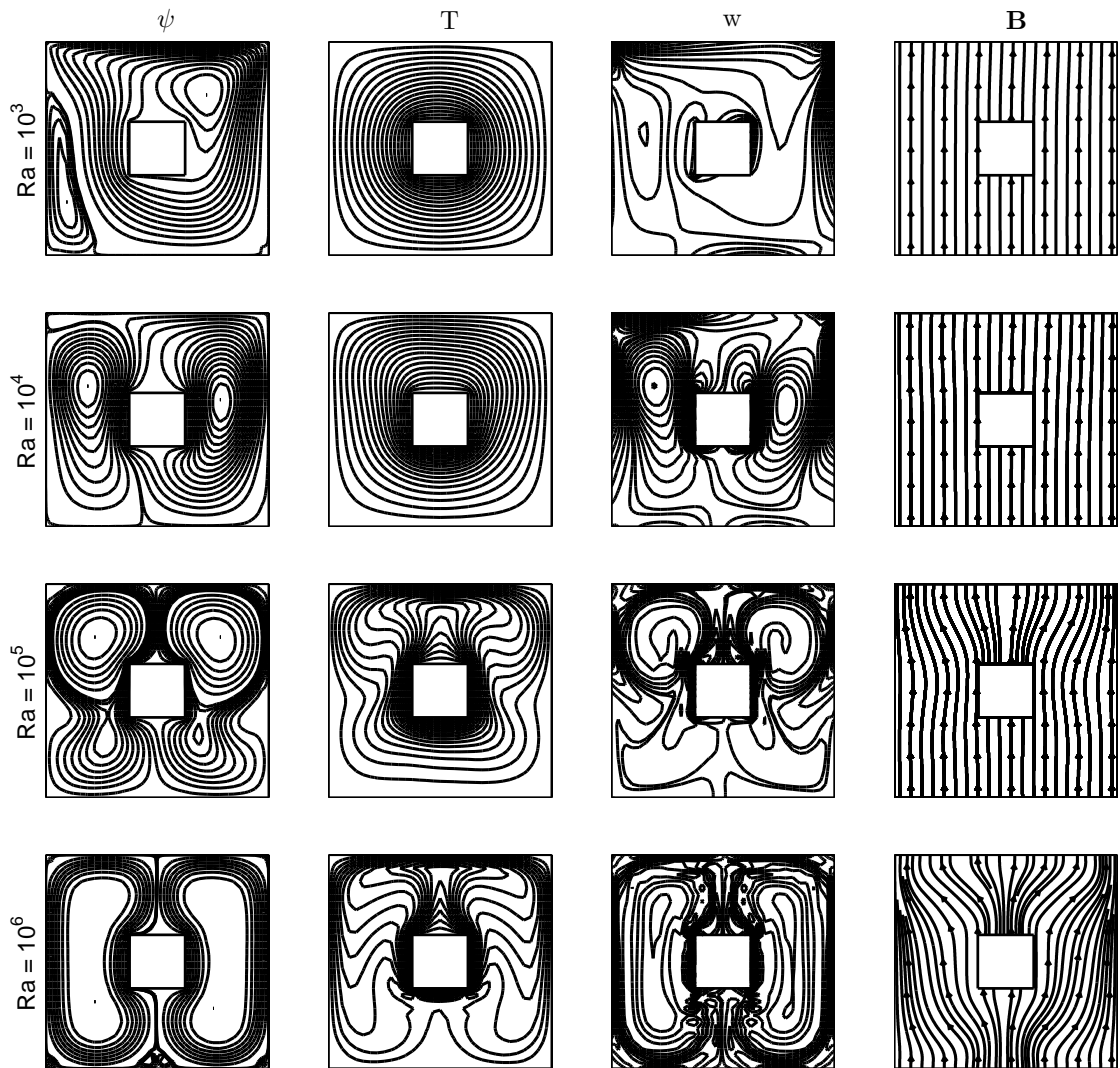


Figure 3.17: Problem 3.2.2:  $Re = 100$ ,  $Rem = 1$ ,  $Ha = 10$ ,  $Pr = 0.1$ ,  $\Delta t = 0.25$  ( $Ra = 10^3$ ,  $Ra = 10^4$ ),  $\Delta t = 0.1$  ( $Ra = 10^5$ ),  $\Delta t = 0.01$  with  $\gamma = 0.1$  ( $Ra = 10^6$ ).

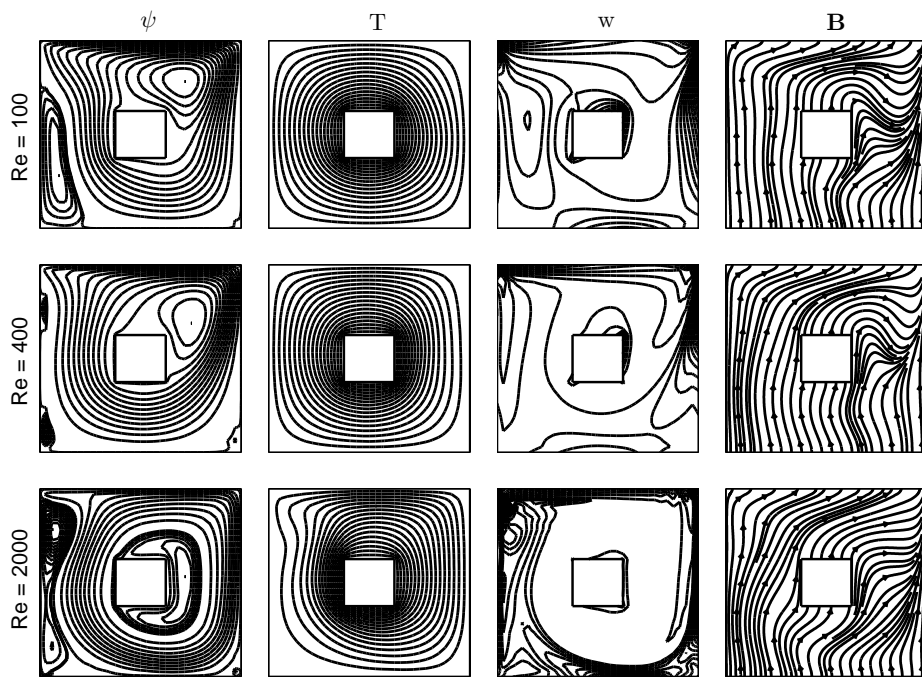


Figure 3.18: Problem 3.2.2:  $Rem = 100$ ,  $Ha = 10$ ,  $Pr = 0.1$ ,  $Ra = 10^3$ ,  $\Delta t = 0.25$  ( $Re = 100, 400, 1000$ ),  $\Delta t = 0.1$  ( $Re = 2500$ ).

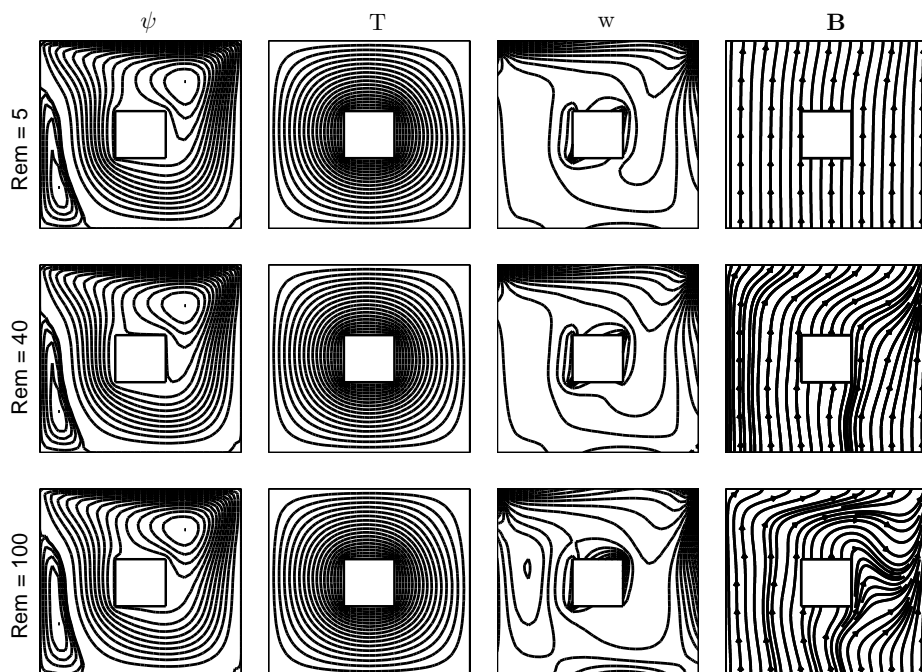


Figure 3.19: Problem 3.2.2:  $Re = 100$ ,  $Ha = 10$ ,  $Pr = 0.1$ ,  $Ra = 10^3$ ,  $\Delta t = 0.25$ .

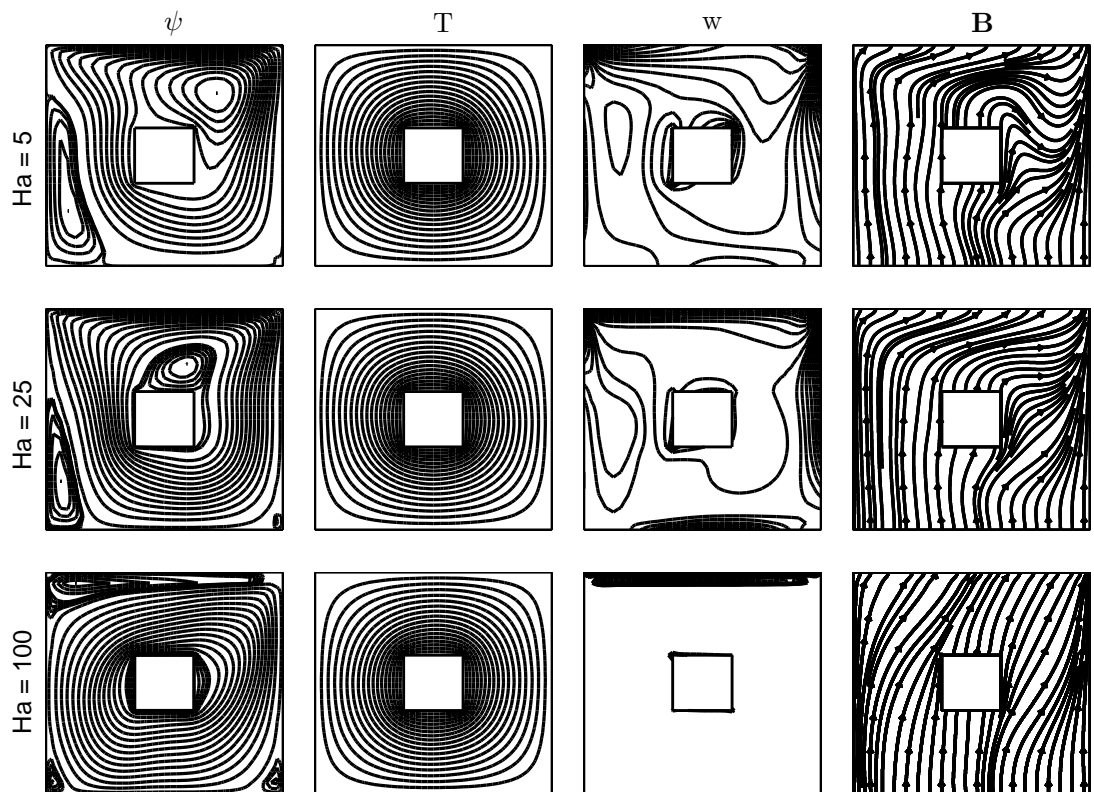
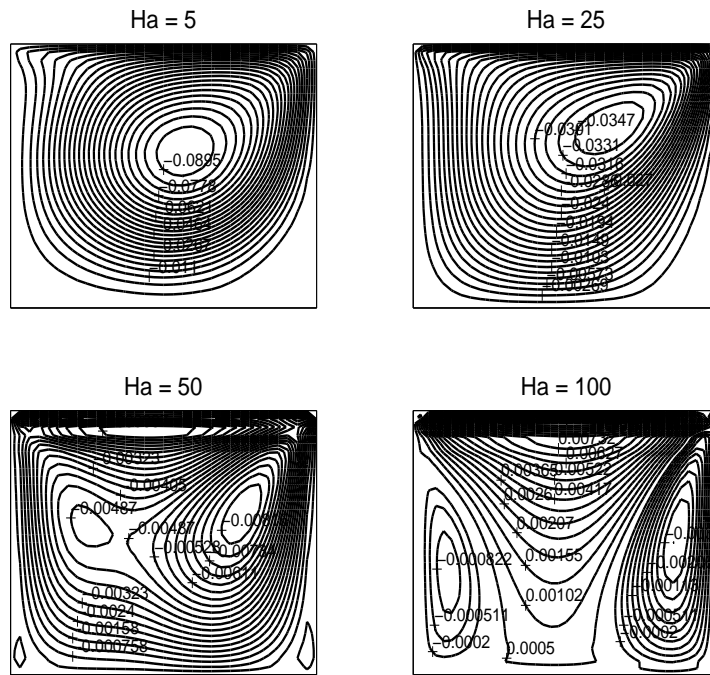
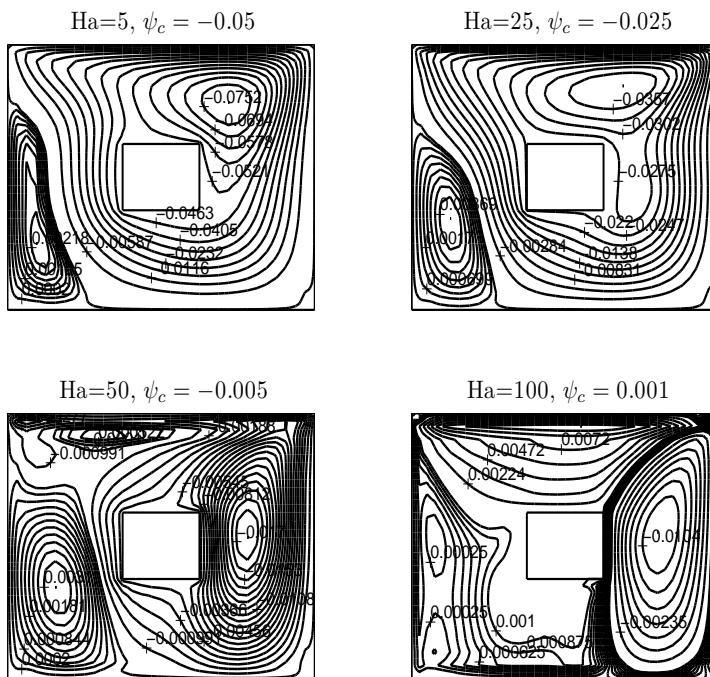


Figure 3.20: Problem 3.2.2:  $Re = Rem = 100$ ,  $Ra = 10^3$ ,  $Pr = 0.1$ ,  $\Delta t = 0.25$  ( $Ha = 5$ ,  $Ha = 25$ ),  $\Delta t = 0.25$  with  $\gamma = 0.5$  ( $Ha = 50$ ),  $\Delta t = 0.1$  with  $\gamma = 0.1$  ( $Ha = 100$ ).





(a) Without Square Blockage



(b) With Square Blockage

Figure 3.21: Problem 3.2.2: Observation on streamlines,  $Re = Rem = 100$ ,  $Ra = 10^3$ ,  $Pr = 0.1$ .

### 3.3 Buoyancy MHD flow with magnetic potential ( $\psi - T - A - j - w$ )

In this section, both the magnetic potential and current density are utilized as unknowns in the full MHD equations with the relations

$$\mathbf{J} = \frac{1}{\mu_m} (\nabla \times \mathbf{B}), \quad j = \frac{1}{\mu_m} \left( \frac{\partial B_y}{\partial x} - \frac{\partial B_x}{\partial y} \right) = -\frac{1}{\mu_m} \nabla^2 A, \quad (3.10)$$

instead of induced magnetic field components. Also, heat transfer mechanism is taken into account.

The governing non-dimensional equations in terms of stream function  $\psi$ , temperature  $T$ , magnetic potential  $A$ , current density  $j$  and vorticity  $w$  are ((Appendix A)) given as

$$\nabla^2 \psi = -w \quad (3.11a)$$

$$\frac{1}{PrRe} \nabla^2 T = \frac{\partial T}{\partial t} + u \frac{\partial T}{\partial x} + v \frac{\partial T}{\partial y} \quad (3.11b)$$

$$\nabla^2 A = -Rem j \quad (3.11c)$$

$$\begin{aligned} \frac{1}{Rem} \nabla^2 j = \frac{\partial j}{\partial t} + u \frac{\partial j}{\partial x} + v \frac{\partial j}{\partial y} - \frac{1}{Rem} \left( B_x \frac{\partial w}{\partial x} + B_y \frac{\partial w}{\partial y} \right) \\ - \frac{2}{Rem} \left[ \frac{\partial B_x}{\partial x} \left( \frac{\partial v}{\partial x} + \frac{\partial u}{\partial y} \right) + \frac{\partial v}{\partial y} \left( \frac{\partial B_x}{\partial y} + \frac{\partial B_y}{\partial x} \right) \right] \end{aligned} \quad (3.11d)$$

$$\frac{1}{Re} \nabla^2 w = \frac{\partial w}{\partial t} + u \frac{\partial w}{\partial x} + v \frac{\partial w}{\partial y} - \frac{Ha^2}{Re} \left( B_x \frac{\partial j}{\partial x} + B_y \frac{\partial j}{\partial y} \right) - \frac{Ra}{PrRe^2} \frac{\partial T}{\partial x} \quad (3.11e)$$

Again, the space derivatives in the inhomogeneous source terms are achieved with the help of coordinate matrix  $\mathbf{F}$ , and the time derivative are discretized by Backward-Euler formula finite difference scheme. The iterative system with the iteration with respect to time occurs as

$$\mathbf{H}\psi^{m+1} - \mathbf{G}\psi_q^{m+1} = -\mathbf{S}w^m \quad (3.12a)$$

$$\left( \mathbf{H} - \frac{PrRe}{\Delta t} \mathbf{S} - PrRe \mathbf{S} \mathbf{M} \right) T^{m+1} - \mathbf{G}T_q^{m+1} = -\frac{PrRe}{\Delta t} \mathbf{S}T^m \quad (3.12b)$$

$$\mathbf{H}A^{m+1} - \mathbf{G}A_q^{m+1} = -Rem \mathbf{S}j^m \quad (3.12c)$$

$$\begin{aligned} \left( \mathbf{H} - \frac{Rem}{\Delta t} \mathbf{S} - Rem \mathbf{S} \mathbf{M} \right) j^{m+1} - \mathbf{G}j_q^{m+1} = -\frac{Rem}{\Delta t} \mathbf{S}j^m - \mathbf{S} \left( [\mathbf{B}_x]_d \mathbf{D}_x + [\mathbf{B}_y]_d \mathbf{D}_y \right) w^m \\ - 2\mathbf{S} \left( \mathbf{D}_x [\mathbf{B}_x]_d (\mathbf{D}_x v^{m+1} + \mathbf{D}_y u^{m+1}) - \mathbf{D}_y [\mathbf{v}]_d (\mathbf{D}_y B_x^{m+1} + \mathbf{D}_x B_y^{m+1}) \right) \end{aligned} \quad (3.12d)$$

$$\begin{aligned} \left( \mathbf{H} - \frac{Re}{\Delta t} \mathbf{S} - Re \mathbf{S} \mathbf{M} \right) w^{m+1} - \mathbf{G}w_q^{m+1} = -\frac{Re}{\Delta t} \mathbf{S}w^m \\ - Ha^2 \mathbf{S} \left( [\mathbf{B}_x]_d \mathbf{D}_x + [\mathbf{B}_y]_d \mathbf{D}_y \right) j^{m+1} - \frac{Ra}{PrRe} \mathbf{S} \mathbf{D}_x T^{m+1} \end{aligned} \quad (3.12e)$$

where  $\mathbf{D}_x = \frac{\partial \mathbf{F}}{\partial \mathbf{x}} \mathbf{F}^{-1}$ ,  $\mathbf{D}_y = \frac{\partial \mathbf{F}}{\partial \mathbf{y}} \mathbf{F}^{-1}$ ,  $\mathbf{S} = \left( \mathbf{H} \hat{\mathbf{U}} - \mathbf{G} \hat{\mathbf{Q}} \right) \mathbf{F}^{-1}$ ,  $\mathbf{M} = [\mathbf{u}]_d \mathbf{D}_x + [\mathbf{v}]_d \mathbf{D}_y$ ,

and the matrices  $[\mathbf{u}]_d, [\mathbf{v}]_d, [\mathbf{B}_x]_d, [\mathbf{B}_y]_d$  are diagonal having the diagonal entries from the vectors  $u^{m+1}, v^{m+1}, B_x^{m+1}, B_y^{m+1}$ , respectively, and are of size  $(N + K) \times (N + K)$ .

Initially,  $T^0, A^0, j^0$  and  $w^0$  are taken accordingly with the given boundary values and as zero at all interior points. The rearranged systems of equations (reducing to the form  $\mathbf{C}\mathbf{x} = \mathbf{b}$ ) (3.12) are solved iteratively with respect to time in the given order. Once the stream function equation (3.12a) and magnetic potential equation (3.12c) are solved, velocity components and induced magnetic field components are computed using their definitions

$$u^{m+1} = \mathbf{D}_y \psi^{m+1}, \quad v^{m+1} = -\mathbf{D}_x \psi^{m+1}, \quad (3.13)$$

$$B_x^{m+1} = \mathbf{D}_y A^{m+1}, \quad B_y^{m+1} = -\mathbf{D}_x A^{m+1}, \quad (3.14)$$

and the coordinate matrix  $\mathbf{F}$  gives rise to  $\mathbf{D}_x$  and  $\mathbf{D}_y$ . Then, boundary conditions for the velocity and the induced magnetic field components are inserted. Unknown boundary conditions for current density  $j$  and vorticity  $w$  are found again by using DRBEM coordinate matrix  $\mathbf{F}$  in their definitions as

$$j = \frac{1}{Rem} (\mathbf{D}_x B_y^{m+1} - \mathbf{D}_y B_x^{m+1}) \quad (3.15a)$$

$$w = \mathbf{D}_x v^{m+1} - \mathbf{D}_y u^{m+1}. \quad (3.15b)$$

The iterative solution process continues up to the steady-state solution with the criterion

$$\sum_{l=1}^5 \frac{\|\phi_l^{m+1} - \phi_l^m\|_\infty}{\|\phi_l^{m+1}\|_\infty} < \epsilon \quad (3.16)$$

satisfied with a tolerance  $\epsilon = 1e - 4$  where  $\phi_l$  stands for  $\psi, T, j, A$  and  $w$  values at the boundary and interior points, respectively.

In order to validate the presented numerical procedure, the problem is reduced to the form (taking  $Re = 1/Pr$ ) of the study [38] (in which horizontal walls are adiabatic, left wall is the hot wall, right wall is the cold wall, and the velocity is zero on the walls) and solved by DRBEM. Table 3.4 shows the good agreement of the presented results (obtained by at most  $N = 112, K = 961$ ) with the study [38] (in which the given results in this table are obtained by  $41 \times 41$  mesh size).

Table 3.4: Average Nusselt number through the heated left wall.

Ra	Present	[38]
$10^3$	1.114	1.116
$10^4$	2.241	2.242
$10^5$	4.556	4.564

Numerical results are depicted as streamlines, isotherms, magnetic potential (induced magnetic field) lines, current density, and vorticity contours. Two types of geometry are used which are staggered double lid-driven cavity and backward-facing step in order to observe the flow separation which occurs with a sudden change in the channel. For approximating function  $f$ ,  $1 + r$  is fixed together with the 20-point Gaussian quadrature for the integrals in BEM matrices  $\mathbf{H}$  and  $\mathbf{G}$ .

Table 3.5: Problem 3.3.1: Analyzing the grid independence.

N	K	$\overline{Nu}$		
		Ha=25	Ha=50	Ha=100
84	328	1.8483	2.1466	2.3070
112	601	1.9037	2.2094	2.3878
140	956	1.9272	2.2326	2.4263
168	1393	1.9370	2.2390	2.4438

### 3.3.1 Case 1. Staggered double lid-driven cavity MHD flow

The flow is driven down the channel by means of a pressure gradient  $\nabla p$ , and the fluid action is maintained with the movements of the top and bottom walls of the cavity in the opposite directions. Externally applied magnetic field influences the flow in the cavity by means of Lorentz force in the momentum equations, and electrically conducting fluid in turn produces induced magnetic field inside of the cavity. Heat transfer in the fluid due to the cold and hot walls is coupled to the momentum equations with the buoyancy force. Thus, the flow is visualized in terms of stream function and vorticity, heat exchange with the temperature of the fluid, and the induced magnetic field with the magnetic potential and current density, respectively.

The problem configuration is illustrated in Figure 3.22 [95]. Stream function and velocity component  $v$  are all zero on the walls.  $u = 1$  on the top wall and  $u = -1$  on the bottom wall. The jagged walls are adiabatic ( $\partial T/\partial n = 0$ ), the top wall is the hot wall  $T_h = 0.5$  and the bottom wall is the cold wall  $T_c = -0.5$ . Magnetic potential is  $A = -x$  on the walls due to the  $y$ -component of external magnetic field  $\mathbf{B} = (0, B_0, 0)$  with  $B_0 = 1$ ,  $h_z = 0.4$ .

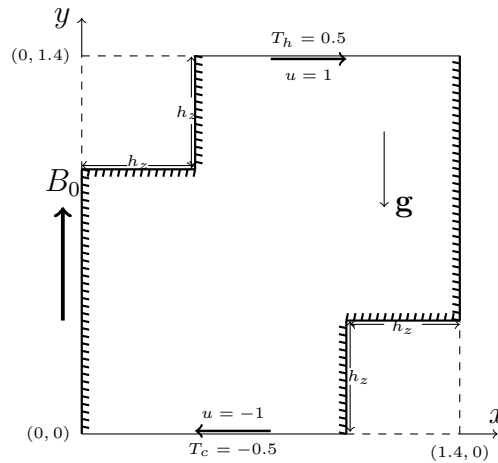


Figure 3.22: Problem 3.3.1: Staggered double lid-driven cavity.

As can be seen from Table 3.5, average Nusselt number does not change much for  $N > 140$ . Therefore,  $N = 140$  boundary elements with  $K = 956$  interior nodes are used in all computations of this case. In order to accelerate the convergence for large

values of parameters, once the vorticity equation Eq.(3.12e) is solved, a relaxation parameter  $0 < \gamma < 1$  is used as  $w^{m+1} \leftarrow \gamma w^{m+1} + (1 - \gamma)w^m$ . Moreover, the average Nusselt number at the hot top wall is computed from  $\overline{Nu}_t = \int_{0.4}^{1.4} \frac{\partial T}{\partial y} \Big|_{y=1.4} dx$  using composite Trapezoidal rule (Appendix B).

As  $Re$  increases (Figure 3.23), twin primary eddies in the flow pattern turn out to be one main circulation at the center of cavity. Temperature gradient increases through the top and bottom walls pointing to the increase in convection in isotherms. Symmetric behavior in magnetic potential lines in staggered channels is combined to a uniform behavior. Strong boundary layer formation in the vorticity and current density through the moving walls is seen with an increase in  $Re$ .

With the increase in  $Rem$  (Figure 3.24), the main alteration is observed in magnetic potential lines and current density. Since the effect of diffusion terms weakened in these equations, new cells at the lower left and upper right corners emerge. Not much of a variation in vorticity occurs while counter-clockwise symmetric cells in streamlines start to be formed.

As  $Ha$  increases up to 100 (Figure 3.25), the center of the streamlines rotate in counter-clockwise direction trying to form Hartmann and boundary layers. The formation of the strong temperature gradient shows the increase in convective heat transfer. Current density and vorticity contours have the similar behavior which is the clustering through the moving walls and stagnancy at the center. Magnetic potential stays the same since  $Rem$  is not changed.

Since the MHD flow in the cavity is mostly influenced with the electrical conductivity and magnetic permeability of the fluid, the flow and magnetic potential behaviors depend on the variations of  $Ha$  and  $Rem$  values. In figures 3.26-3.27 the variations of  $Rem$  and  $Ha$  are investigated together on streamlines and magnetic potential lines. For a small value of  $Ha$  ( $Ha = 5$ ), although four symmetric cells are formed in streamlines, these cells are diminished and become one main primary cell from one inner corner to the other inner corner as  $Rem$  increases (Figure 3.26). Boundary layer formation through the moving walls and corner walls is observed as  $Ha$  increases. This may be due to the increase in velocity up to  $Ha = 100$ . While the symmetric cells in magnetic potential lines become prominent as increasing  $Rem$  with  $Ha = 5$  (Figure 3.27), the increase in  $Ha$  suppresses this symmetric circulative nature of magnetic potential lines and force them to be directed in its direction. In other words, magnetic potential obeys the direction of external magnetic field as  $Ha$  increases.

Counter-rotating cells (counter clockwise center cell and clockwise top and bottom cells), and the motion of moving lids become prominent in streamlines as  $Ra$  increases (Figure 3.28). This is an increase in buoyancy which results in a stronger primary eddy, and upper and lower secondary eddies near the moving lids balancing the effect of shear force due to the movement of the lids. Isotherms become perpendicular to the vertical walls due to the increase in buoyancy effect. The circulation of vorticity through the moving lids is shrunk and intensified through the top and bottom walls being stagnant at the center. The top and bottom small cells of current density

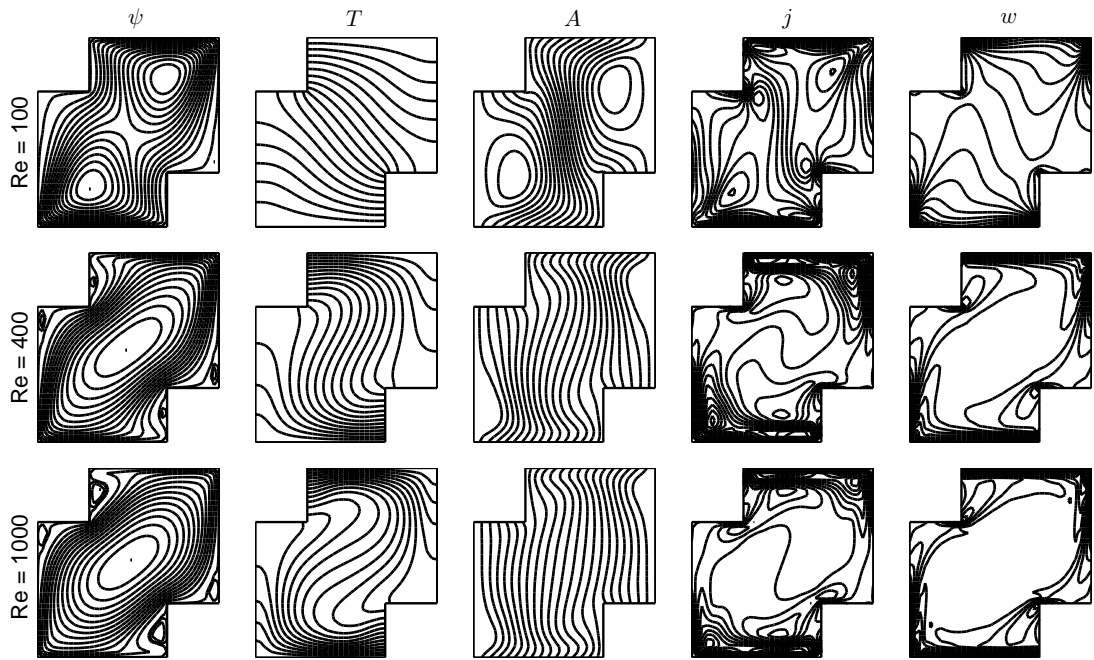


Figure 3.23: Problem 3.3.1:  $Rem = 100$ ,  $Ha = 10$ ,  $Ra = 10$ ,  $Pr = 0.1$ ,  $\Delta t = 0.2$ .

with  $Ra = 10^3$  are expanded with the increase in  $Ra$  while inner corner cells almost disappear.

The average Nusselt number at the hot top wall is analyzed in Figure 3.29. As  $Ha$  increases, convection dominated effect in  $\overline{Nu}_t$  is pronounced up to  $Ha \leq 100$  in Fig.3.29a ( $Rem = 10$ ,  $Re = 400$ ,  $Pr = 0.1$ ,  $Ra = 10^3$ ). This may be due to the opposite motions of top and bottom lids. The increase in  $Rem$  ( $Ha = 10$ ,  $Re = 400$ ,  $Pr = 0.1$ ,  $Ra = 10^3$ ) points to the decrease in mean Nusselt number through the hot top wall (Fig.3.29b) which means that the convection decreases with the increase in magnetic Reynolds number. This is due to the increase in intensity of induced magnetic field weakening the fluid motion.

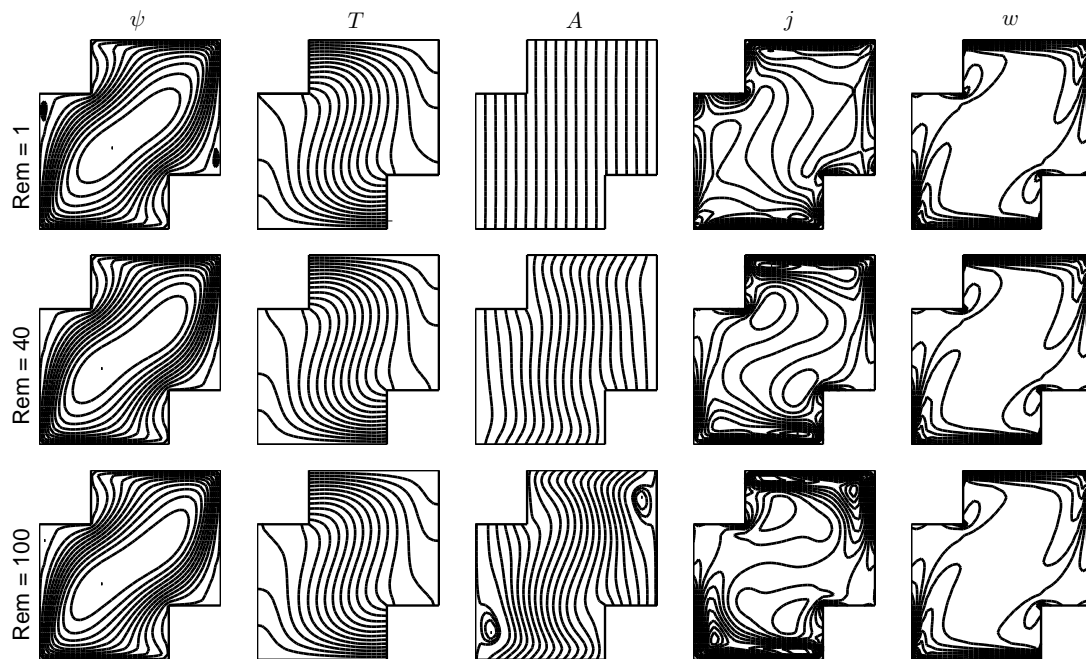


Figure 3.24: Problem 3.3.1:  $Re = 400$ ,  $Ha = 10$ ,  $Ra = 10^3$ ,  $Pr = 0.1$ ,  $\Delta t = 0.01, 0.1, 0.1$ .

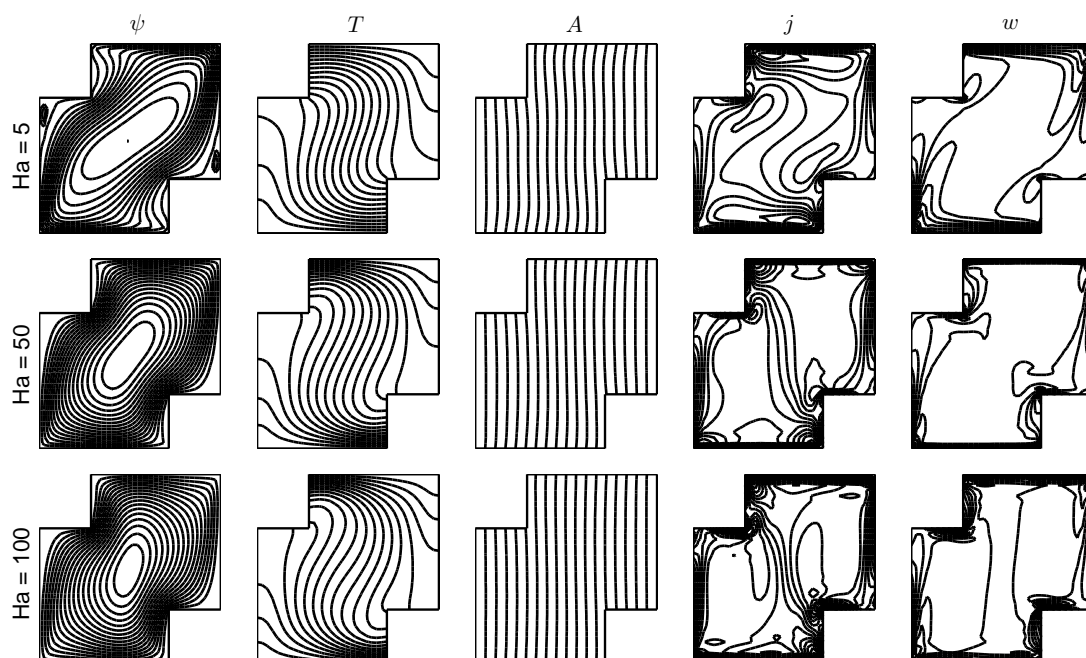


Figure 3.25: Problem 3.3.1:  $Re = 400$ ,  $Rem = 10$ ,  $Ra = 10^3$ ,  $Pr = 0.1$ ,  $\Delta t = 0.1(Ha = 5, 50)$ ,  $\Delta t = 0.1$  with  $\gamma = 0.5(Ha = 100)$ .

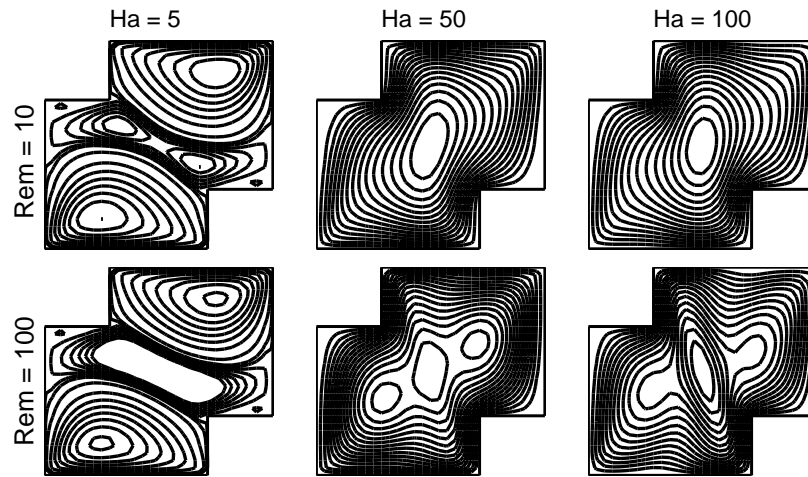


Figure 3.26: Problem 3.3.1: Streamlines  $Re = 100$ ,  $Pr = 0.1$ ,  $Ra = 10^3$ .

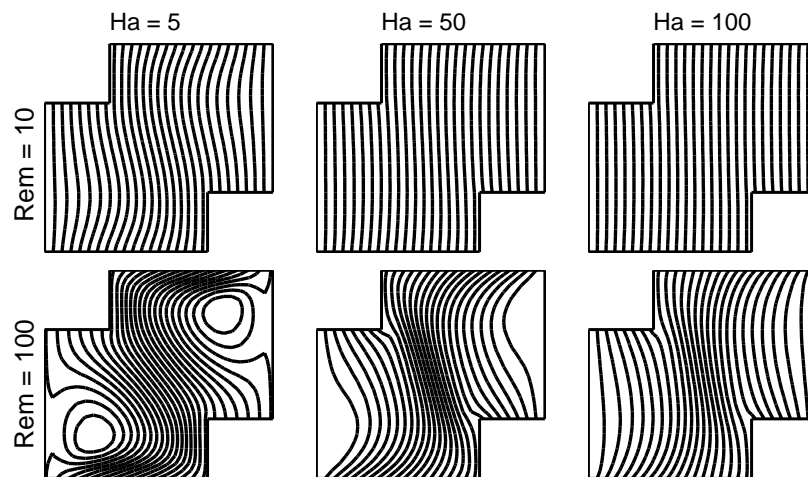


Figure 3.27: Problem 3.3.1: Magnetic potential  $Re = 100$ ,  $Pr = 0.1$ ,  $Ra = 10^3$



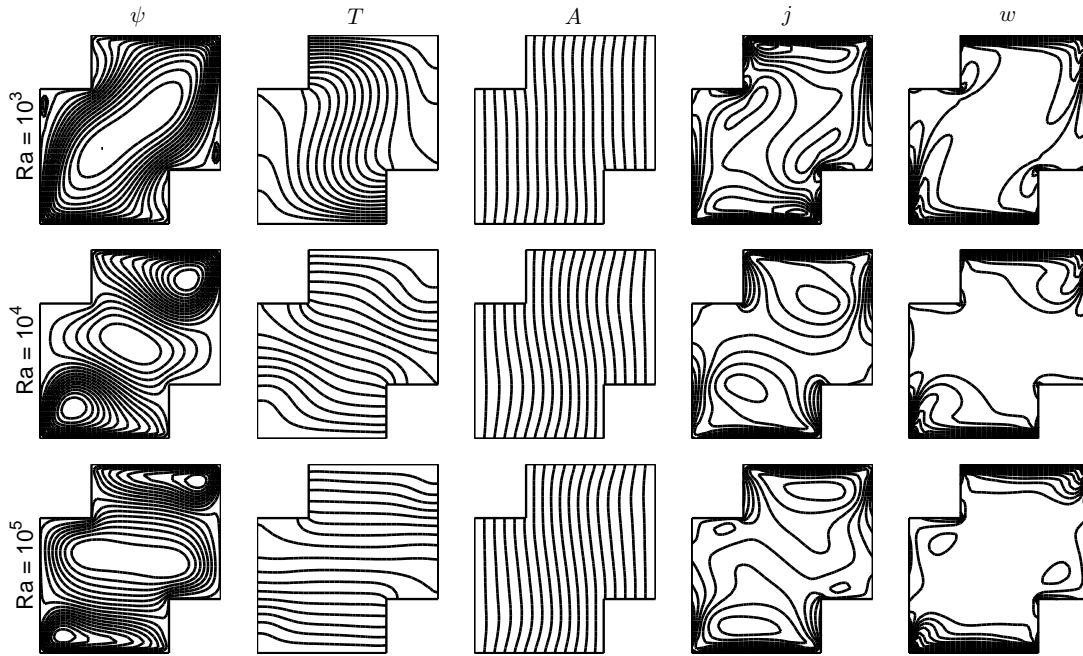


Figure 3.28: Problem 3.3.1:  $Re = 400$ ,  $Rem = Ha = 10$ ,  $Pr = 0.1$ ,  $\Delta t = 0.1$ .

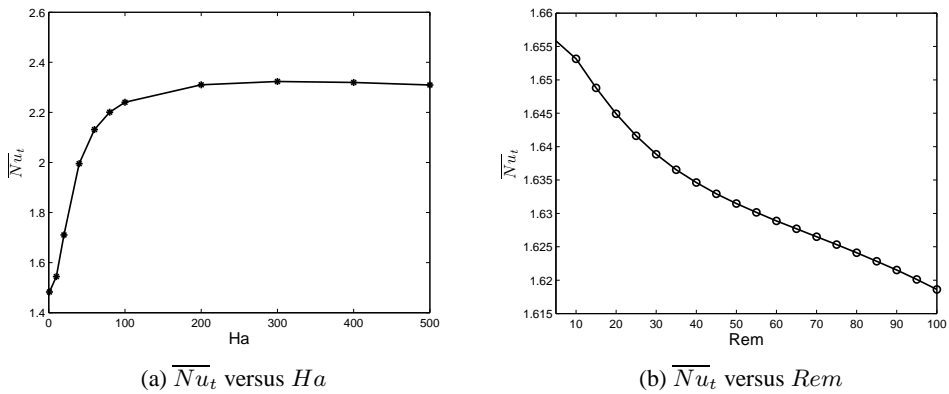


Figure 3.29: Problem 3.3.1:  $\overline{Nu}_t$  at the hot top wall is observed w.r.t  $Ha$  and  $Rem$ .

### 3.3.2 Case 2. Backward facing step MHD flow

MHD flow in a channel with a backward-facing step is considered as depicted in Figure 3.30. The flow is in  $x$ -direction prescribed with a parabolic profile at the inlet. Applied magnetic field is through  $+y$ -direction ( $B_0 = 1$ ), thus  $A = -x$  everywhere on the boundary. A heater is placed on the step, and temperature distribution decreases linearly through the walls. The top and bottom walls of the channel are cold. Exit condition ( $\partial/\partial n = 0$ ) is applied for unknowns  $\psi, T, j$  and  $w$ .

In general,  $N = 200$  linear boundary elements with  $K = 1421$  interior points, and  $\Delta t = 0.1$  are used in the computations. In order to accelerate the convergence for large values of  $Ha$  or  $Rem$ , a relaxation parameter  $0 < \gamma < 1$  is employed in vorticity as  $w^{m+1} \leftarrow \gamma w^{m+1} + (1 - \gamma)w^m$  or current density as  $j^{m+1} \leftarrow \gamma j^{m+1} + (1 - \gamma)j^m$ , respectively. The length of the channel is taken as  $\ell = 10$ . Furthermore, the vorticity boundary condition at the inlet of BFS is computed from  $w = -\nabla^2\psi$  while Eq.(3.15b) is made use of on the other boundaries, and the current density boundary conditions are computed from Eq.(3.15a) except at the exit of the channel.

Numerical results are validated with the incompressible fluid flow and the natural convection MHD flow in terms of streamlines. Reattachment length after the step increases as  $Re$  increases and the formation of secondary vortex at the upper wall is seen from  $Re = 500$  onwards (Figure 3.31) which is consistent with the study [73]. For increasing values of  $Ra$  ( $10^2 - 10^5$ ) with  $Pr = 0.71$  and  $\ell = 4$  (Figure 3.32), the recirculation region expands with the increase in  $Ra$ , and new vortexes are formed above the heater as in [10].

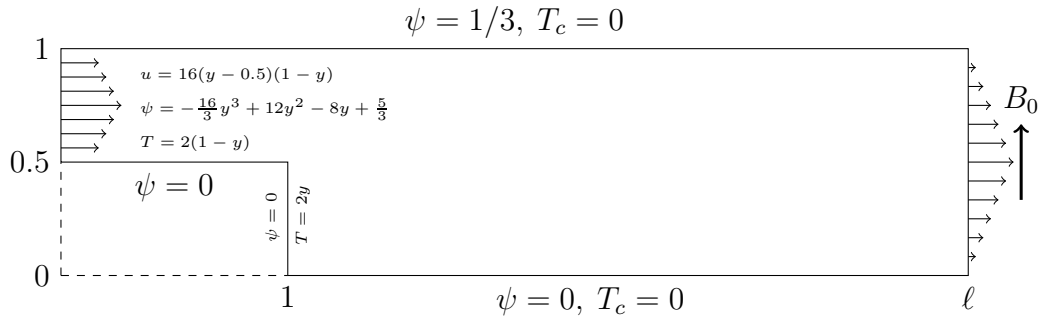


Figure 3.30: Problem 3.3.2: Backward facing step MHD flow configuration.

As  $Re$  increases (Figure 3.33), reattachment length (the distance from the step to the reattachment point) increases. Isotherms cover almost all the cavity due to the dominance of convection terms in energy equation. Magnetic potential lines is not affected much. Current density spreads along the channel forming boundary layers on the top and bottom walls. Vorticity shows similar behavior with streamlines.

With the increase in  $Ha$  (Figure 3.34), reattachment length decreases, and almost disappears with  $Ha = 50$ . This is due to retarding effect of Lorentz force. Since the top and bottom walls are cold walls, not much variation is seen on isotherms while  $Ha$

varies. The increasing strength of the applied magnetic field directs the magnetic potential lines to its direction, and make them nearly perpendicular to the top and bottom walls. Current density and vorticity form the strong boundary layers (Hartmann layers) through the top and bottom walls, and they are stagnant at the center.

As expected, the variation of  $Rem$  (Figure 3.35) affects the magnetic potential lines (induced magnetic field lines) and current density lines. While magnetic potential lines are almost perpendicular to the top and bottom walls, perturbation on them increases with large values of  $Rem$ . Similar perturbed movement on the current density through the center of the region is observed. The strong boundary layer formations on the top and bottom walls are also seen in current density. These developments are due to the decrease in the effect of diffusion terms in magnetic potential and current density equations. For large values of  $Ha$  and  $Rem$ , one needs to use relaxation parameters especially for vorticity and current density due to the great alterations in their behaviors.

The vortex after the step is expanded, and a new secondary cell emerges close to this vortex as  $Ra$  gets larger (Figure 3.36). Since the buoyancy effect increases with the increase in  $Ra$ , fluid velocity also increases. The terms with Rayleigh number are reaction terms in vorticity equation, and thus an effect on vorticity is also seen for large values of  $Ra$ , so is in current density. Magnetic potential lines tend to form new circulated cells after the step with the increase in  $Ra$ . This may be due to the dominance of buoyancy effect on vorticity, and so on current density and magnetic potential. This points that the increase in buoyancy force affects the magnetic potential lines.

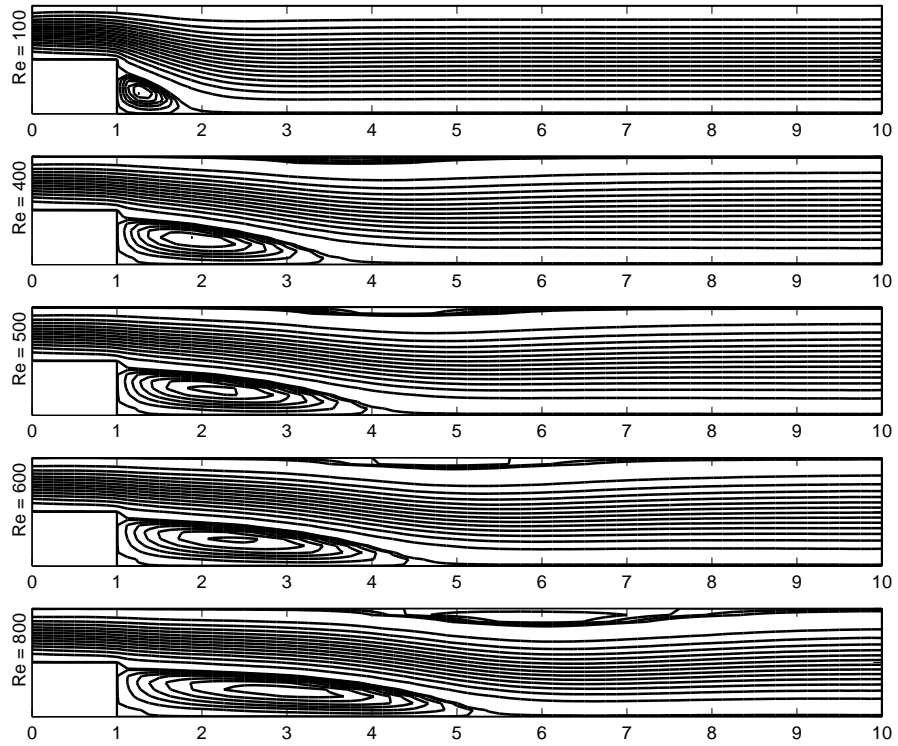


Figure 3.31: Problem 3.3.2: Streamlines in BFS for incompressible fluid flow for varying  $Re$ .

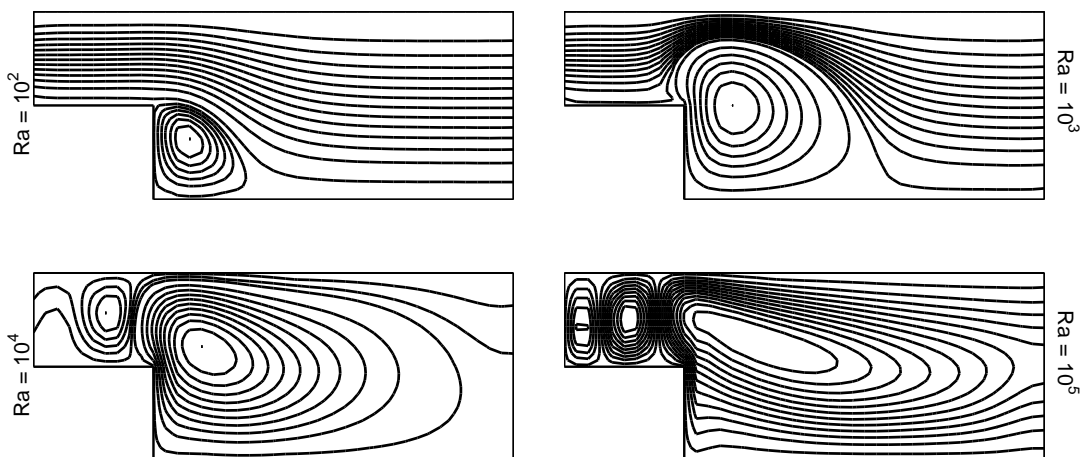


Figure 3.32: Problem 3.3.2: Streamlines in natural convection flow varying  $Ra$ .

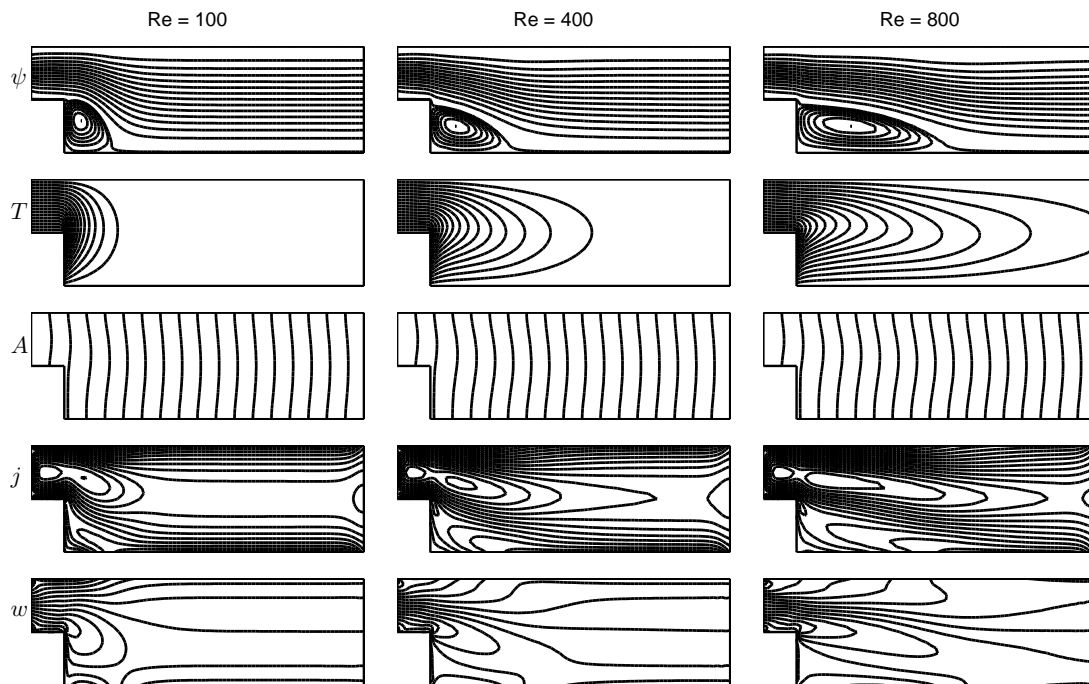


Figure 3.33: Problem 3.3.2:  $Rem = 10$ ,  $Ha = 5$ ,  $Ra = 10^3$ ,  $Pr = 0.1$ .

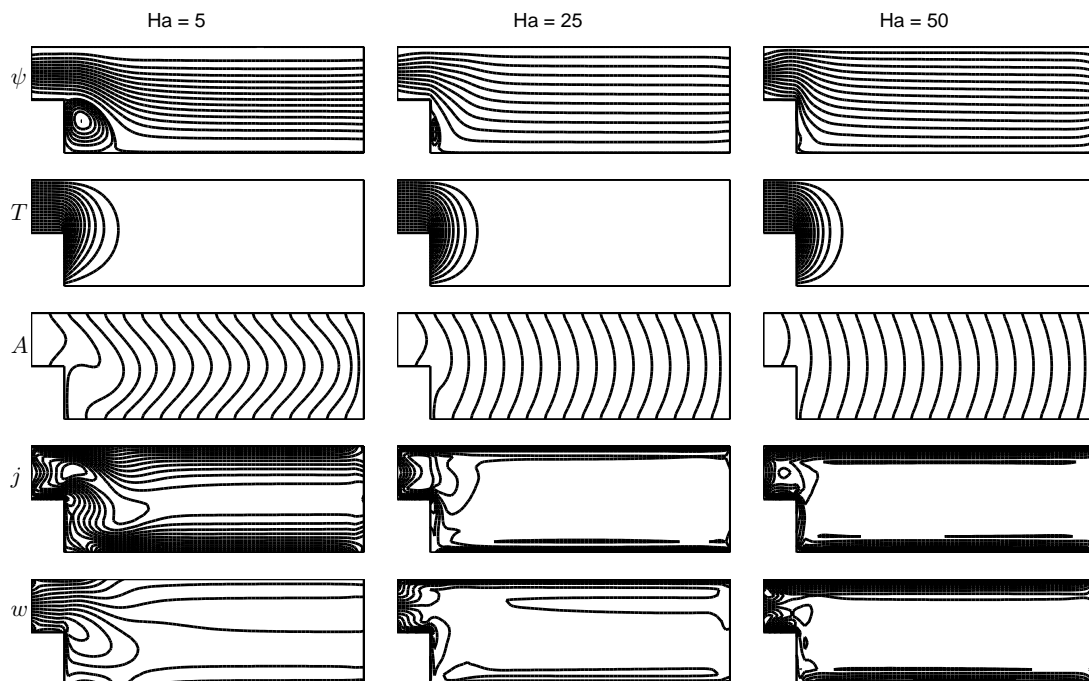


Figure 3.34: Problem 3.3.2:  $Re = Rem = 100$ ,  $Ra = 10^3$ ,  $Pr = 0.1$

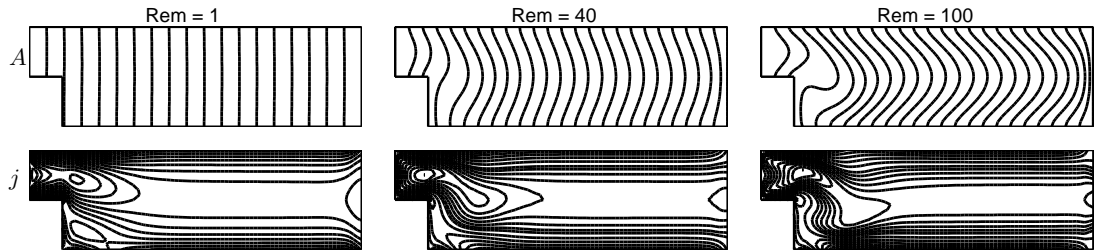


Figure 3.35: Problem 3.3.2:  $Re = 100$ ,  $Ha = 5$ ,  $Ra = 10^3$ ,  $Pr = 0.1$ .

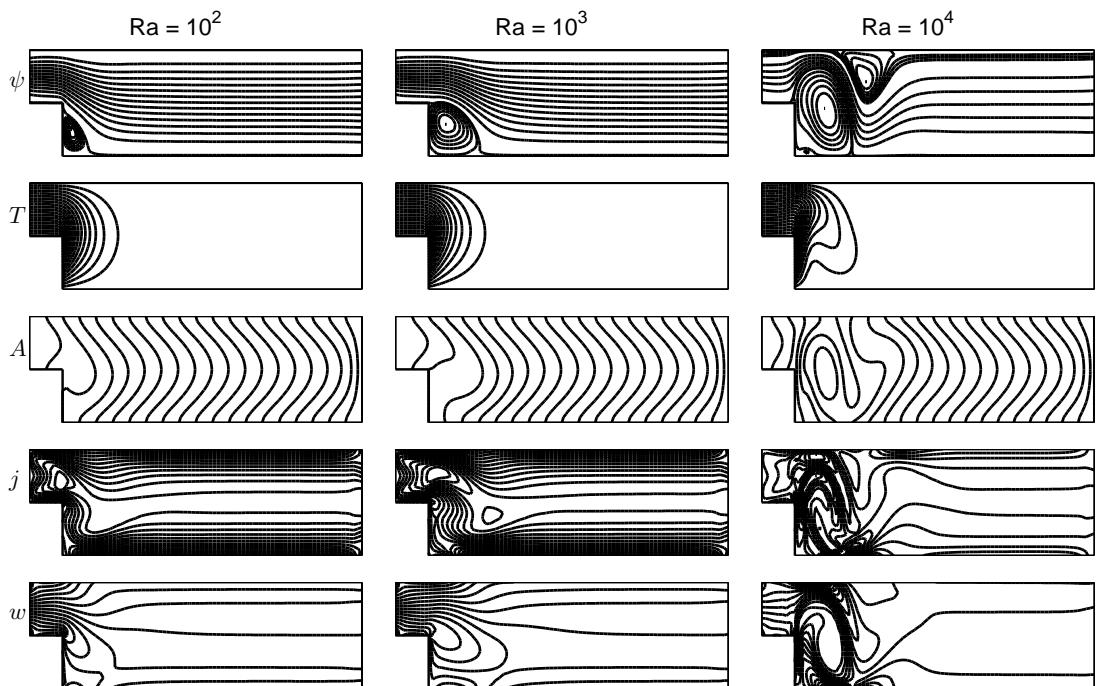


Figure 3.36: Problem 3.3.2:  $Re = Rem = 100$ ,  $Ha = 5$ ,  $Pr = 0.1$

### 3.4 Incompressible MHD flow with magnetic potential ( $\psi - A - w$ )

In this case, the temperature difference does not exist. Therefore, the momentum equations do not contain the buoyant term. Further, the magnetic potential  $A$  is taken into account instead of induced magnetic field components.

The two-dimensional, laminar MHD flow of an incompressible, viscous and electrically conducting fluid is considered adopting magnetic potential. The non-dimensional governing equations in terms of stream function  $\psi$ , vorticity  $w$ , and magnetic potential  $A$  are (Chapter 1, section 1.1.5, Appendix A)

$$\nabla^2 \psi = -w \quad (3.17a)$$

$$\frac{1}{Rem} \nabla^2 A = \frac{\partial A}{\partial t} + u \frac{\partial A}{\partial x} + v \frac{\partial A}{\partial y} \quad (3.17b)$$

$$\begin{aligned} \frac{1}{Re} \nabla^2 w = & \frac{\partial w}{\partial t} + u \frac{\partial w}{\partial x} + v \frac{\partial w}{\partial y} \\ & - \frac{Ha^2}{ReRem} \left[ B_x \frac{\partial}{\partial x} \left( \frac{\partial B_y}{\partial x} - \frac{\partial B_x}{\partial y} \right) + B_y \frac{\partial}{\partial y} \left( \frac{\partial B_y}{\partial x} - \frac{\partial B_x}{\partial y} \right) \right], \end{aligned} \quad (3.17c)$$

where the dimensionless parameters are the Reynolds number  $Re = UL/\nu$ , the magnetic Reynolds number  $Rem = UL\sigma\mu_m$ , and the Hartmann number  $Ha = B_0L\sqrt{\sigma/\mu}$ .

By using coordinate matrix  $\mathbf{F}$  for evaluating the space derivatives in non-homogeneous terms  $\mathbf{b}$  and the Backward-Euler formula for the time derivatives, the iteration with respect to time is carried between the system of equations for  $\psi$ ,  $A$  and  $w$  as

$$\mathbf{H}\psi^{m+1} - \mathbf{G}\psi_q^{m+1} = -\mathbf{S}w^m \quad (3.18a)$$

$$u^{m+1} = \mathbf{D}_y\psi^{m+1}, \quad v^{m+1} = -\mathbf{D}_x\psi^{m+1} \quad (3.18b)$$

$$\left( \mathbf{H} - \frac{Rem}{\Delta t} \mathbf{S} - Rem \mathbf{S} \mathbf{M} \right) A^{m+1} - \mathbf{G}A_q^{m+1} = -\frac{Rem}{\Delta t} \mathbf{S}A^m \quad (3.18c)$$

$$B_x^{m+1} = \mathbf{D}_y A^{m+1}, \quad B_y^{m+1} = -\mathbf{D}_x A^{m+1} \quad (3.18d)$$

$$\left( \mathbf{H} - \frac{Re}{\Delta t} \mathbf{S} - Re \mathbf{S} \mathbf{M} \right) w^{m+1} - \mathbf{G}w_q^{m+1} = -\frac{Re}{\Delta t} \mathbf{S}w^m \quad (3.18e)$$

$$- \frac{Ha^2}{Rem} \mathbf{S} \left( [\mathbf{B}_x]_d \mathbf{D}_x \xi + [\mathbf{B}_y]_d \mathbf{D}_y \xi \right)$$

where

$$\mathbf{S} = \left( \mathbf{H}\hat{\mathbf{U}} - \mathbf{G}\hat{\mathbf{Q}} \right) \mathbf{F}^{-1}, \quad \mathbf{D}_x = \frac{\partial \mathbf{F}}{\partial \mathbf{x}} \mathbf{F}^{-1}, \quad \mathbf{D}_y = \frac{\partial \mathbf{F}}{\partial \mathbf{y}} \mathbf{F}^{-1}$$

$$\mathbf{M} = [\mathbf{u}]_d \mathbf{D}_x + [\mathbf{v}]_d \mathbf{D}_y, \quad \xi = \left( \mathbf{D}_x B_y^{m+1} - \mathbf{D}_y B_x^{m+1} \right),$$

and the diagonal matrices  $[\mathbf{u}]_d$ ,  $[\mathbf{v}]_d$ ,  $[\mathbf{B}_x]_d$ ,  $[\mathbf{B}_y]_d$  are formed using the vectors  $u^{m+1}$ ,  $v^{m+1}$ ,  $B_x^{m+1}$ ,  $B_y^{m+1}$ . Once the shuffling of known and unknown nodal values is done, the reduced systems of the form  $\mathbf{C}\mathbf{x} = \mathbf{b}$  are solved by Gaussian elimination with partial pivoting.

Initially,  $w^0$  and  $A^0$  are taken as zero everywhere except on the boundary. Stream function Eq.(3.18a) is solved using  $m$ th time level values of vorticity  $w$ . The velocity components are computed by using Eq.(3.18b), and then their boundary conditions are inserted. The magnetic potential at  $(m + 1)$ th time level is found using Eq.(3.18c). Then, the induced magnetic field components are obtained from Eq.(3.18d), and the insertion of their boundary conditions is carried out. Vorticity boundary conditions are found by using the definition of vorticity with the help of coordinate matrix  $\mathbf{F}$

$$w = \nabla \times \mathbf{u} = \mathbf{D}_x v - \mathbf{D}_y u = \frac{\partial \mathbf{F}}{\partial \mathbf{x}} \mathbf{F}^{-1} v - \frac{\partial \mathbf{F}}{\partial \mathbf{y}} \mathbf{F}^{-1} u. \quad (3.19)$$

Using these boundary conditions for  $w$ , vorticity equation (3.18e) is solved at the  $(m + 1)$ th time level. Iteration continues in this way until the criterion

$$\frac{\|\psi^{m+1} - \psi^m\|_\infty}{\|\psi^{m+1}\|_\infty} + \frac{\|A^{m+1} - A^m\|_\infty}{\|A^{m+1}\|_\infty} + \frac{\|w^{m+1} - w^m\|_\infty}{\|w^{m+1}\|_\infty} < \epsilon \quad (3.20)$$

is satisfied where  $\epsilon = 1e - 4$  is the tolerance for the steady-state solution  $\psi$ ,  $A$  and  $w$ , respectively. Transient level solutions can also be obtained at any time value  $t_m = m\Delta t$ .

In the numerical computations, the radial basis functions are chosen as  $f = 1 + r$ . Further, 16-point Gaussian quadrature is used for the integrals in  $\mathbf{H}$  and  $\mathbf{G}$  matrices. In order to validate the present method, the  $|\psi_{\min}|$  values for an incompressible flow in a lid-driven cavity are given in Table 3.6. As can be seen, the results using considerably small number of grid points are in good agreement with the results given in [62].

Table 3.6: Problem 3.4:  $|\psi_{\min}|$  values of streamlines of Navier-Stokes flow in a lid-driven cavity.

Re	Present		[62]	
	Mesh pts.	$ \psi_{\min} $	Mesh pts.	$ \psi_{\min} $
100	$17 \times 17$	0.1034	$129 \times 129$	0.1034
400	$41 \times 41$	0.1135	$257 \times 257$	0.1139
1000	$55 \times 55$	0.1140	$129 \times 129$	0.1179

### 3.4.1 Case 1. Lid-driven cavity MHD flow

The problem geometry is given in Figure 3.37. Stream function and velocity component  $v$  are all zero on the walls, and the top wall is moving with a velocity  $u = 1$ . Magnetic potential is  $A = -x + C'$  on the walls due to the  $y$ -component of external magnetic field  $B_0 = (0, B_0, 0) = (0, 1, 0)$ , and the constant  $C'$  is taken as zero similar to the stream function on the boundary. In general, 120 linear boundary elements and 841 interior points are used for this case. Since implicit time integration scheme is used, time increment  $\Delta t$  can be taken not too small.

The center of streamlines which is in the direction of moving lid for small  $Re$  numbers shifts through the center of the cavity forming new eddies at the lower corners of the



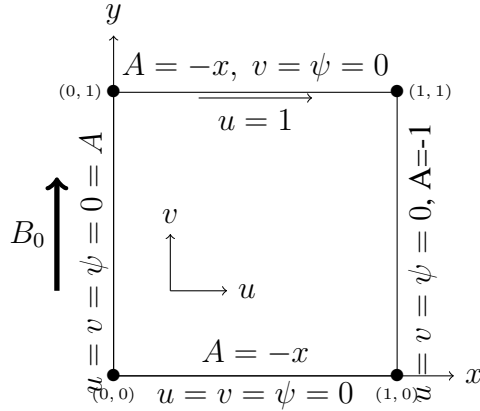


Figure 3.37: Problem 3.4.1: Configuration of the lid-driven cavity MHD flow.

cavity as  $Re$  increases. The circulation of vorticity is pronounced for large values of  $Re$ . These are the expected behaviors for a lid-driven cavity MHD flow for fixed  $Rem$  and  $Ha$  as can be seen from Figure 3.38. Magnetic potential lines are not affected much with the variation of  $Re$ .

The variation in magnetic Reynolds number causes the magnetic potential lines to circulate inside the cavity due to the dominance of convection terms in magnetic potential equation as  $Rem$  gets larger. Not much alteration occurs in streamlines and vorticity (Figure 3.39) to steady-state.

Vorticity becomes stagnant at the center clustering through the walls as  $Ha$  increases (Figure 3.40). Thin boundary layers (side layers) and Hartmann layers, respectively, on perpendicular and parallel walls to the direction of  $B_0$ , are well observed with an increase in  $Ha$  in streamlines. Magnetic potential lines become perpendicular to the top and bottom walls pointing to the decrease in convection terms of magnetic potential equation due to the decrease in velocities, and also, they obey the direction of the externally applied magnetic field as  $Ha$  increases. Since the reaction term dominates in vorticity transport equation for large value of  $Ha = 100$ , a relaxation parameter  $0 < \gamma = 0.1 < 1$  is used as  $w^{m+1} = \gamma w^{m+1} + (1 - \gamma)w^m$  to accelerate the convergence of vorticity.

The magnitude of the velocity of the fluid decreases due to the retarding effect of Lorentz force in the presence of high magnetic field intensity  $B_0$ . This is confirmed by the centerline velocity components as  $Ha$  increases in Figure 3.41. This is the well-known flattening tendency of the MHD flow [141].

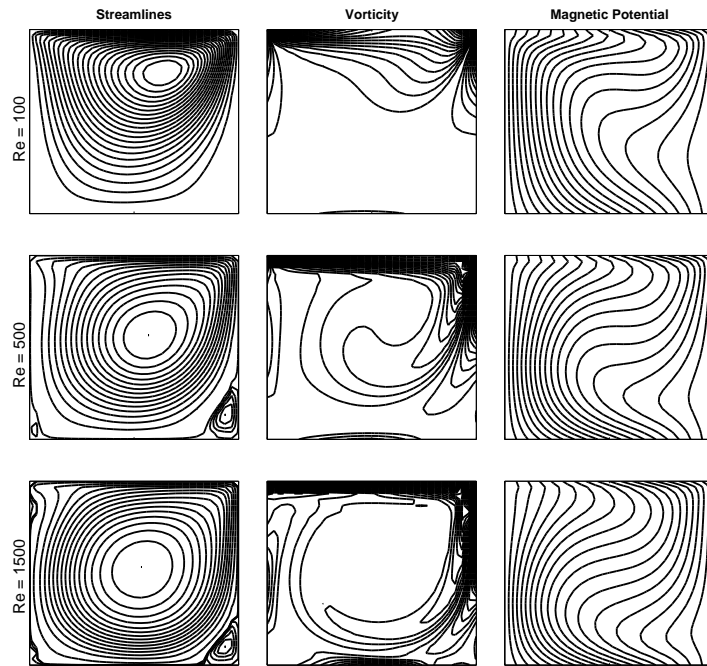


Figure 3.38: Problem 3.4.1:  $Re = 100$ ,  $Ha = 10$ ,  $\Delta t = 0.25$ .

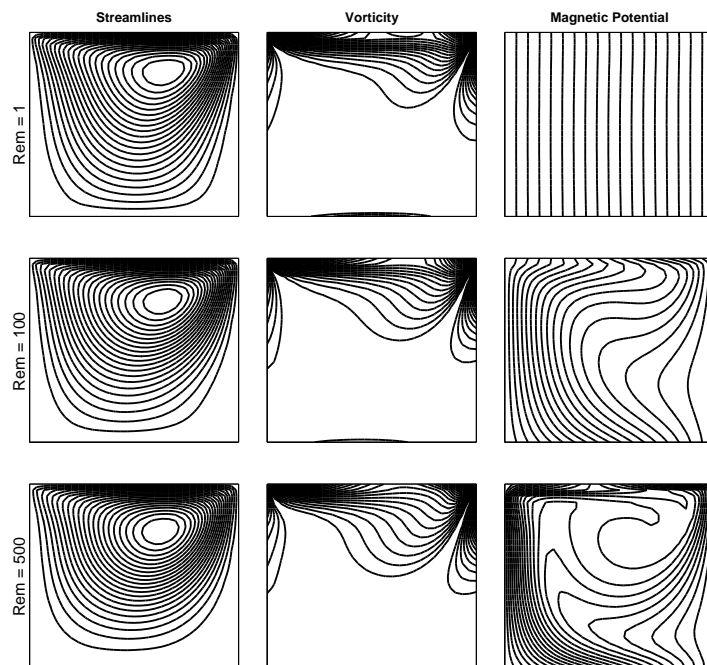


Figure 3.39: Problem 3.4.1:  $Re = 100$ ,  $Ha = 10$ ,  $\Delta t = 0.1$ .

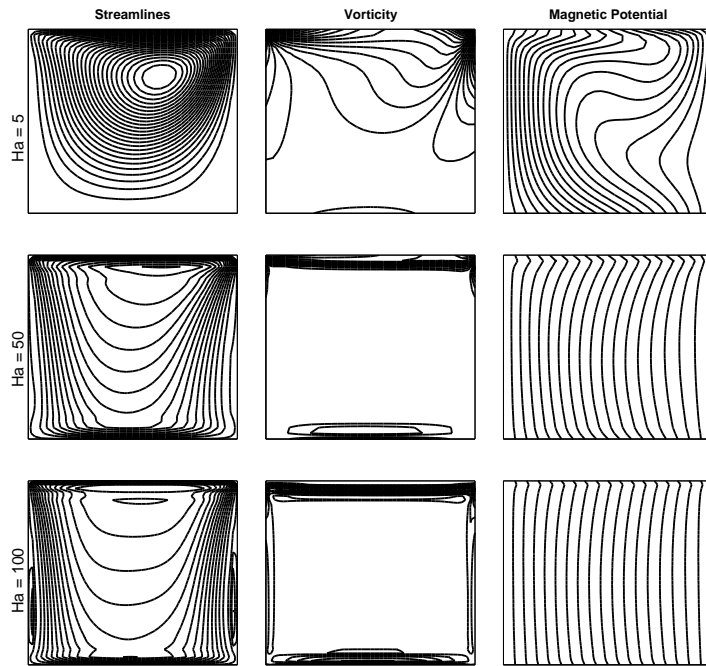


Figure 3.40: Problem 3.4.1:  $Re = Rem = 100$ ,  $\Delta t = 0.5, 0.2, 0.1$ , for  $Ha = 5, 50, 100$ .

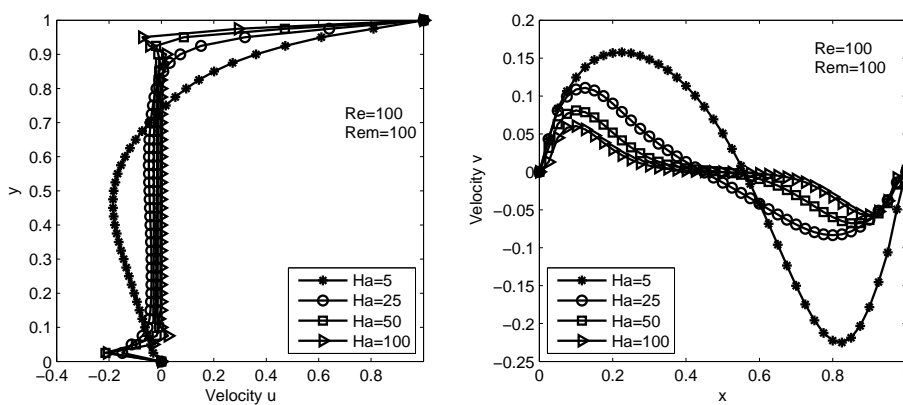


Figure 3.41: Problem 3.4.1: Velocity profiles at mid-sections of the cavity with various  $Ha$ .

### 3.4.2 Case 2. MHD flow over a square cylinder

In this case, the MHD flow around a square cylinder confined in a channel between parallel walls is considered. The inlet velocity profile is uniform, and the flow in the far field is also assumed to be a uniform flow ( $u = 1$ ). The behaviors of the flow and magnetic potential are investigated around the square cylinder under the influence of an externally applied magnetic field which is in  $+y$ -direction.

The problem configuration is given in Figure 3.42. The boundary conditions which are also seen on the figure may be written as follows. At the inlet  $\psi = y - 0.5$ ,  $w = 0$ ,  $u = 1$ ,  $v = 0$ ,  $A = 0$ ; at the exit  $\partial\psi/\partial n = 0$ ,  $\partial w/\partial n = 0$ ,  $A = -4$ ; on the square cylinder  $u = v = \psi = 0$ ,  $A = -x$ , the distance of the left bottom corner of the square cylinder to both the inlet and the bottom wall is 0.25, and  $l_s = 0.5$ . In the computations,  $N = 280$  boundary elements with  $K = 1380$  interior points are used.

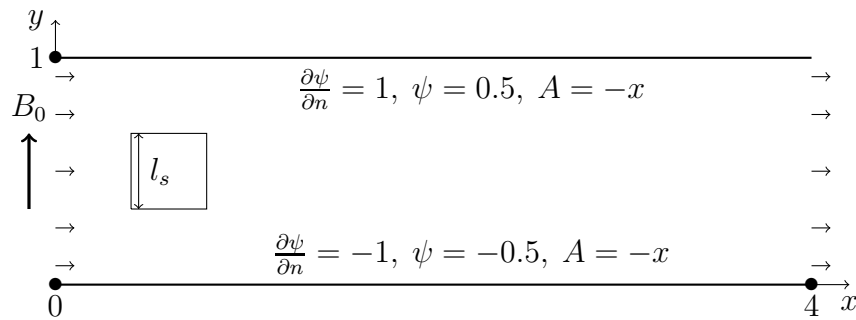


Figure 3.42: Problem 3.4.2: Configuration of the MHD flow past a square cylinder.

In Figures 3.43, 3.44 and 3.45, streamline variations with respect to Reynolds and Hartmann numbers, and magnetic potential variation with respect to magnetic Reynolds number are illustrated, respectively. With the increase in  $Re$  (Figure 3.43), symmetric vortices emerge behind the cylinder, and they elongate through  $+x$ -direction. The increase in Hartmann number suppress this elongation of vortices behind the cylinder as is seen in Figure 3.44. As expected, magnetic potential lines are perturbed in  $+x$ -direction as  $Rem$  is increased since external magnetic field is perpendicular to the channel walls where the boundary layers start to develop (Figure 3.45).

In Figures 3.46-3.47, the vortex changes in the streamlines behind the square cylinder at transient levels are reported. As can be seen, the symmetric vortices are shrunk and a periodic behavior of the flow is observed as time passes. As the fluid move away behind the square cylinder, the periodic behavior diminishes and the flow becomes uniform at the exit of the channel. This may be due to the uniform flow field on the channel walls.

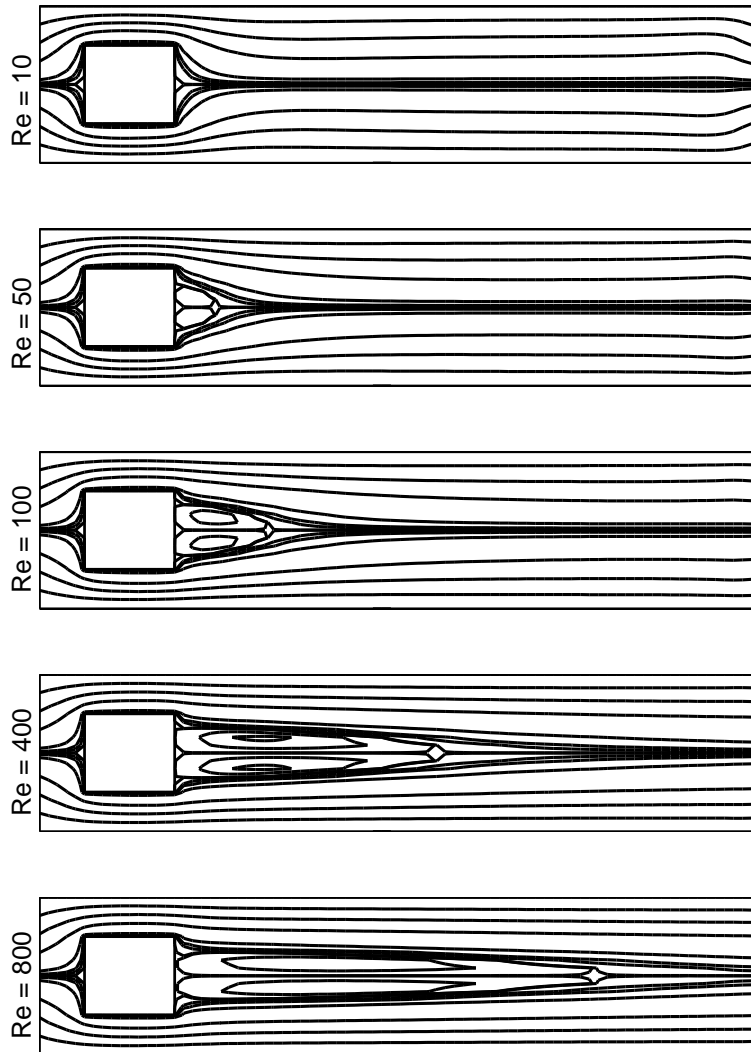


Figure 3.43: Problem 3.4.2: Streamlines at steady-state,  $Rem = 10$ ,  $Ha = 5$ .

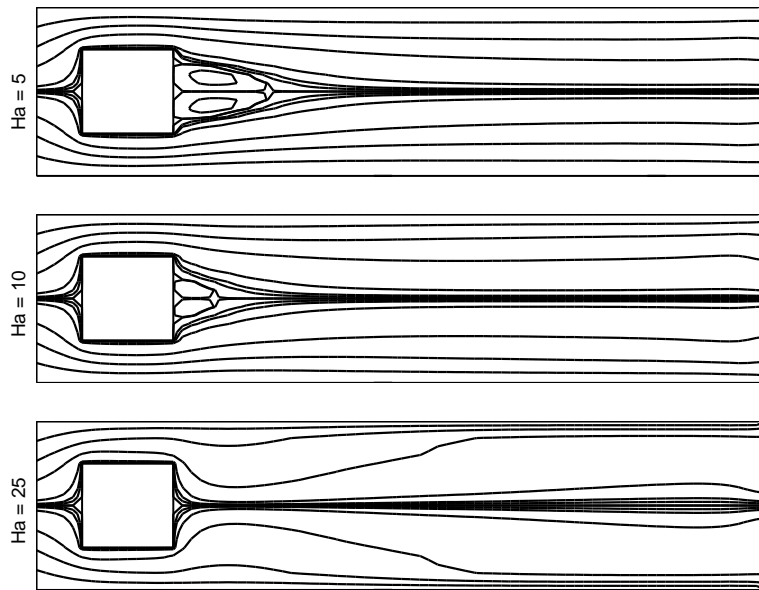


Figure 3.44: Problem 3.4.2: Streamlines at steady-state,  $Re = 100$ ,  $Rem = 10$ .

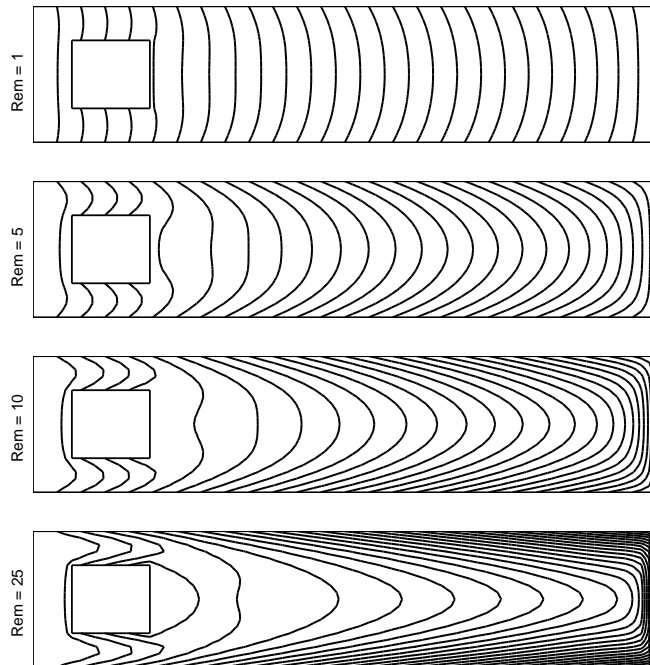


Figure 3.45: Problem 3.4.2: Magnetic potential lines at steady-state,  $Re = 100$ ,  $Ha = 5$ .

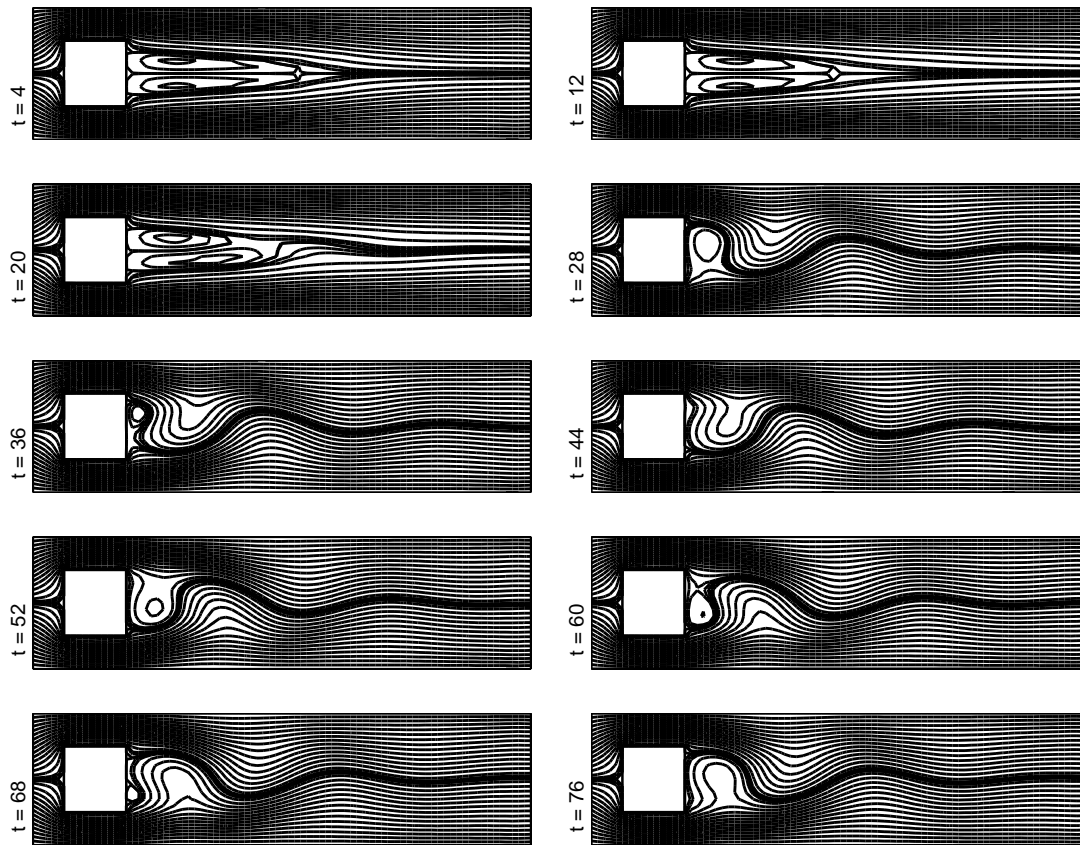


Figure 3.46: Problem 3.4.2: Streamlines at transient levels,  $Re = 300$ ,  $Rem = 10$ ,  $Ha = 5$ .

The remarkable observations throughout this chapter may be summarized as follows. In a porous medium, the decrease in Darcy number slows the fluid motion due to the decrease in permeability of the porous medium, and directs the magnetic potential lines in the direction of applied magnetic field diminishing the lid effect.

Both in a porous or non-porous medium, the increase in the intensity of the externally applied magnetic field causes the fluid to flow slowly due to the retarding effect of Lorentz force. The alteration in the magnetic Reynolds number affects the induced magnetic field or magnetic potential due to the dominance of convection terms either in the induction equations or in the magnetic potential equation. Magnetic potential lines (or induced magnetic field lines) obey the direction of externally applied magnetic field as the strength of the applied magnetic field increases.

The exceptional case is seen on the staggered double driven cavity where the effect of fluid movement seems to be decreased with the increase in  $Rem$ . Also, in the same problem, the opposite movement of lids dominate over the applied magnetic field, and thus, the fluid velocity still increases a little bit as  $Ha$  increases up to 100.

Heat transfer is retarded under the effect of an intense applied magnetic field, and the weak permeability of a porous medium. The change in magnetic Reynolds number does not affect much the heat transfer except in the case of staggered double lid-driven

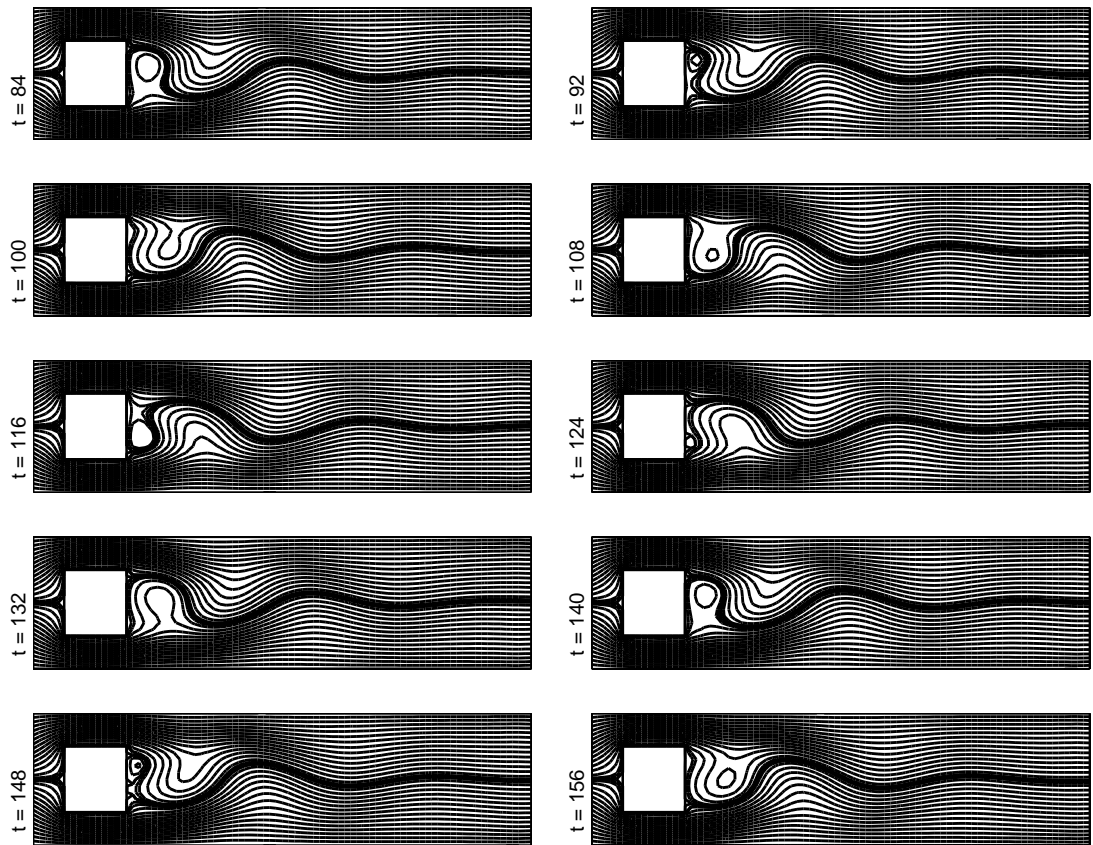


Figure 3.47: Problem 3.4.2: Streamlines at transient levels,  $Re = 300$ ,  $Rem = 10$ ,  $Ha = 5$ .

cavity.

The increase in buoyancy force (the increase in Grashof or Rayleigh number) suppresses the induced magnetic field effect from the mid-part to the bottom of the cavity making them parallel to side walls. The other physical dimensionless parameter, Reynolds number, demonstrates the expected behavior of an incompressible flow in channels.





## CHAPTER 4

### DQM TIME-DQM SPACE APPLICATIONS TO HYPERBOLIC and COUPLED PARABOLIC EQUATIONS

Differential Quadrature Method (DQM) is a global discretization method. DQM expresses a partial derivative of a function as a linear weighted sum of all the functional values at the grid points in the interval for that variable. The method is inspired from the integral quadrature. Initially, Bellman et al. [15] proposed DQM. Then, the method is improved by Shu et al. [144] for computation of weighting coefficients.

The main idea of DQM is to compute the weighting coefficients for any order of derivative. Bellman et al. [15] employed two approaches. However, the algebraic system of equations in one of these approaches results in ill-conditioned matrix as the system size increases. In order to overcome this difficulty, Shu [142] developed a way of computing the weighting coefficients of first order derivatives in a simple, explicit formulation, and then second and higher order derivatives by a recurrence relation. In this improvement, as base functions, Lagrange interpolation polynomials are used due to the unlimited characteristic on the choice of the grid points. Further, these formulations are based on the linear vector space analysis and the analysis of a high order polynomial approximation.

DQM is capable of yielding highly accurate solutions using considerably small number of grid points resulting with less computational cost. Although equally spaced grid distribution is preferred at most of the studies, unequally spaced grid points (e.g. the roots of Chebyshev polynomials) have been proved to be more reliable and efficient than equally spaced points.

In this chapter, the application of either polynomial-based or Fourier expansion-based DQM both in space and time directions is presented. Thus, the solution can be obtained at once (also in blocks) without the need of an iterative procedure in the time domain. The iteration is only used to eliminate the nonlinearities in the equations. These are the main reasons of treating the time dependent problems considered in this Chapter by DQM. Applications include some prominent physical problems defined by hyperbolic type telegraph equation, Klein and sine-Gordon equations, Burgers' equations, and parabolic type MHD duct flow equations.

## 4.1 Differential quadrature method

DQM is based on the derivative approximation of a function at a grid point using all the functional values of the domain.

The first and second derivatives of a function  $f(x)$  at  $x_i$  are approximated by

$$f_x(x_i) = \sum_{j=1}^N a_{ij} f(x_j) \quad (4.1a)$$

$$f_{xx}(x_i) = \sum_{j=1}^N b_{ij} f(x_j), \quad (4.1b)$$

where  $N$  is the number of grid points,  $i = 1, 2, \dots, N$ , and  $a_{ij}$ ,  $b_{ij}$  are the weighting coefficients. These weighting coefficients can be determined by polynomials or Fourier series expansion.

### 4.1.1 Polynomial-based differential quadrature (PDQ) method

PDQ approximates the function  $f(x)$  as

$$f(x) = \sum_{k=1}^N f(x_k) r_k(x), \quad (4.2)$$

where  $f(x_k)$  is a constant known value,  $k = 1, 2, \dots, N$ , and the Lagrange interpolation polynomials  $r_k(x)$  are

$$r_k(x) = \frac{Q(x)}{(x - x_k)Q^{(1)}(x_k)}, \quad (4.3)$$

with

$$Q(x) = \prod_{i=1}^N (x - x_i) \quad \text{and} \quad Q^{(1)}(x_k) = \prod_{\substack{j=1 \\ j \neq k}}^N (x_k - x_j). \quad (4.4)$$

Setting  $N(x_i, x_j) = Q^{(1)}(x_i) \delta_{ij}$  with the Kronecker operator  $\delta_{ij}$ ,  $r_k(x)$  is shortly written as

$$r_k(x) = \frac{N(x, x_k)}{Q^{(1)}(x_k)}, \quad k = 1, 2, \dots, N. \quad (4.5)$$

Substitution of the last form of  $r_k(x)$  into the Eq.(4.2), and then the derivation with respect to  $x$  yields

$$f(x) = \sum_{k=1}^N f(x_k) \frac{N(x, x_k)}{Q^{(1)}(x_k)} \implies f_x(x) = \sum_{k=1}^N f(x_k) \frac{N^{(1)}(x, x_k)}{Q^{(1)}(x_k)}$$

which gives

$$f_x(x_i) = \sum_{j=1}^N f(x_j) \underbrace{\frac{N^{(1)}(x_i, x_j)}{Q^{(1)}(x_j)}}_{a_{ij}}.$$

For evaluation of  $N^{(1)}(x_i, x_j)$ ,  $Q(x)$  is successively differentiated with respect to  $x$  as follows

$$\begin{aligned} Q(x) &= N(x, x_k)(x - x_k) \\ Q^{(1)}(x) &= N^{(1)}(x, x_k)(x - x_k) + N(x, x_k) \\ Q^{(2)}(x) &= N^{(2)}(x, x_k)(x - x_k) + 2N^{(1)}(x, x_k) \\ &\vdots \\ Q^{(n)}(x) &= N^{(n)}(x, x_k)(x - x_k) + nN^{(n-1)}(x, x_k), \end{aligned} \quad (4.6)$$

where  $n = 1, 2, \dots, N - 1$ ;  $k = 1, 2, \dots, N$ . So,

$$N^{(1)}(x_i, x_j) = \frac{Q^{(1)}(x_i)}{x_i - x_j} \quad \text{if } i \neq j, \quad (4.7a)$$

$$N^{(1)}(x_i, x_i) = \frac{Q^{(2)}(x_i)}{2} \quad (4.7b)$$

Eq.(4.7b) is not convenient to find  $a_{ii}$  due to the difficulty in computation of  $Q^{(2)}(x_i)$ . Since a linear operator is satisfied at all sets of base polynomials in linear vector analysis, utilizing the base polynomial  $x^{k-1}$  when  $k = 1$ , the following implication eases to express  $a_{ii}$

$$f(x) = \sum_{k=1}^N f(x_k)x^{k-1} \xrightarrow{k=1} f_x(x_i) = 0 = \sum_{j=1}^N a_{ij}. \quad (4.8)$$

Eq.(4.7b) is simplified, and thus the weighting coefficients for the first order derivative is written as

$$a_{ij} = \frac{Q^{(1)}(x_i)}{(x_i - x_j)Q^{(1)}(x_j)} \quad \text{if } i \neq j, \quad (4.9a)$$

$$a_{ii} = - \sum_{\substack{j=1 \\ j \neq i}}^N a_{ij} \quad (4.9b)$$

Continuing with the same idea for obtaining the weighting coefficient for the first derivatives, the weighting coefficients for the second and higher order derivatives in a recursive relationship may be derived as [142]

$$w_{ij}^n = n \left( a_{ij}w_{ii}^{n-1} - \frac{w_{ij}^{n-1}}{x_i - x_j} \right) \quad \text{if } i \neq j, \quad (4.10a)$$

$$w_{ii}^n = - \sum_{\substack{j=1 \\ j \neq i}}^N w_{ij}^n, \quad (4.10b)$$

where  $n = 2, \dots, N-1$ ,  $i, j = 1, 2, \dots, N$ , and  $w_{ij}^1 = a_{ij}$ .

#### 4.1.2 Fourier expansion-based differential quadrature (FDQ) method

FDQ approximates the function  $f(x)$  by a Fourier series expansion in the form

$$f(x) = c_0 + \sum_{k=1}^{N/2} (c_k \cos(kx) + d_k \sin(kx)), \quad (4.11)$$

where  $c_k$  and  $d_k$  are constants. Also, the Lagrange interpolated trigonometric polynomials are taken as [143]

$$r_k(x) = \frac{Q(x)}{\sin \frac{x-x_k}{2} P(x_k)}, \quad (4.12)$$

where

$$Q(x) = \prod_{k=0}^N \sin \frac{x-x_k}{2} = N(x, x_k) \sin \frac{x-x_k}{2},$$

$$P(x_k) = N(x_k, x_k) = \prod_{\substack{j=0, \\ j \neq k}}^N \sin \frac{x_k-x_j}{2} \quad \text{and} \quad N(x_i, x_j) = N(x_i, x_i) \delta_{ij}.$$

With the same idea in PDQ, the weighting coefficients are obtained in FDQ. The details are given in the book [142]. The weighting coefficients for the first and second order derivatives are found as

$$a_{ij} = \frac{1}{2} \frac{\alpha P(\tau_i)}{\sin \frac{\tau_i-\tau_j}{2} P(\tau_j)} \quad \text{if } i \neq j \quad (4.13a)$$

$$a_{ii} = - \sum_{\substack{j=1 \\ j \neq i}}^N a_{ij} \quad (4.13b)$$

$$b_{ij} = a_{ij} \left[ 2a_{ii} - \alpha \cot \frac{\tau_i-\tau_j}{2} \right] \quad \text{if } i \neq j \quad (4.13c)$$

$$b_{ii} = - \sum_{\substack{j=1 \\ j \neq i}}^N b_{ij}, \quad (4.13d)$$

where  $\tau$  and  $\alpha$  are specified as

$$\tau = 2\pi \frac{x-a}{b-a}, \quad \alpha = \frac{2\pi}{b-a}, \quad \text{for periodic problems} \quad (4.14a)$$

$$\tau = \pi \frac{x-a}{b-a}, \quad \alpha = \frac{\pi}{b-a}, \quad \text{for non-periodic problems.} \quad (4.14b)$$

Note that by Eqs.(4.14), any interval  $[a, b]$  is transformed to  $[0, \pi]$  (non-periodic problems) or  $[0, 2\pi]$  (periodic problems), respectively.

### 4.1.3 Grid points distribution

#### Equally spaced (ES) grid points

In this grid distribution, the distance between each grid point is equal to each other. Let the physical domain of the problem (in  $\mathbb{R} \times \mathbb{R}$ ) is given as  $[a, b] \times [a, b]$ , and let the region be divided into  $N \times M$  meshes. The mesh size in both  $x$ - and  $y$ -spaces will be  $h_x = (b-a)/(N-1)$  and  $h_y = (b-a)/(M-1)$ , respectively, such that  $x_i = x_1 + (i-1)h_x$ ,  $y_j = y_1 + (j-1)h_y$ ,  $i = 1, 2, \dots, N$ ;  $j = 1, 2, \dots, M$ .

#### Chebyshev and Gauss-Chebyshev-Lobatto(GCL) grid points

Chebyshev polynomials defined in  $[-1, 1]$  for  $N^{\text{th}}$  degree polynomial are given by

$$T_N(x) = \cos(N\theta), \quad 0 \leq \theta \leq \pi, \quad \theta = \arccos(x). \quad (4.15)$$

The roots of Chebyshev polynomials are

$$T_N(x_i) = 0 \implies x_i = \cos \frac{(2i-1)\pi}{2N}, \quad i = 1, 2, \dots, N. \quad (4.16)$$

Chebyshev points in a physical domain  $[a, b]$  are obtained by the transformation

$$\tilde{x}_i = \frac{b+a}{2} - \frac{b-a}{2} \cos \frac{(2i-1)\pi}{2N}, \quad i = 2, \dots, N-1. \quad (4.17)$$

GCL grid points are the points  $x_i$  satisfying  $|T_N(x_i)| = 1 = |\cos(N\theta_i)|$  in which  $\theta_i = i\frac{\pi}{N}$ ,  $i = 1, 2, \dots, N$ . Thus,  $x_i = \cos \frac{i\pi}{N}$  and  $x_i \in [-1, 1]$ . For nodes over an arbitrary interval  $[a, b]$ , the following transformation gives GCL grid points as

$$\tilde{x}_i = \frac{b+a}{2} - \frac{b-a}{2} \cos \left( \frac{i-1}{N-1} \pi \right), \quad i = 1, 2, \dots, N. \quad (4.18)$$

As an example, let the physical domain be  $[0, 1]$  and  $N = 17$  is the number of division on both  $x$  and  $y$  axes. The node distributions for Chebyshev and GCL grid points is illustrated in Figure 4.1.

In this Chapter, DQM is applied for both space and time derivatives either using the equally spaced or non-uniform grid distributions. Test problems are 1D and 2D hyperbolic Telegraph equations, Klein and sine-Gordon equations, Burgers' equations, and MHD duct flow equations.

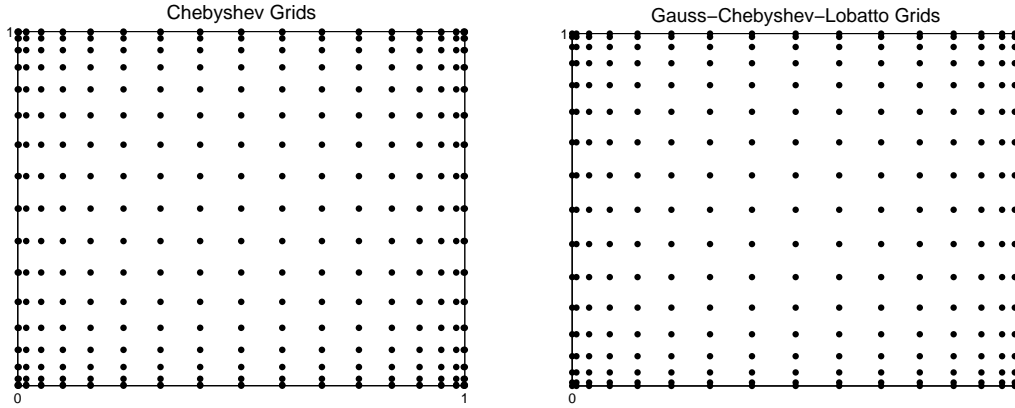


Figure 4.1: Non-uniform grid distribution examples.

## 4.2 One- and two-dimensional hyperbolic telegraph equations

The hyperbolic differential equations are the basis for fundamental equations of atomic physics. They are commonly used in signal analysis for transmission and propagation of electrical signals.

Hyperbolic telegraph equations are encountered in the study of pulsate blood flow in arteries, the acoustic waves in Darcy-type porous media, parallel flow of viscous Maxwell fluids. These equations also model the vibrations of structures (e.g. buildings, beams).

In this section, DQM in both time and space directions is applied to obtain numerical solutions of one- and two-dimensional linear hyperbolic telegraph equations which contain second order time derivatives.

The use of DQM in both space and time direction, which also discretizes the initial condition  $u_t$ , automatically results with an overdetermined system. The numerical scheme then provides the solution at any time level without an iteration. This makes the main difference from the conventional time integration methods. The solution is obtained directly at all required time levels by solving one overdetermined system which contains the solution at the grid points in space and time directions. The Gauss-Chebyshev-Lobatto (GCL) points are used in space direction while either equally spaced or GCL grid points are taken in time direction. The numerical procedure requires very small number of grid points in space directions and appropriate number of time grid points for reaching a certain time level.

Consider the second-order linear hyperbolic telegraph equation in one-dimensional space in  $\Omega_1$ ,

$$u_{tt}(x, t) + 2\alpha u_t(x, t) + \beta^2 u(x, t) = u_{xx}(x, t) + f(x, t), \quad (4.19)$$

and the second-order two-dimensional hyperbolic telegraph equation in  $\Omega_2$ ,

$$u_{tt}(x, y, t) + 2\alpha u_t(x, y, t) + \beta^2 u(x, y, t) - g(x, y, t) = u_{xx}(x, y, t) + u_{yy}(x, y, t), \quad (4.20)$$

where  $\Omega_1 = [a < x < b] \times [t > 0]$  and  $\Omega_2 = [0 < x, y < 1] \times [t > 0]$ . Eqs.(4.19-4.20) are damped wave equations for  $\alpha > 0$ ,  $\beta = 0$  of which the solution is of great importance in wave phenomena, and telegraph equation for  $\alpha \geq \beta > 0$ . For Eq.(4.19), the initial conditions are assumed to be

$$u(x, 0) = v_1(x), \quad u_t(x, 0) = v_2(x), \quad a < x < b \quad (4.21)$$

with Dirichlet

$$u(a, t) = h_1(t), \quad u(b, t) = h_2(t), \quad t \geq 0, \quad (4.22)$$

or Neumann type boundary conditions

$$u_x(a, t) = k_1(t), \quad u_x(b, t) = k_2(t), \quad t \geq 0, \quad (4.23)$$

and for Eq.(4.20)

$$u(x, y, 0) = \phi_1(x, y), \quad u_t(x, y, 0) = \phi_2(x, y), \quad 0 < x, y < 1 \quad (4.24)$$

with Dirichlet

$$u(x, y, t) = p_1(x, y, t) \quad \text{at } x, y = \pm 1, \quad t \geq 0, \quad (4.25)$$

or Neumann boundary conditions

$$u_x(x, y, t) = p_2(x, y, t) \quad \text{at } x = \pm 1, \quad t \geq 0 \quad (4.26)$$

$$u_y(x, y, t) = p_3(x, y, t) \quad \text{at } y = \pm 1, \quad t \geq 0. \quad (4.27)$$

The functions  $f(x, t), h_1(t), h_2(t), v_1(x), v_2(x), k_1(t), k_2(t)$  are continuous functions defined on  $\Omega_1$ , and similarly  $g(x, y, t), \phi_1(x, y), \phi_2(x, y), p_1(x, y, t), p_2(x, y, t), p_3(x, y, t)$  are defined and continuous on  $\Omega_2$ .

In the following two sections, polynomial based DQM application to 1D and 2D hyperbolic equations is explained. Fourier expansion based DQM application is also done in a similar way with a difference in weighting coefficients. Some test problems, which have analytical solution, for different  $\alpha$  and  $\beta$  values to observe the accuracy and efficiency of the DQ method is presented. Thus, the accuracy of the proposed method is measured by the following errors defined as [40, 44]

$$\text{RMS error} = \frac{\|u_{\text{exact}} - u_{\text{computed}}\|_2}{\sqrt{nod}}$$

$$\text{Relative error} = \frac{\|u_{\text{exact}} - u_{\text{computed}}\|_2}{\|u_{\text{exact}}\|_2},$$

where  $nod$  is the total number of all grid points in space direction, and the errors can be computed at any time level.

#### 4.2.1 One-dimensional hyperbolic telegraph equation

PDQ approximations for the derivatives in Eq.(4.19) can be written as

$$u_x = \sum_{k=1}^N a_{ik} u_{kl}, \quad u_{xx} = \sum_{k=1}^N b_{ik} u_{kl}, \quad (4.28a)$$



$$u_t = \sum_{k=1}^L \bar{a}_{lk} u_{ik}, \quad u_{tt} = \sum_{k=1}^L \bar{b}_{lk} u_{ik} \quad (4.28b)$$

where  $i = 1, 2, \dots, N$ ;  $l = 1, 2, \dots, L$ ,  $N$  and  $L$  are the number of discretization points, and  $a_{ik}$ ,  $b_{ik}$ , and  $\bar{a}_{lk}$ ,  $\bar{b}_{lk}$  are the weighting coefficients for the first and second order derivatives, in space and time directions, respectively. These coefficients are computed by Eqs.(4.9)-(4.10) when PDQ is used. Therefore, Eq.(4.19) will be discretized as

$$\sum_{k=1}^L \bar{b}_{lk} u_{ik} + 2\alpha \sum_{k=1}^L \bar{a}_{lk} u_{ik} + \beta^2 u_{il} - \sum_{k=1}^N b_{ik} u_{kl} = f(x_i, t_l), \quad (4.29)$$

where  $i = 1, 2, \dots, N$  and  $l = 1, 2, \dots, L$ .

The main system Eq.(4.29) may be denoted as an algebraic system

$$[B] \{u\} = \{f\}, \quad (4.30)$$

where  $u$  is the unknown vector to be determined with the entries at the grid points  $(x_i, t_l)$ , and the matrix  $[B]$  consists of the known weighting coefficients. The known vector  $f$  contains the function values  $f(x_i, t_l)$  as entries. The initial condition  $u(x, 0) = v_1(x)$  is inserted to the system (4.30) directly modifying the matrix  $[B]$  and the vector  $f$ . The other initial condition  $u_t(x, 0)$  is expanded by DQM formulation as

$$v_2(x_i) = u_t(x_i, 0) = \sum_{k=1}^L \bar{a}_{1k} u_{ik}, \quad i = 1, 2, \dots, N. \quad (4.31)$$

Eq.(4.31) will also be a system which can be described as

$$[B_0] \{u\} = \{v_2\}. \quad (4.32)$$

where the matrix  $[B_0]$  and the vector  $\{v_2\}$  contain coefficients  $\bar{a}_{1k}$  and  $v_2(x_i)$  as entries, respectively.

If Dirichlet type boundary conditions are given, these conditions are directly inserted to Eq.(4.30) and Eq.(4.32) with the given initial conditions  $u(x, 0)$ . So, the coefficient matrices  $[B]$  and  $[B_0]$  will be of size  $(N-2)(L-1) \times (N-2)(L-1)$  and  $(N-2) \times (N-2)(L-1)$ , respectively.

The systems (4.30) and (4.32) form an overdetermined system. Therefore, least square method or QR factorization will be made use of for obtaining the solution vector  $\{u\}$ .

If Neumann type boundary conditions are given, the sizes of the new coefficient matrix  $[B^{neu}]$  in Eq.(4.30) and  $[B_0^{neu}]$  in Eq.(4.32) will be  $(L-1)N \times (L-1)N$  and  $N \times (L-1)N$ , respectively. Neumann boundary conditions are also discretized using PDQ as

$$k_1(t_l) = u_x(a, t_l) = \sum_{k=1}^N a_{1k} u_{kl}, \quad (4.33a)$$

$$k_2(t_l) = u_x(b, t_l) = \sum_{k=1}^N a_{Nk} u_{kl}, \quad l = 1, \dots, L, \quad (4.33b)$$

which can be formed as a system

$$[B_{\partial\Omega_1}] \{u\} = \{k\}, \quad (4.34)$$

where  $[B_{\partial\Omega_1}]$  is a matrix of size  $2(L-1) \times (L-1)N$  containing the coefficients  $a_{1k}$ ,  $a_{Nk}$  and the vector  $\{k\}$  contains  $k_1(t_i)$ ,  $k_2(t_i)$  as entries. Then, the whole system (4.30) with  $[B^{neu}]$ , (4.32) with  $[B_0^{neu}]$  and (4.34) again is an overdetermined system which will be solved either by QR or least square method.

Also, the ordering of the unknown vector is important since the structure of  $[B]$  or  $[B^{neu}]$  depends on this ordering. To get a well-conditioned matrix  $[B]$ , the unknown vector  $\{u\}$  is arranged as in the following order

$$\{u\} = \{u_{i1}, u_{i2}, u_{i3}, \dots, u_{iL}\}^T,$$

where  $i = 2, 3, \dots, N-1$  if boundary conditions are Dirichlet type, and  $i = 1, 2, \dots, N$  if Neumann type boundary conditions are used.

GCL grid points in  $x$ -space on an interval  $[a, b]$  are computed by Eq.(4.18). In the time direction, equally spaced (ES) grid points are used on an interval  $[0, T]$  as

$$t_l = \frac{(l-1)T}{L-1}, \quad l = 1, 2, \dots, L. \quad (4.35)$$

#### 4.2.1.1 Test problem.

Consider the one-dimensional hyperbolic telegraph equation (4.19) in the interval  $0 \leq x \leq 2\pi$ ,  $0 < t \leq 3$  with  $\alpha = 4$ ,  $\beta = 2$ . The exact solution is taken as [51]

$$u(x, t) = e^{-t} \sin(x). \quad (4.36)$$

In this case,  $f(x, t) = (2 - 2\alpha + \beta^2) e^{-t} \sin(x)$ . The initial and boundary conditions are extracted from the exact solution as

$$u(x, 0) = \sin(x), \quad u_t(x, 0) = -\sin(x), \quad (4.37)$$

$$u(0, t) = 0, \quad u(2\pi, t) = 0, \quad t \in [0, 3], \quad (4.38)$$

$$u_x(0, t) = e^{-t}, \quad u_x(2\pi, t) = e^{-t}, \quad t \in [0, 3]. \quad (4.39)$$

Table 4.1 shows RMS errors obtained by using Dirichlet type boundary conditions (4.38) with different  $\Delta t$  (equally spaced time grid is used) values. It is noticed that  $10^{-5}$  accuracy is achieved even with a coarse mesh ( $\Delta t = 0.5$ ) in time direction. It is improved with a finer mesh ( $\Delta t = 0.25$ ).

Table 4.2 reports RMS errors obtained by Neumann boundary conditions (4.39). Although the accuracy is decreased with Neumann boundary conditions using PDQ for

both time and space derivatives, the results are improved in terms of accuracy increasing  $N$ . When FDQ weighting coefficients are used in space direction and PDQ weighting coefficients in time direction, the results by using FDQ even with  $N = 11$  have better accuracy than the results obtained by PDQ.

Figure 4.2 depicts the very well agreement of DQM and exact solutions at different time levels even with equally spaced time grid points. The number of GCL grid points in space is small ( $N = 17$ ) and  $\Delta t = 0.25$  is considerably large compared to other time integration schemes.

Table 4.1: Problem 4.2.1.1: RMS errors with  $N = 11$  using Dirichlet BCs.

t	$\Delta t = 0.25$	$\Delta t = 0.5$
0.5	8.57e-07	6.20e-05
1	3.94e-07	3.90e-05
2	1.66e-07	3.00e-05
3	6.23e-08	2.93e-05

Table 4.2: Problem 4.2.1.1: RMS errors with  $\Delta t = 0.25$  with Neumann BCs.

t	PDQ			FDQ
	$N = 11$	$N = 13$	$N = 17$	$N = 11$
0.5	2.82e-05	7.74e-07	2.26e-10	1.79e-10
1	1.52e-05	3.78e-07	1.45e-10	1.39e-10
2	4.44e-06	1.41e-07	8.32e-11	8.03e-11
3	3.09e-06	7.63e-08	5.72e-11	5.53e-11

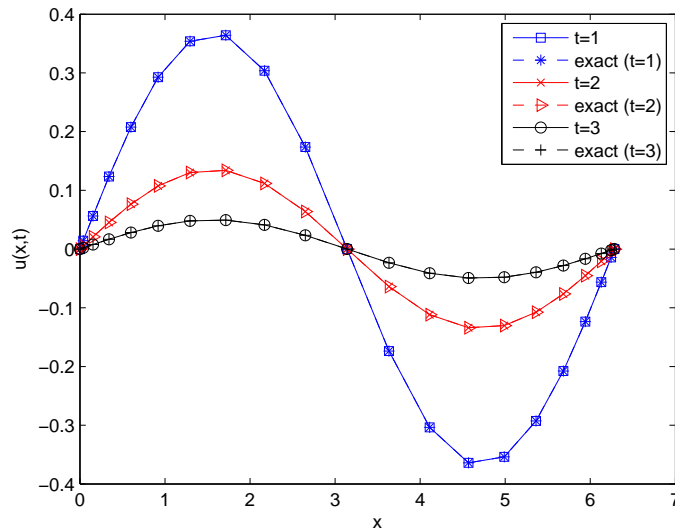


Figure 4.2: Problem 4.2.1.1: Numerical and exact solutions at different times with  $\Delta t = 0.25$ ,  $N = 17$  using Neumann BCs.

## 4.2.2 Two-dimensional hyperbolic telegraph equation

The space and time derivatives in Eq.(4.20) can be discretized by using PDQ as

$$u_x = \sum_{k=1}^N a_{ik} u_{kjl}, \quad u_{xx} = \sum_{k=1}^N b_{ik} u_{kjl}, \quad (4.40a)$$

$$u_y = \sum_{k=1}^M \bar{a}_{jk} u_{ikl}, \quad u_{yy} = \sum_{k=1}^M \bar{b}_{jk} u_{ikl}, \quad (4.40b)$$

$$u_t = \sum_{k=1}^L \bar{\bar{a}}_{lk} u_{ijk}, \quad u_{tt} = \sum_{k=1}^L \bar{\bar{b}}_{lk} u_{ijk}, \quad (4.40c)$$

and the discretized form of Eq.(4.20) is

$$\sum_{k=1}^L \bar{\bar{b}}_{lk} u_{ijk} + 2\alpha \sum_{k=1}^L \bar{\bar{a}}_{lk} u_{ijk} + \beta^2 u_{ijl} - \sum_{k=1}^N b_{ik} u_{kjl} - \sum_{k=1}^M \bar{b}_{jk} u_{ikl} = g(x_i, y_j, t_l), \quad (4.41)$$

where  $N, M, L$  are the number of discretization points in  $x, y, t$  directions, and  $i = 1, 2, \dots, N; j = 1, 2, \dots, M; l = 1, 2, \dots, L$ , respectively.

The initial condition  $u_t(x, y, 0)$  and the Neumann type boundary conditions are added to the system Eq.(4.41) discretizing them using PDQ approximations as follows

$$\begin{aligned} u_t(x, y, 0) &= \sum_{k=1}^L \bar{\bar{a}}_{1k} u_{ijk}, \quad l = 1; \quad i = 1, \dots, N, \quad j = 1, \dots, M, \\ u_x(0, y, t) &= \sum_{k=1}^N a_{1k} u_{kjl}, \quad i = 1, \\ u_x(1, y, t) &= \sum_{k=1}^N a_{Nk} u_{kjl}, \quad i = N; \quad j = 1, \dots, M, \quad l = 1, \dots, L, \\ u_y(x, 0, t) &= \sum_{k=1}^M \bar{a}_{1k} u_{ikl}, \quad j = 1, \\ u_y(x, 1, t) &= \sum_{k=1}^M \bar{a}_{Mk} u_{ikl}, \quad j = M; \quad i = 1, \dots, N, \quad l = 1, \dots, L. \end{aligned} \quad (4.42)$$

As in one-dimensional telegraph equation, the DQM discretized system (4.41) will be solved together with the initial and boundary conditions. If the boundary conditions are of Dirichlet type, they will be inserted to the overdetermined system combined with the system resulting from initial conditions. For Neumann boundary conditions, the system (4.41) and (4.42) will be solved together.

One of the difficulties in two-dimensional hyperbolic telegraph equation is that the system to be solved becomes larger as  $N, M, L$  are increased. This causes more memory

and CPU usage. To overcome this problem, the system is reduced by removing the entries on the coefficient matrix of the system which correspond to known information (e.g. initial condition  $u(x, y, 0)$  and the Dirichlet type boundary conditions). Meanwhile, the right hand side of the reduced system is also modified taking into account removed known entries in the coefficient matrix.

The order of the unknown vector  $\{u\}$  in this case is organized to get a well-conditioned system. Consider the unknown vector as a matrix  $U$  whose each row entry corresponds to a time level. Notationally,

$$\begin{bmatrix} u_{1j1} & u_{2j1} & \dots & u_{Nj1} \\ u_{1j2} & u_{2j2} & \dots & u_{Nj2} \\ \vdots & \vdots & \ddots & \vdots \\ u_{1jL} & u_{2jL} & \dots & u_{NjL} \end{bmatrix},$$

where  $j = 1, 2, \dots, M$ , and the matrix of size  $L \times NM$  will be rewritten as a vector writing columns consecutively.

The solution is obtained by solving only one system with the inserted initial and boundary conditions, and the aforementioned reduction of known entries is performed to reduce the size of the system. The solution vector contains all required time level values in it.

The solvability of the overdetermined system of equations depends on the column rank of the coefficient matrix which is  $NML$  in this case. When the initial and/or Neumann type boundary conditions are discretized using DQM, and added to the system, the row size is certainly greater than  $NML$  which makes the system overdetermined. The choice of the grid points in both space and time domains affects the stability of the system. As mentioned in the Shu's book [142], the solution with GCL grid points becomes more stable than equally spaced grid points in both space and time directions. Moreover, appropriate choice of  $N$ ,  $M$  and  $L$  makes the final coefficient matrix full column rank.

GCL grid points on  $[0, 1]$  for  $x$ - and  $y$ -spaces are taken as

$$x_i = \frac{1}{2} \left( 1 - \cos \left( \frac{i-1}{N-1} \pi \right) \right), \quad i = 1, 2, \dots, N, \quad (4.43)$$

$$y_j = \frac{1}{2} \left( 1 - \cos \left( \frac{j-1}{M-1} \pi \right) \right), \quad j = 1, 2, \dots, M. \quad (4.44)$$

Furthermore, time direction is divided equally as in (4.35) or by GCL grid points on an interval  $[0, T]$  as

$$t_l = \frac{T}{2} \left( 1 - \cos \left( \frac{l-1}{L-1} \pi \right) \right), \quad l = 1, 2, \dots, L. \quad (4.45)$$

#### 4.2.2.1 Test problem 1.

Now, the two-dimensional telegraph equation (4.20) is considered in the region  $0 \leq x, y \leq 1, t > 0$ , with  $\alpha = \beta = 1$ . The analytical solution given by [40] is

$$u(x, y, t) = \cos(t) \sin(x) \sin(y), \quad (4.46)$$

from which initial condition, Dirichlet boundary conditions and  $g(x, y, t)$  are extracted as

$$u(x, y, 0) = \sin(x) \sin(y), \quad u_t(x, y, 0) = 0, \quad (4.47a)$$

$$u(x, 0, t) = 0, \quad 0 \leq x \leq 1, \quad y = 0, \quad (4.47b)$$

$$u(0, y, t) = 0, \quad 0 \leq y \leq 1, \quad x = 0, \quad (4.47c)$$

$$u(1, y, t) = \cos(t) \sin(1) \sin(y), \quad 0 \leq y \leq 1, \quad t \geq 0 \quad (4.47d)$$

$$u(x, 1, t) = \cos(t) \sin(x) \sin(1), \quad 0 \leq x \leq 1, \quad t \geq 0 \quad (4.47e)$$

$$g(x, y, t) = 2 \sin(x) \sin(y) [\cos(t) - \sin(t)]. \quad (4.47f)$$

Table 4.3 presents the comparison of the DQM solution and the exact solution in terms of relative errors for different  $\Delta t$  values when equally spaced time grid points are used. In this two-dimensional problem, FDQ approximation for space derivatives, keeping PDQ approximation for time derivatives is also studied. As can be seen from the Table, both PDQ and FDQ approximations in space directions give almost the same accuracy even with coarse time grid points ( $\Delta t = 0.5$  and  $\Delta t = 0.25$ ) taking a little more space grid points in FDQ. Furthermore, as  $L$  is increased ( $\Delta t$  is decreased), accuracy increases.

Table 4.3: Problem 4.2.2.1: Relative errors.

t	PDQ (N=M=17)		FDQ (N=M=21)	
	$\Delta t = 0.25$	$\Delta t = 0.5$	$\Delta t = 0.25$	$\Delta t = 0.5$
0.5	1.18e-09	8.80e-05	3.62e-09	8.93e-05
1	1.11e-09	5.94e-05	3.62e-09	6.03e-05
2	4.28e-10	9.17e-05	3.43e-09	9.31e-05
3	1.36e-10	1.09e-04	3.66e-09	1.10e-04

#### 4.2.2.2 Test problem 2.

In this case, Eq.(4.20) is taken into account with  $\alpha = \beta = 1$  and  $\alpha = 5, \beta = 1$  in the region  $0 \leq x, y \leq 1, t > 0$ . The analytical solution is given by [47]

$$u(x, y, t) = \ln(1 + x + y + t), \quad (4.48)$$

with the initial conditions

$$u(x, y, 0) = \ln(1 + x + y), \quad u_t(x, y, 0) = \frac{1}{1 + x + y}, \quad (4.49)$$

and the boundary conditions are of Dirichlet and Neumann type

$$\begin{aligned} u_y(x, 0, t) &= \frac{1}{1+x+t}, & 0 \leq x \leq 1, \\ u_x(1, y, t) &= \frac{1}{2+y+t}, & 0 \leq y \leq 1, & t \geq 0, \\ u(x, 1, t) &= \ln(2+x+t), & 0 \leq x \leq 1, \\ u(0, y, t) &= \ln(1+y+t), & 0 \leq y \leq 1. \end{aligned}$$

The inhomogeneity is extracted from the exact solution as

$$g(x, y, t) = \frac{2\alpha}{1+x+y+t} + \beta^2 \ln(1+x+y+t) + \frac{1}{(1+x+y+t)^2}. \quad (4.50)$$

Relative errors between numerical solution (PDQ) and exact solution for different  $\Delta t$  values are presented in Table 4.4. Even with a large  $\Delta t = 1$ , about  $10^{-4}$  accuracy is reached. As  $\Delta t$  is decreased, accuracy is increased as expected. The error decreases with a higher  $\alpha$  value. Again, it is noticed that with considerably small number of grid points both in space direction ( $N = M = 11$ ) and time direction ( $\Delta t = 0.5$  or  $\Delta t = 0.25$ ), at least  $10^{-6}$  accuracy is obtained.

Table 4.4: Problem 4.2.2.2: Relative errors with different values of  $\alpha$ .

t	$\alpha = \beta = 1$			$\alpha = 5, \beta = 1$	
	$\Delta t = 0.25$	$\Delta t = 0.5$	$\Delta t = 1$	$\Delta t = 0.25$	$\Delta t = 0.5$
1	9.65e-08	6.55e-05	1.18e-03	5.02e-08	9.67e-06
3	8.24e-09	9.65e-07	2.60e-04	7.75e-09	2.03e-06
5	1.53e-08	1.04e-05	5.68e-04	2.69e-08	9.64e-06

### 4.2.2.3 Test problem 3.

Consider the homogeneous ( $g(x, y, t) = 0$ ) Eq.(4.20) in the region  $0 \leq x, y \leq 1, t > 0$ , with  $\alpha = 1 + \pi^2, \beta = 1$ . The exact solution is given by [54]

$$u(x, y, t) = e^{-t} \sin(\pi x) \sin(\pi y),$$

with the initial conditions

$$\begin{aligned} u(x, y, 0) &= \sin(\pi x) \sin(\pi y), \\ u_t(x, y, 0) &= -\sin(\pi x) \sin(\pi y), \end{aligned}$$

and Dirichlet and Neumann boundary conditions on parallel walls are

$$\begin{aligned} u(x, 0, t) &= 0, & 0 \leq x \leq 1, \\ u(1, y, t) &= 0, & 0 \leq y \leq 1, & t \geq 0, \\ u_y(x, 1, t) &= -\pi e^{-t} \sin(\pi x), & 0 \leq x \leq 1 \end{aligned}$$

$$u_x(0, y, t) = \pi e^{-t} \sin(\pi y), \quad 0 \leq y \leq 1.$$

Table 4.5 compares the numerical solution (both PDQ and FDQ) with the exact solution for different time levels in terms of RMS errors. FDQ weighting coefficients are used in space directions remaining PDQ weighting coefficients in time direction (FDQ-PDQ) as well as PDQ approximation is used in both directions (PDQ-PDQ). In this problem, we use GCL grid points in both space and time directions. FDQ-PDQ approximation gives better accuracy than PDQ-PDQ approximation for this problem.

To emphasize the importance of the GCL grid points in time direction, Figures 4.3-4.4 present RMS errors versus the number of grid points in time direction. The number of GCL grid points in space direction ( $N = M = 11$ ) at  $T = 3$  is fixed and only PDQ-PDQ approximation is considered. When the number of equally spaced points in time exceeds 28, the system becomes rank deficient. This means that large number of ES grid points in time direction causes unstable solution. On the other hand, GCL grid points in time direction still gives very good accuracy for  $11 \leq L \leq 41$  as can be seen in Figure 4.4. Moreover, RMS error using 11 to 23 ES grid points increases faster than RMS error using the same number of GCL grid points in time. The accuracy with *GCL* grid points in time direction remains in a scale between  $0.2 \times 10^{-9}$  and  $1.8 \times 10^{-9}$ .

This observation is important for physical problems which require the solution at a high time level. In that case, the number of grid points in time direction should be large and endure oscillations of the solution. Thus, GCL grid points in time are more preferable than ES grid points.

Table 4.5: Problem 4.2.2.3: RMS errors for  $u(x,t)$  using  $M = N = 11$ ,  $L = 13$ .

t	PDQ-PDQ	FDQ-PDQ
0.75	1.31e-09	1.38e-11
2.25	1.04e-09	9.40e-12
3	6.71e-10	7.74e-12



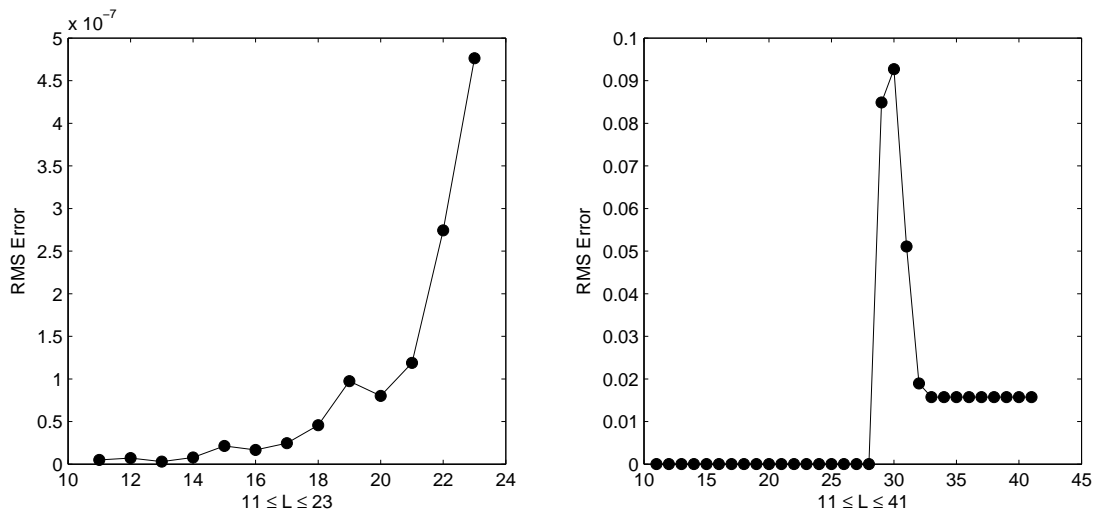


Figure 4.3: Problem 4.2.2.3: RMS error versus ES grid points in time direction.

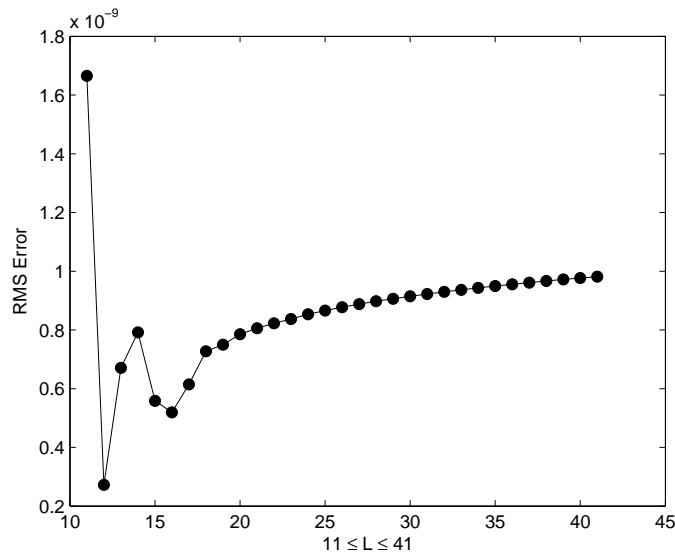


Figure 4.4: Problem 4.2.2.3: RMS error versus GCL grid points in time direction.

### 4.3 Klein-Gordon and sine-Gordon equations

The Klein-Gordon equation (KGE) arises in many scientific areas such as nonlinear optics, solid state physics and quantum field theory [161]. This equation has a great importance in relativistic quantum mechanics, which is used to describe spinless particles. Furthermore, soliton-like structures have gained a great deal of interest in the last years. Soliton waves do not create any deformation due to dispersion while progressing. Soliton solutions are encountered in various nonlinear differential equations such as Korteweg & de Vries equation, the Schrödinger equation, the sine-Gordon equation. The two-dimensional sine-Gordon equation (SGE) arises in quantum tunnelling

related with Josephson junction.

In this section, the one-dimensional quadratic and cubic Klein-Gordon equations, and two-dimensional sine-Gordon equation are solved by using differential quadrature method in space direction and also blockwise in time direction. Initial and derivative boundary conditions are also approximated by DQM.

### 4.3.1 Klein-Gordon equation (KGE)

The nonlinear KGE has the general form

$$u_{tt} + \tau u_{xx} + \alpha u + \gamma u^k = f(x, t), \quad a \leq x \leq b, \quad t \geq 0, \quad (4.51)$$

with the initial conditions

$$u(x, 0) = \phi_1(x), \quad u_t(x, 0) = \phi_2(x), \quad (4.52)$$

and with the Dirichlet or Neumann type boundary conditions, where  $\tau$ ,  $\alpha$ ,  $\gamma$  are known constants. The Eq.(4.51) is called Klein-Gordon equation with quadratic nonlinearity if  $k = 2$ , with cubic nonlinearity if  $k = 3$ .

The linearization of the Eq.(4.51) is done as

$$u_{tt}^{n+1} + \tau u_{xx}^{n+1} + \alpha u^{n+1} + \gamma (u^n)^{k-1} u^{n+1} = f(x, t) \quad (4.53)$$

where  $n$  is the iteration number.

The discretized form of the Eq.(4.53) using the derivative approximations by DQM (Eq.(4.28)) is

$$\sum_{k=1}^L \bar{b}_{lk} u_{ik}^{n+1} + \tau \sum_{k=1}^N b_{ik} u_{kl}^{n+1} + \alpha u_{il}^{n+1} + \gamma \underbrace{(u_{il}^n)^{k-1}} u_{il}^{n+1} = f(x_i, t_l) \quad (4.54)$$

where  $i = 1, \dots, N; l = 1, \dots, L; L, N$  are the total number of grid points in time and space domains, respectively, and  $b_{ik}$  and  $\bar{b}_{lk}$  are the weighting coefficients for the second order derivatives in space and time. The underbraced terms are formed as a diagonal matrix.

The initial condition  $u_t(x, 0)$  is also discretized as

$$u_t(x_i, 0) = \sum_{k=1}^L \bar{a}_{1k} u_{ik} = \phi_2(x_i), \quad i = 1, \dots, N, \quad (4.55)$$

where  $\phi_2$  values are known, and contain the other initial values  $u(x, 0) = \phi_1(x)$  (the values of  $u_{i1}$ ). The algebraic system from Eq.(4.55) is added to the system of Eq.(4.54) resulting in an overdetermined system.

The boundary conditions may be Dirichlet

$$u(a, t) = h_1(t), \quad u(b, t) = h_2(t), \quad t \geq 0, \quad (4.56)$$

or Neumann type

$$u_x(a, t) = r_1(t), \quad u_x(b, t) = r_2(t), \quad t \geq 0. \quad (4.57)$$

Dirichlet type boundary conditions are directly inserted to the system of Eq.(4.54). On the other hand, Neumann type boundary conditions are also discretized by DQM as

$$u_x(a, t_l) = \sum_{k=1}^N a_{1k} u_{kl} = r_1(t_l), \quad (4.58)$$

$$u_x(b, t_l) = \sum_{k=1}^N a_{Nk} u_{kl} = r_2(t_l), \quad l = 1, \dots, L \quad (4.59)$$

which give also an algebraic system and added to the system (4.54) together with Eq.(4.55).

The order of the unknown vector  $\{u\}$  is arranged as

$$\{u\} = \{u_{i1}, u_{i2}, u_{i3}, \dots, u_{iL}\}^T,$$

where  $i = 2, 3, \dots, N-1$  if boundary conditions are Dirichlet type, and  $i = 1, 2, \dots, N$  if Neumann type boundary conditions are used.

When Dirichlet type boundary conditions are given, the system (4.55) of size  $(N-2) \times (N-2)(L-1)$  with the system (4.54) of size  $(N-2)(L-1) \times (N-2)(L-1)$  constructs an overdetermined system of size  $(N-2)L \times (N-2)(L-1)$ . With Neumann boundary conditions, the systems (4.54), (4.55) and (4.58-4.59) will be of sizes  $N(L-1) \times N(L-1)$ ,  $N \times N(L-1)$  and  $2(L-1) \times N(L-1)$ , respectively. Thus, the resulting overdetermined system will be of size  $2(N+L-1) \times N(L-1)$ . Obviously, the system size becomes larger with large values of  $N$  and  $L$ . This may cause unstable results especially when high time-levels are considered. Therefore, we divide the time direction into blocks and consider each block in itself as is shown in Figure 4.5. The advantageous part of DQM emerges from the use of small number of grid points in each time-block as well as in space domain.

As can be seen from Figure 4.5, initial conditions  $u(x, 0)$ ,  $u_t(x, 0)$  for the first block are given.  $u(x, 0)$  for the other blocks is taken as  $u(x, t_L)$  which is the computed result at the last time-value of the previous time-block.

Moreover, we need to define new  $u_t(x, 0)$  condition for the next blocks after the first one. Using the computed results at previous time block, we construct the  $u_t(x, 0)$  for the next time-block by using again DQM approximation of  $u_t$  as

$$u_t(x_i, t_0^m) = u_t(x_i, t_L^{m-1}) = \sum_{k=1}^L \bar{a}_{Lk}^{m-1} u_{ik}^{m-1}, \quad i = 1, 2, \dots, N \quad (4.60)$$

where  $m = 2, \dots, bl$ ,  $bl$  is the number of blocks and  $\bar{a}_{Lk}$  shows the weighting coefficients for the second order derivative in time for one block.

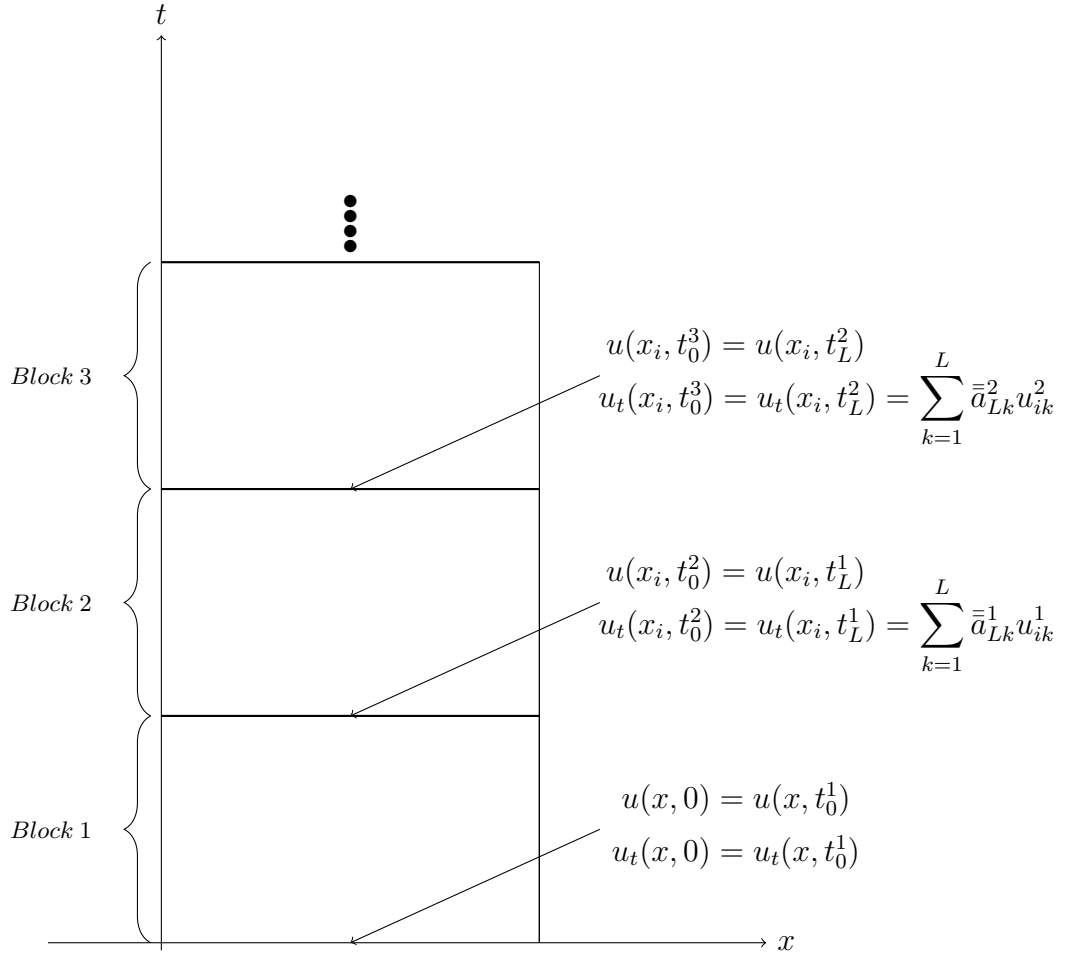


Figure 4.5: Time blocks for 1D KGE.

### 4.3.2 sine-Gordon equation (SGE)

The general form of the two-dimensional sine-Gordon equation is

$$\frac{\partial^2 u}{\partial t^2} + \beta \frac{\partial u}{\partial t} = \frac{\partial^2 u}{\partial x^2} + \frac{\partial^2 u}{\partial y^2} - \Phi(x, y) \sin(u), \quad (x, y) \in \Omega, \quad t > 0. \quad (4.61)$$

where  $\Omega = \left\{ (x, y) \mid a \leq x \leq b, \quad c \leq y \leq d \right\}$ . The initial conditions are given as

$$u(x, y, 0) = f(x, y), \quad \frac{\partial u}{\partial t}(x, y, 0) = g(x, y), \quad (x, y) \in \Omega, \quad (4.62)$$

with boundary conditions

$$\frac{\partial u}{\partial n}(x, y, t) = h(x, y, t), \quad (x, y) \in \partial\Omega, \quad t > 0, \quad (4.63)$$

where  $f, g$  and  $h$  are known continuous functions, and  $\partial u/\partial n$  is the normal derivative of  $u$ .

The function  $\Phi(x, y)$  can be interpreted as a Josephson current density, and  $f(x, y)$  and  $g(x, y)$  are wave modes or kinks and velocity, respectively. The parameter  $\beta$  is called dissipative term, which is assumed to be a real number  $\beta \geq 0$ . When  $\beta = 0$ , equation (4.61) reduces to the undamped SGE in two space variables. When  $\beta > 0$ , the damped SGE is obtained.

The solution procedure for solving SGE using DQM is similar to the solution procedure given for KGE. In that case, domain is two-dimensional and both first and second order time derivatives are approximated by Eqs.(4.40).

Thus, the nonlinear undamped SGE (4.61) is discretized and linearized as

$$\sum_{k=1}^L \bar{b}_{lk} u_{ijk}^{n+1} - \sum_{k=1}^N b_{ik} u_{kjl}^{n+1} - \sum_{k=1}^M \bar{b}_{jk} u_{ikl}^{n+1} = -\Phi(x, y) \sin(u^n) \quad (4.64)$$

where  $n$  is the iteration number,  $i = 1, \dots, N; j = 1, \dots, M; k = 1, \dots, L$ , and  $b_{ik}, \bar{b}_{jk}, \bar{b}_{lk}$  are the weighting coefficients for the second order derivatives in  $x$ -,  $y$ -,  $t$ -domains, respectively, and  $\bar{a}_{lk}$  is the weighting coefficient for the first derivative in time.

The initial and boundary conditions are also discretized by using DQM

$$u_t(x_i, y_j, 0) = g(x_i, y_j) = \sum_{k=1}^L \bar{a}_{1k} u_{ijk}^{n+1} = 0, \quad (4.65a)$$

$$u_y(x_i, c, t_l) = \sum_{k=1}^M \bar{a}_{1k} u_{ikl}^{n+1} = 0, \quad u_y(x_i, d, t_l) = \sum_{k=1}^M \bar{a}_{Mk} u_{ikl}^{n+1} = 0, \quad (4.65b)$$

$$u_x(a, y_j, t_l) = \sum_{k=1}^N a_{Nk} u_{kjl}^{n+1} = 0, \quad u_x(b, y_j, t_l) = \sum_{k=1}^N a_{1k} u_{kjl}^{n+1} = 0, \quad (4.65c)$$

where  $i = 1, \dots, N; j = 1, \dots, M; l = 1, \dots, L$ .

As in the case of Klein-Gordon equation, the system (4.64) together with the initial condition (4.65a) and Neumann boundary conditions (4.65b)-(4.65c) give an overdetermined system for the numerical solution of sine-Gordon equation. The solution procedure is also blockwise in time direction. Time blocks in this two-dimensional case are constructed as shown in Figure 4.6.

The discretized systems in (4.54) and (4.64) are solved iteratively by taking the initial unknown vector  $u^0$  as a zero solution. Then, the iteration is carried till the preassigned convergence criteria is achieved.

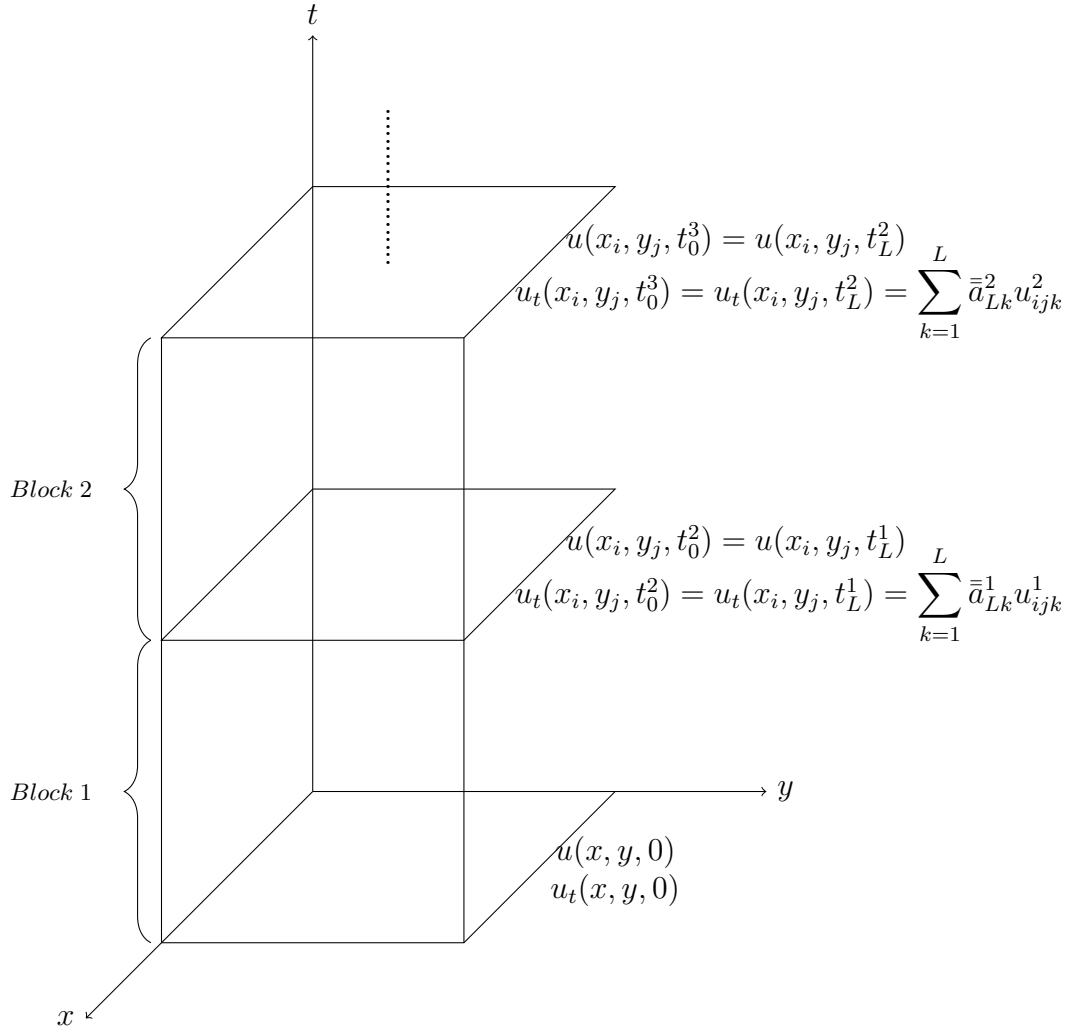


Figure 4.6: Time blocks for 2D sine-Gordon equation.

### 4.3.3 Solution procedure

Numerical solutions are obtained with DQM by using Gauss-Chebyshev-Lobatto(GCL) grid points in space intervals, and GCL grid points in each equally divided time blocks. Due to the overdetermined systems resulting from the insertion of boundary conditions, QR factorization is used for the solution.

The stopping (convergence) criterion is  $\|u^{n+1} - u^n\|_\infty < \epsilon$  with  $\epsilon = 1e - 09$ .

The first and the last time level values of any time block are computed as

$$t_0^m = (m - 1)\frac{T}{bl}, \quad t_L^m = m\frac{T}{bl},$$

where  $T$  is the up time-value.

Some error definitions used in the problems are

$$\begin{aligned} L_\infty &= \max_i \left| u_i^{\text{exact}} - u_i^{\text{computed}} \right|, \quad i = 1, \dots, nod \\ L_2 &= \sqrt{\sum_{i=1}^{nod} (u_i^{\text{exact}} - u_i^{\text{computed}})^2} \\ \text{RMS} &= L_2 / \sqrt{nod}, \end{aligned}$$

where  $nod$  is the total number of grid points in space. These errors at any time-value are computed once the system is solved at one stroke at any time-block.

The energy of cubic nonlinear Klein-Gordon equation is given

$$\begin{aligned} E(t) &= \frac{1}{2} \int_{\mathbb{R}} [u_t^2 + \tau u_x^2 + 2G(u)] dx, \\ &= \frac{1}{2} \int_{\mathbb{R}} \left[ u_t^2 + \tau u_x^2 + \alpha u^2 + \frac{\gamma u^4}{2} \right] dx, \end{aligned} \quad (4.66)$$

and of the sine-Gordon equation (for undamped case  $\beta = 0$ ) is also computed

$$E(t) = \frac{1}{2} \int \int [u_x^2 + u_y^2 + u_t^2 + 2(1 - \cos u)] dx dy. \quad (4.67)$$

as in [96, 55], respectively. For computing integrals (4.66) and (4.67), Clenshaw-Curtis Quadrature [151] is employed since we use GCL grid points in space direction.

#### 4.3.4 Klein-Gordon problems

##### 4.3.4.1 Quadratic Klein-Gordon equation

Consider the Klein-Gordon equation with quadratic nonlinearity and exact solution  $u(x, t) = x \cos(t)$  [130]

$$u_{tt} - u_{xx} + u^2 = -x \cos t + x^2 \cos^2 t, \quad x \in (-1, 1), \quad t > 0, \quad (4.68)$$

subject to the initial conditions

$$u(x, 0) = x, \quad u_t(x, 0) = 0, \quad x \in [-1, 1], \quad (4.69)$$

and Dirichlet boundary conditions

$$u(-1, t) = -\cos(t), \quad u(1, t) = \cos(t), \quad t \geq 0. \quad (4.70)$$

The results in Table 4.6 are obtained by using  $N = 21$  GCL grid points in space direction, and 10 time-blocks with 11 GCL grid points in each block which is a quite coarse grid. It is found that DQM both in space and blockwise in time procedure gives very good accuracy compared to numerical procedures in [53, 130] using considerably small number of grid points both in time and space domains. The accuracy is almost doubled in terms of RMS errors than the errors given in [53], and much better than the accuracy obtained in [130] as can be seen from Table 4.6. Both space and time increments used in our solution procedure are much larger than the ones used in [53, 130].

Table 4.6: Problem 4.3.4.1: Errors in quadratic Klein-Gordon equation.

t	Present Results			In [53]	In [130], Method II
	$L_\infty$	$L_2$	RMS	RMS	RMS
1	1.74e-13	3.96e-13	8.64e-14	6.51e-06	4.89e-10
3	2.68e-12	4.37e-12	9.54e-13	1.17e-05	4.66e-10
5	3.19e-12	5.16e-12	1.13e-12	2.19e-05	9.41e-11
7	2.89e-12	4.91e-12	1.07e-12	2.58e-05	5.09e-10
10	3.60e-12	6.08e-12	1.33e-12	7.95e-06	3.96e-10

#### 4.3.4.2 Kink Wave (Cubic Klein-Gordon equation)

This is a cubic nonlinear KGE in the form [130]

$$u_{tt} - \alpha^2 u_{xx} + \alpha u - \beta u^3 = 0 \quad (4.71)$$

in the region  $-10 \leq x \leq 10$  with initial conditions

$$u(x, 0) = \sqrt{\frac{\alpha}{\beta}} \tanh(\kappa x), \quad u_t(x, 0) = -c \sqrt{\frac{\alpha}{\beta}} \kappa \operatorname{sech}^2(\kappa x), \quad (4.72)$$

where  $\kappa = \sqrt{\frac{\alpha}{2(c^2 - \alpha^2)}}$ , and  $\alpha, \beta, c^2 - \alpha^2 > 0$ . The exact solution is

$$u(x, t) = \sqrt{\frac{\alpha}{\beta}} \tanh(\kappa(x - ct)), \quad (4.73)$$

from which Neumann boundary conditions may be extracted as

$$u_x(-10, t) = \kappa \sqrt{\frac{\alpha}{\beta}} \operatorname{sech}^2(\kappa(-10 - ct)) \quad (4.74)$$

$$u_x(10, t) = \kappa \sqrt{\frac{\alpha}{\beta}} \operatorname{sech}^2(\kappa(10 - ct)). \quad (4.75)$$

Table 4.7 shows the accuracy of the computed solutions with the variations of number of grid points in space and  $\alpha, \beta$  values at  $t = 1$ . As can be seen, when  $\alpha$  is increased (amplitude of the Kink wave  $\sqrt{\alpha/\beta}$  increases), the accuracy reduces. As expected, accuracy is improved when the number of grid points in space direction is increased.

Table 4.8 gives the Kink wave numerical solutions at different times. These results are obtained by dividing  $T = 24$  into 24 time blocks. 11 GCL grid points are used at each time block where the number of iterations carried is 5. Moreover, Table 4.8 presents solutions with  $N = 96$  GCL grid points in space, and  $\alpha = 0.1, \beta = 1, c = 0.3$ .

Figure 4.7 shows the space-time graph of numerical solution of kink wave with  $N = 96$  and  $L = 11$  GCL points in each time blocks up to  $t = 12$ .

In Tables 4.7 and 4.8, the energy differences in magnitude between specific and initial times are also presented.



Table 4.7: Problem 4.3.4.2: Errors for Kink Wave with different number of grid points in space at  $t = 1$ .

N	$L_\infty$	RMS	E(0)	$ E(t) - E(0) $
$\alpha = 0.1, \beta = 1, c = 0.3$				
16	2.13e-03	8.08e-04	0.0509468	3.50e-06
32	1.80e-04	7.32e-05	0.0510529	9.57e-08
64	2.21e-07	1.13e-07	0.0510541	4.19e-12
128	3.07e-12	8.29e-13	0.0510541	2.02e-15
256	1.86e-12	2.11e-13	0.0510541	5.90e-16
$\alpha = 0.1, \beta = 10, c = 0.3$				
16	6.73e-04	2.56e-04	0.0050947	3.50e-07
32	5.69e-05	2.31e-05	0.0051053	9.57e-09
64	6.99e-08	3.56e-08	0.0051054	4.20e-13
128	9.74e-13	2.62e-13	0.0051054	9.80e-17
256	5.92e-13	6.69e-14	0.0051054	2.26e-16
$\alpha = 0.2, \beta = 1, c = 0.3$				
16	1.13e-02	4.42e-03	0.2090723	7.10e-05
32	3.21e-03	9.40e-04	0.2142506	4.59e-05
64	1.55e-04	4.10e-05	0.2150807	1.87e-07
128	1.71e-07	6.72e-08	0.2150849	2.04e-12
256	6.19e-12	2.20e-12	0.2150849	1.52e-13

Table 4.8: Problem 4.3.4.2: Errors for Kink Wave at different times.

t	$L_\infty$	RMS	$ E(t) - E(0) $
9	4.41e-09	1.09e-09	1.66e-12
12	5.25e-09	1.21e-09	6.99e-12
18	3.56e-08	1.38e-08	1.52e-09
24	4.17e-07	1.81e-07	4.37e-07

#### 4.3.4.3 Single-Soliton.

The same nonlinear Klein-Gordon equation  $u_{tt} - \alpha^2 u_{xx} + \alpha u - \beta u^3 = 0$  is solved in the region  $-10 \leq x \leq 10$  with the initial conditions [39, 48, 130]

$$u(x, 0) = \sqrt{\frac{2\alpha}{\beta}} \operatorname{sech}(\lambda x), \quad u_t(x, 0) = c\lambda \sqrt{\frac{2\alpha}{\beta}} \operatorname{sech}(\lambda x) \tanh(\lambda x), \quad (4.76)$$

where  $\lambda = \sqrt{\frac{\alpha}{\alpha^2 - c^2}}$  and  $\alpha, \beta, \alpha^2 - c^2 > 0$ . The exact solution is

$$u(x, t) = \sqrt{\frac{2\alpha}{\beta}} \operatorname{sech}(\lambda(x - ct)), \quad (4.77)$$

where  $c$  is the velocity and the real parameter  $\sqrt{2\alpha/\beta}$  is the amplitude of the wave.

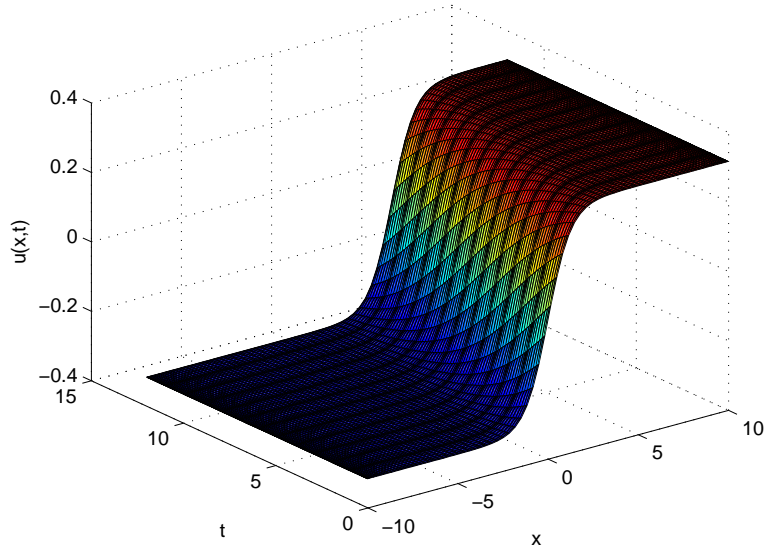


Figure 4.7: Problem 4.3.4.2: Space-time graph of numerical solution of Kink Wave up to  $t = 12$ .

Neumann boundary conditions is extracted from the exact solution as

$$u_x(-10, t) = -\sqrt{\frac{2a}{b}}\lambda \operatorname{sech}(\lambda(-10 - ct)) \tanh(\lambda(-10 - ct)), \quad (4.78)$$

$$u_x(10, t) = -\sqrt{\frac{2a}{b}}\lambda \operatorname{sech}(\lambda(10 - ct)) \tanh(\lambda(10 - ct)). \quad (4.79)$$

Table 4.9 shows errors for the DQM solution using several number of grid points in space direction for  $t = 1$  with  $L = 11$  GCL grid points in one time-block, and  $\alpha = 0.3$ ,  $\beta = 1$ ,  $c = 0.25$ . Furthermore, Table 4.10 shows that DQM gives very good accuracy with  $L = 11$  GCL grid points in each 12 time-blocks up to  $T = 12$  using  $N = 256$ . This again corresponds approximately to  $h = 0.08$  (in the sense of equally spaced grid points) space increment which is larger than the ones used in other numerical methods [48, 130]. Figure 4.8 depicts the space-time numerical solution at different time-levels up to  $t = 12$ .

Energy differences with the initial energy are also tabulated in Table 4.9 and 4.10. It is seen that energy does not change as time progresses.

Table 4.9: Problem 4.3.4.3: Errors for Single Soliton with different number of grid points in space at  $t = 1$ .

N	$L_\infty$	RMS	E(0)	$ E(t) - E(0) $
64	5.96e-02	9.56e-03	0.124433	2.38e-04
128	3.17e-03	4.49e-04	0.119067	2.42e-06
192	1.02e-04	2.08e-05	0.118905	8.52e-09
256	9.01e-06	1.60e-06	0.118904	2.10e-10
320	2.82e-07	5.00e-08	0.118904	5.12e-14

Table 4.10: Problem 4.3.4.3: Errors for Single Soliton at different times.

t	$L_\infty$	RMS	$ E(t) - E(0) $
6	1.64e-05	3.32e-06	4.94e-08
9	1.62e-05	3.71e-06	6.27e-08
12	2.23e-05	4.47e-06	6.81e-08

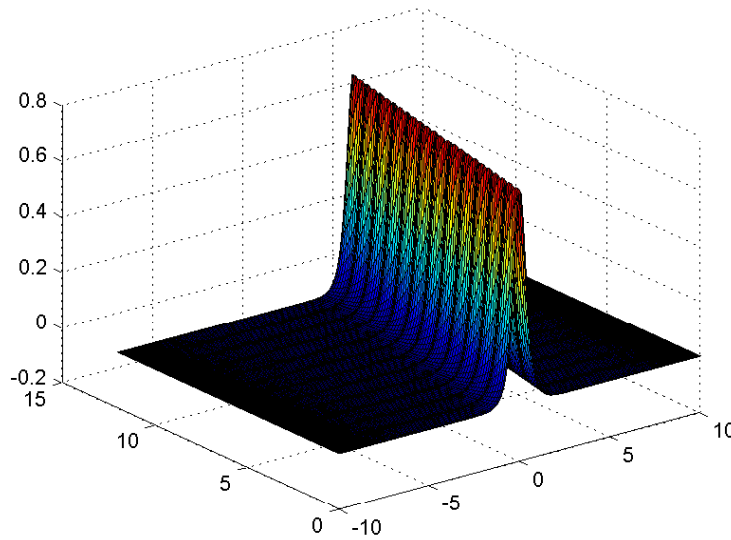


Figure 4.8: Problem 4.3.4.3: Surface plot of Single-Soliton.

#### 4.3.4.4 Double Soliton.

Now, the equation Eq.(4.71) is considered in the region  $-10 \leq x \leq 10$  with the initial conditions [130]

$$u(x, 0) = \sqrt{\frac{2\alpha}{\beta}} [\operatorname{sech}(\lambda_1(x - x_0^1)) + \operatorname{sech}(\lambda_2(x - x_0^2))], \quad (4.80)$$

$$u_t(x, 0) = c_1 \lambda_1 \sqrt{\frac{2\alpha}{\beta}} \operatorname{sech}(\lambda_1(x - x_0^1)) \tanh(\lambda_1(x - x_0^1)) \quad (4.81)$$

$$+ c_2 \lambda_2 \sqrt{\frac{2\alpha}{\beta}} \operatorname{sech}(\lambda_2(x - x_0^2)) \tanh(\lambda_2(x - x_0^2)), \quad (4.82)$$

where  $\lambda_i = \sqrt{\frac{\alpha}{\alpha^2 - c_i^2}}$ ,  $i = 1, 2$  and  $\alpha, \beta, \alpha^2 - c_i^2 > 0$ . The exact solution is

$$u(x, t) = \sum_{i=1}^2 \sqrt{\frac{2\alpha}{\beta}} \operatorname{sech}(\lambda_i(x - c_i t - x_0^i)). \quad (4.83)$$

Since the Neumann boundary conditions  $u_x(-10, t)$  and  $u_x(10, t)$  are almost zero even for large time values, we will also take the zero gradient on the boundary for this case as in [23, 48].

The parameters are taken as  $\alpha = 0.3$ ,  $\beta = 1$ ,  $c_1 = 0.25$ ,  $c_2 = -0.25$ ,  $x_0^1 = -2$  and  $x_0^2 = 2$  as in [23] where  $x_0^1$ ,  $x_0^2$  and  $c_1$ ,  $c_2$  are the initial ( $t=0$ ) positions and velocities of two solitons, respectively.

Table 4.11 shows  $L_\infty$  errors at different time levels.  $L = 11$  GCL grid points in each 7 time blocks up to  $T = 7$  and  $N = 256$  GCL grid points in space are employed. At the collision time  $t = 7.5$ , a blow-up occurs as can be seen in Figure 4.9 for which we used  $N = 320$  GCL points in space and 9 GCL grid points in  $bl = 15$  time blocks up to  $T = 7.5$ .

For the last three examples, the meaning of small difference  $|E(t) - E(0)|$  is that the energy is conserved at any time level.

Table 4.11: Problem 4.3.4.4: Errors for Double Soliton at different times with  $E(0) = 0.237807$ .

t	$L_\infty$	$ E(t) - E(0) $
1	8.76e-06	1.49e-10
2	5.92e-05	1.90e-09
3	3.33e-04	4.17e-09
4	1.79e-03	6.46e-09
5	9.54e-03	8.26e-09
6	5.32e-02	9.74e-09
7	4.02e-01	2.33e-07

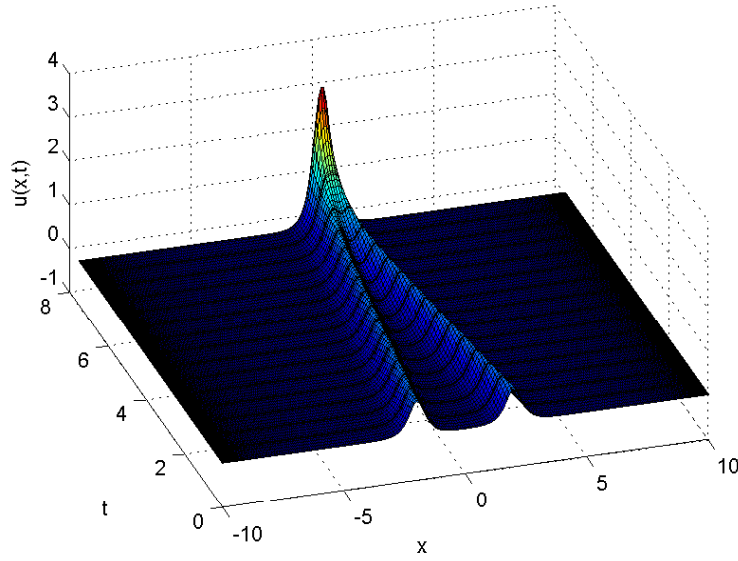


Figure 4.9: Problem 4.3.4.4: Surface plot of collision of two solitons at  $t = 7.5$ .

### 4.3.5 sine-Gordon problems.

#### 4.3.5.1 Test sine-Gordon problem.

The aim of this test problem is to show the advantage of DQM application when the boundary conditions are time dependent.

The SGE Eq.(4.61) is considered with  $\beta = 0$  and  $\Phi = 1$  and the analytical solution [50] as  $u(x, y, t) = 4 \arctan(\exp(x + y - t))$ , and thus the initial conditions [50, 55]

$$u(x, y, 0) = 4 \arctan(\exp(x + y)), \quad -7 \leq x, y \leq 7,$$

$$u_t(x, y, 0) = -\frac{4 \exp(x + y)}{1 + \exp(2x + 2y)}, \quad -7 \leq x, y \leq 7,$$

and boundary conditions are

$$u_x = \frac{4 \exp(x + y + t)}{\exp(2t) + \exp(2x + 2y)}, \quad \text{for } x=-7 \text{ and } x=7, \quad -7 \leq y \leq 7, t > 0,$$

$$u_y = \frac{4 \exp(x + y + t)}{\exp(2t) + \exp(2x + 2y)}, \quad \text{for } y=-7 \text{ and } y=7, \quad -7 \leq x \leq 7, t > 0.$$

As can be seen in Table 4.12, the  $L_\infty$  errors with DQM are less than the  $L_\infty$  errors using RBF in [50]. The errors with DQM are obtained using  $N = M = 36$  GCL grid points in  $xy$ -space with  $bl = 7$  blocks in time and  $L = 5$  GCL grid points in each time block. When the number of grid points in the space domain  $-7 \leq x, y \leq 7$  or in time domain is increased, the increase in accuracy in terms of  $L_\infty$ ,  $L_2$  and RMS errors may be obtained.

The numerical solution at  $t = 7$  is depicted in Figure 4.10(a), and Figure 4.10(b) shows the agreement between numerical and exact solutions when  $y = x$ .

Table 4.12: Problem 4.3.5.1: Errors for sine-Gordon test problem.

t	Present Results			In [50], RBF method
	RMS	$L_2$	$L_\infty$	$L_2$
1	0.0008	0.0279	0.0050	0.2860
3	0.0012	0.0423	0.0062	0.5872
5	0.0016	0.0593	0.0096	0.8288
7	0.0025	0.0893	0.0157	1.0706

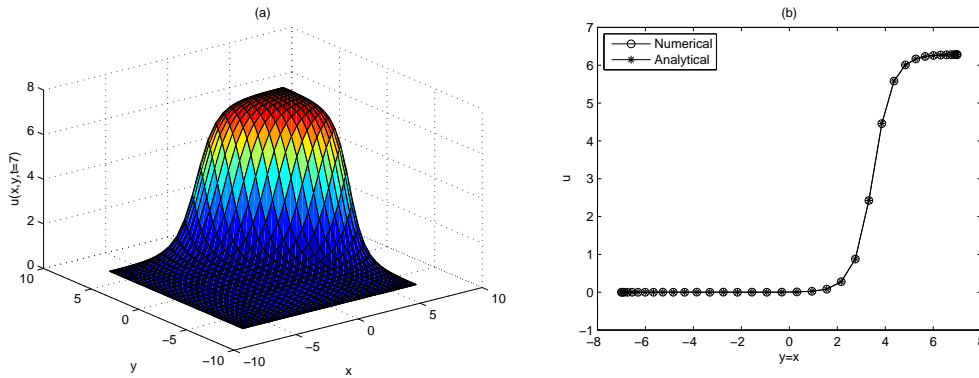


Figure 4.10: Problem 4.3.5.1: Plots for test sine-Gordon problem.

### 4.3.5.2 Line soliton in an inhomogeneous medium

Consider SGE with  $\Phi = 1 + \text{sech}^2 \sqrt{x^2 + y^2}$  while  $\beta = 0$  over the region  $-7 \leq x, y \leq 7$  with the initial conditions [8, 32]

$$u(x, y, 0) = 4 \arctan \left[ \exp \left( \frac{x - 3.5}{0.954} \right) \right],$$

$$u_t(x, y, 0) = 0.629 \text{sech} \left( \frac{x - 3.5}{0.954} \right),$$

and zero gradient on the boundary.

Figures 4.11 are obtained using  $N = M = 21$  GCL grid points in  $xy$ -space,  $L = 5$  GCL points at each 18 time-blocks. These figures are depicted in terms of  $\sin(u/2)$  at times  $t = 0, 6, 12, 18$ . The line soliton is going through  $x$ -direction without undergoing any deformations as in [8]. It is transmitted as a straight line soliton. The deformation occurred in the study of Christiansen and Lomdahl [32] at  $t = 12$  was due to the boundary conditions. In this study, the discretization of Neumann boundary conditions using DQM and adding to the main system is an appropriate approach to eliminate this deformation. DQM has the capability of capturing this transmission through the inhomogeneity.

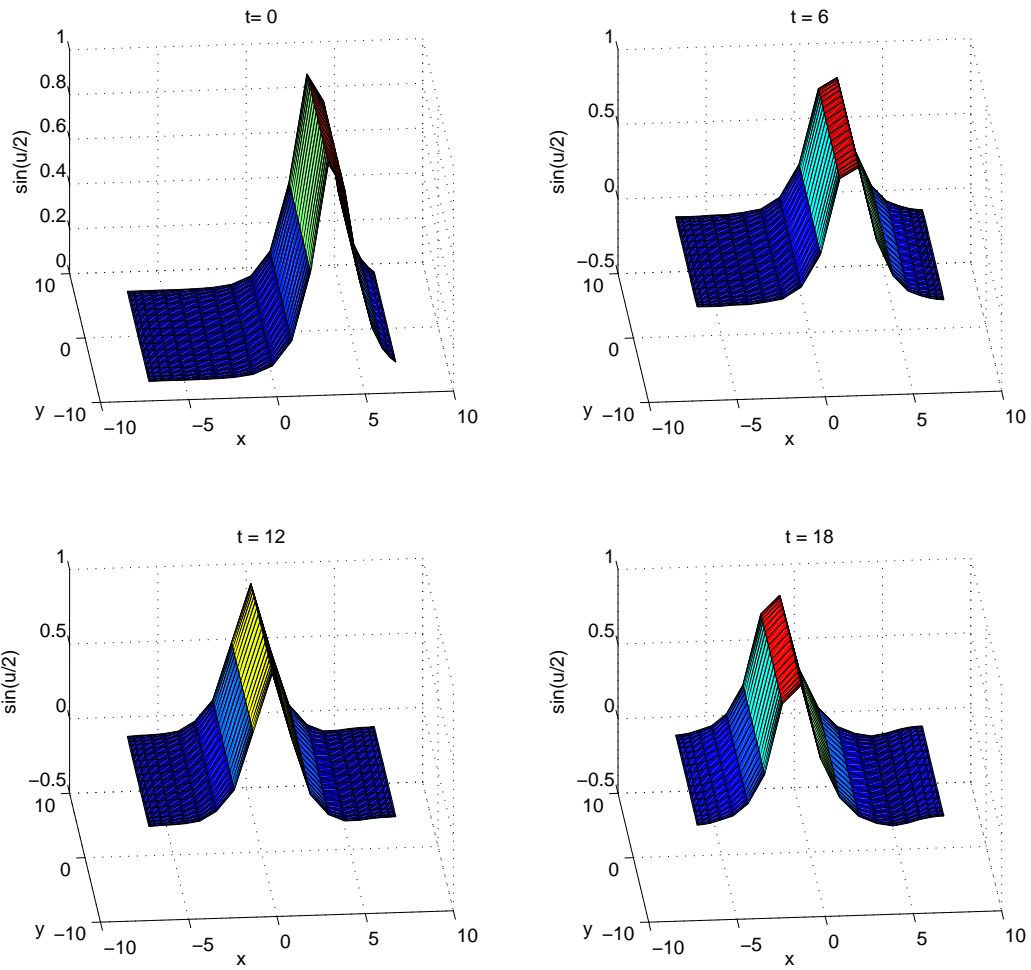


Figure 4.11: Problem 4.3.5.2: Line soliton in an inhomogenous medium.

### 4.3.5.3 Circular ring solitons

For the case  $\Phi = 1$ ,  $\beta = 0$  over the region  $-7 \leq x, y \leq 7$ , the circular ring solitons are obtained with the initial conditions

$$u(x, y, 0) = 4 \arctan \left[ \exp \left( 3 - \sqrt{x^2 + y^2} \right) \right],$$

$$u_t(x, y, 0) = 0,$$

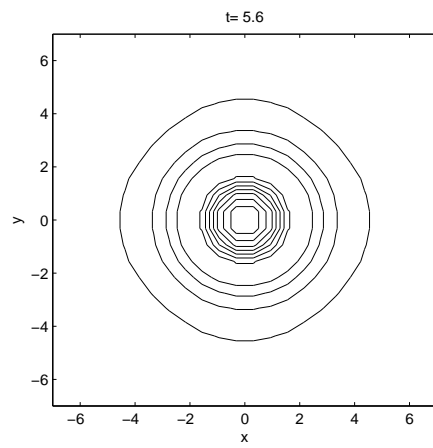
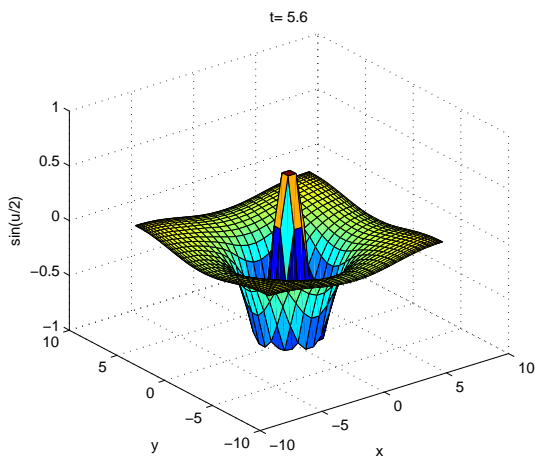
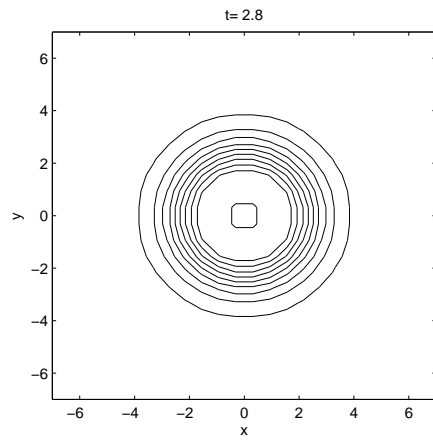
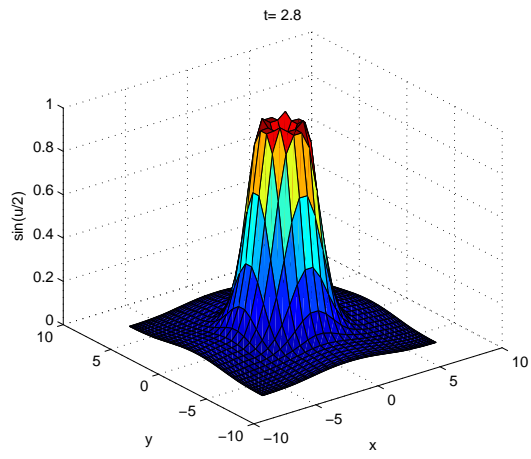
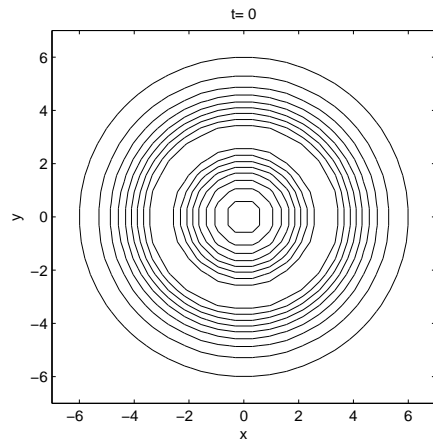
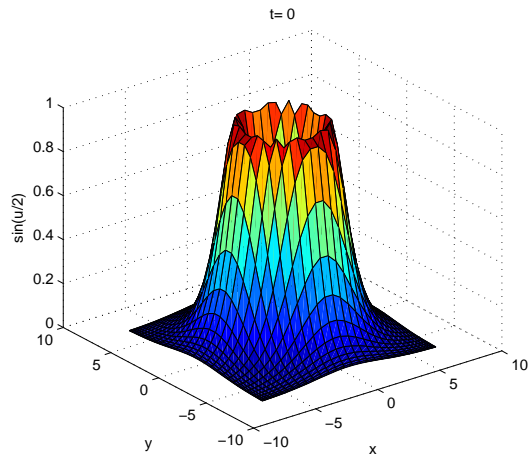
and the zero gradient on the boundary.

Table 4.13 shows the energy at some values of  $t$ . The results are obtained by using  $bl = 18$  time-blocks with  $L = 6$  GCL grid points at each block. It can be seen that the energy is conserved when dissipative term is zero.  $N = M = 36$  GCL grid points are used in space direction to capture good behavior in Figures 4.12. The soliton wave in terms of  $\sin(u/2)$  is drawn with the corresponding contours at different times. From the initial stage to  $t = 2.8$ , shrinks are observed. As time goes on, oscillations and radiations begin to form and continue. Furthermore, the center of soliton does not change during all transformations. The results are in good agreement with [22, 46, 96].

Table 4.13: Problem 4.3.5.3: The energy of the circular ring soliton when  $E(0) = 150.7983$ .

t	t=2.8	t=5.6	t=8.4	t=11.2	t=12.6
$E(t)$	150.7938	150.7588	150.7559	150.7671	150.7724
$ E(t) - E(0) $	0.0045	0.0395	0.0424	0.0312	0.0259





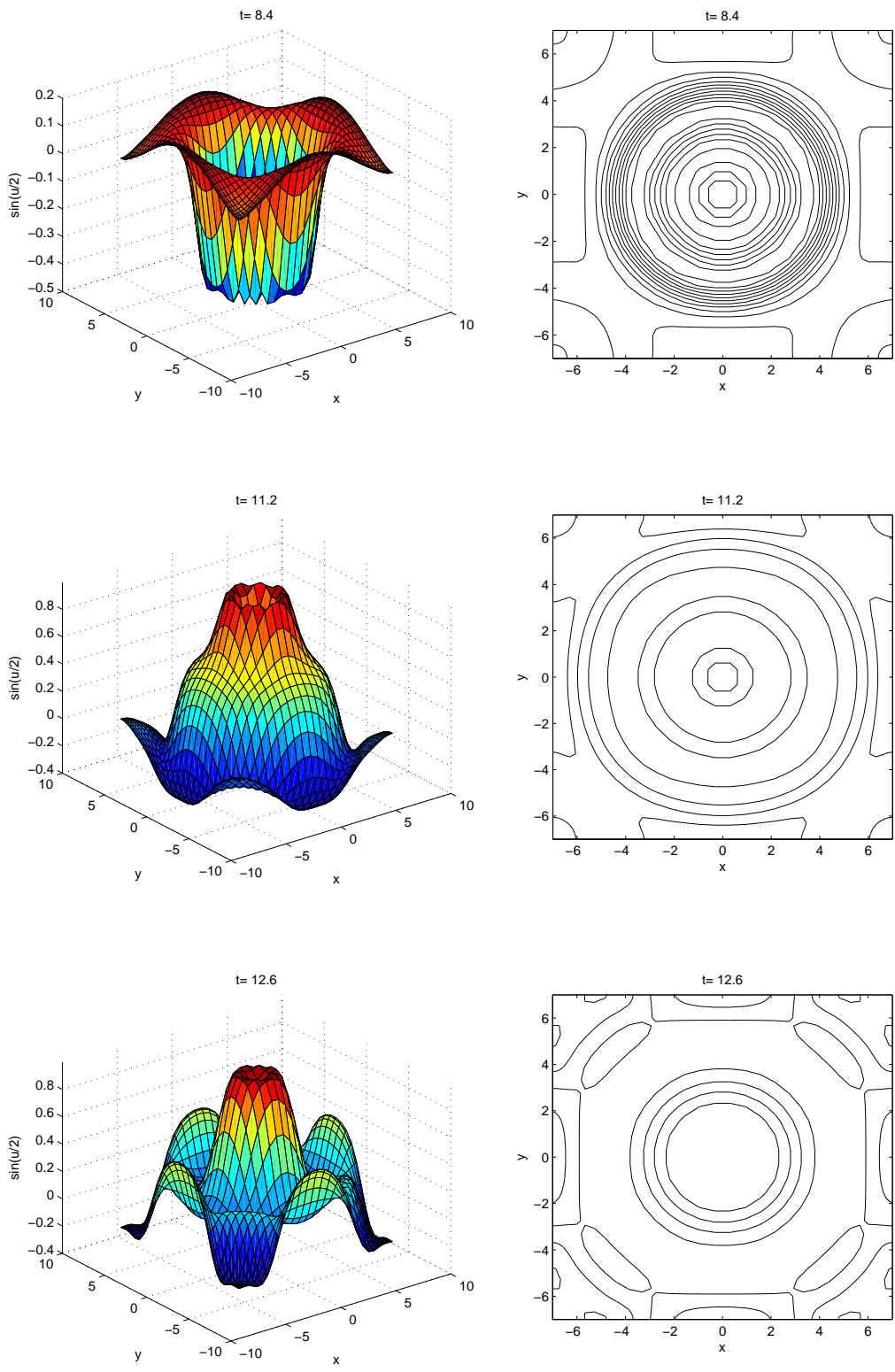


Figure 4.12: Problem 4.3.5.3: Circular ring solitons.

#### 4.3.5.4 Collision of two circular solitons

Two circular ring solitons collide in case of  $\Phi = 1$  and initial conditions [96]

$$u(x, y, 0) = 4 \arctan \left[ \exp \left( \frac{4 - \sqrt{(x+3)^2 + (y+7)^2}}{0.436} \right) \right],$$

$$u_t(x, y, 0) = 4.13 \sinh \left( \frac{4 - \sqrt{(x+3)^2 + (y+7)^2}}{0.436} \right),$$

over the region  $-30 \leq x \leq 10$  and  $-21 \leq y \leq 7$ .

The system is solved in the region  $-10 \leq x \leq 10$  and  $-7 \leq y \leq 7$  and then the solution is expanded by symmetry relations.

In Figures 4.13, surface plots of the collision of two expanding circular ring solitons which are in terms of  $\sin(u/2)$  are depicted using  $N = M = 36$  GCL grid points in space, and 11 time-blocks with  $L = 5$  GCL grid points in each block. A large oval ring soliton which is resulted with the collision between two expanding circular ring solitons is emerged by two oval ring solitons bounding on an annular region. These are in good agreement with the results in [8, 96].

#### 4.3.5.5 Collision of four circular solitons

In this case, four circular ring solitons ( $\Phi = 1$ ,  $\beta = 0$ ) collide with the initial conditions

$$u(x, y, 0) = 4 \arctan \left[ \exp \frac{4 - \sqrt{(x+3)^2 + (y+3)^2}}{0.436} \right],$$

$$u_t(x, y, 0) = 4.13 \operatorname{sech} \left( \frac{4 - \sqrt{(x+3)^2 + (y+3)^2}}{0.436} \right)$$

over the region  $-30 \leq x, y \leq 10$ . The Sine-Gordon equation is solved in  $-10 \leq x, y \leq 10$ , then the solution is expanded using symmetry relations.

We obtain Figures 4.14 in terms of  $\sin(u/2)$  using  $N = M = 41$  GCL points in space and 11 time-blocks up to  $t = 11$  with  $L = 5$  GCL points in each block. As can be observed, there is a complex interaction of the four circular solitons in the center where the values of  $u$  vary rapidly. These are also in good agreement with the results in [8, 96].

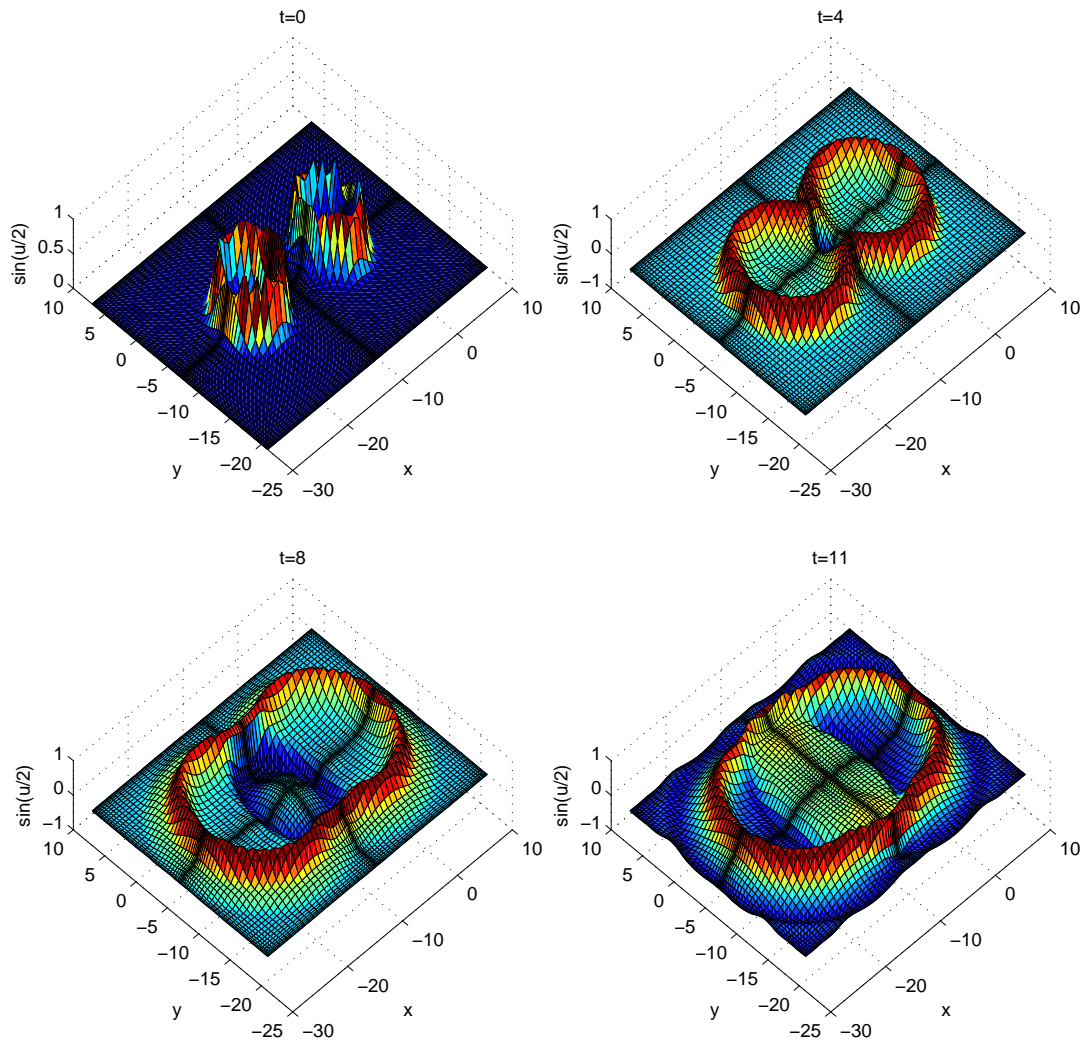


Figure 4.13: Problem 4.3.5.4: Collision of two circular solitons

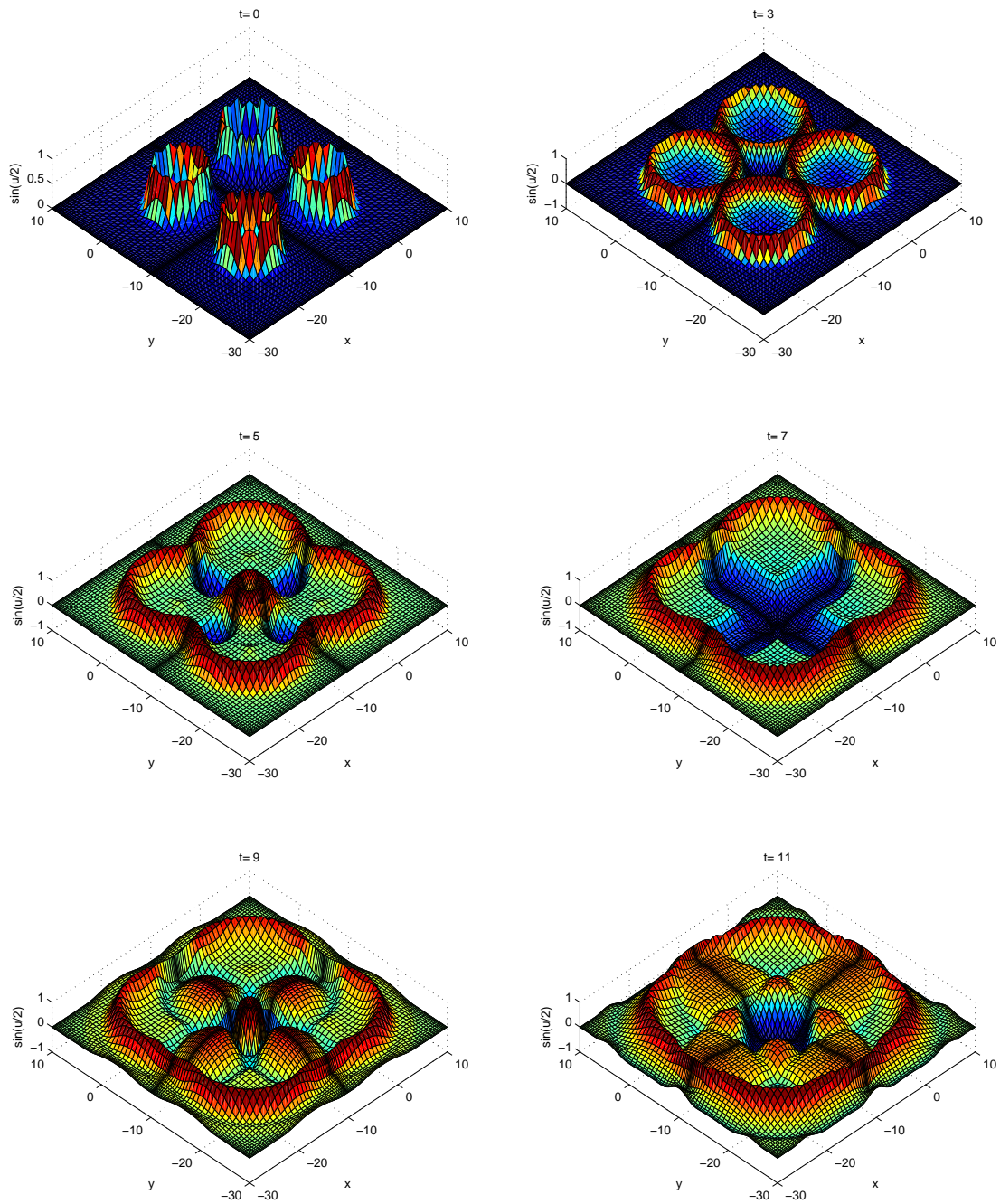


Figure 4.14: Problem 4.3.5.5: Collision of four circular solitons

#### 4.4 The Burgers equations in one- and two-space

As a fundamental partial differential equation from fluid dynamics, Burgers' equation occurs in various areas of applied mathematics such as flow through a shock wave traveling in a viscous fluid, modelling of dynamics, heat conduction, and acoustic waves. Also, Burgers' equation in two-space is a simplified model of incompressible Navier-Stokes equations without considering pressure term. Therefore, the study of Burgers' equation can be considered as a prerequisite to the study of Navier-Stokes equations.

The coupled viscous Burgers' equation in one-space is given by [100]

$$\begin{aligned} u_t - u_{xx} + \eta uu_x + \alpha(vu_x + uv_x) &= 0, & x \in (a, b), t \in (0, T] \\ v_t - v_{xx} + \eta vv_x + \beta(vu_x + uv_x) &= 0, & x \in (a, b), t \in (0, T] \end{aligned} \quad (4.84)$$

with initial and the boundary conditions

$$u(x, 0) = f_1(x), \quad v(x, 0) = f_2(x), \quad (4.85a)$$

$$u(a, t) = \psi_1(a, t), \quad u(b, t) = \psi_2(b, t), \quad (4.85b)$$

$$v(a, t) = \phi_1(a, t), \quad v(b, t) = \phi_2(b, t), \quad (4.85c)$$

where  $\eta$  is a real constant,  $\alpha, \beta$  are arbitrary constants depending on the system parameters such as Peclet number, Stokes velocity of particles due to gravity and Brownian diffusivity [114].

Moreover, the system of two-dimensional Burgers' equations (Navier-Stokes equations without pressure gradient) are [167]

$$u_t + uu_x + vu_y = \frac{1}{Re} (u_{xx} + u_{yy}), \quad (x, y) \in D, t > 0 \quad (4.86a)$$

$$v_t + uv_x + vv_y = \frac{1}{Re} (v_{xx} + v_{yy}), \quad (x, y) \in D, t > 0 \quad (4.86b)$$

subject to initial conditions and Dirichlet or Neumann boundary conditions

$$u(x, y, 0) = h(x, y), \quad v(x, y, 0) = k(x, y), \quad (x, y) \in D \quad (4.87a)$$

$$u(x, y, t) = p(x, y, t), \quad v(x, y, t) = r(x, y, t), \quad (x, y) \in \partial D, t > 0 \quad (4.87b)$$

$$\frac{\partial u}{\partial n} = m(x, y, t) \quad \& \quad \frac{\partial v}{\partial n} = l(x, y, t), \quad (x, y) \in \partial D, t > 0 \quad (4.87c)$$

where  $Re$  is the Reynolds number,  $D = \{(x, y) | a \leq x, y \leq b\}$ ,  $\partial D$  is its boundary, and  $h, k, p, r, m, l$  are known functions.

##### 4.4.1 The coupled Burgers' equations in one-space

The system of Eqs.(4.84) is linearized first with the following iterative procedure

$$\frac{\partial u^{n+1}}{\partial t} - \frac{\partial^2 u^{n+1}}{\partial x^2} + \eta u^n \frac{\partial u^n}{\partial x} + \alpha \left( \frac{\partial u^n}{\partial x} v^n + u^n \frac{\partial v^n}{\partial x} \right) = 0 \quad (4.88a)$$

$$\frac{\partial v^{n+1}}{\partial t} - \frac{\partial^2 v^{n+1}}{\partial x^2} + \eta v^n \frac{\partial v^n}{\partial x} + \beta \left( \frac{\partial u^{n+1}}{\partial x} v^n + u^{n+1} \frac{\partial v^n}{\partial x} \right) = 0. \quad (4.88b)$$

The procedure exploits  $u^{n+1}$  by solving Eq.(4.88a), and then using this  $u^{n+1}$  in Eq.(4.88b) for obtaining  $v^{n+1}$ . Initially,  $u^0$  and  $v^0$  are given, and  $n$  denotes the iteration number.

The differential quadrature method is applied both in time and space directions to the linearized form of the equations Eqs.(4.88a-4.88b). Polynomial based DQ approximations for the derivatives in Eqs.(4.88a-4.88b) can be written as

$$\begin{aligned} u_x &= \sum_{k=1}^N a_{ik} u_{kl}, & u_{xx} &= \sum_{k=1}^N b_{ik} u_{kl}, & i &= 1, \dots, N, \\ v_x &= \sum_{k=1}^N a_{ik} v_{kl}, & v_{xx} &= \sum_{k=1}^N b_{ik} v_{kl}, & i &= 1, \dots, N, \\ u_t &= \sum_{k=1}^L \bar{a}_{lk} u_{ik}, & v_t &= \sum_{k=1}^L \bar{a}_{lk} v_{ik}, & l &= 1, \dots, L, \end{aligned} \quad (4.89)$$

where  $a_{ik}$ ,  $b_{ik}$  are the coefficients of first and second order space derivatives respectively, and  $\bar{a}_{lk}$  are the first order time derivative coefficients.  $N$  and  $L$  are the number of discretization points in  $x$ - and  $t$ -directions, respectively.

The DQM discretization of Eqs.(4.88a-4.88b) are written now

$$\sum_{k=1}^L \bar{a}_{lk} u_{ik}^{n+1} - \sum_{k=1}^N b_{ik} u_{kl}^{n+1} + (\eta u_{il}^n + \alpha v_{il}^n) \sum_{k=1}^N a_{ik} u_{kl}^n + \alpha u_{il}^n \sum_{k=1}^N a_{ik} v_{kl}^n = 0 \quad (4.90a)$$

$$\sum_{k=1}^L \bar{a}_{lk} v_{ik}^{n+1} - \sum_{k=1}^N b_{ik} v_{kl}^{n+1} + (\eta v_{il}^n + \beta u_{il}^{n+1}) \sum_{k=1}^N a_{ik} v_{kl}^n + \beta v_{il}^n \sum_{k=1}^N a_{ik} u_{kl}^{n+1} = 0. \quad (4.90b)$$

Then, the system of Eqs.(4.90a-4.90b) is solved at one stroke in the whole region  $[a, b] \times [0, T]$ .

The iteration between Eq.(4.90a) and Eq.(4.90b) is carried until the convergence criterion

$$\frac{\|u^{n+1} - u^n\|_\infty}{\|u^{n+1}\|_\infty} + \frac{\|v^{n+1} - v^n\|_\infty}{\|v^{n+1}\|_\infty} < \epsilon \quad (4.91)$$

is satisfied with a tolerance  $\epsilon = 1e - 7$ .

#### 4.4.1.1 Test problem for 1D viscous Burgers' equation

In this case, Eq.(4.84) is taken with  $\eta = 2$  for different values of  $\alpha, \beta$  in the region  $x \in [-10, 10]$ ,  $t \in (0, 1]$ . The exact solution is given by [147] as

$$u(x, t) = a_0 (1 - \tanh(A(x - 2At))),$$

$$v(x, t) = a_0 \left( \frac{2\beta - 1}{2\alpha - 1} - \tanh(A(x - 2At)) \right),$$

where  $A = 0.5a_0 \frac{4\alpha\beta - 1}{2\alpha - 1}$  and  $a_0$  is an arbitrary constant. Initial and boundary conditions are extracted from the exact solution.

Table 4.14 shows the  $L_2$  and  $L_\infty$  errors for several values of  $\alpha$  and  $\beta$  at the time values  $t = 0.5$  and  $1.0$ .  $N = 51$  and  $L = 11$  GCL grid points are computed in space (by Eq.(4.18)) and time domains (by Eq.(4.45)). It is noticed that accuracy increases with the decrease in  $a_0$ .

Table 4.14: Problem 4.4.1.1: Errors for 1D Burgers' equations with  $N = 51$ ,  $L = 11$ .

t	$a_0$	$\alpha$	$\beta$	u		v	
				$L_2$	$L_\infty$	$L_2$	$L_\infty$
0.5	0.05	0.1	0.3	7.09e-04	6.78e-05	5.65e-04	3.55e-05
	0.05	0.3	0.03	1.01e-03	1.48e-04	1.45e-03	3.37e-04
	0.005	0.1	0.3	3.54e-05	4.47e-07	2.70e-05	1.78e-07
	0.0005	0.1	0.3	3.49e-06	4.27e-09	2.66e-06	1.63e-09
1	0.05	0.1	0.3	1.21e-03	1.06e-04	9.08e-04	5.45e-05
	0.05	0.3	0.03	1.46e-03	1.48e-04	2.43e-03	4.03e-04
	0.005	0.1	0.3	3.78e-05	4.48e-07	2.84e-05	1.78e-07
	0.0005	0.1	0.3	3.59e-06	4.28e-09	2.73e-06	1.64e-09

#### 4.4.2 The Burgers equations in two-spaces

In order to eliminate the nonlinearity, an iterative system for Eqs.(4.86) is formed as follows

$$\frac{\partial u^n}{\partial t} + u^{n-1} \frac{\partial u^n}{\partial x} + v^{n-1} \frac{\partial u^n}{\partial y} = \frac{1}{Re} \left( \frac{\partial^2 u^n}{\partial x^2} + \frac{\partial^2 u^n}{\partial y^2} \right) \quad (4.92a)$$

$$\frac{\partial v^n}{\partial t} + u^n \frac{\partial v^n}{\partial x} + v^{n-1} \frac{\partial v^n}{\partial y} = \frac{1}{Re} \left( \frac{\partial^2 v^n}{\partial x^2} + \frac{\partial^2 v^n}{\partial y^2} \right), \quad (4.92b)$$

where  $n$  is the iteration number.  $u^n$  is obtained from Eq.(4.92a) and substituted into Eq.(4.92b) for computing  $v^n$ .

Polynomial based DQ is constructed for all derivatives in  $x$ -,  $y$ - and  $t$ -directions in Eq.(4.92a) as

$$u_x = \sum_{k=1}^N a_{ik} u_{kjl}, \quad u_y = \sum_{k=1}^M \bar{a}_{jk} u_{ikl}, \quad u_t = \sum_{k=1}^L \bar{\bar{a}}_{lk} u_{ijk}, \quad (4.93a)$$

$$u_{xx} = \sum_{k=1}^N b_{ik} u_{kjl}, \quad u_{yy} = \sum_{k=1}^M \bar{b}_{jk} u_{ikl}, \quad (4.93b)$$



where  $i = 1, 2, \dots, N$ ;  $j = 1, \dots, M$ ;  $l = 1, 2, \dots, L$ , and  $N, M, L$  are the number of grid points in  $x, y$  and  $t$  spaces, respectively. Similarly, derivatives in Eq.(4.92b) are defined for the  $v$  unknown.

The resulting discretized system of equations may be written as

$$\sum_{k=1}^L \bar{a}_{lk} u_{ijk}^n + \sum_{k=1}^N \left( u_{ijl}^{n-1} a_{ik} - \frac{b_{ik}}{Re} \right) u_{kjl}^n + \sum_{k=1}^M \left( v_{ijl}^{n-1} \bar{a}_{jk} - \frac{\bar{b}_{jk}}{Re} \right) u_{ikl}^n = 0 \quad (4.94a)$$

$$\sum_{k=1}^L \bar{a}_{lk} v_{ijk}^n + \sum_{k=1}^N \left( u_{ijl}^n a_{ik} - \frac{b_{ik}}{Re} \right) v_{kjl}^n + \sum_{k=1}^M \left( v_{ijl}^{n-1} \bar{a}_{jk} - \frac{\bar{b}_{jk}}{Re} \right) v_{ikl}^n = 0. \quad (4.94b)$$

At the beginning,  $u^0$  and  $v^0$  are taken as zero everywhere  $((x_i, y_j, t_l))$ . Firstly, the Eq.(4.94a) is solved at one stroke in each time block. Then, the obtained values of  $u$  are carried out in the second equation (4.94b). The solution procedure continues in this iterative way between these two coupled equations until the stopping criterion Eq.(4.91) is satisfied with  $\epsilon = 1e - 11$ . Also, it is noticed that the computed values at an up time value of a time block are the initial values of the next time block.

#### 4.4.2.1 Test problem for 2D viscous Burgers' equation.

Eqs.(4.86) is concerned in the region  $(x, y) \in [0, 1]$  with the exact solution [167]

$$u(x, y, t) = \frac{3}{4} - \frac{1}{4(1 + \exp(Re(-t - 4x + 4y)/32))} \quad (4.95a)$$

$$v(x, y, t) = \frac{3}{4} + \frac{1}{4(1 + \exp(Re(-t - 4x + 4y)/32))}, \quad (4.95b)$$

and the initial and boundary conditions are taken from this exact solution. The boundary conditions also change with time.

For small  $Re$  numbers, GCL grid points in both directions (by Eq.(4.18) and Eq.(4.45)) give good agreement with the exact results. This is due to strong stability and convergence properties of GCL grid points [142]. In Table 4.15,  $L_\infty$  error is given at different time levels for several values of  $Re$ . Due to the dominance of convection terms with the increase in  $Re$ , the increase in the number of spatial discretization points improves the results. In Table 4.16, DQM results are compared with the exact results at some specific GCL grid points in space with  $Re = 100$ .

For a much larger value of  $Re$ , concerning the system as one block up to  $t = 2$  increasing the number of grid points makes the whole system very large. Therefore, keeping  $N = M$  fixed, time is equally divided into blocks and each block is solved as a whole system. By this way, one enables to make the time increment smaller. Iteration is carried out at each block taking the previous block values as initial iteration values. The results in Table 4.17 obtained by using  $N = M = 23$  with  $L = 7$  in each 9 blocks up to  $t = 2$  (i.e. 0.25 is the time block increment) capture at least  $10^{-2}$  accuracy. Mittal et al. [99] has also solved the same problem by using DQM in space and 4th order Runge

Kutta method in time direction. In that study, for the same Reynolds number, at least  $10^{-2}$  accuracy in  $L_\infty$  error is also seen at equally spaced spatial points.

Table 4.15: Problem 4.4.2.1:  $L_\infty$  errors for 2D Burgers' equations for various values of  $L$  and  $Re$ .

$N = M$	$L$	$Re$	t=1.0		t=2.0	
			$u$	$v$	$u$	$v$
11	11	1	2.00e-15	6.00e-15	2.55e-15	5.22e-15
11	11	10	3.55e-12	3.54e-12	2.80e-12	2.80e-12
11	11	100	1.47e-03	1.47e-03	1.20e-03	1.20e-03
11	21	100	1.48e-03	1.48e-03	1.20e-03	1.20e-03
21	11	100	1.75e-05	1.75e-05	1.04e-05	1.04e-05

Table 4.16: Problem 4.4.2.1: 2D Burgers' equations solution with  $Re = 100$ ,  $N = M = 21$ ,  $L = 13$  at  $t = 0.5, 2$ .

	u		v	
	Exact	DQM	Exact	DQM
t=0.5				
(0.5000,0.0955)	0.50033	0.50033	0.99967	0.99967
(0.2730,0.2730)	0.54332	0.54333	0.95668	0.95667
(0.6545,0.2730)	0.50044	0.50045	0.99956	0.99955
(0.5,0.5)	0.54332	0.54332	0.95668	0.95668
(0.5,0.9045)	0.74263	0.74263	0.75737	0.75737
t=2				
(0.5000,0.0955)	0.50000	0.50000	1.00000	1.00000
(0.2730,0.2730)	0.50048	0.50048	0.99952	0.99952
(0.6545,0.2730)	0.50000	0.50000	1.00000	1.00000
(0.0955,0.5)	0.55815	0.55814	0.94185	0.94186
(0.5,0.5)	0.50048	0.50048	0.99952	0.99952
(0.5,0.9045)	0.55815	0.55815	0.94185	0.94185

Table 4.17: Problem 4.4.2.1: 2D Burgers' equations with  $Re = 1000$ ,  $N = M = 23$ ,  $bl = 9$ ,  $L = 7$  at  $t = 0.5, 2$ .

	u		v	
	Exact	DQM	Exact	DQM
t=0.5				
(0.0794,0.0794)	0.50000	0.49672	1.00000	1.00328
(0.0794,0.5000)	0.75000	0.75243	0.75000	0.74757
(0.0794,0.9206)	0.75000	0.75601	0.75000	0.74398
(0.5000,0.0794)	0.50000	0.49882	1.00000	1.00118
(0.5000,0.5000)	0.50000	0.51162	1.00000	0.98838
(0.5000,0.9206)	0.75000	0.75750	0.75000	0.74252
(0.9206,0.0794)	0.50000	0.50559	1.00000	0.99441
(0.9206,0.5000)	0.50000	0.49212	1.00000	1.00788
(0.9206,0.9206)	0.50000	0.51456	1.00000	0.98548
t=2				
(0.0794,0.0794)	0.50000	0.50984	1.00000	0.99016
(0.0794,0.5000)	0.50001	0.47327	0.99999	1.02673
(0.0794,0.9206)	0.75000	0.73039	0.75000	0.76961
(0.5000,0.0794)	0.50000	0.50356	1.00000	0.99645
(0.5000,0.5000)	0.50000	0.49451	1.00000	1.00548
(0.5000,0.9206)	0.50001	0.48653	0.99999	1.01347
(0.9206,0.0794)	0.50000	0.49954	1.00000	1.00046
(0.9206,0.5000)	0.50000	0.50094	1.00000	0.99906
(0.9206,0.9206)	0.50000	0.49977	1.00000	1.00024

#### 4.5 MHD flow in a rectangular duct

The governing equations of the unsteady MHD duct flow of an incompressible, electrically conducting fluid are of diffusion-convection type, and the velocity field  $V$  is coupled with the induced magnetic field  $B$  in the equations. These coupled equations are easily treated by DQM. Therefore, the DQM discretization of the governing equations in terms of transformed variables, and the numerical results are presented in this section.

Coupled MHD equations are

$$\nabla^2 V + Ha \frac{\partial B}{\partial x} - \frac{\partial V}{\partial t} = -1, \quad (4.96a)$$

$$\nabla^2 B + Ha \frac{\partial V}{\partial x} - \frac{\partial B}{\partial t} = 0, \quad (4.96b)$$

where  $V = B = 0$  on the boundary of the duct which is insulated.  $Ha$  is the Hartmann number given by  $B_0 L \sqrt{\sigma/\nu\rho}$ .

The decoupled form of the dimensionless MHD duct flow equations (4.96) by the

change of variables  $\Psi = V + B$ ,  $\Phi = V - B$  are

$$\nabla^2 \Psi + Ha \frac{\partial \Psi}{\partial x} - \frac{\partial \Psi}{\partial t} = -1, \quad (4.97a)$$

$$\nabla^2 \Phi - Ha \frac{\partial \Phi}{\partial x} - \frac{\partial \Phi}{\partial t} = -1, \quad (4.97b)$$

with the initial and boundary conditions

$$\Psi(x, y, 0) = \Phi(x, y, 0) = 0, \quad (x, y) \in \Omega$$

$$\Psi(x, y, t) = \Phi(x, y, t) = 0, \quad (x, y) \in \partial\Omega.$$

Equations (4.97) are parabolic convection-diffusion equations which become convection dominated for large values of  $Ha$ .

Applying the polynomial based DQ, all the derivatives in Eqs.(4.97) may be arranged as follows

$$\frac{\partial \Psi}{\partial x} = \sum_{k=1}^N a_{ik} \Psi_{kjl}, \quad \frac{\partial^2 \Psi}{\partial x^2} = \sum_{k=1}^N b_{ik} \Psi_{kjl} \quad (4.98)$$

$$\frac{\partial \Psi}{\partial y} = \sum_{k=1}^M \bar{a}_{jk} \Psi_{ikl}, \quad \frac{\partial^2 \Psi}{\partial y^2} = \sum_{k=1}^M \bar{b}_{jk} \Psi_{ikl} \quad (4.99)$$

$$\frac{\partial \Psi}{\partial t} = \sum_{k=1}^L \bar{\bar{a}}_{lk} \Psi_{ijk}, \quad \frac{\partial^2 \Psi}{\partial t^2} = \sum_{k=1}^L \bar{\bar{b}}_{lk} \Psi_{ijk} \quad (4.100)$$

where  $i = 1, \dots, N; j = 1, \dots, M; l = 1, 2, \dots, L$  discretization points on  $x$ -axis,  $y$ -axis and  $t$ -axis, respectively. This formulation is similar for  $\Phi$ .

The discretized forms of the Eq.(4.97a) and Eq.(4.97b) are as follows

$$\sum_{k=1}^N b_{ik} \Psi_{kjl} + \sum_{k=1}^M \bar{b}_{jk} \Psi_{ikl} + Ha \sum_{k=1}^N a_{ik} \Psi_{kjl} - \sum_{k=1}^L \bar{\bar{a}}_{lk} \Psi_{ijk} = -1. \quad (4.101a)$$

$$\sum_{k=1}^N b_{ik} \Phi_{kjl} - \sum_{k=1}^M \bar{b}_{jk} \Phi_{ikl} - Ha \sum_{k=1}^N a_{ik} \Phi_{kjl} - \sum_{k=1}^L \bar{\bar{a}}_{lk} \Phi_{ijk} = -1. \quad (4.101b)$$

The systems (4.101a) and (4.101b) will be solved at one time. The solution set will give all values at each time level. Left hand side of Eq.(4.101a) gives a huge block matrix of size  $(L \times M \times N) \times (L \times M \times N)$ . Concerning the unknown vector as a matrix, each row corresponds to one time level. In order to reduce the system size, Dirichlet boundary conditions are inserted. Furthermore, an iterative solver generalized minimum residual norm (GMRES) is employed to solve the deduced system of equations of the form  $Ax = b$  due to the increase in the system size to obtain the reasonable behavior for large values of  $Ha$ .

Gauss-Chebyshev-Lobatto (GCL) grid points on  $x$  and  $y$  spaces and equally spaced grid points on  $t$ -axis are used. For the rectangular duct  $(-1 \leq x \leq 1, -1 \leq y \leq 1)$ ,

all grid points are computed as

$$x_i = -\cos\left(\frac{i-1}{N-1}\right), \quad y_j = -\cos\left(\frac{j-1}{M-1}\right), \quad t_l = \frac{(l-1)T}{L-1}, \quad (4.102)$$

where  $i = 1, 2, \dots, N; j = 1, 2, \dots, M; l = 1, 2, \dots, L$  and  $T$  is the up time value.

Figure 4.15 shows the behaviors of velocity and induced magnetic field along the  $x$ -axis ( $y = 0, 0 \leq x \leq 1$ ) for  $Ha = 10$  at several time levels. As is seen, almost the same values are obtained at  $t = 0.3$  and  $t = 0.5$ . Namely, the steady-state solution starts at  $t = 0.3$ .

Figures 4.16-4.18 show the surface plots and contours of velocity and induced magnetic field lines from top to bottom at the left column and right column part of the figures, respectively. With the increase in Hartmann number, strong boundary layer formations clustering through the walls is observed both in the velocity and induced magnetic field. Further, the velocity becomes stagnant at the center of the duct.

Due to the small up time values,  $L$  is taken as small in high values of  $Ha$ . As an observation, although the up time value is small, large values of  $L$  may be taken as well as  $N = M$ . However, the expected behavior is not well observed. If the tolerance  $\epsilon = 1e-3$  is attained to determine the steady state ( $\|\Psi_{i,j,n+1} - \Psi_{i,j,n}\|_\infty < \epsilon$  and  $\|\Phi_{i,j,n+1} - \Phi_{i,j,n}\|_\infty < \epsilon$ ), the steady state time values with  $Ha = 10, 100, 500$  are computed as 0.3, 0.1, 0.1, respectively. Alteration in this tolerance and up time value naturally affect the time value to reach the steady-state. Blocks in time also work in this problem.

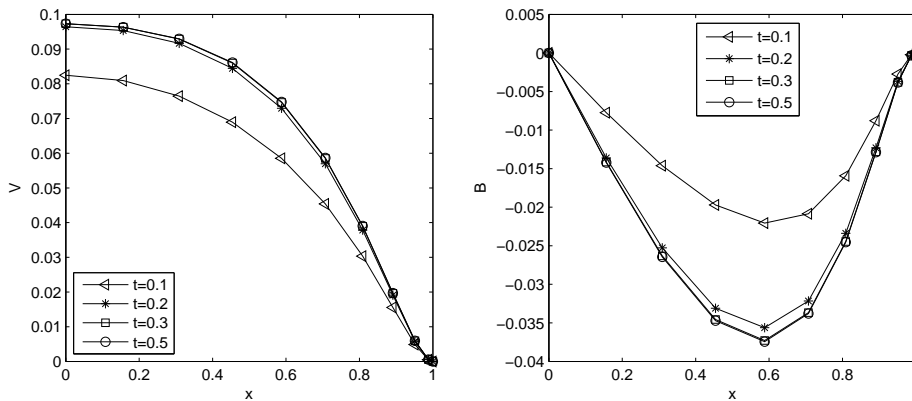


Figure 4.15: Problem 4.5:  $Ha = 10, T = 0.5, N = M = 21, L = 6$

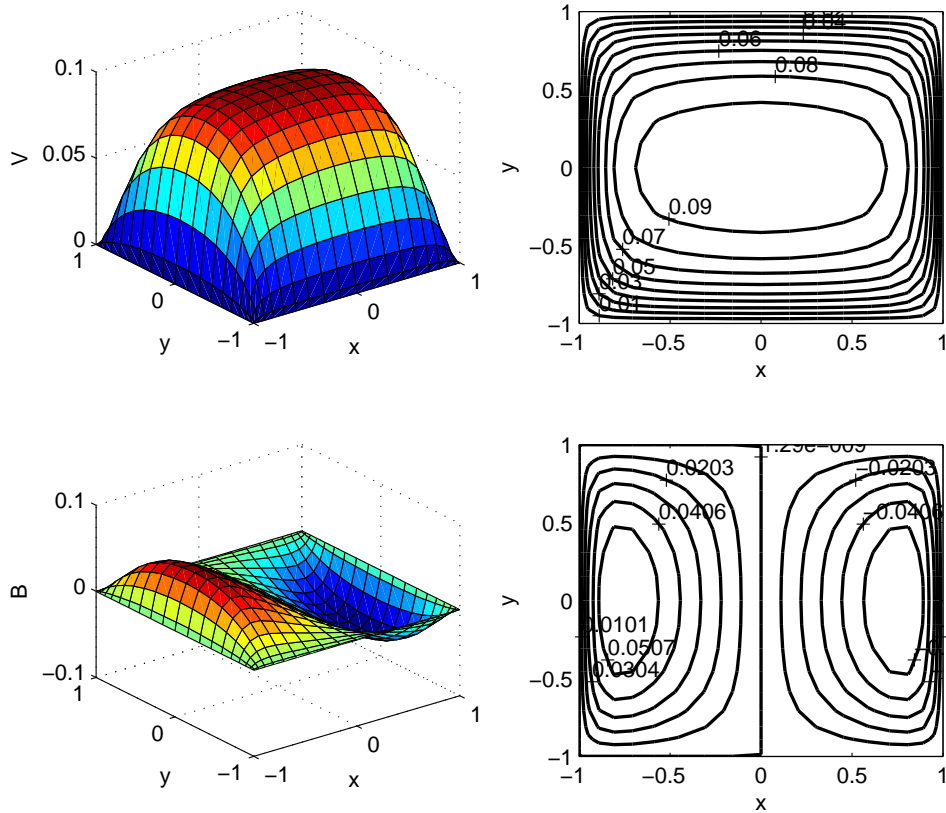


Figure 4.16: Problem 4.5: Surface and contour plots of velocity and induced magnetic field lines with  $Ha = 10$ .

In this chapter, differential quadrature method (DQM) is applied to some prominent physical problems such as 1D and 2D hyperbolic telegraph equations, Klein and sine-Gordon equations, Burgers' equations and MHD duct flow equations. In all problems, time dependent governing equations are discretized by DQM both in time and space directions. In some cases in which the small up time level is required or exists, the system is considered as a whole meaning that the numerical solution is obtained at one stroke. For some other cases, as the space derivatives are discretized by DQM, time derivatives are discretized at each time blocks. That is, the solution is obtained at one stroke in one block and these results provide the progress of iteration for the next time levels. Nonlinearity at all problems is eliminated by an iteration depending on initial condition(s).

The accuracy of the proposed method (DQM both in time and space) is very good when the results are compared with the existent analytical solutions. In general, the results are obtained using considerably small number of grid points. However, the system considered as a whole has large size for 2D problems resulting with high computational cost and much more memory usage than 1D problems. In order to alleviate this drawback, block by block time iterations, boundary conditions (Dirichlet type)

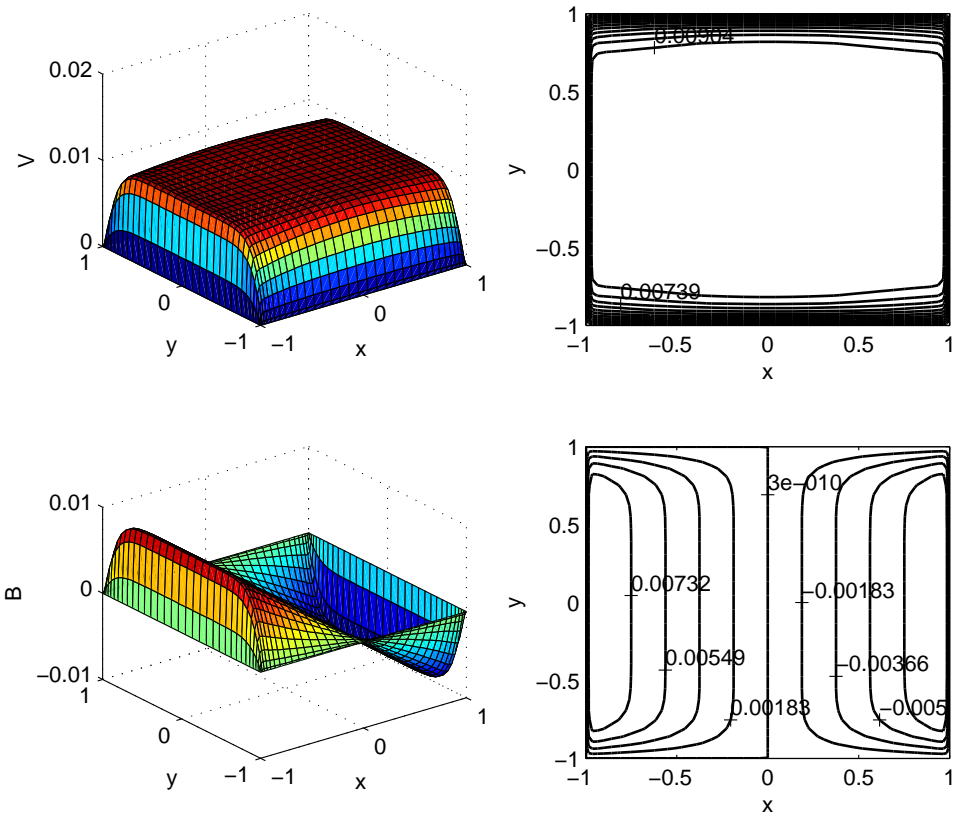


Figure 4.17: Problem 4.5: Surface and contour plots of velocity and induced magnetic field lines with  $Ha = 100$ ,  $T = 0.3$ ,  $N = M = 36$ ,  $L = 4$ .

implementation and the iterative solvers are utilized. Another remarkable point is that the usage of non-uniform grid point distribution exhibits numerically stable results.

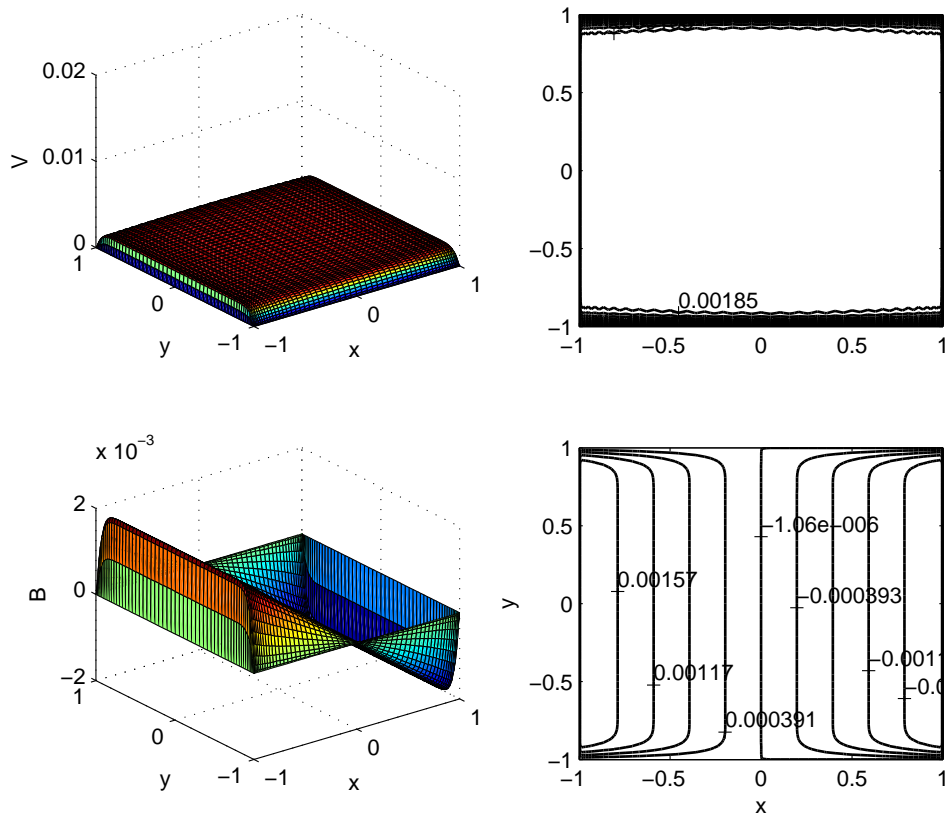


Figure 4.18: Problem 4.5: Surface and contour Plots of velocity and induced magnetic field lines with  $Ha = 500$ ,  $T = 0.3$ ,  $N = M = 61$ ,  $L = 4$ .





## CHAPTER 5

### CONCLUSION

The most parts of this thesis involve the dual reciprocity boundary element solution of mixed (natural and forced) convection flow problems in porous and non-porous medium either in the presence of an applied magnetic field or without the magnetic effect. The two-dimensional incompressible fluid flow governed by the Navier-Stokes equations, and the Maxwell's equations in the presence of magnetic effect are solved numerically. DRBEM is chosen due to the boundary-only nature of the method, and linear boundary elements are adopted throughout the thesis. Further, the DRBEM is capable of using the fundamental solution of Laplace equation, and approximating the inhomogeneous terms by radial basis functions. In particular, DRBEM is used to compute space derivatives with the help of coordinate matrix constructed by radial basis functions.

In an isotropic, homogeneous porous medium, Brinkman-extended Darcy model is adopted. In this case, the decrease in the effective parameter Darcy number gives rise to the slow fluid movement. Under the effect of an applied magnetic field, the problems are considered either neglecting the induced magnetic field or not, according to the value of magnetic Reynolds number. In most of the applications, induced magnetic field is neglected due to the small magnetic permeability of the electrically conducting fluid. The intense imposition of an applied magnetic field (the increase in Hartmann number) causes the fluid to flow slowly, and heat transfer is suppressed. This is a similar effect as in the decrease in Darcy number in a porous medium. Further, the natural convection is pronounced with the increase in buoyancy. In other words, the forced convection (e.g. due to the lid movement in a lid-driven cavity) diminishes.

In addition to the momentum equations and energy equation, considering the induction equations which means that the induced magnetic field is not neglected, the two-dimensional, unsteady, laminar MHD flow of an incompressible, viscous fluid is also solved by DRBEM utilizing a conventional time integration scheme. The governing equations referred as full MHD equations are solved either in terms of magnetic induction components or only magnetic potential and current density variables. In these problems, induced magnetic field or magnetic potential behaviors are altered with the variation in magnetic Reynolds number.

Apart from the applications of DRBEM to fluid flow problems, differential quadrature method is also used for solving mostly hyperbolic, and parabolic type partial differ-

ential equations. DQM is applied both in discretization of time and space derivatives. This enables one to obtain the numerical results at one stroke. However, in 2D problems, the discretized system both in space and time results in a large sized system of equations causing high computational cost and memory usage. Therefore, the proposed method progresses block by block in time dividing time into blocks. In general, the computed results are obtained by using considerably small number of grid points by DQM compared to the other domain discretization methods.

Further investigations should be concentrated on the domain decompositions in the applications of DRBEM and DQM for complicated regions. Also, mixed convection flow in a porous enclosure containing an electrically conducting obstruction under the effect of an applied magnetic field should be investigated.

## REFERENCES

- [1] R. Abazari and A. Borhanifar, Numerical study of the solution of the Burgers and coupled Burgers equations by a differential transformation method, *Computers & Mathematics with Applications*, 59(8), pp. 2711–2722, 2010.
- [2] S. Abbasbandy, Numerical solution of non-linear Klein-Gordon equations by variational iteration method, *International Journal for Numerical Methods in Engineering*, 70(7), pp. 876–881, 2007.
- [3] H. Abbassi and S. Ben Nasrallah, MHD flow and heat transfer in a backward-facing step, *International Communications in Heat and Mass Transfer*, 34, pp. 231–237, 2007.
- [4] M. A. Abdou and A. A. Soliman, Variational iteration method for solving Burger's and coupled Burger's equations, *Journal of Computational and Applied Mathematics*, 181(2), pp. 245–251, 2005.
- [5] N. M. Al-Najem, K. M. Khanafer, and M. M. El-Refae, Numerical study of laminar natural convection in tilted enclosure with transverse magnetic field, *International Journal of Numerical Methods for Heat & Fluid Flow*, 8(6), pp. 651–672, 1998.
- [6] S. Alchaar, P. Vasseur, and E. Bilgen, The effect of a magnetic field on natural convection in a shallow cavity heated from below, *Chemical Engineering Communications*, 134(1), pp. 195–209, 1995.
- [7] M. H. Aliabadi and P. H. Wen, *Boundary Element Methods in Engineering and Sciences*, Imperial College Press, 2011.
- [8] J. Argyris, M. Haase, and J. C. Heinrich, Finite Element Approximation to two-dimensional sine-Gordon solitons, *Computer Method in Applied Mechanics and Engineering*, 86(1), pp. 1–26, 1991.
- [9] F. Armero and J. C. Simo, Long-term dissipativity of time-stepping algorithms for an abstract evolution equation with applications to the incompressible MHD and Navier-Stokes equations, *Computer Methods in Applied Mechanics and Engineering*, 131(1-2), pp. 41–90, 1996.
- [10] S. H. Aydin, Two-level finite element method with a stabilizing subgrid for the natural convection flow simulation in different geometries, *Numerical Heat Transfer, Part A*, 59(10), pp. 799–813, 2011.
- [11] S. H. Aydin, A. I. Neslitürk, and M. Tezer-Sezgin, Two-level finite element method with a stabilizing subgrid for the incompressible MHD equations, *International Journal For Numerical Methods in Fluids*, 62, pp. 188–210, 2010.

- [12] T. Basak, P. V. K. Pradeep, S. Roy, and I. Pop, Finite element based heatline approach to study mixed convection in a porous square cavity with various wall thermal boundary conditions, *International Journal of Heat and Mass Transfer*, 54(9-10), pp. 1706–1727, 2011.
- [13] T. Basak, S. Roy, S. K. Singh, and I. Pop, Analysis of mixed convection in a lid-driven porous square cavity with linearly heated side wall(s), *International Journal of Heat and Mass Transfer*, 53(9-10), pp. 1819–1840, 2010.
- [14] A. C. Baytas and I. Pop, Free convection in oblique enclosures filled with a porous medium, *International Journal of Heat and Mass Transfer*, 42(6), pp. 1047–1057, 1999.
- [15] R. E. Bellman, B. G. Kashef, and J. Casti, Differential quadrature: A technique for the rapid solution of nonlinear partial differential equations, *Journal of Computational Physics*, 10(1), pp. 40–52, 1972.
- [16] P. Bhave, A. Narasimhan, and D. Rees, Natural convection heat transfer enhancement using adiabatic block: Optimal block size and Prandtl number effect, *International Journal of Heat and Mass Transfer*, 49(21-22), pp. 3807–3818, 2006.
- [17] W. Bian, P. Vasseur, E. Bilgen, and F. Meng, Effect of an electromagnetic field on natural convection in an inclined porous layer, *International Journal of Heat and Fluid Flow*, 17(1), pp. 36–44, 1996.
- [18] G. Biswas, M. Breuer, and F. Durst, Backward-facing step flows for various expansion ratios at low and moderate Reynolds numbers, *Journal of Fluids Engineering*, *Transaction of the ASME*, 126, pp. 362–374, 2004.
- [19] C. Bozkaya and M. Tezer-Sezgin, Boundary element solution of unsteady magnetohydrodynamics duct flow with differential quadrature time integration scheme, *International Journal for Numerical Methods in Fluids*, 51(5), pp. 567–584, 2006.
- [20] N. Bozkaya and M. Tezer-Sezgin, The DRBEM solution of incompressible MHD flow equations, *International Journal For Numerical Methods in Fluids*, 67(10), pp. 1264–1282, 2011.
- [21] A. G. Bratsos, An explicit numerical scheme for the sine-Gordon equation in 2+1 dimensions, *Applied Numerical Analysis and Computational Mathematics*, 2(2), pp. 189–211, 2005.
- [22] A. G. Bratsos, The solution of the two-dimensional sine-Gordon equation using the method of lines, *Journal of Computational and Applied Mathematics*, 206(1), pp. 251–277, 2007.
- [23] A. G. Bratsos, On the numerical solution of the Klein-Gordon equation, *Numerical Methods for Partial Differential Equations*, 25(4), pp. 939–951, 2009.
- [24] C. A. Brebbia and J. Dominguez, *Boundary Element - An Introductory Course*, WIT Press; Computational Mechanics Publications, 1996.

- [25] M. Breuer, J. Bernsdorf, T. Zeiser, and F. Durst, Accurate computations of the laminar flow past a square cylinder based on two different methods: lattice-Boltzmann and finite-volume, *International Journal of Heat and Fluid Flow*, 21(2), pp. 186–196, 2000.
- [26] T. R. Bridges and L. C. Wrobel, A dual reciprocity formulation for elasticity problems with body forces using augmented thin plate splines, *Communications in Numerical Methods in Engineering*, 12(3), pp. 209–220, 1996.
- [27] A. J. Chamkha, Hydromagnetic combined convection flow in a vertical lid-driven cavity with internal heat generation or absorption, *Numerical Heat Transfer, Part A: Applications*, 41(5), pp. 529–546, 2002.
- [28] T. S. Chang and Y. L. Tsay, Natural convection heat transfer in an enclosure with a heated backward step, *International Journal of Heat and Mass Transfer*, 44(20), pp. 3963 – 3971, 2001.
- [29] S. C. Chapra, *Applied numerical methods with MATLAB for engineers and scientists*, New York : McGraw-Hill, 2012.
- [30] D. Chatterjee, MHD mixed convection in a lid-driven cavity including a heated source, *Numerical Heat Transfer, Part A*, 64, pp. 235 – 254, 2013.
- [31] C. Y. Choi and E. Balaras, A dual reciprocity boundary element formulation using the fractional step method for the incompressible Navier-Stokes equations, *Engineering Analysis with Boundary Elements*, 33(6), pp. 741–749, 2009.
- [32] P. L. Christiansen and P. S. Lomdahl, Numerical solution of 2+1 dimensional sine-Gordon solitons, *Physica 2D*, pp. 482–494, 1981.
- [33] R. Codina and N. Hernández-Silva, Stabilized finite element approximation of the stationary magneto-hydrodynamics equations, *Computational Mechanics*, 38(4-5), pp. 344–355, 2006.
- [34] M. J. Colaço, G. S. Dulikravich, and H. R. B. Orlande, Magnetohydrodynamic simulations using radial basis functions, *International Journal of Heat and Mass Transfer*, 52(25-26), pp. 5932–5939, 2009.
- [35] V. A. F. Costa, A. C. M. Sousa, and P. Vasseur, Natural convection in square enclosures filled with fluid-saturated porous media under the influence of the magnetic field introduced by two parallel vertical electric currents, *International Journal of Heat and Mass Transfer*, 55(23-24), pp. 7321–7329, 2012.
- [36] S. Das and R. Sahoo, Effect of Darcy, fluid Rayleigh and heat generation parameters on natural convection in a porous square enclosure: A Brinkman-extended Darcy model, *International Communications in Heat and Mass Transfer*, 26(4), pp. 569–578, 1999.
- [37] P. A. Davidson, *An Introduction to Magnetohydrodynamics*, Cambridge University Press, 2001.

- [38] G. V. Davis, Natural convection of air in a square cavity: A bench mark numerical solution, *International Journal for Numerical Methods in Fluids*, 3(3), pp. 249–264, 1983.
- [39] M. Dehghan and A. Ghesmati, Application of the dual reciprocity boundary integral equation technique to solve the nonlinear Klein-Gordon equation, *Computer Physics Communications*, 181(8), pp. 1410–1418, 2010.
- [40] M. Dehghan and A. Ghesmati, Combination of meshless local weak and strong (MLWS) forms to solve the two dimensional hyperbolic telegraph equation, *Engineering Analysis with Boundary Elements*, 34(4), pp. 324–336, 2010.
- [41] M. Dehghan and A. Ghesmati, Numerical simulation of two-dimensional sine-Gordon solitons via a local weak meshless technique based on the radial point interpolation method (RPIM), *Computer Physics Communications*, 181(4), pp. 772–786, 2010.
- [42] M. Dehghan and A. Ghesmati, Solution of the second-order one-dimensional hyperbolic telegraph equation by using the dual reciprocity boundary integral equation (DRBIE) method, *Engineering Analysis with Boundary Elements*, 34(1), pp. 51–59, 2010.
- [43] M. Dehghan, A. Hamidi, and M. Shakourifar, The solution of coupled Burgers' equations using Adomian-Padé technique, *Applied Mathematics and Computation*, 189(2), pp. 1034–1047, 2007.
- [44] M. Dehghan and M. Lakestani, The use of Chebyshev cardinal functions for the solution of the second-order one-dimensional telegraph equation, *Numerical Methods for Partial Differential Equations*, 25(4), pp. 931–938, 2009.
- [45] M. Dehghan and D. Mirzaei, The boundary integral equation approach for numerical solution of the one-dimensional sine-Gordon Equation, *Numerical Methods for Partial Differential Equations*, 24(6), pp. 1405–1415, 2008.
- [46] M. Dehghan and D. Mirzaei, The dual reciprocity boundary element method (DRBEM) for two-dimensional sine-Gordon equation, *Computer Methods in Applied Mechanics and Engineering*, 197(6-8), pp. 476–486, 2008.
- [47] M. Dehghan and A. Mohebbi, High order implicit collocation method for solution of two-dimensional linear hyperbolic equation, *Numerical Methods for Partial Differential Equations*, 25(1), pp. 232–243, 2009.
- [48] M. Dehghan, A. Mohebbi, and Z. Asgari, Fourth-order compact solution of the nonlinear Klein-Gordon equation, *Numerical Algorithms*, 52(4), pp. 523–540, 2009.
- [49] M. Dehghan and A. Shokri, A numerical method for one-dimensional nonlinear sine-Gordon equation using collocation and radial basis functions, *Numerical Methods for Partial Differential Equations*, 24(2), pp. 687–698, 2008.
- [50] M. Dehghan and A. Shokri, A numerical method for solution of the two-dimensional sine-Gordon equation using the radial basis functions, *Mathematics and Computers in Simulation*, 79(3), pp. 700–715, 2008.

- [51] M. Dehghan and A. Shokri, A numerical method for solving the hyperbolic telegraph equation, *Numerical Methods for Partial Differential Equations*, 24(4), pp. 1080–1093, 2008.
- [52] M. Dehghan and A. Shokri, A meshless method for numerical solution of a linear hyperbolic equation with variable coefficients in two space dimensions, *Numerical Methods for Partial Differential Equations*, 25(2), pp. 494–506, 2009.
- [53] M. Dehghan and A. Shokri, Numerical solution of the nonlinear Klein-Gordon equation using radial basis functions, *Journal of Computational and Applied Mathematics*, 230(2), pp. 400–410, 2009.
- [54] H. Ding and Y. Zhang, A new fourth order compact finite difference scheme for the two-dimensional second-order hyperbolic equation, *Journal of Computational and Applied Mathematics*, 230(2), pp. 626–632, 2009.
- [55] K. Djidjeli, W. G. Price, and E. H. Twizell, Numerical Solutions of a damped sine-Gordon in two space variables, *Journal of Engineering Mathematics*, 29(4), pp. 347–369, 1995.
- [56] M. C. Ece and E. Büyük, Natural-convection flow under a magnetic field in an inclined rectangular enclosure heated and cooled on adjacent walls, *Fluid Dynamics Research*, 38(8), pp. 564–590, 2006.
- [57] M. M. El-Refae, M. M. Elsayed, N. M. Al-Najem, and A. A. Noor, Natural convection in a partially cooled tilted cavities, *International Journal for Numerical Methods in Fluids*, 28(3), pp. 477–499, 1998.
- [58] J. P. Garandet, T. Alboussiere, and R. Moreau, Buoyancy driven convection in a rectangular enclosure with a transverse magnetic field, *International Journal of Heat and Mass Transfer*, 35(4), pp. 741–748, 1992.
- [59] D. K. Gartling, A test problem for outflow boundary conditions - Flow over a backward-facing step, *International Journal For Numerical Methods in Fluids*, 11(7), pp. 953–967, 1990.
- [60] J. F. Gerbeau, A stabilized finite element method for the incompressible magnetohydrodynamic equations, *Numerische Mathematik*, 87(1), pp. 83–111, 2000.
- [61] F. Ghadi, V. Ruas, and M. Wakrim, Numerical solution of the time-dependent incompressible Navier-Stokes equations by piecewise linear finite elements, *Journal of Computational and Applied Mathematics*, 215(2), pp. 429–437, 2008.
- [62] U. Ghia, K. N. Ghia, and C. T. Shin, High-Re solutions for incompressible flow using the Navier-Stokes equations and a multigrid method, *Journal of Computational Physics*, 48(3), pp. 387–411, 1982.
- [63] M. A. Golberg and C. S. Chen, The theory of radial basis functions applied to the BEM for inhomogeneous partial differential equations, *Boundary Element Communications*, 5, pp. 57–61, 1994.



- [64] T. Grosan, C. Revnic, I. Pop, and D. B. Ingham, Magnetic field and internal heat generation effects on the free convection in a rectangular cavity filled with a porous medium, *International Journal of Heat and Mass Transfer*, 52(5-6), pp. 1525–1533, 2009.
- [65] M. Ha, I. Kim, H. Yoon, K. Yoon, J. Lee, S. Balachandar, and H. Chun, Two-dimensional and unsteady natural convection in a horizontal enclosure with a square body, *Numerical Heat Transfer, Part A*, 41(2), pp. 183–210, 2002.
- [66] A. Hasanpour, M. Farhadi, K. Sedighi, and H. R. Ashorynejad, Numerical study of Prandtl effect on MHD flow at lid-driven porous cavity, *International Journal for Numerical Methods in Fluids*, 70(7), pp. 886–898, 2012.
- [67] M. A. Hossain and M. Wilson, Natural convection flow in a fluid-saturated porous medium enclosed by non-isothermal walls with heat generation, *International Journal of Thermal Sciences*, 41(5), pp. 447–454, 2002.
- [68] H. Hosseinzadeh, M. Dehghan, and D. Mirzaei, The boundary elements method for magneto-hydrodynamic (MHD) channel flows at high Hartmann number, *Applied Mathematical Modelling*, 37, pp. 2337–2351, 2013.
- [69] S. Hussain and A. Hussein, Numerical investigation of natural convection phenomena in a uniformly heated circular cylinder immersed in square enclosure filled with air at different vertical locations, *International Communications in Heat and Mass Transfer*, 37(8), pp. 1115–1126, 2010.
- [70] D. Ingham and I. Pop, *Transport phenomena in porous media*, Pergamon, 2005.
- [71] A. Islam, M. Sharif, and E. Carlson, Mixed convection in a lid-driven square cavity with an isothermally heated square blockage inside, *International Journal of Heat and Mass Transfer*, 55(19-20), pp. 5244–5255, 2012.
- [72] R. Iwatsu, J. M. Hyun, and K. Kuwahara, Mixed convection in a driven cavity with a stable vertical temperature gradient, *International Journal of Heat and Mass Transfer*, 36(6), pp. 1601–1608, 1993.
- [73] J. C. Kalita and M. M. Gupta, A streamfunction-velocity approach for 2D transient incompressible viscous flows, *International Journal For Numerical Methods in Fluids*, 62(3), pp. 237–266, 2010.
- [74] R. P. Kanna and M. K. Das, Conjugate heat transfer study of backward-facing step flow - A benchmark problem, *International Journal of Heat and Mass Transfer*, 49(21-22), pp. 3929–3941, 2006.
- [75] A. S. V. R. Kanth and K. Aruna, Differential transform method for solving the linear and nonlinear Klein-Gordon equation, *Computer Physics Communications*, 180(5), pp. 708–711, 2009.
- [76] S. R. Karur and P. A. Ramachandran, Augmented thin plate spline approximation in DRM, *Boundary Elements Communications*, 6, pp. 55–58, 1995.

- [77] K. Khanafer, B. Al-Azmi, A. Al-Shammari, and I. Pop, Mixed convection analysis of laminar pulsating flow and heat transfer over a backward-facing step, *International Journal of Heat and Mass Transfer*, 51(25-26), pp. 5785–5793, 2008.
- [78] K. M. Khanafer, M. A. Al-Amiri, and I. Pop, Numerical simulation of unsteady mixed convection in a lid-driven cavity using an externally excited sliding lid, *European Journal of Mechanics B/Fluids*, 26(5), pp. 669–687, 2007.
- [79] K. M. Khanafer and A. J. Chamkha, Hydromagnetic natural convection from an inclined porous square enclosure with heat generation, *Numerical Heat Transfer, Part A: Applications*, 33(8), pp. 891–910, 1998.
- [80] M. K. Khanafer and A. Chamkha, Mixed convection flow in a lid-driven enclosure filled with fluid-saturated porous medium, *International Journal of Heat and Mass Transfer*, 42, pp. 2465–2481, 1999.
- [81] A. H. Khater, R. S. Temsah, and M. M. Hassan, A Chebyshev spectral collocation method for solving Burgers’-type equations, *Journal of Computational and Applied Mathematics*, 222(2), pp. 333–350, 2008.
- [82] S. A. Khuri and A. Sayfy, A spline collocation approach for the numerical solution of a generalized nonlinear Klein-Gordon equation, *Applied Mathematics and Computation*, 216(4), pp. 1047–1056, 2010.
- [83] B. Kim, D. Lee, M. Ha, and H. Yoon, A numerical study of natural convection in a square enclosure with a circular cylinder at different vertical locations, *International Journal of Heat and Mass Transfer*, 51(7-8), pp. 1888–1906, 2008.
- [84] D. S. Kumar, K. Murugesan, and A. Gupta, Effect of thermo-solutal stratification on recirculation flow patterns in a backward-facing step channel flow, *International Journal For Numerical Methods in Fluids*, 64(2), pp. 163–186, 2010.
- [85] R. V. B. Kumar and B. Kumar, Parallel computation of natural convection in trapezoidal porous enclosures, *Mathematics and Computers in Simulation*, 65(3), pp. 221–229, 2004.
- [86] M. Lakestani and M. Dehghan, Collocation and finite difference-collocation methods for the solution of nonlinear Klein-Gordon equation, *Computer Physics Communications*, 181(8), pp. 1392–1401, 2010.
- [87] K. Le-Cao, N. Mai-Duy, C.-D. Tran, and T. Tran-Cong, Numerical study of stream-function formulation governing flows in multiply-connected domains by integrated RBFs and cartesian grids, *Computers & Fluids*, 44(1), pp. 32–42, 2011.
- [88] J. R. LeVeque, *Finite difference methods for ordinary and partial differential equations : steady-state and time-dependent problems*, Society for Industrial and Applied Mathematics : PA, Philadelphia, 2007.

- [89] J. T. Lin, B. F. Armaly, and T. S. Chen, Mixed convection in buoyancy-assisting, vertical backward-facing step flows, *International Journal of Heat and Mass Transfer*, 33(10), pp. 2121–2132, 1990.
- [90] F. Liu and W. Shi, Numerical solutions of two-dimensional Burgers' equations by lattice Boltzmann method, *Communications in Nonlinear Science and Numerical Simulation*, 16(1), pp. 150–157, 2011.
- [91] D. C. Lo, High-resolution simulations of magnetohydrodynamic free convection in an enclosure with a transverse magnetic field using a velocity-vorticity formulation, *International Communications in Heat and Mass Transfer*, 37(5), pp. 514–523, 2010.
- [92] D. C. Lo, D. L. Young, and C. C. Tsai, High resolution of 2D natural convection in a cavity by the DQ method, *Journal of Computational and Applied Mathematics*, 203(1), pp. 219–236, 2007.
- [93] O. Martynenko and P. Khramtsov, *Free-Convective Heat Transfer*, Springer, 2005.
- [94] J. H. Mathews and K. D. Fink, *Numerical Methods using MATLAB*, Pearson Prentice Hall, 2004.
- [95] S. H. Meraji, A. Ghaheri, and P. Malekzadeh, An efficient algorithm based on the differential quadrature method for solving Navier-Stokes equations, *International Journal For Numerical Methods in Fluids*, 71(4), pp. 422–445, 2012.
- [96] D. Mirzaei and M. Dehghan, Boundary element solution of the two-dimensional sine-Gordon equation using continuous linear elements, *Engineering Analysis with Boundary Elements*, 33(1), pp. 12–24, 2009.
- [97] D. Mirzaei and M. Dehghan, Meshless local Petrov-Galerkin (MLPG) approximation to the two dimensional sine-Gordon equation, *Journal of Computational and Applied Mathematics*, 233(10), pp. 2737–2754, 2010.
- [98] R. C. Mittal and G. Arora, Numerical solution of coupled viscous Burgers' equation, *Communications in Nonlinear Science and Numerical Simulation*, 16(3), pp. 1304–1313, 2011.
- [99] R. C. Mittal and R. Jiwari, Differential Quadrature Method for two-dimensional Burgers' equations, *International Journal for Computational Methods Engineering Science and Mechanics*, 10(6), pp. 450–459, 2009.
- [100] R. C. Mittal and P. Singhal, Numerical solution of Burger's equation, *Communications in Numerical Methods in Engineering*, 9(5), pp. 397–406, 1993.
- [101] M. K. Moallemi and K. S. Jang, Prandtl number effects on laminar mixed convection heat transfer in a lid-driven cavity, *International Journal of Heat and Mass Transfer*, 35(8), pp. 1881 – 1892, 1992.

- [102] R. K. Mohanty, An operator splitting method for an unconditionally stable difference scheme for a linear hyperbolic equation with variable coefficients in two space dimensions, *Applied Mathematics and Computation*, 152(3), pp. 799–806, 2004.
- [103] R. K. Mohanty, New unconditionally stable difference schemes for the solution of multi-dimensional telegraphic equations, *International Journal of Computer Mathematics*, 86(2), pp. 2061–2071, 2009.
- [104] R. K. Mohanty and M. K. Jain, An unconditionally stable alternating direction implicit scheme for two space dimensional linear hyperbolic equation, *Numerical Methods for Partial Differential Equations*, 17(6), pp. 684–688, 2001.
- [105] R. K. Mohanty, M. K. Jain, and U. Arora, An unconditionally stable ADI method for the linear hyperbolic equation in three space dimensional, *International Journal of Computer Mathematics*, 79(1), pp. 133–142, 2002.
- [106] R. K. Mohanty, M. K. Jain, and K. George, On the use of high order difference methods for the system of one space second order non-linear hyperbolic equation with variable coefficients, *Journal of Computational and Applied Mathematics*, 72(2), pp. 421–431, 1996.
- [107] A. Mohebbi and M. Dehghan, High order compact solution of the one-space-dimensional linear hyperbolic equation, *Numerical Methods for Partial Differential Equations*, 24(5), pp. 1222–1235, 2008.
- [108] A. Mohebbi and M. Dehghan, High-order solution of one-dimensional sine-Gordon equation using compact finite difference and DIRKN methods, *Mathematical and Computer Modelling*, 51(5-6), pp. 537–549, 2010.
- [109] R. Moreau, *Magnetohydrodynamics*, Kluwer Academic Publishers, 1990.
- [110] A. Mukhopadhyay, G. Biswas, and T. Sundararajan, Numerical investigation of confined wakes behind a square cylinder in a channel, *International Journal for Numerical Methods in Fluids*, 14(12), pp. 1473–1484, 1992.
- [111] A. Narasimhan, *Essentials of Heat and Fluid Flow in Porous Media*, CRC Press; Taylor & Francis Group, 2013.
- [112] B. Natalini and V. Popov, An alternative approach for calculation of the first and higher order derivatives in the drm-md, *Engineering Analysis with Boundary Elements*, 28(1), pp. 61–78, 2004.
- [113] H. A. Navarro, L. Cabezas-Gómez, R. C. Silva, and A. N. Montagnoli, A generalized alternating-direction implicit scheme for incompressible magnetohydrodynamic viscous flows at low Reynolds number, *Applied Mathematics and Computation*, 189(2), pp. 1601–1613, 2007.
- [114] J. Nee and J. Duan, Limit set of trajectories of the coupled viscous Burgers' equations, *Applied Mathematics Letters*, 11(1), pp. 57–61, 1998.

- [115] A. I. Neslitürk and M. Tezer-Sezgin, The finite element method for MHD flow at high Hartmann numbers, *Computer methods in applied mechanics and engineering*, 194(9-11), pp. 1201–1224, 2005.
- [116] D. A. Nield and A. Bejan, *Convection in Porous Media*, Springer, 2006.
- [117] P. Nithiarasu and C. B. Liu, Steady and unsteady incompressible flow in a double driven cavity using the artificial compressibility (AC)-based characteristic-based split (CBS) scheme, *International Journal for Numerical Methods in Engineering*, 63(3), pp. 380–397, 2005.
- [118] H. Oztop, Z. Zhao, and B. Yu, Fluid flow due to combined convection in lid-driven enclosure having a circular body, *International Journal of Heat and Fluid Flow*, 30(5), pp. 886–901, 2009.
- [119] H. F. Oztop, Combined convection heat transfer in a porous lid-driven enclosure due to heater with finite length, *International Journal of Heat and Mass Transfer*, 33(6), pp. 772–779, 2006.
- [120] H. F. Oztop, Natural convection in partially cooled and inclined porous rectangular enclosures, *International Journal of Thermal Sciences*, 46(2), pp. 149–156, 2007.
- [121] P. W. Partridge, Towards criteria for selecting approximation functions in the dual reciprocity method, *Engineering Analysis with Boundary Elements*, 24(7-8), pp. 519–529, 2000.
- [122] P. W. Partridge, C. A. Brebbia, and L. C. Wrobel, *The Dual Reciprocity Boundary Element Method*, Computational Mechanics Publications, Elsevier Science, 1992.
- [123] B. Pekmen and M. Tezer-Sezgin, DRBEM solution of free convection in porous enclosures under the effect of a magnetic field, *International Journal of Heat and Mass Transfer*, 56(1-2), pp. 454–468, 2013.
- [124] R. H. Pletcher, J. C. Tannehill, and D. A. Anderson, *Computational Fluid Mechanics and Heat Transfer*, CRC Press; Taylor & Francis Group, 2013.
- [125] I. Pop and D. Ingham, *Convective heat transfer: mathematical and computational modelling of viscous fluid and porous media*, Pergamon, 2001.
- [126] M. Rahman, M. Alim, and M. Sarker, Numerical study on the conjugate effect of joule heating and magneto-hydrodynamics mixed convection in an obstructed lid-driven square cavity, *International Communications in Heat and Mass Transfer*, 37(5), pp. 524–534, 2010.
- [127] D. Ramakrishna, T. Basak, S. Roy, and I. Pop, Numerical study of mixed convection within porous square cavities using Bejan’s heatlines: Effects of thermal aspect ratio and thermal boundary conditions, *International Journal of Heat and Mass Transfer*, 55(21-22), pp. 5436–5448, 2012.

- [128] M. Ramšak, L. Škerget, M. Hriberšek, and Z. Žunič, A multidomain boundary element method for unsteady laminar flow using stream function-vorticity equations, *Engineering Analysis with Boundary Elements*, 29(1), pp. 1–14, 2005.
- [129] J. Rashidinia, M. Ghasemi, and R. Jalilian, Numerical solution of the nonlinear Klein-Gordon equation, *Journal of Computational and Applied Mathematics*, 233(8), pp. 1866–1878, 2010.
- [130] J. Rashidinia and R. Mohammadi, Tension spline approach for the numerical solution of nonlinear Klein-Gordon equation, *Computer Physics Communications*, 181(1), pp. 78–91, 2010.
- [131] J. N. Reddy and D. K. Gartling, *The finite element method in heat transfer and fluid dynamics*, Taylor & Francis, 2010.
- [132] C. Revnic, T. Grosan, I. Pop, and D. B. Ingham, Magnetic field effect on the unsteady free convection flow in a square cavity filled with a porous medium with a constant heat generation, *International Journal of Heat and Mass Transfer*, 54(9-10), pp. 1734–1742, 2011.
- [133] A. Saadatmandi and M. Dehghan, Numerical solution of hyperbolic telegraph equation using the Chebyshev tau method, *Numerical Methods for Partial Differential Equations*, 26(1), pp. 239–252, 2010.
- [134] N. H. Saeid and I. Pop, Non-Darcy natural convection in a square cavity filled with a porous medium, *Fluid Dynamics Research*, 36(1), pp. 35–43, 2005.
- [135] H. Saleh, R. Roslan, and I. Hashim, Natural convection in a porous trapezoidal enclosure with an inclined magnetic field, *Computers & Fluids*, 47(1), pp. 155–164, 2011.
- [136] M. Sathiyamoorthy and A. Chamkha, Effect of magnetic field on natural convection flow in liquid gallium filled square cavity for linearly heated side wall(s), *International Journal of Thermal Sciences*, 49(9), pp. 1856–1865, 2010.
- [137] F. W. Schmidt, R. E. Henderson, and C. H. Wolgemuth, *Introduction to Thermal Sciences; Thermodynamics, Fluid Dynamics, Heat Transfer*, John Wiley & Sons, Inc., 1993.
- [138] K. Sentürk, M. Tassarotto, and N. Aslan, Numerical solutions of liquid metal flows by incompressible magneto-hydrodynamics with heat transfer, *International Journal For Numerical Methods in Fluids*, 60(11), pp. 1200–1221, 2009.
- [139] F. Shakeri and M. Dehghan, Numerical solution of the Klein-Gordon equation via He's variational iteration method, *Nonlinear Dynamics*, 51(1-2), pp. 89–97, 2008.
- [140] F. Shakeri and M. Dehghan, A finite volume spectral method for solving magnetohydrodynamic (MHD) equations, *Applied Numerical Mathematics*, 61(1), pp. 1–23, 2011.
- [141] J. Shercliff, *A Textbook of Magnetohydrodynamics*, Pergamon Press, 1965.

- [142] C. Shu, *Differential Quadrature and Its Applications in Engineering*, Springer, 2000.
- [143] C. Shu and T. Chew, Fourier expansion-based differential quadrature and its application to Helmholtz eigenvalue problems, *Communications in Numerical Methods in Engineering*, 13(8), pp. 643–653, 1997.
- [144] C. Shu and B. R. Richards, Application of generalized differential quadrature to solve the two-dimensional incompressible Navier-Stokes equations, *International Journal for Numerical Methods in Fluids*, 15(7), pp. 791–798, 1992.
- [145] C. Shu and K. H. A. Wee, Numerical simulation of natural convection in a square cavity by SIMPLE-generalized differential quadrature method, *Computers & Fluids*, 31, pp. 209–226, 2002.
- [146] C. Shu, Q. Yao, and K. S. Yeo, Block-marching in time with DQ discretization: an efficient method for time-dependent problems, *Computer Methods in Applied and Mechanics and Engineering*, 191(41-42), pp. 4587–4597, 2002.
- [147] A. A. Soliman, The modified extended tanh-function method for solving Burgers-type equations, *Physica A: Statistical Mechanics and its Applications*, 361(2), pp. 394–404, 2006.
- [148] M. Tezer-Sezgin, Solution of magnetohydrodynamic flow in a rectangular duct by differential quadrature method, *Computers & Fluids*, 33(4), pp. 533–547, 2004.
- [149] M. Tezer-Sezgin and S. H. Aydin, Dual reciprocity boundary element method for magnetohydrodynamic flow using radial basis functions, *International Journal of Computational Fluid Dynamics*, 16(1), pp. 49–63, 2002.
- [150] M. Tezer-Sezgin and S. H. Aydin, Solution of magnetohydrodynamic flow problems using the boundary element method, *Engineering Analysis with Boundary Elements*, 30(5), pp. 411–418, 2006.
- [151] L. N. Trefethen, *Spectral Methods in Matlab*, SIAM; Philadelphia, 2000.
- [152] C. H. Tsai, D. L. Young, and C. C. Hsiang, The localized differential quadrature method for two-dimensional stream function formulation of Navier-Stokes equations, *Engineering Analysis with Boundary Elements*, 35(11), pp. 1190–1203, 2011.
- [153] Y. Varol, H. F. Oztop, and I. Pop, Numerical analysis of natural convection in an inclined trapezoidal enclosure filled with a porous medium, *International Journal of Thermal Sciences*, 47(10), pp. 1316–1331, 2008.
- [154] Y. Varol, H. F. Oztop, and I. Pop, Natural convection in right-angle porous trapezoidal enclosure partially cooled from inclined wall, *International Communications in Heat and Mass Transfer*, 36(1), pp. 6–15, 2009.
- [155] Y. Varol, H. F. Oztop, and A. Varol, Free convection in porous media filled right-angle triangular enclosures, *International Communications in Heat and Mass Transfer*, 33(10), pp. 1190–1197, 2006.

- [156] E. Vishnuvardhanarao and M. K. Das, Laminar mixed convection in a parallel two-sided lid-driven differentially heated square cavity filled with a fluid saturated porous medium, *Numerical Heat Transfer, Part A : Applications*, 53(1), pp. 88–110, 2007.
- [157] B. Šarler, D. Gobin, B. Goyeau, J. Perko, and H. Power, Natural convection in porous media - dual reciprocity boundary element method solution of the Darcy model, *International Journal for Numerical Methods in Fluids*, 33(2), pp. 279–312, 2000.
- [158] B. Šarler, J. Perko, D. Gobin, B. Goyeau, and H. Power, Dual reciprocity boundary element method solution of natural convection in Darcy-Brinkman porous media, *Engineering Analysis with Boundary Elements*, 28(1), pp. 23–41, 2004.
- [159] Q. W. Wang, J. Yang, M. Zeng, and G. Wang, Three dimensional numerical study of natural convection in an inclined porous cavity with time sinusoidal oscillating boundary conditions, *International Journal of Heat and Fluid Flow*, 31, pp. 70–82, 2010.
- [160] A. M. Wazwaz, Compactons, solitons and periodic solutions for some forms of nonlinear Klein-Gordon equations, *Chaos, Solitons and Fractals*, 28(4), pp. 1005–1013, 2006.
- [161] A. M. Wazwaz, New travelling wave solutions to the Boussinesq and the Klein-Gordon equations, *Communications in Nonlinear Science and Numerical Simulation*, 13(5), pp. 889–901, 2008.
- [162] Y. Yoshida and T. Nomura, A transient solution method for the finite element incompressible Navier-Stokes equations, *International Journal for Numerical Methods in Fluids*, 5, pp. 873–890, 1985.
- [163] D. L. Young, C. M. Fan, S. P. Hu, and S. N. Atluri, The Eulerian-Lagrangian method of fundamental solutions of two-dimensional unsteady Burgers' equations, *Engineering Analysis with Boundary Elements*, 32(5), pp. 395–412, 2008.
- [164] L. Zhang, J. Ouyang, and X. Zhang, The two-level element free Galerkin method for MHD flow at high Hartmann number, *Physics Letters A*, 371(35), pp. 5625–5638, 2008.
- [165] Z. Zhang and X. Zhang, Direct simulation of Low-Re flow around a square cylinder by numerical manifold method for Navier-Stokes equations, *Journal of Applied Mathematics*, 2012(465972), pp. 1–14, 2012.
- [166] Y. C. Zhou, B. S. Patnaik, D. C. Wan, and G. W. Wei, DSC solution for flow in a staggered double lid driven cavity, *International Journal for Numerical Methods in Engineering*, 57(2), pp. 211–234, 2003.
- [167] H. Zhu, H. Shu, and M. Ding, Numerical solutions of two-dimensional Burgers' equations by discrete Adomian decomposition method, *Computers & Mathematics with Applications*, 60(3), pp. 840–848, 2010.





## APPENDIX A

### Non-dimensionalizations

Defining the non-dimensional variables as,

$$\begin{aligned}x' &= \frac{x}{L}, \quad y' = \frac{y}{L}, \quad u' = \frac{u}{U}, \quad v' = \frac{v}{U}, \quad t' = \frac{tU}{L} \\T' &= \frac{T - T_c}{T_h - T_c}, \quad B'_x = \frac{B_x}{B_0}, \quad B'_y = \frac{B_y}{B_0} \\A' &= \frac{A}{B_0 L}, \quad \psi' = \frac{\psi}{UL}, \quad w' = \frac{wL}{U}, \quad j' = \frac{j}{B_0 U \sigma}.\end{aligned}$$

the dimensionless equations for stream function, temperature, vorticity transport and induced magnetic field are derived as follows.

#### A.1 Stream function equation

Note that

$$w = \nabla \times \mathbf{u} = \frac{\partial v}{\partial x} - \frac{\partial u}{\partial y} = -\nabla^2 \psi$$

Applying the non-dimensional variables, we obtain

$$\frac{UL}{L^2} \nabla^2 \psi' = -\frac{Uw'}{L}$$

Cancelling the same terms and dropping the primes, the stream function equation

$$\nabla^2 \psi = -w \tag{A.1}$$

is obtained.

#### A.2 Energy equation

The dimensional governing equation for energy is

$$\alpha \nabla^2 T = \frac{\partial T}{\partial t} + \mathbf{u} \cdot \nabla T \tag{A.2}$$

The non-dimensional parameters are used as

$$\frac{\alpha \Delta T}{L^2} \nabla^2 T' = \frac{U \Delta T}{L} \frac{\partial T'}{\partial t'} + \frac{U \Delta T}{L} u' \frac{\partial T'}{\partial x'} + \frac{U \Delta T}{L} v' \frac{\partial T'}{\partial y'}. \quad (\text{A.3})$$

If each term is multiplied by  $L/(U \Delta T)$ , and the prime notation is dropped, the non-dimensional form of the energy equation will be

$$\frac{1}{PrRe} \nabla^2 T = \frac{\partial T}{\partial t} + u \frac{\partial T}{\partial x} + v \frac{\partial T}{\partial y} \quad (\text{A.4})$$

where

$$\frac{\alpha}{L^2} \cdot \frac{L}{U} = \frac{\nu}{LU} \cdot \frac{\alpha}{\nu} = \frac{1}{PrRe}$$

### A.3 Induction, magnetic potential and current density equations

In Eq.(1.31),

$$\frac{1}{\sigma \mu_m} \nabla^2 \mathbf{B} = \frac{\partial \mathbf{B}}{\partial t} - \nabla \times (\mathbf{u} \times \mathbf{B}), \quad (\text{A.5})$$

and

$$\nabla \times (\mathbf{u} \times \mathbf{B}) = \underbrace{\mathbf{u}(\nabla \cdot \mathbf{B})}_0 - \underbrace{\mathbf{B}(\nabla \cdot \mathbf{u})}_0 + (\mathbf{B} \cdot \nabla) \mathbf{u} - (\mathbf{u} \cdot \nabla) \mathbf{B} \quad (\text{A.6})$$

where

$$\begin{aligned} (\mathbf{B} \cdot \nabla) \mathbf{u} &= \left( B_x \frac{\partial}{\partial x} + B_y \frac{\partial}{\partial y} \right) \mathbf{u} = \left\langle B_x \frac{\partial u}{\partial x} + B_y \frac{\partial u}{\partial y}, B_x \frac{\partial v}{\partial x} + B_y \frac{\partial v}{\partial y} \right\rangle \\ (\mathbf{u} \cdot \nabla) \mathbf{B} &= \left( u \frac{\partial}{\partial x} + v \frac{\partial}{\partial y} \right) \mathbf{B} = \left\langle u \frac{\partial B_x}{\partial x} + v \frac{\partial B_x}{\partial y}, u \frac{\partial B_y}{\partial x} + v \frac{\partial B_y}{\partial y} \right\rangle \end{aligned}$$

such that

$$\nabla \times (\mathbf{u} \times \mathbf{B}) = \left\langle B_x \frac{\partial u}{\partial x} + B_y \frac{\partial u}{\partial y} - u \frac{\partial B_x}{\partial x} - v \frac{\partial B_x}{\partial y}, B_x \frac{\partial v}{\partial x} + B_y \frac{\partial v}{\partial y} - u \frac{\partial B_y}{\partial x} - v \frac{\partial B_y}{\partial y} \right\rangle \quad (\text{A.7})$$

Thus, the induction equations for the  $x$ - and  $y$ - components of  $\mathbf{B}$  in dimensional form are

$$\frac{1}{\sigma \mu_m} \nabla^2 B_x = \frac{\partial B_x}{\partial t} + u \frac{\partial B_x}{\partial x} + v \frac{\partial B_x}{\partial y} - B_x \frac{\partial u}{\partial x} - B_y \frac{\partial u}{\partial y} \quad (\text{A.8a})$$

$$\frac{1}{\sigma \mu_m} \nabla^2 B_y = \frac{\partial B_y}{\partial t} + u \frac{\partial B_y}{\partial x} + v \frac{\partial B_y}{\partial y} - B_x \frac{\partial v}{\partial x} - B_y \frac{\partial v}{\partial y} \quad (\text{A.8b})$$

which are employed by non-dimensional variables as

$$\frac{B_0}{\sigma \mu_m L^2} \nabla^2 B'_x = \frac{B_0 U}{L} \frac{\partial B'_x}{\partial t'} + \frac{B_0 U}{L} u' \frac{\partial B'_x}{\partial x'} + \frac{B_0 U}{L} v' \frac{\partial B'_x}{\partial y'} - \frac{B_0 U}{L} B'_x \frac{\partial u'}{\partial x'} - \frac{B_0 U}{L} B'_y \frac{\partial u'}{\partial y'}$$

$$\frac{B_0}{\sigma\mu_m L^2} \nabla^2 B'_y = \frac{B_0 U}{L} \frac{\partial B'_y}{\partial t'} + \frac{B_0 U}{L} u' \frac{\partial B'_y}{\partial x'} + \frac{B_0 U}{L} v' \frac{\partial B'_y}{\partial y'} - \frac{B_0 U}{L} B'_x \frac{\partial v'}{\partial x'} - \frac{B_0 U}{L} B'_y \frac{\partial v'}{\partial y'}$$

Multiplying all the terms by  $L/(B_0 U)$  and dropping the prime notation, the non-dimensional form of the induction equations are obtained as

$$\frac{1}{Rem} \nabla^2 B_x = \frac{\partial B_x}{\partial t} + u \frac{\partial B_x}{\partial x} + v \frac{\partial B_x}{\partial y} - B_x \frac{\partial u}{\partial x} - B_y \frac{\partial u}{\partial y} \quad (\text{A.9a})$$

$$\frac{1}{Rem} \nabla^2 B_y = \frac{\partial B_y}{\partial t} + u \frac{\partial B_y}{\partial x} + v \frac{\partial B_y}{\partial y} - B_x \frac{\partial v}{\partial x} - B_y \frac{\partial v}{\partial y} \quad (\text{A.9b})$$

where

$$\frac{B_0}{\sigma\mu_m L^2} \frac{L}{B_0 U} = \frac{1}{Rem}.$$

Since the current displacement is assumed to be negligibly small, current density is

$$\mathbf{J} = \frac{1}{\mu_m} (\nabla \times \mathbf{B}). \quad (\text{A.10})$$

Considering  $\mathbf{J} = (0, 0, j)$  and  $\mathbf{B} = (B_x, B_y, 0)$ , we can write

$$j = \frac{1}{\mu_m} \left( \frac{\partial B_y}{\partial x} - \frac{\partial B_x}{\partial y} \right). \quad (\text{A.11})$$

Now, it can be given in non-dimensional form as

$$j' B_0 U \sigma = \frac{B_0}{\mu_m L} \left( \frac{\partial B'_y}{\partial x'} - \frac{\partial B'_x}{\partial y'} \right), \quad (\text{A.12})$$

and canceling the terms  $B_0 U \sigma$  on both sides of Eq.(A.12), and then dropping the prime notation, non-dimensional current density is

$$j = \frac{1}{Rem} \left( \frac{\partial B_y}{\partial x} - \frac{\partial B_x}{\partial y} \right). \quad (\text{A.13})$$

Applying the operator  $-\partial/\partial y$  to Eq.(A.8a) and  $\partial/\partial x$  to Eq.(A.8b), and then adding these two, it can be written

$$\begin{aligned} \frac{1}{\sigma\mu_m} \nabla^2 \left( \frac{\partial B_y}{\partial x} - \frac{\partial B_x}{\partial y} \right) &= \frac{\partial}{\partial t} \left( \frac{\partial B_y}{\partial x} - \frac{\partial B_x}{\partial y} \right) \\ &+ \underbrace{\frac{\partial u}{\partial x} \frac{\partial B_y}{\partial x}}_1 + \underbrace{u \frac{\partial^2 B_y}{\partial x^2}}_2 - \underbrace{\frac{\partial u}{\partial y} \frac{\partial B_x}{\partial x}}_3 - \underbrace{u \frac{\partial^2 B_y}{\partial y \partial x}}_2 \\ &+ \underbrace{\frac{\partial v}{\partial x} \frac{\partial B_y}{\partial y}}_{3'} + \underbrace{v \frac{\partial^2 B_y}{\partial x \partial y}}_4 - \underbrace{\frac{\partial v}{\partial y} \frac{\partial B_x}{\partial y}}_{1'} - \underbrace{v \frac{\partial^2 B_x}{\partial y^2}}_4 \end{aligned}$$

$$\begin{aligned}
& \underbrace{-\frac{\partial B_x}{\partial x} \frac{\partial v}{\partial x}}_3 - \underbrace{B_x \frac{\partial^2 v}{\partial x^2}}_5 + \underbrace{\frac{\partial B_x}{\partial y} \frac{\partial u}{\partial x}}_1 + \underbrace{B_x \frac{\partial^2 u}{\partial y \partial x}}_5 \\
& \underbrace{-\frac{\partial B_y}{\partial x} \frac{\partial v}{\partial y}}_{1'} - \underbrace{B_y \frac{\partial^2 v}{\partial y \partial x}}_6 + \underbrace{\frac{\partial B_y}{\partial y} \frac{\partial u}{\partial y}}_{3'} + \underbrace{B_y \frac{\partial^2 u}{\partial y^2}}_6
\end{aligned}$$

$$\begin{aligned}
\frac{\partial u}{\partial x} &= -\frac{\partial v}{\partial y} \Rightarrow \textcircled{1} + \textcircled{1}' = -2 \frac{\partial v}{\partial y} \left( \frac{\partial B_x}{\partial y} + \frac{\partial B_y}{\partial x} \right) \\
\textcircled{2} \quad u \frac{\partial}{\partial x} \left( \frac{\partial B_y}{\partial x} - \frac{\partial B_x}{\partial y} \right) &= \mu_m u \frac{\partial j}{\partial x} \\
\frac{\partial B_y}{\partial y} &= -\frac{\partial B_x}{\partial x} \Rightarrow \textcircled{3} + \textcircled{3}' = -2 \frac{\partial B_x}{\partial x} \left( \frac{\partial u}{\partial y} + \frac{\partial v}{\partial x} \right) \\
\textcircled{4} \quad v \frac{\partial}{\partial y} \left( \frac{\partial B_y}{\partial x} - \frac{\partial B_x}{\partial y} \right) &= \mu_m v \frac{\partial j}{\partial y} \\
\textcircled{5} \quad -B_x \frac{\partial}{\partial x} \left( \frac{\partial v}{\partial x} - \frac{\partial u}{\partial y} \right) &= -B_x \frac{\partial w}{\partial x} \\
\textcircled{6} \quad -B_y \frac{\partial}{\partial y} \left( \frac{\partial v}{\partial x} - \frac{\partial u}{\partial y} \right) &= -B_y \frac{\partial w}{\partial y}.
\end{aligned}$$

Thus, the dimensional form of the current density equation is

$$\begin{aligned}
\frac{1}{\sigma} \nabla^2 j &= \mu_m \left( \frac{\partial j}{\partial t} + u \frac{\partial j}{\partial x} + v \frac{\partial j}{\partial y} \right) - \left( B_x \frac{\partial w}{\partial x} + B_y \frac{\partial w}{\partial y} \right) \\
&\quad - 2 \left[ \frac{\partial B_x}{\partial x} \left( \frac{\partial v}{\partial x} + \frac{\partial u}{\partial y} \right) + \frac{\partial v}{\partial y} \left( \frac{\partial B_x}{\partial y} + \frac{\partial B_y}{\partial x} \right) \right].
\end{aligned}$$

With the help of the defined non-dimensional parameters, we can write

$$\begin{aligned}
\frac{B_0 U \sigma}{\sigma L^2} \nabla^2 j' &= \mu_m \frac{B_0 U^2 \sigma}{L} \left( \frac{\partial j'}{\partial t'} + u' \frac{\partial j'}{\partial x'} + v' \frac{\partial j'}{\partial y'} \right) - \frac{B_0 U}{L^2} \left( B'_x \frac{\partial w'}{\partial x'} + B'_y \frac{\partial w'}{\partial y'} \right) \\
&\quad - 2 \frac{B_0 U}{L^2} \left[ \frac{\partial B'_x}{\partial x'} \left( \frac{\partial v'}{\partial x'} + \frac{\partial u'}{\partial y'} \right) + \frac{\partial v'}{\partial y'} \left( \frac{\partial B'_x}{\partial y'} + \frac{\partial B'_y}{\partial x'} \right) \right]
\end{aligned}$$

Once the each term is multiplied by  $L^2/(UB_0)$ , and the prime notation is dropped, the non-dimensional form of the current density equation is also obtained as

$$\begin{aligned}
\nabla^2 j &= Rem \left( \frac{\partial j}{\partial t} + u \frac{\partial j}{\partial x} + v \frac{\partial j}{\partial y} \right) - \left( B_x \frac{\partial w}{\partial x} + B_y \frac{\partial w}{\partial y} \right) \\
&\quad - 2 \left[ \frac{\partial B_x}{\partial x} \left( \frac{\partial v}{\partial x} + \frac{\partial u}{\partial y} \right) + \frac{\partial v}{\partial y} \left( \frac{\partial B_x}{\partial y} + \frac{\partial B_y}{\partial x} \right) \right] \tag{A.14}
\end{aligned}$$

The  $x$ - and  $y$ -components of  $\mathbf{B}$  in terms of vector potential  $\mathbf{A} = (0, 0, A)$  is written as  $B_x = \partial A / \partial y$  and  $B_y = -\partial A / \partial x$  satisfying the solenoidal nature  $\nabla \cdot \mathbf{B} = 0$ . Putting these definitions into Eq.(A.11), and then non-dimensionalizing, we obtain, in succession,

$$\begin{aligned}\nabla^2 A &= -\mu_m j \\ \frac{B_0 L}{L^2} \nabla^2 A' &= -\mu_m B_0 U \sigma j' \\ \nabla^2 A' &= -\mu_m U L \sigma j' \\ \nabla^2 A &= -Rem j\end{aligned}$$

Or, with already non-dimensionalized equations, substituting the definitions of  $B_x$  and  $B_y$  into Eq.(A.13), the magnetic potential equation is obtained as

$$\begin{aligned}j &= \frac{1}{Rem} \left( -\frac{\partial^2 A}{\partial x^2} - \frac{\partial^2 A}{\partial y^2} \right) \\ \nabla^2 A &= -Rem j\end{aligned}\tag{A.15}$$

An alternative magnetic potential equation may be derived instead of Eq.(A.15). Using Eq.(A.9a) and  $B_x = \partial A / \partial y$ ,

$$\begin{aligned}\frac{1}{Rem} \nabla^2 \left( \frac{\partial A}{\partial y} \right) &= \frac{\partial}{\partial t} \left( \frac{\partial A}{\partial y} \right) + u \frac{\partial}{\partial x} \left( \frac{\partial A}{\partial y} \right) + v \frac{\partial}{\partial y} \left( \frac{\partial A}{\partial y} \right) - B_x \frac{\partial u}{\partial x} - B_y \frac{\partial u}{\partial y} \\ \nabla^2 \left( \frac{\partial A}{\partial y} \right) &= \frac{\partial^2}{\partial x^2} \left( \frac{\partial A}{\partial y} \right) + \frac{\partial^2}{\partial y^2} \left( \frac{\partial A}{\partial y} \right) = \frac{\partial}{\partial y} \left( \frac{\partial^2 A}{\partial x^2} \right) + \frac{\partial}{\partial y} \left( \frac{\partial^2 A}{\partial y^2} \right) = \frac{\partial}{\partial y} (\nabla^2 A) \\ \frac{1}{Rem} \frac{\partial}{\partial y} (\nabla^2 A) &= \frac{\partial}{\partial y} \left( \frac{\partial A}{\partial t} \right) + \frac{\partial}{\partial y} \left( u \frac{\partial A}{\partial x} \right) - \frac{\partial \mathbf{u}}{\partial \mathbf{y}} \frac{\partial \mathbf{A}}{\partial \mathbf{x}} \\ &\quad + \frac{\partial}{\partial y} \left( v \frac{\partial A}{\partial y} \right) - \frac{\partial \mathbf{v}}{\partial \mathbf{y}} \frac{\partial \mathbf{A}}{\partial \mathbf{y}} - B_x \frac{\partial u}{\partial x} - B_y \frac{\partial u}{\partial y}\end{aligned}$$

Cancelling bold terms by the last two terms using continuity equation and the definition  $B_y = -\partial A / \partial x$ , and then dropping the operator  $\partial / \partial y$  from both sides, the following magnetic potential equation is obtained

$$\frac{1}{Rem} \nabla^2 A = \frac{\partial A}{\partial t} + u \frac{\partial A}{\partial x} + v \frac{\partial A}{\partial y}.\tag{A.16}$$

#### A.4 Vorticity transport equation

In Eq.(1.32b),

$$-\frac{1}{\rho} (\mathbf{J} \times \mathbf{B}) = \frac{1}{\rho} (\mathbf{B} \times \mathbf{J}) = \frac{1}{\rho \mu_m} (\mathbf{B} \times (\nabla \times \mathbf{B})),$$

where

$$\begin{aligned}\mathbf{B} \times (\nabla \times \mathbf{B}) &= \mathbf{B} \times \begin{vmatrix} \vec{i} & \vec{j} & \vec{k} \\ \frac{\partial}{\partial x} & \frac{\partial}{\partial y} & 0 \\ B_x & B_y & 0 \end{vmatrix} = \begin{vmatrix} \vec{i} & \vec{j} & \vec{k} \\ B_x & B_y & 0 \\ 0 & 0 & \frac{\partial B_y}{\partial x} - \frac{\partial B_x}{\partial y} \end{vmatrix} \\ &= \langle B_y \left( \frac{\partial B_y}{\partial x} - \frac{\partial B_x}{\partial y} \right), -B_x \left( \frac{\partial B_y}{\partial x} - \frac{\partial B_x}{\partial y} \right) \rangle,\end{aligned}$$

and note that  $\mathbf{g} = (0, -g, 0)$  is considered.

Thus, momentum equations for  $u$  and  $v$  components, respectively, are

$$\nu \nabla^2 u = \frac{\partial u}{\partial t} + u \frac{\partial u}{\partial x} + v \frac{\partial u}{\partial y} + \frac{1}{\rho} \frac{\partial P}{\partial x} + \frac{B_y}{\rho \mu_m} \left( \frac{\partial B_y}{\partial x} - \frac{\partial B_x}{\partial y} \right) \quad (\text{A.17})$$

$$\nu \nabla^2 v = \frac{\partial v}{\partial t} + u \frac{\partial v}{\partial x} + v \frac{\partial v}{\partial y} + \frac{1}{\rho} \frac{\partial P}{\partial y} - \frac{B_x}{\rho \mu_m} \left( \frac{\partial B_y}{\partial x} - \frac{\partial B_x}{\partial y} \right) - g\beta(T - T_c) \quad (\text{A.18})$$

When the non-dimensional variables are performed with the non-dimensional definition of pressure as  $P' = P/(\rho U^2)$ ,

$$\begin{aligned}\frac{\nu U}{L^2} \nabla^2 u' &= \frac{U^2}{L} \frac{\partial u'}{\partial t'} + \frac{U^2}{L} u' \frac{\partial u'}{\partial x'} + \frac{U^2}{L} v' \frac{\partial u'}{\partial y'} + \frac{\rho U^2}{\rho L} \frac{\partial P'}{\partial x'} + \frac{B_0^2}{\rho \mu_m L} B_y' \left( \frac{\partial B_y'}{\partial x'} - \frac{\partial B_x'}{\partial y'} \right) \\ \frac{\nu U}{L^2} \nabla^2 v' &= \frac{U^2}{L} \frac{\partial v'}{\partial t'} + \frac{U^2}{L} u' \frac{\partial v'}{\partial x'} + \frac{U^2}{L} v' \frac{\partial v'}{\partial y'} + \frac{\rho U^2}{\rho L} \frac{\partial P'}{\partial y'} + \frac{B_0^2}{\rho \mu_m L} B_x' \left( \frac{\partial B_y'}{\partial x'} - \frac{\partial B_x'}{\partial y'} \right) - g\beta \Delta T T',\end{aligned}$$

and each term is multiplied by  $L/U^2$ , then dropping the prime notations, non-dimensional form of  $u$ - and  $v$ -components of velocity are deduced as

$$\frac{1}{Re} \nabla^2 u = \frac{\partial u}{\partial t} + u \frac{\partial u}{\partial x} + v \frac{\partial u}{\partial y} + \frac{\partial P}{\partial x} + \frac{Ha^2}{Re Rem} B_y \left( \frac{\partial B_y}{\partial x} - \frac{\partial B_x}{\partial y} \right) \quad (\text{A.19a})$$

$$\frac{1}{Re} \nabla^2 v = \frac{\partial v}{\partial t} + u \frac{\partial v}{\partial x} + v \frac{\partial v}{\partial y} + \frac{\partial P}{\partial y} - \frac{Ha^2}{Re Rem} B_x \left( \frac{\partial B_y}{\partial x} - \frac{\partial B_x}{\partial y} \right) - \frac{Ra}{Pr Re^2} T \quad (\text{A.19b})$$

where

$$\frac{\nu U}{L^2} \frac{L}{U^2} = \frac{\nu}{LU} = \frac{1}{Re} \quad (\text{A.20a})$$

$$\frac{g\beta \Delta T L}{U^2} \frac{\alpha \cdot \nu \cdot L^2}{\alpha \cdot \nu \cdot L^2} = \frac{g\beta \Delta T L^3 \alpha}{\alpha \nu} \frac{\nu^2}{\nu U^2 L^2} = \frac{Ra}{Pr Re^2} \quad (\text{A.20b})$$

$$\frac{B_0^2}{\rho \mu_m L} \frac{L}{U^2} = \frac{B_0^2}{\rho \mu_m U^2} \frac{L^2 \cdot \sigma \cdot \mu}{L^2 \cdot \sigma \cdot \mu} = \frac{B_0^2 L^2 \sigma}{\mu} \frac{1}{\sigma \mu_m UL UL} \frac{\nu}{UL} = \frac{Ha^2}{Re Rem} \quad (\text{A.20c})$$

Applying the operators  $\partial/\partial y$  and  $-\partial/\partial x$  to the Eqs.(A.19a) and (A.19b), respectively, pressure terms are eliminated and the non-dimensional vorticity transport equation is obtained as

$$\frac{1}{Re} \nabla^2 w = \frac{\partial w}{\partial t} + u \frac{\partial w}{\partial x} + v \frac{\partial w}{\partial y} - \frac{Ra}{Pr Re^2} \frac{\partial T}{\partial x} \quad (\text{A.21})$$

$$- \frac{Ha^2}{ReRem} \left[ B_x \frac{\partial}{\partial x} \left( \frac{\partial B_y}{\partial x} - \frac{\partial B_x}{\partial y} \right) + B_y \frac{\partial}{\partial y} \left( \frac{\partial B_y}{\partial x} - \frac{\partial B_x}{\partial y} \right) \right]$$

Since  $\frac{1}{Rem} \left( \frac{\partial B_y}{\partial x} - \frac{\partial B_x}{\partial y} \right) = j$ , Eq.(A.21) may also be written as

$$\frac{1}{Re} \nabla^2 w = \frac{\partial w}{\partial t} + u \frac{\partial w}{\partial x} + v \frac{\partial w}{\partial y} - \frac{Ha^2}{Re} \left( B_x \frac{\partial j}{\partial x} + B_y \frac{\partial j}{\partial y} \right) - \frac{Ra}{PrRe^2} \frac{\partial T}{\partial x} \quad (A.22)$$

Note that the dimensional vorticity equation may be extracted by Eqs.(A.17)-(A.18) eliminating the pressure at dimensional stage. Then, applying the non-dimensional variable definitions to this dimensional form of the vorticity equation, non-dimensional vorticity equation as in Eq.(A.21) is obtained. In other words, consider the equation

$$\nu \nabla^2 w = \frac{\partial w}{\partial t} + u \frac{\partial w}{\partial x} + v \frac{\partial w}{\partial y} - g\beta \frac{\partial T}{\partial x} - \frac{1}{\rho\mu_m} \left[ B_x \frac{\partial}{\partial x} \left( \frac{\partial B_y}{\partial x} - \frac{\partial B_x}{\partial y} \right) + B_y \frac{\partial}{\partial y} \left( \frac{\partial B_y}{\partial x} - \frac{\partial B_x}{\partial y} \right) \right], \quad (A.23)$$

and the dimensionless definition of vorticity  $w' = wL/U$  with the other dimensionless variables defined at the beginning of this appendix. In prime notations,

$$\frac{\nu U}{L^3} \nabla'^2 w' = \frac{U^2}{L^2} \frac{\partial w'}{\partial t'} + \frac{U^2}{L^2} u' \frac{\partial w'}{\partial x'} + \frac{U^2}{L^2} v' \frac{\partial w'}{\partial y'} - \frac{g\beta\Delta T}{L} T' - \frac{B_0^2}{\rho\mu_m L^2} \left[ B'_x \frac{\partial}{\partial x'} \left( \frac{\partial B'_y}{\partial x'} - \frac{\partial B'_x}{\partial y'} \right) + B'_y \frac{\partial}{\partial y'} \left( \frac{\partial B'_y}{\partial x'} - \frac{\partial B'_x}{\partial y'} \right) \right]. \quad (A.24)$$

Once each term is multiplied by  $L^2/U^2$ , then Eq.(A.24) is rewritten as

$$\frac{\nu}{LU} \nabla'^2 w' = \frac{\partial w'}{\partial t'} + u' \frac{\partial w'}{\partial x'} + v' \frac{\partial w'}{\partial y'} - \frac{g\beta L\Delta T}{U^2} T' - \frac{B_0^2}{\rho\mu_m U^2} \left[ B'_x \frac{\partial}{\partial x'} \left( \frac{\partial B'_y}{\partial x'} - \frac{\partial B'_x}{\partial y'} \right) + B'_y \frac{\partial}{\partial y'} \left( \frac{\partial B'_y}{\partial x'} - \frac{\partial B'_x}{\partial y'} \right) \right]. \quad (A.25)$$

Dropping the prime notation, and with the definitions of dimensionless numbers (A.20), the vorticity transport equation (A.21) in dimensionless form is obtained.





## APPENDIX B

### Composite quadrature rules with equally spaced points

#### B.1 Composite trapezoidal rule

Suppose that the interval  $[a, b]$  is subdivided into  $n$  subintervals  $[x_i, x_{i+1}]$  of width  $h = (b - a)/n$  by using the equally spaced nodes  $x_i = a + ih$ , for  $i = 0, 1, 2, \dots, n$ . The composite trapezoidal rule for  $n$  subintervals for the approximation of the integral of  $f(x)$  over  $[a, b]$  is [94]

$$\int_a^b f(x)dx \approx \frac{h}{2}(f(a) + f(b)) + h \sum_{i=1}^{n-1} f(x_i), \quad (\text{B.1})$$

and the error term is  $-\frac{b-a}{12}h^2 f''(\tau)$ ,  $\tau \in (a, b)$ . Note that  $n$  can either be an even or an odd number.

#### B.2 Composite Simpson's rule

Suppose that the interval  $[a, b]$  is subdivided into  $2n$  subintervals  $[x_i, x_{i+1}]$  of equal width  $h = (b - a)/(2n)$  by using  $x_i = a + ih$  for  $i = 0, 1, 2, \dots, 2n$ . The composite Simpson's rule for  $2n$  subintervals for the approximation to the integral of  $f(x)$  over  $[a, b]$  is [94]

$$\int_a^b f(x)dx \approx \frac{h}{3} \left( f(a) + f(b) + 2 \sum_{i=1}^{n-1} f(x_{2i}) + 4 \sum_{i=1}^n f(x_{2i-1}) \right), \quad (\text{B.2})$$

and the error term is  $-\frac{b-a}{180}h^4 f^{(4)}(\tau)$ ,  $\tau \in (a, b)$ . Note that the number of subintervals should be an even number ( $2n$ ).

#### B.3 Composite Simpson's 3/8 rule

Suppose that the interval  $[a, b]$  is subdivided into  $3n + 1$  subintervals  $[x_i, x_{i+1}]$  of equal width  $h = (b-a)/(3n+1)$  by using  $x_i = a + (i-1)h$  for  $i = 1, 2, \dots, 3n+1$ . Extending

the Simpson's 3/8 rule [29], the composite Simpson's rule for  $3n + 1$  subintervals for the approximation to the integral of  $f(x)$  over  $[a, b]$  is derived as

$$\int_a^b f(x)dx \approx \frac{3h}{8} \left( f(x_1) + 3 \sum_{i=1}^n f(x_{3i-1}) + 3 \sum_{i=1}^n f(x_{3i}) + 2 \sum_{i=1}^{n-1} f(x_{3i+1}) + f(x_N) \right), \quad (\text{B.3})$$

and the error term is  $-\frac{b-a}{80}h^4 f^{(4)}(\tau)$ ,  $\tau \in (a, b)$ . Note that  $N - 1$  should be divided by 3.

# CURRICULUM VITAE

## PERSONAL INFORMATION

**Surname, Name:** Pekmen, Bengisen  
**Nationality:** Turkish  
**Date and Place of Birth:** December 1, 1986; Babaeski  
**Marital Status:** Single  
**Phone:** +90 537 210 83 09

## EDUCATION

Degree	Institution	Year of Graduation
M.S.	IAM, METU, Scientific Computing	2009
B.S.	Major: METU Math, Minor: METU Phys	2007
High School	Muğla Turgut Reis Lisesi	2003

## PROFESSIONAL EXPERIENCE

Year	Place	Enrollment
2009 - Present	Department of Mathematics, Atılım University	Teaching Assistant

## PUBLICATIONS

### Publications in International Journals

- B. Pekmen, M. Tezer-Sezgin, *Differential Quadrature Solution of Nonlinear Klein- Gordon and sine-Gordon Equations*, Computer Physics Communications, 183 (2012) 1702-1713.
- B. Pekmen, M. Tezer-Sezgin, *Differential Quadrature Solution of Hyperbolic Telegraph Equation*, Journal of Applied Mathematics, Volume 2012, Article ID 924765.
- B. Pekmen, M. Tezer-Sezgin, *DRBEM solution of free convection in porous enclosures under the effect of a magnetic field*, International Journal of Heat and Mass Transfer, 56 (2013) 454-468.

- B. Pekmen, M. Tezer-Sezgin, *DRBEM Solution of Incompressible MHD Flow with Magnetic Potential*, CMES-Computer Modeling in Engineering & Sciences, 96:4 (2013) 275-292.
- B. Pekmen, M. Tezer-Sezgin, *MHD flow and heat transfer in a lid-driven porous enclosure*, Computers & Fluids, 89 (2014) 191-199.
- B. Pekmen, M. Tezer-Sezgin, *Numerical solution of buoyancy MHD flow with magnetic potential*, International Journal of Heat and Mass Transfer, 71 (2014) 172-182.

### **International Conference Publications (Proceedings)**

- B. Pekmen, M. Tezer-Sezgin, Unsteady mixed convection in a porous lid-driven enclosure under a magnetic field, International Association for Boundary Element Methods, pp.140-145, January 9-11, 2013, Santiago, Chile.
- M. Tezer-Sezgin, B. Pekmen, DRBEM solution of Liquid Metal MHD Flow in a Staggered Double Lid-Driven Cavity, International Conference on Boundary Element Techniques, pp.341-346, July 16-18, 2013, Paris, France.
- B. Pekmen, M. Tezer-Sezgin, DRBEM Solution for the Incompressible MHD Equations in terms of Magnetic Potential, International Conference on Boundary Element Techniques, pp.347-352, July 16-18, 2013, Paris, France.

### **Presentations in International Conferences**

- B. Pekmen, M. Tezer-Sezgin, DQM Time - DQM Space Solution of Hyperbolic Telegraph Equation, 24th Biennial Conference on Numerical Analysis, University of Strathclyde in Glasgow, Scotland, June 28th - July 1st, 2011.
- B. Pekmen, M. Tezer-Sezgin, Numerical Solution of Unsteady Magnetohydrodynamic Flow in a Rectangular Duct by using differential quadrature method both in time and space, International School on Magnetohydrodynamics and Fusion Applications, September 9th-16th 2011, ITAP, Turunc, Marmaris, Mugla.
- B. Pekmen, M. Tezer-Sezgin, DRBEM solution of MHD free convection in a square cavity filled with a porous medium, International Conference on Applied and Computational Mathematics, October 3rd-6th 2012, Institute of Applied Mathematics, METU, Ankara.
- M. Tezer-Sezgin, B. Pekmen, DRBEM solution of liquid metal MHD flow in a staggered double lid-driven cavity, July 16th-18th 2013, BETEQ (Boundary Element Technique An International Conference) 2013, Paris, France.
- B. Pekmen, M. Tezer-Sezgin, DRBEM solution for the incompressible MHD equations in terms of magnetic potential, July 16th-18th 2013, BETEQ (Boundary Element Technique An International Conference) 2013, Paris, France.

- M. Tezer-Sezgin, B. Pekmen, DRBEM Solution of full MHD and temperature equations in a lid-driven cavity, ENUMATH 2013, The European Numerical Mathematics and Advanced Applications, August 26th-20th 2013, Lausanne, Switzerland. Two pages abstract published.
- B. Pekmen, M. Tezer-Sezgin, Steady Mixed convection in a Heated Lid-Driven Square Cavity filled with a Fluid-Saturated Porous Medium, ENUMATH 2013, The European Numerical Mathematics and Advanced Applications, 26-30 August 2013, Lausanne, Switzerland. Two pages abstract published.